Nanocrystalline sol-gel Nb_2O_5 coatings

Preparation, characterisation and application to photovoltaic cell, lithium battery and electrochromic device

Dissertation

Zur Erlangung des Grades
des Doktors der Ingenieurwissenschaften
der Naturwissenschaftlich-Technischen Fakultät III -
Chemie, Pharmazie und Werkstoffwissenschaften
der Universität des Saarlandes

von

Yeping Guo

Saarbrücken

2002

Tag des Kolloquiums:	07.02.2003
Dekan:	Professor Dr. Horst Vehoff
Berichterstatter:	Professor Dr. Michel A. Aegerter
	Professor Dr. Michael Veith
Vorsitzender:	Professor Dr. Wulff Possart
Beisitzer	Dr. Hermann Sachdev

Acknowledgements

My doctoral research work was realized under the supervision of Prof. Dr. Michel A. Aegerter, Director of Department of Coating Technology, Institut für Neue Materialien, gem. GmbH, Saarbrücken, Germany. I would like to thank him for his guidance and discussions during the course of this work and for his constructive criticism and English correction during the writing of this thesis.

I am greatly indebted to the Institut für Neue Materialien, gem. GmbH for financial support and to the Federal Ministry for Education, Research and Technology of Germany and the State of Saarland.

I cannot forget to mention Dr. Thomas Krajewski (HRTEM and SEM), Rudolf Karos (XRD), Institut für Neue Materialien, gem. GmbH, and Mr. Jörg Schmauch (Thermal Analysis), Lehrstuhl für Technische Physik der Universität des Saarlandes, for their assistance during various experiments and for their many suggestions. I also thank Mr. Zhong-Fan Liu, Lehrstuhl für Functionswerkstoffe der Universität des Saarlandes, for his scanning white light interferometric measurements.

I am grateful to Dr. Sabine Heusing, Dr. Michael Schmitt and Mr. Roman Maschek for their friendly supports and help during initial stage of this works.

Special thans to Dr. Sabine Heusing, Guido Gasparro who translated the abstract and summary of this thesis into Germany.

Many thanks to my colleagues Christian Göbbert, Harish Bisht, Dr. Jörg Pütz, Guido Gasparro, Rolf Danzebrink and Thomas Schuler for their friendship, understanding and their support.

I also thank my other friends and colleagues, from and outside INM, who made this work affordable and my life in Germany so pleasant.

Finally, I offer my appreciation to my wife, Li-Hua Tang, and my daughter, Wen-Qian, as well as my parents, for their patience, understanding, encouragement and help in many ways that gave me faith and strength to finish this dissertation research work.

Abstract

Thick and thin films of Nb_2O_5 have been prepared by the sol-gel process using cheap niobium pentachloride as precursor and a new synthesis route. The microstructure of the films was tailored by adding poly(ethylene glycol) (PEG) and carbon soot into the sol and varying the sintering temperature. The thesis describes the properties of the sols and their influence on the properties of the resulting nanocrystalline Nb_2O_5 films as electrodes in dye sensitised solar cells, electrochromic devices and rechargeable lithium batteries. A solar light-to-electric conversion efficiency of Ru(II) sensitised Nb_2O_5 solar cell as high as 7% under 120 W/m^2 illumination was obtained. An equivalent electric circuit of the dye sensitised electrode/electrolyte interface based on the electrochemical impedance spectroscopy was modelled and found to fit all the results. The values obtained for the electric elements from the simulation of the results were found to relate material parameters to the cell performance and their influence on the cell performance are illustrated. The electrochromism and Li^+-charge and discharge of the Nb_2O_5 films exhibited also good performance.

Kurzfassung

Dicke und dünne Nb_2O_5-Schichten wurden mit der Sol-Gel Technologie hergestellt, wobei günstiges Niob(IV)-Chlorid als Precursor und eine neue Syntheseroute eingesetzt wurden. Die Mikrostruktur der Schichten konnte durch den Zusatz von Polyethylenglykol (PEG) und Kohlenstoff-Ruß zum Sol und durch Variation der Sintertemperatur verändert werden. Im Rahmen der Arbeit wurden die Eigenschaften der Sole und deren Einflüsse auf die Eigenschaften der resultierenden nanokristallinen Nb_2O_5-Schichten als Elektroden in farbstoffsensibilisierten Solarzellen, in elektrochromen Zellen und in Lithiumakkumulatoren untersucht. Mit einer Ru(II)-sensibilisierten Nb_2O_5-Solarzelle wurde zur Umwandlung von solarer in elektrische Energie ein Wirkungsgrad von 7% bei Belichtung mit 120 W/m^2 erzielt. Basierend auf der elektrochemischen Impedanzspektroskopie wurde ein Ersatzschaltbild als Modell für die farbstoffsensibilisierte Nb_2O_5-Elektroden/Elektrolyt-Grenzfläche erstellt, mit welchem die gemessenen Werte gut simuliert werden können. Die elektrischen Elemente und deren Werte, die aus der Simulation der Meßwerte erhalten wurden, konnten Materialparametern der Zelle zugeordnet und ihr Einfluß auf die photoelektrochemischen Eigenschaften der Zelle beschrieben werden. Die Nb_2O_5-Schichten zeigten darüber hinaus auch gute elektrochrome Eigenschaften und gute Li^+-Beladungs- und Entladungscharakteristiken.

Zusammenfassung

Unter Verwendung von billigem $NbCl_3$ wurden viskose kolloidale Nb_2O_5-Sole über den Sol-Gel Prozess hergestellt, die zur Abscheidung von dünnen und dicken Nioboxid Schichten auf Glassubstraten geeignet sind. Durch Zugabe einer definierten Menge Wasser, findet eine teilweise Hydrolyse des Niobchloroethoxy-acetat statt, das sich beim Lösen des $NbCl_3$ in einem Ethanol/Eisessig Gemisch bildet. In einer Komplexierungsreaktion werden Chlorid-Ionen durch Sauerstoffatome des PEG in den Kolloiden ersetzt. Es resultiert ein hochviskoses und stabiles Sol, bestehend aus kleinen kolloidalen Partikeln. Die Reaktionsabläufe während der Reaktion werden diskutiert. Ein Erhitzen des Sols auf 96°C verbessert dessen Stabilität. Durch Zugabe eines Binders wird eine starke physikalische Adhesion und mechanische Belastbarkeit des Films während des Trocknungs- und Sinterungsprozess gewährleistet. Ein Einbringen von Polyethylenglycol (PEG) und Russ in die Beschichtungslösung beeinflusst die Struktur und die Morphologie der resultierenden Schichten deutlich. Die Herstellung dicker Nb_2O_5 Schichten erfolgte im Spin-Coatingprozess. Bei einer Sintertemperatur von 400°C beginnen die Schichten zu kristallisieren und bestehen aus einer einzelnen hexagonalen Phase. Wird die Sintertemperatur auf 600°C erhöht, kristallisieren die Schichten in einer orthorombischen Nb_2O_5 Phase aus. Ohne Zugabe von PEG und Russ bestehen die Schichten wenn sie bei einer Temperatur von 400°C gesintert werden, aus hexagonalen Nioboxid und orthorombischen Nb_3O_7Cl Phasen. Bei Sintertemperaturen grösser als 600°C enthalten die Schichten neben orthorombischen Nb_2O_5 noch einen kleinen Anteil von orthorombischen Nb_3O_7Cl Phasen. Durch die Seperation bzw. Dispersion des PEG und das Austreiben der organischen Rückstände aus der Schicht während des Sinterprozesses, nimmt ihre Oberfläche und ihr Rauhigkeitsfaktors erheblich zu. Beide Faktoren bestimmen die Menge des Farbstoffes, der von der Schicht absorbiert werden kann. Direkt verknüpft mit der Menge des absorbierten Farbstoffes ist die Lichtausbeute. Je höher die Menge Des absorbierten farbstoffes ist, umso grösser ist die Lichtausbeute. Durch die Temperaturbehandlung der Schichten verändert sich die Grössenverteilung und die Form (von einer tintenfassartigen Form mit engem Hals zu einer mehr zylindrischen Form) der Poren. Darüber hinaus wird die Verbindung zwischen den Kristalliten verbessert. Die hohe spezifische Oberfläche, die passenden Korngrössen, die hohe Porosität und die gewünschte Phasenbeschaffenheit des nanocrystallinen Nb_2O_5, durch die Zugabe von PEG und C, sind verantwortlich dafür, das das Material, als Elektrode in Farbstoff-Sensibilisierten Solarzellen eingesetzt werden kann. Mittels Thermoanalyse, Infrarotspektroskopie, Röntgenbeugungsanalyse und BET Oberflächenanalyse konnte gezeigt werden dass die Veränderung in der Zusammensetzung und Mikrostruktur der Schichten von der Zugabe der Additive und der Temperaturbehandlung abhängig ist. TEM und SEM bestätigen die Ergebnisse. Die hergestellten Nb_2O_5 Proben wurden mit kommerziellen TiO_2 (P25, Degussa) verglichen.

Nicht Farbstoff-Sensibilisierte Nb_2O_5 Elektroden zeigen photoelektrochemische Eigenschaften bei Bestrahlung mit UV Licht. Die Bandlücke des Materials wurde mit E_g= 3.06eV bestimmt. Außerdem konnte bestätigt werden, dass die Schichten einen kleineren photokatalytischen Effekt bei der Photoelektrolyse von Wasser als TiO_2-Schichten besitzen.

Die photoelektrochemische Eigenschaften von verschiedenen mit Ru(II)- Komplexen sensibilisierten Nb_2O_5 Elektroden wurden mit Hilfe der linear sweep Voltametrie untersucht und das Photostrom Aktionsspektrum gemessen. Die photoelektrochemische Eigenschaften der Elektroden werden entscheidend von den Additiven, der Sintertemperatur, der Schichtdicke und der Art des Redoxsystems beeinflusst. IPCE bis zu 64% bei 545 nm konnten erreicht werden

Weiterhin wurden das Verhalten von Farbstoff sensibilisierten Nioboxidschichten mitttels von Elektrochemischer Impedanz Spektroskopie untersucht. Der Nyquist Plot zeigt zwei Halbkreise. Alle Ergebnisse konnten mit einem Ersatzschaltbild angefittet werden. Es besteht aus einem in Serie geschalteten Widerstand R_s, und 2 Schaltkreisen, die sich aus einem Widerstand und einem parallel angeordneten CPE Element zusammensetzten. Für die aus der Simulation erhaltenen Werte der elektrischen Komponeten, findet man eine Abhängigkeit vom Elektrodenmaterial, von den in das Sol eingebrachten Additiven, von der Sintertemperatur, von der Schichtdicke und von der Zusammensetzung des Elektroyts. Der Gesamtwiderstand von Elektrolyt und Elektrode (Nb_2O_5+TCO) kann mit Hilfe eines frequenz-unabhängigen Widerstand beschrieben werden. Der erste parallele RC Stromkreis im hoch frequenz Bereich ist verknüpft mit frquenzantwort der Schichtmikrostruktur, der Kontaktierungseigenschaften zwischen Schicht und Substrat und der Verbindung zwischen den Nanokristalliten. Der zweite parallele RC Stromkreis bei niedrigen Frequenzen (f> 1 kHz) beschreibt die photoelektrochemischen Eigenschaften der Farbstoff sensibilisierten Elektroden. Dabei steht R_{ct} für einen kinetischen Faktor und C_{dl} für einen thermodynamischen Faktor.

Die photovoltaische Leistung von Solarzellen hängt im starken Maße vom verwendeten Lösungsmittel im Redoxsystem, von der Geometrie der Elektroden und der Lichtintensität ab. Bei einer Bestrahlung von 100W/m^2 beträgt der Wirkungsgrad 7%. Allerdings sinkt der Wirkungsgrad kontinuierlich mit steigenden Lichtintensitäten. Trotzdem sind die beobachteten Ergebnisse als besser, als vergleichbare aus der Literatur. Der allmähliche Rückgang des Umwandlungswirkungsgrades unter Sonneneinstrahlung kann durch einen höhren Serienwiderstand der Zelle und einer steigenden Anzahl von Umkehrreaktionen erklärt werden. Der Wirkungsgrad der Nioboxidsolarzellen ist niedriger als von Solarzellen bei denen TiO_2 verwendet wird.

Dicke nanokristalline Nioboxid Schichten wurden ebenfalls hinsichtlich ihrer Eigenschaft als Lithium Ionen speichernde Elektroden für Batterien untersucht. Obwohl sie eine hohe Entladungskapazität besitzen, ist die Reversibilität der Elektroden schlecht und nur eine kleiner Teil der anfänglichen Entladungskapazität kann durch einen Wiederaufladungsprozess wieder hergestellt werden. Es konnte gezeigt werden das die

Entladungskapazität durch Einsetzen eines cut-off Potential für die Ladung gesteuert werden kann. Bei niedrigeren Kapazität zeigen die Nb_2O_5 Schichten eine gute Reversibilität (>1000 Zyklen).

Es wurden dünne transparente Nb_2O_5-Schichten mit Hilfe des Spin Coating Verfahren hergestellt. Als Beschichtungslösung wurde eine Nb_2O_5 +PEG20000 Lösung verwendet. Die electrochromen Eigenschaften der Schichten wurden bestimmt. Der Ein- und Ausbau Vorgang von Lithium in 1 M $LiClO_4$-PC Lösung führt zu einer Änderung der optischen Transmission (ΔT_{550nm} =41%). Die Untersuchung der Kinetik des Einfärbungs- und Entfärbungsprozess zeigt, das der Übergang der Lithiumionen an der Grenzfläche Elektrolyt Schicht der geschwindigkeitsbestimmende Schritt während der Einfärbung ist. Bei der Entfärbung ist die Geschwindigkeit von der Bewegung der Lithiumionen in der Schicht abhängig . Es konnten keine besseren Ergebnisse als die Literaturbekannten gefunden werden.

Gegenwärtig ist Nb_2O_5 das zweitbeste Material um eine Graetzelzelle herzustellen. Extrapoliert man die in dieser Arbeit gefunden Ergebnisse auf eine bessere Zellgeometrie (0,5 cm x 0,5 cm^2) und wird ein besserer Elektrolyt ausgewählt, kann ein Wirkungsgrad von bis zu 7% bei Sonneneinstrahlung erwartet werden. Verbesserung sind möglich, wenn es gelingt die Porengrösse zu erhöhen oder durch die Verwendung besserer Farbstoffe, wie z. B. dem sogenannten Schwarzfarbstoff. Gegenwärtig wird für Solarzellen mit vergleichbarer Effizienz TiO_2 aufgrund seines günstigen Preises bevorzugt. Bedenkt man aber, das der Anteil des Preises für Nano-TiO_2 nur 7% der Gesamtkosten der Solarzelle beträgt, TiO_2 Zellen gegen UV- Bestrahlung geschützt werden müssen und das Nioboxid weniger photokatalytisches Verhalten als TiO_2 zeigt, kann Nioboxid als vielversprechendes Material, gerade für großflächige Einzelssolarzellen oder Module, angesehen werden.

Contents

List of Abbreviations

AC	alternating current
Ac	aceto, -O-CH_2-CH_3
ACN	acetonitrile
AM	air mass
BET	Brunauer-Emmett-Teller
BJH	Barrett-Joyher-Halenda
Bu	Butyl, -$(CH_2)_3$-CH_3
CA	chronoamperometry
CAS-No.	chemical abstracts registry number
CB	conduction band
CE	(a) chronopotentiometry (b) counter electrode
CNRLS	complex non-linear regression least squares
CPE	constant phase element
CV	cyclic voltammetry
CVD	chemical vapour deposition
DBU	1.8-diazabicyclo (5.4.0) undec-7-ene (1.5-5)
DIN	Deutsche Industrie-Norm
DMF	N,N-dimethylformamide
DTA	differential thermal analysis
e	electron
DTG	differential thermogravimetry
EC	electrochromic electrode
e.g.	*exempli gratia* (for example)
EIS	electrochemical impedance spectroscopy
Et	ethyl, -CH_2-CH_3
et al.	*et alii* (and others)
etc.	*et cetera*
FF	fill factor
FTIR	Fourier transform infrared spectroscopy
FTO	fluorine-doped tin oxide
h	hour
HRTEM	high resolution transmission electron microscopy
i.e.	*idest* (that is)
INAP	Institut für angewandte Photovoltaik
INM	Institut für Neue materialien, gem. GmbH
IPCE	incident photo-to-current conversion efficiency
IS	impedance spectroscopy
ITO	tin-doped indium oxide
IUPAC	International Union of Pure and Applied Chemistry
JCPDS	Joint Committee on Powder Diffraction Standards
LHE	light harvesting efficiency
min.	minute
MS	mass spectroscopy
nc-DSC	nanocrystalline dye sensitised solar cell
NHE	normal hydrogen electrode
NIR	near infrared

NMR	nuclear magnetic resonance
OC	open circuit
OCV	open circuit potential
Ox	oxidised species
PC	propylene carbonate
PCS	photon correlation spectroscopy
PEC	photoelectrochemical/photoelectrochemistry
PEG	poly(ethylene glycol)
Pr	propyl, $-(CH_2)_2-CH_3$
PV	photovoltaic
PVD	physical vapour deposition
Red	reduced species
RMS	root-mean-square
SC	(a) semiconductor
	(b) short circuit
SCE	saturated calomel electrode
SEM	scanning electron microscopy
STP	standard temperature and pressure
TCO	transparent conducting oxide
TG	thermogravimetry
UV	ultaviolet
VASRA	variable angle specular reflectance accessory
VB	valence band
VIS	visible
vol.-%	volume per cent
vs.	*versus*
wt.-%	weight per cent
XRD	X-ray diffraction

Major symbols and units

A	(a) area of electrode, cm^2 (b) constant
A_{dye}	area of a dye molecule, nm^2
a, b, x, y	number of atoms in molecular formula
C	(a) capacitance, F (b) function of the energy of interaction between adsorbent and adsorptive
$C^*_{I^-}$	bulk concentration of I, M, mol/cm^3
$C^*_{I_3^-}$	bulk concentration of I_3^-, M, mol/cm^3
$C_{I^-}(0,t)$	surface concentration of I^- at time t, M, mol/cm^3
$C_{I_3^-}(0,t)$	surface concentration of I_3^- at time t, M, mol/cm^3
C_{dl}	capacitance of double charge layer, mF or μF
C_o^*	bulk concentration of Li^+, M, mol/cm^3
C_{sc}	space charge capacity, F
D	diffusion coefficient, cm^2/s
D_f	fractal dimension
d	(a) average grain size, nm (b) thickness of film, μm
d_{BET}	average particle size, nm
E	potential or potential phasor, V
E_{CB}	energy of the conduction band edge, eV
E_f^n	quasi-Fermi level of electrons, eV
E_f^p	quasi-Fermi level of holes, eV
E_g	band gap of semiconductor, eV
E_{redox}	electrode potential, V
$E^o_{\mathrm{Re}dox}$	formal potential, V
$E^{oc}_{\mathrm{Re}dox}$	electrode potential under open circuit condition
F	the faraday, charge of one mole of electrons, C
f	frequency of a sinusoidal oscillation, s^{-1}
g	gravitational acceleration constant, cm/s^2
h	Planck´s constant
h_c	critical thickness
h_o	(a) deposited film thickness in dip coating process (b) initial thickness in spin coating process
h(t)	thickness at time t
I_m	cell photocurrent at maximum power output, mA
I_o	intensity of light, mW/cm^2
I_{sc}	short circuit photocurrent density, mA/cm^2
Im(ω)	imaginary part of a frequency dependent complex function
i	photocurrent density, mA/cm^2
i_d	dark current density, mA/cm^2
i_{inj},	electron injection current density, mA/cm^2
i_o^{ph}	exchange current density at illumination, mA/cm^2
i_o^r	surface recombination exchange current density in the dark, mA/cm^2
i_{ph}	photocurrent density, mA/cm^2

i_r	surface recombination current density, mA/cm^2
i(t)	current density at time t, mA/cm^2
K	capillary constant, mm^2/s^2
K_{ic}	critical stress intensity
k	Boltzmann´s constant, J/K
k_a	rate constant of light excited dye to its ground state
k_b	rate constant of a conduction band electron returning back to oxidised dye molecule
k_{ct}^o	standard reaction rate constant
k_2	rate constant for electron injection into conduction band of semiconductor
k_3	rate constant for reduction of oxidised dye molecule
L	length, µm
m	constant, ½ or 2
m_e^*	effective mass of electron
N_A	Avogadro´s constant, mol^{-1}
N_{CB}	effective density of state
n	(a) electrons per molecule oxidised or reduced (b) refractive index
n_e	electron density
ΔOD	change of the optical density between bleached and coloured state
Q	total charge during coloration, C
q	charge of an electron, 1.60218×10^{-19} C
q_1	heat of interaction for the first layer
q_L	latent heat of condensation for the adsorbate
R	(a) gas constant, Jmol^{-1}K^{-1} (b) resistance, Ω
R_{ct}	charge transfer resistance, Ω
R_q	surface roughness (rms), µm
R_s	total resistance independent on measured frequency, Ω
R_{sc}	resistance of semiconductor, Ω
R_{sc}^{dark}	resistance of semiconductor in the dark, Ω
$R_{sc}^{illumination}$	resistance of semiconductor under illumination, Ω
Re(ω)	real part of a frequency dependent complex function
r	core diameter of a cylindrical pore, nm
r_a	core diameter of a pore neck
r_b	core diameter of a pore body
S_{BET}	BET surface area, m^2/g
S_{dye}	surface area occupied by the dyes, m^2/g
T	absolute temperature, K
T_s	sintering temperature, °C
t	time, h, min., s
U_o	withdrawal speed
U(t)	voltage at time t, V
V_{fb}	flat band potential, V
V_m	(a) cell voltage at maximum power output, V (b) monolayer capacity, cm^3
V_{oc}	photovoltage under open circuit condition, V
v	(a) kinematic viscosity, mm^2/s

x	(a) distance
	(b) number of atoms
Y	height, μm
Y_{Lv}	liquid-vapour surface tension
$Z(\omega)$	impedance, Ω
α, α'	transfer coefficient
$\alpha(\lambda)$	absorptivity of dye
β	full width at half maximum of the diffraction peak
Γ, Γ_{area}	number of moles of dye per square centimetre, mol/cm^2
Γ_g	number of moles of dye per gram, mol/g
η	(a) coloration efficiency
	(b) liquid viscosity
	(c) photo-to-electric conversion efficiency
η_e	charge collection efficiency
θ	diffraction angle
θ_B	Brewster´s angle
λ	wavelength, nm
ν	frequency of light
ρ	density, g/cm^3
ρ_p	density of porous film, g/cm^3
σ	(a) conductivity, S
	(b) stress of the film
$\sigma(\lambda)$	absorption, cm^2/mol
τ	time constant
ϕ	(a) diameter, nm, mm
	(b) phase shift
Φ_{inj}	quantum yield for charge injection
$\Delta\Phi(H)$	galvanic electrical potential across the Helmholtz layer, eV
$\Phi(\lambda)$	incident photon flux density at wavelength λ
Ω	function that depends on the ratio of the elastic modulus of the film and substrate
ω	(a) angular frequency of a sinusoidal oscillation, $2\pi f$
	(b) angular velocity

1 Introduction and objectives

Global environmental problems have attracted increasing attention in recent years. Fossil fuels such as petroleum are a result of processes that used solar energy at an energy conversion efficiency of about 0.02% for a period of about 200 million year. Humans activities are close to depleting these energy sources in just 100 - 200 years and are also resulting in a rapid increase of carbon dioxide and sulphur oxide in our atmosphere, thereby causing abnormalities in our global environment.

The increase of the world's population combined with the growth per capita of energy consumption are expected to bring an explosive rise in energy consumption. To solve these problems, we need to save energy, increase the efficiency of equipment's transforming energy and develop the use of new sources of energy.

Solar energy is attracting a great deal of attention because it is a clean energy source and will not be depleted. Among the devices available for utilising the sun's energy, the most prominent one is the solar cell, which uses the photovoltaic effect of semiconductors to convert solar light energy to electric energy [1-4]. A conventional p-n junction photovoltaic cell can be made for example from silicon. When light enters the cell, an electron is excited, leaving behind a hole, these entities separate across the p-n junction and the positive and negative charges diffuse toward two supported electrodes. To avoid charge carrier recombination during the diffusion, the concentration of defects in the solid must be small. This impose severe requirements on the purity of the semiconductor material, rendering solid-state devices of the conventional type expensive.

Grätzel et al. [5-14] have developed an original molecular photovoltaic system for solar light harvesting and conversion to electricity. It is based on the spectral sensitisation of a TiO_2 nanocrystalline semiconductor film by suitable transition-metal complexes. Grätzel has ingeniously found a solution in which the light harvesting efficiency reaches nearly 100% by using a high surface area TiO_2 film with a 1000-fold roughness factor. In contrast to the conventional system, the function of the light absorption and that of the carrier transport are separated. The light harvesting is carried out by the sensitizer which is excited by photons to produce electrons rather than electron-hole pairs. This renders unnecessary the use of expensive solid-state components in the system. The system is also not sensitive to defects in the semiconductor. Oxide semiconductors such as TiO_2, ZnO, Nb_2O_5, WO_3, SnO_2, In_2O_3 and $SrTiO_3$ can be used. The photovoltaic performance of the solar cell depends remarkably on the semiconductor materials and their microstructures. The combination of dye and semiconductor is also very important to obtain highly efficient dye-sensitised solar cells.

The dye-sensitised nanocrystalline solar cell is at present a potential competitor to solid state junction devices for conversion of solar energy into electricity. The INAP consortium in

Germany has recently produced a 120 cm^2 Z-type interconnected module having an efficiency of 7% [15]. A watch powered with a dye-sensitised nanocrystalline solar cell produced by the Swatch Group Corp. of Switzerland was reported in the technical press [16].

Nb_2O_5 possesses similar semiconductor properties as TiO_2. It is known from works of Aegerter et al. [17-28] that Nb_2O_5 films can be prepared by many sol-gel routes and open the way to new wide-ranging application. In the field of solar cell Nb_2O_5 appears as an alternative electrode material which does not decompose the dyes, contrary to TiO_2. The unique optical and electronic features of nanocrystalline Nb_2O_5 can be also exploited to realise opto-electronic devices exhibiting outstanding performance. They include super-capacitor, sensors, photovoltaic cells and electrochromic windows, as well as intercalation batteries. This work deals with the synthesis of niobia sols and porous nanocrystalline Nb_2O_5 coatings, their microstructural characterisation and their application for solar-to-electric energy conversion, batteries and electrochromic devices.

Fundamental aspects of solar cells, rechargeable batteries, electrochromic devices as well as the physical and chemical properties of Nb_2O_5 and a brief description of the sol-gel process are given in chapter 2.

Chapter 3 presents the state of the art of the preparation of Nb_2O_5 semiconducting coatings and their use for the development of the above devices.

The experimental procedure, synthesis of sols, preparation of niobia films and powders and devices and the different techniques used for their characterisation, is the subject of chapter 4.

In particular section 4.1 a new sols synthesis to prepare both thick and thin films using cheap niobium pentachloride as precursor is described.

Chapter 5 presents the results and several discussions. The influence of the chemical composition, the content of water added into the sols, the hydrolysing and reflux time, the addition of binders etc. on the viscosity of the sols and sol-to-gel transition is studied to give an understanding about the Nb_2O_5 sol-gel process is shown in section 5.1.

The preparation of powders and porous, nanocrystalline Nb_2O_5 films deposited on conducting transparent oxide (TCO) glass by dip or spin coating techniques and the optimization of the coating conditions and drying and sintering processing is shown in section 4.2, 4.3, 5.2 and 5.3 respectively.

The characterisation of their microstructural properties such as specific surface area, pore size, pore volume, density nanocrystallite size, crystal phase, and morphology of Nb_2O_5 films and powders using thermal analysis, infrared spectroscopy, X-ray diffraction, nitrogen adsorption and desorption, scanning electron microscopy, high resolution transmission electron microscopy, and scanning white interferometer is shown in section 5.2 and 5.3. The microstructure of films tailored by adding organic binders into the sol and varying the sintering temperature is also discussed.

The main objective, i.e. the study of their properties as electrodes in dye sensitised solar cells, rechargeable lithium batteries and electrochromic devices is reported in section 5.4, 5.5, 5.6 and 5.7, respectively. In such multi-component systems, the overall performance of the devices where found to critically depends on the individual properties of the constituent components and processes. Particularly, by dealing with dye sensitised nanocrystalline solar cell, the structure, morphology, optical and electrical properties of the nanoporous Nb_2O_5 layer, the chemical, redox, photophysical and photochemical properties of the dye, the visco-elastic and electrical properties of the electrolyte carrying the redox mediator, the redox and optical properties of the redox mediator, the electrical and optical properties of the counter electrode are some of the major properties which are discussed. For this complicate system regarding key processes are investigated using an electrochemical impedance technique. A comprehensive understanding of the operating mechanism of dye sensitised solar cells and the key factors controlling the power conversion of the solar cells are given. Moreover, commercial TiO_2 powder (P25) and TiO_2 films (INAP) are compared with our Nb_2O_5 powders and films. In addition, the electrochromism and Li^+-charge and discharge of the Nb_2O_5 films are reported.

2 Fundamental aspects

2.1 Principle of solar cells

2.1.1 Conventional photovoltaic solar cells

Solar cells are devices which convert solar energy (light) into electricity either directly via the photovoltaic effect or indirectly by first converting the solar energy into heat or chemical energy.

The most common form of solar cells uses the photovoltaic (PV) effect in which light falling on a two layer semiconductor device produces a photovoltage (potential difference) between the layers. This voltage is capable of driving a current through an external circuit and thereby producing a useful work. The silicon p-n junction solar cell serves as a reference device for all solar cells. In such a cell the silicon is doped in such a way to create a p-type and a n-type region and thereby producing a p-n junction. A silicon atom has 4 relatively weakly bound (valence) electrons, which bond to adjacent atoms. Replacing silicon atoms with atoms that have either 3 or 5 valence electrons, e.g. boron or phosphorus respectively, will therefore produce either a space with excess holes (p-type) or excess electrons (n-type) that can move more freely than the former (figure 1).

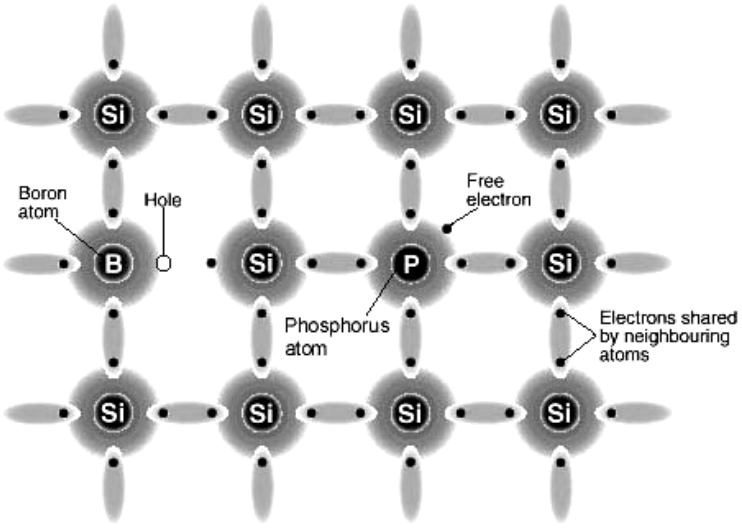

Figure 1: Silicon crystal lattice with dopant atoms [29].

Figure 2 shows the principle of a typical silicon p-n junction solar cell. Visible and UV light inciting on the front surface generates electron-hole pairs on both sides of the junction, i.e. in the n-layer and in the p-layer, and the internal electric field produced at the junction separates positive charges ("holes") from the negative charges (electrons) within the photovoltaic device:

the holes diffuse to the positive p-layer and the electrons diffuse to the negative n-layer. Although these opposite charges attracted each other, most of them can only recombine by passing through an external circuit outside the material because of the internal potential energy barrier. Therefore power can be produced from the cells under illumination, since the free electrons have to pass through the load to recombine with the positive holes.

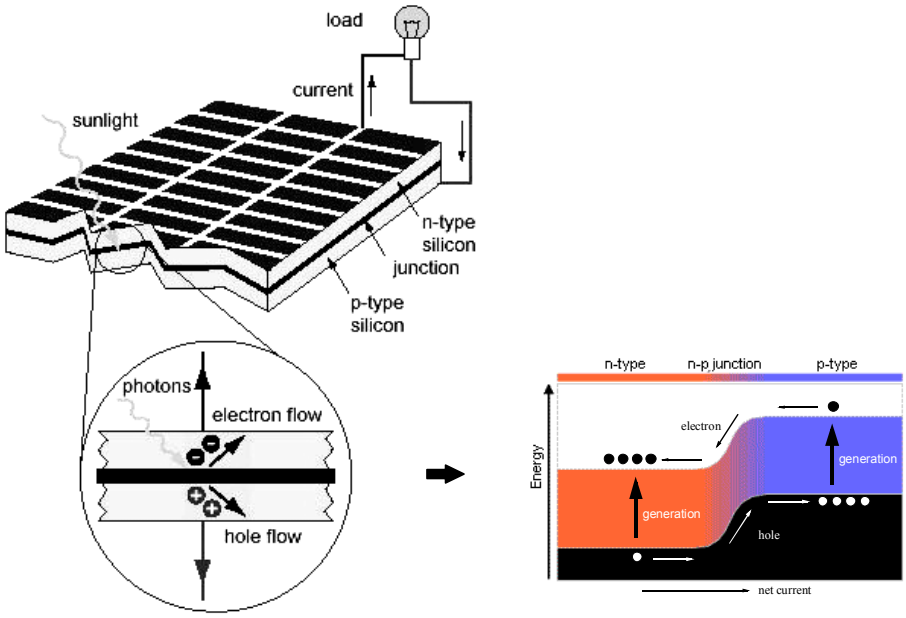

Figure 2: Principle of a silicon p-n junction solar cell [29].

The amount of power available from a PV device is determined by the type and area of the material, the intensity and the wavelength of the sunlight.

Currently single crystal silicon solar cells, for example, can convert up to 25% of the solar energy into electricity, and the values is limited by the radiation in the infrared region of the electromagnetic spectrum which does not have enough energy to create positive and negative charges in the material.

Polycrystalline silicon solar cells have an efficiency of less than 20% while that of amorphous silicon cells is presently about 10%, due to their higher internal energy losses.

2.1.2 Photoelectrochemical solar cells

Besides the semiconductor solid-state contacts used in photovoltaic cells, the semiconductor-electrolyte contact can also be used for conversion of light energy into electric power [30-38]. A photoelectrochemical cell (PEC) is defined as an electrochemical cell having photoactivity, in other words, a cell generating an electric potential or inducing electrochemical reactions under illumination. A typical photoelectrochemical cell is made of a semiconducting electrode, a counter metal electrode and an aqueous solution containing a redox couple, as shown in figure 3.

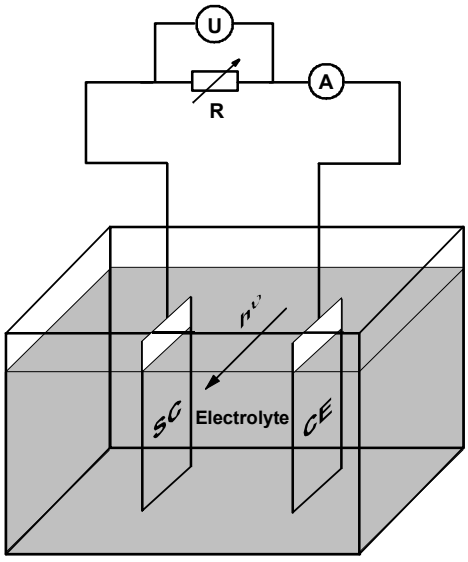

Figure 3: A typical PEC cell, composed of a semiconducting (SC) and a metal electrode (CE) immersed in a redox solution (electrolyte).

Figure 4 shows the principle of a typical regenerative photoelectrochemical solar cell. For the case of a n-type semiconductor, having its Fermi level higher than that of the redox solution, electron transfer occurs in the equilibrium state from the semiconductor electrode into the redox species, reducing the oxidised species Ox to Red until the Fermi levels of both the electrode and the solution become equal. In this way, a depletion layer and a band bending are formed in the semiconductor, as in a Schottky junction between a semiconductor and a metal where a potential barrier is formed between them.

Under illumination, electron-hole pairs are generated in a space charge region by absorption of the photon energy. Holes in the valence band reach the semiconductor surface, and oxidise the reduced species Red to oxidised species Ox. As the Ox concentration increased near the electrode surface, they diffuse toward the counter electrode and are reduced there. Electrons in the conduction band of the semiconductor reach the counter electrode surface through the external circuit. A photovoltage and a photocurrent are generated in the PEC cell. This therefore produces a steady regenerative photovoltaic cell.

Table 1 summarises the results obtained for energy conversion efficiencies in regenerative photoelectrochemical solar cell on a laboratory scale.

Although conversion efficiencies of over 15% have been obtained in the eighties, the photocorrosion of semiconductor electrodes still remains a serious problem limiting the practical application of this type of liquid-junction solar cells.

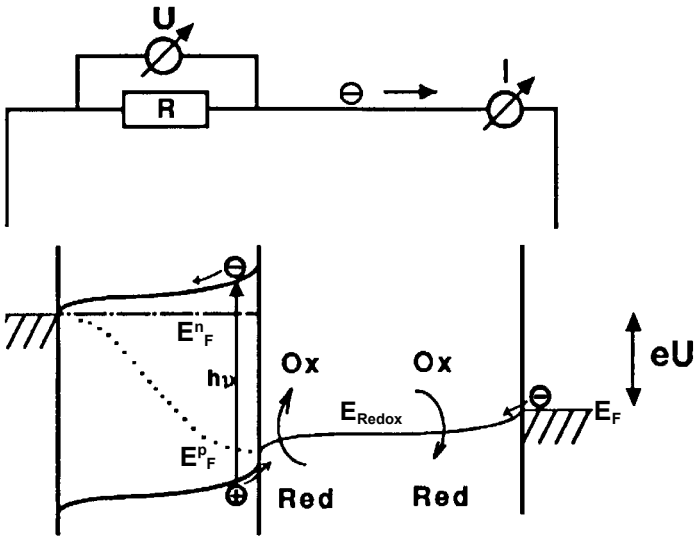

Figure 4: Principle of a typical regenerative photoelectrochemical solar cell [32].

Table 1: Energy conversion efficiencies using regenerative photoelectrochemical cells.

Semiconductor	E_g, eV	Redox couple	Solvent	η, %	References
n-CdSe	1.7	$Fe(Cn)_6^{3-/4-}$	NaOH/NaCN	16.4	[39-41]
n-Si/Pt In SiO_x	1.1	Br^-/Br_2	H_2O	14.9	[42]
n-WSe_2	1.2	I^-/I_3^-	H_2O	>14	[43]
n-Si	1.1	Fc/Fc^+	CH_3OH	14	[44-47]
n-Cd(Se, Te)	1.6	Se^{2-}/Se_n^{2-}	H_2O	12.7	[48, 49]
n-GaAs	1.4	Se^{2-}/Se_n^{2}	NaOH	12	[50-53]
n-Si/Pt In SiO_x	1.1	Br^-/Br_2	H_2O	12	[54]
n-$CuInSe_2/In_2O_3$	1.01	I^-/I_3^-	H_2O	11.7	[55]
p-InP	1.3	V^{2+}/V^{3+}	HCl	11.5	[56]
n-Si	1.1	Br^-/Br_2	H_2O	11.4	[57, 58]
n-GaAs	1.4	Fc/Fc^+	CH_3CN	11	[59]
poly-n-$CuInS_2$	1.01	I^-/I_3^-	H_2O/H^+	9.7	[60]
n-CdS	2.5	I^-/I_3^-	CH_3CN	9.5	[61]
n-$MoSe_2$	1.2	I^-/I_3^-	H_2O	9.4	[62]
n-CdSe	1.7	$S^{2-}/S_n^{2-}/Se^{2-}$	NaOH	6.9	[63]
n-FeS_2	0.95	I^-/I_3^-	H_2O	2.8	[64]

Fc: ferrocene derivative

2.1.3 Dye sensitised solar cells

2.1.3.1 Principle

Oxide semiconductors such as TiO_2 or Nb_2O_5 have exceptional thermal and photochemical stability against corrosion but their large band gap reduces enormously the fraction of solar irradiation that can be harvested. The spectral response can be improved by doping the semiconductor with appropriate metal ions or by coating them with highly colored dry molecules. It is therefore possible to induce photocurrents with light of energy lower than the band gap. The sensitization of large band gap semiconductors using colored dye molecules has

been under investigation since many years [65-67] and there is an extensive industrial interest in this field for possible applications such as photography, photochromism and photolithography [68-70]. Although attempts to use dye sensitised photoelectrochemical cells in energy conversion have been made before, the efficiency of such devices was extremely low and practical application was remote. One problem was the poor light harvesting. On a smooth surface, a monomolecular layer of sensitizer absorbs less than 1% of incident light. A dye sensitised solar cell was developed by Grätzel in the early 90s [7] and is attracting considerable interest since then [71-95]. The key factors were, first, to increase the roughness of the semiconductor surface so that a larger number of dye molecules can be adsorbed on it and be simultaneously in direct contact with the redox electrolyte and, second, the development of a ruthenium(II) complex dye which absorbs most photons in the visible light region and effectively allows to inject electrons into the semiconductor conduction band.

The nanocrystalline dye sensitised solar cell (nc-DSC or DSSC) of the Grätzel type consists of a nanocrystalline thick film deposited on a transparent conducting glass substrate where the particles are coated with a monolayer of a Ru(II)-complex adsorbed chemically, an electrolyte containing an iodide/triiodide redox mediator and a counter electrode comprising a catalyst. A scheme of the operating principle of the nc-DSC is given in figure 5. This type of cell is based on the mechanism of a regenerative photoelectrochemical process (section 2.1.2) and it differs from the conventional semiconductor devices in that the function of the light absorption is separated from that of the charge carrier transport. The heart of the system is a mesoporous oxide layer composed of nanometer size particles sintered together to allow electronic conduction to take place. Attached to the surface of the particles is a monolayer of the charge transfer dye. The solar cell photocurrent is generated by visible light absorption by the dye. The excited electrons are then injected into the conduction band of the semiconductor, diffuse through the interconnecting network of particles and are collected at the transparent conducting electrode. The resulting oxidised dye molecules are reduced by I^- ions, regenerating the original dye molecules. The oxidised iodide ions diffuse back to the Pt counter electrode as I_3^- ions, where reduction occurs to complete the cyclic process, the circuit being completed via electron migration through the external load. The high-surface-area of the nanocrystalline porous film electrode increases the incident light harvesting efficiency as more dye can be attached on the electrode. The voltage generated under illumination corresponds to the difference between the quasi-Fermi level of the electron in the solid and the redox (Nernst) potential of the electrolyte.

2.1.3.2 Model

Many models were introduced by Stangl et al. [97], Ferber et al. [98], Cahen et al. [99], Grätzel et al. [100], Matthews et al. [101], Huang et al. [102] and Gregg et al. [103]. A scheme and a generalised energy diagram are shown in figure 6. The cell is modelled as a one-dimensional, pseudo-homogeneous medium of thickness d consisting of an intermixed meso-

or nanoporous semiconductor, a charge-transfer dye and a redox electrolyte I^-/I_3^-. The direct contact of each dye molecule with the semiconductor is important for an efficient electron injection.

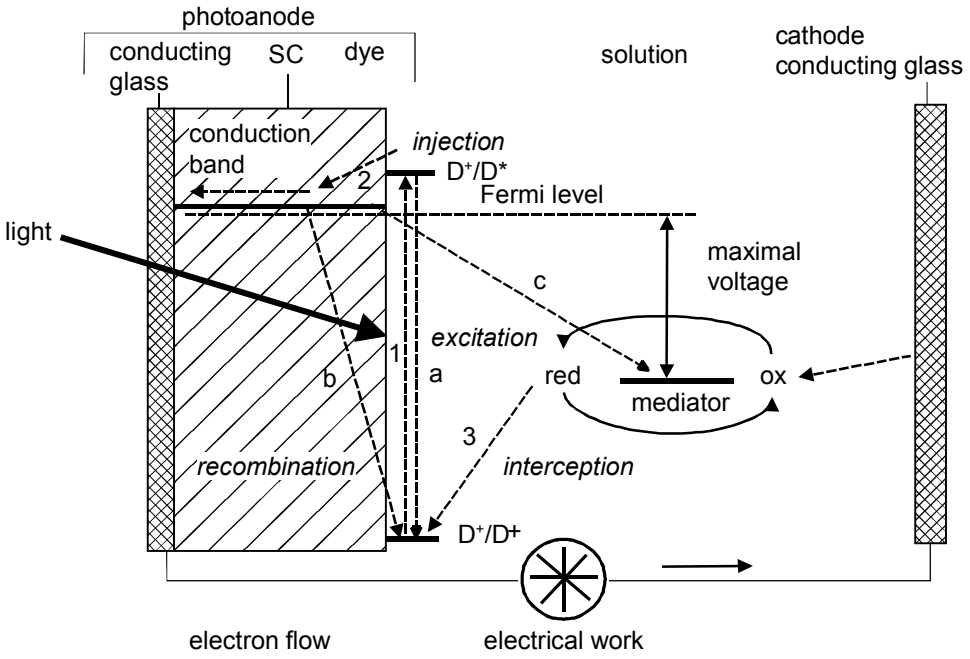

Figure 5: Principle of a regenerative dye sensitised photoelectrochemical cell (adapted from [96]).

A photon is only absorbed by the dye with a rate k_1 which passes from the electronic ground state to the excited state (reaction 1). Neither spurious absorption by direct interband excitation nor the adsorption of triiodide in the blue spectral range is taken into account.

$$h\nu + D \rightarrow D^* \tag{1}$$

The excited electron is then rapidly injected into the conduction band of the semiconductor (reaction 2, rate k_2) and the dye becomes oxidised

$$D^* \rightarrow D^+ + e \tag{2}$$

Simultaneously the oxidised dye molecule is reduced by an electron transfer from the redox species in solution (reaction 3, rate k_3)

$$D^+ + red \rightarrow D + ox \tag{3}$$

Because the reactions 1 to 3 are very fast (typically 10^{10} ~ 10^{12} s^{-1} rate) the light-induced electron injection is directly coupled with the electrolyte oxidation. When the back-reaction b, the recombination of electrons in the conduction band with holes in the dye ground state (10^7 ~ 10^5 s^{-1} rate) in figure 6 is neglected, the desired reactions 1 to 3 can be merged into one and as a consequence, the dye molecules D are not taken into account in the resulting net reaction. They compete with the electron loss reactions a, b and c (figure 6).

(a) A light excited dye molecule may relay directly to its ground state. This process is usually neglected, since the ratio of the relevant rate constants k_2/k_a is of the order 1000 [97].

(b) Conduction band electrons may return back to oxidised dye molecules. Their neutralisation should ideally occur via reaction 3 in the redox electrolyte. Since the rate constant k_3 of the latter reaction is approximately 100 times higher than k_b [97], the reaction b can be neglected, as long as the electron donor (I^-) concentration in the electrolyte remains sufficiently high which will be the case in this study. In practice, this condition is usually met also under open-circuit condition.

(c) Conduction band electrons may also be captured by the triiodide oxidised species of the electrolyte. This will be the only recombination considered in this study.

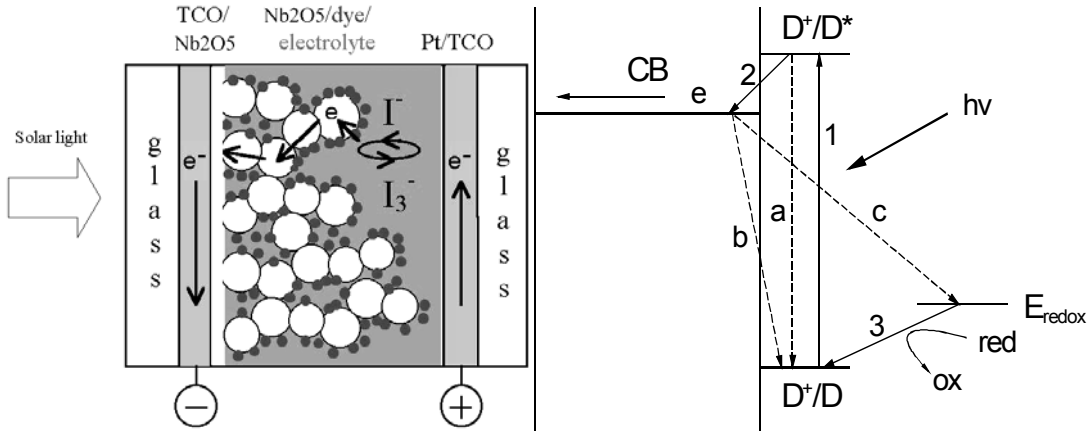

Figure 6: Scheme (lift) and energy diagram (right) of the modelled dye sensitised solar cell (see text) [104].

The total reaction of the iodide/triiodide redox electrolyte is a two-electron reaction:

$$3I^- = I_3^- + 2e^- \tag{4}$$

The observed photocurrent density i_{ph} is thus given by

$$i_{ph} = i_{inj} - i_r \tag{5}$$

where i_{inj} is the electron injection current density resulting from the dye sensitisation and i_r is the surface recombination current density resulting from reaction c.

i_{inj} is related to the incident photon flux density $\Phi(\lambda)$ by the expression [97]

$$i_{inj} = q \int_{300nm}^{800nm} \alpha(\lambda)\Phi(\lambda)\, e^{-\alpha(\lambda)x}\, d\lambda \tag{6}$$

where q is the electron charge, $\alpha(\lambda)$ is the absorptivity of the dye, x is the distance from a point in the semiconductor layer to the surface of the transparent conducting oxide (TCO).

Under illumination the charge is transferred completely at the surface between the electrolyte and the dye sensitised semiconductor according to the equation (4). The electrode reaction can thus be treated as an electrochemical half-cell. If there is a charge-transfer overpotential only, the photocurrent-overpotential characteristic would be given by the Butler-Volmer equation [105].

$$i_{ph} = i_o^{ph}\left\{\frac{C_{I_3^-}(0,t)}{C^*_{I_3^-}} e^{-\frac{\alpha nF}{RT}(E_F^n - E_{\mathrm{Re}dox})} - \frac{C_{I^-}(0,t)}{C^*_{I^-}} e^{\frac{(1-\alpha)nF}{RT}(E_F^n - E_{\mathrm{Re}dox})}\right\} \tag{7}$$

where i_o^{ph}, the exchange current density, is proportional to the standard rate constant k_{ct}^o,

$$i_o^{ph} = nF\, k_{ct}^o\, C^{*(1-\alpha)}_{I_3^-} C^{*\alpha}_{I^-} \tag{8}$$

where n is the number of electrons in the equation (4) (in our case n is 2), F is the Faraday constant, α is the transfer coefficient, $C^*_{I_3^-}$ and $C^*_{I^-}$ are the bulk concentrations of I_3^- and I^-, $C_{I_3^-}(0,t)$ and $C_{I^-}(0,t)$ are the surface concentrations at the electrolyte/semiconductor interface and E_F^n is the quasi-Fermi level. This last parameter depends on the electron density n_e in the conduction band of the semiconductor and is given by

$$E_F^n = E_{CB} - kT \ln \frac{N_{CB}}{n_e} \tag{9}$$

where E_{CB} is the energy of the conduction band edge and N_{CB} is the effective density of states in the semiconductor conduction band [106]

$$N_{CB} = 2\left(\frac{2\pi m_e^* kT}{h^2}\right)^{3/2} \tag{10}$$

where m_e^* is the effective mass of the electron and E_{Redox} is the electrode potential of the electrochemical reaction (equation 4). In open circuit condition no photocurrent is flowing under illumination and this reaction reaches a dynamic equilibrium. $E^{oc}_{\mathrm{Re}dox}$ is given by the Nernst´s equation

$$E^{oc}_{\mathrm{Re}dox} = E^{o}_{\mathrm{Re}dox} + \frac{RT}{2F} \ln \frac{C^*_{I_3^-}}{\left(C^*_{I^-}\right)^3} \tag{11}$$

where $E^o_{\mathrm{Re}dox}$ is the formal potential, an approximate value of the standard redox potential.

By applying a sufficiently small perturbation to the dye sensitised solar cell system in open circuit condition, i.e. $U(t) = E\sin(\omega t) = E_F^n - E^{oc}_{\mathrm{Re}dox}$, $C_{I_3^-}(0,t) = C^*_{I_3^-}$ and $C_{I^-}(0,t) = C^*_{I^-}$ and the equation 7 can be simplified and written as

$$i_{ph} = i_o^{ph}\left(-\frac{2FU(t)}{RT}\right) \tag{12}$$

It shows that the net photocurrent is linearly related to the small perturbation *U(t)* at or near open circuit photopotential E_F^{oc}.

The ratio $-\frac{U(t)}{i_{ph}}$ has the dimension of a resistance and is often called the charge transfer resistance, R_{ct}

$$R_{ct} = \frac{RT}{2F i_o^{ph}} \qquad (13)$$

This parameter can be evaluated by an impedance measurement, and it is a convenient index to describe the kinetic process. For an ideally reversible process the exchange current density and consequently the standard rate constant k_{ct}^{o} are infinitely high (equation 8) and R_{ct} (equation *13*) tends to zero.

The evaluation of the surface recombination current density i_r is guided by the following remarks:

because of the absence of holes in the semiconductor, the recombination process takes only place between electrons injected into the semiconductor and hole carriers localised on the triiodide anions at or within a tunnelling distance of the semiconductor/electrolyte interface, i. e. within an electrochemical double layer (figure 7). This distance (< 3nm) is smaller than the particle size (~30nm). It therefore implies that the probability for tunnelling will be tremendous if the specific surface area of the semiconductor is high. On the other side, because the surface area is large, the recombination process may strongly deteriorate the dye sensitised solar cell performance. However one possible reason that this does not occur is that the hole carrier I_3^- has a negative absolute charge, which will tend to reduce the recombination rate due to an electrical field screening.

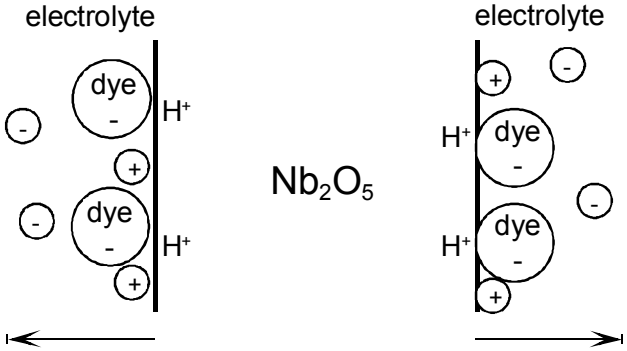

Figure 7: Schematic description of the charge distribution near the Nb_2O_5 surface (adapted from [99]).

The dyes used are acids and release protons upon binding with the semiconductor. These protons, together with other cations in the electrolyte, become part of the oxide surface region. Dipoles are formed across the Helmholtz layer between the negatively charged (iodide and dye) species and cations. The galvanic electrical potential produced by the dipoles drops across the Helmholtz layer by $\Delta\phi(H) \cong 0.3\text{eV}$ [99, 102] and helps to separate the charges and to reduce the recombination. The surface recombination current density I_r is therefore given by

$$i_r = i_o^r \left\{ \frac{C_{I_3^-}(0,t)}{C_{I_3^-}^*} e^{\frac{-\alpha' nF}{RT}\left(E_F^n - E_{\mathrm{Re}dox} - q\Delta\phi(H)\right)} - \frac{C_{I^-}(0,t)}{C_{I^-}^*} e^{\frac{(1-\alpha')nF}{RT}\left(E_F^n - E_{\mathrm{Re}dox} - q\Delta\phi(H)\right)} \right\} \qquad (14)$$

where i_o^r is the surface recombination exchange current density. The reaction c (figure 6) $I_3^- + 2e^- \longrightarrow 3I^-$ is an irreversible process due to the galvani electrical potential $\Delta\phi(H)$ at the semiconductor/electrolyte interface. When the overpotential is larger than 0.118/n V at 25°C, the back reaction of equation (4) (anodic process) contributes less than 1% to the current [105]. It implies that the Butler-Volmer expression can be simplified by neglecting the second exponential term, so that

$$i_r = i_o^r \frac{C_{I_3^-}}{C_{I_3^-}^*} e^{\frac{-\alpha' nF}{RT}\left(E_F^n - E_{\mathrm{Re}dox} - q\Delta\phi(H)\right)} = i_o^r \frac{C_{I_3^-}}{C_{I_3^-}^*} e^{\frac{-\alpha' nF}{RT}\left(U_d - q\Delta\phi(H)\right)} \tag{15}$$

where $U_d = E_F^n - E_{\mathrm{Re}dox}$ is an applied negative bias.

When the system is in the dark, $i_{ph} = 0$ and $i_{inj} = i_r = i_d$, The measured dark current and equation 15 can be written as

$$U_d = q\Delta\phi(H) + \frac{RT}{\alpha' nF}\ln i_o^r - \frac{RT}{\alpha' nF}\ln i_d \tag{16}$$

The parameters α', and i_o^r can be obtained by linear sweep voltammetry as described in section 4.7.2.

2.1.3.3 Parameters used to characterise solar cells

Several parameters are commonly used to characterise the Grätzel´s cell.

The incident monochromatic photon-to-current conversion efficiency (IPCE) or quantum yield is controlled by the position of the conduction band edge of a semiconductor and the kinetic of the electron injection from the dye excited state into the conduction band of the semiconductor (reaction 2, figure 6). Moser et al. [107] has described a model for the interfacial electron transfer reaction. One of the favourable thermodynamic condition is that the lowest level, $\nu' = 0$, of the dye excited states D^* lies above the conduction band edge. They gave a reason why the cell made with Nb_2O_5 has a smaller IPCE in the visible light region and why TiO_2 gives an injection quantum yield close to unity.

The IPCE is given by [19, 108]

$$IPCE(\lambda) = LHE(\lambda) \times \Phi_{inj} \times \eta_e \tag{17}$$

where LHE(λ) is the light harvesting efficiency, Φ_{inj} is the quantum yield for charge injection, η_e is the charge collection efficiency at the back contact.

The light harvesting efficiency is given by

$$LHE(\lambda) = 1 - 10^{-\Gamma\sigma(\lambda)} \tag{18}$$

where Γ is the number of moles of sensitizer per square centimeter of projected surface area of the film, $\sigma(\lambda)$ is the absorption cross section in units of cm^2/mol obtained from the decadic

extinction coefficient (units of $M^{-1}cm^{-1}$) by multiplication with 1000 cm^3/L, and σ is 1.42×10^7 cm^2/mol [19, 108].

The charge injection quantum yield is given by (see figure 6)

$$\Phi_{inj} = \frac{k_2}{k_2 + k_r} \tag{19}$$

where k_2 is the rate constant for charge injection into the conduction band of the semiconductor which can be obtained by time-resolved luminescence and microwave absorption measurement [109], and $k_r = k_b + k_a$ is the sum of the rate constants of the non-productive channels (figure 5 and 6).

The typical current-voltage curve of these cells is shown in figure 8. This curve is described by the following set of parameters: the short-circuit current recorded when the voltage is zero: I_{sc} (in mA/cm^2), the open circuit voltage when the current is zero V_{oc} (in V), the efficiency (η) and the fill factor (FF). From figure 8, the fill factor is given by

$$fill\ factor\,(FF) = \frac{V_m \times I_m}{V_{oc} \times I_{sc}} \tag{20}$$

where V_m (in V) and I_m (in mA/cm^2) are the cell voltage and photocurrent at maximum power output. The conversion efficiency of solar to electric energy is given by the ratio of the electrical power delivered the cell and the power of the light illuminating the cell and calculated using equation 21

$$\eta(\%) = \frac{V_m \times I_m}{light\,\text{int}\,ensity\ (W/cm^2)} \tag{21}$$

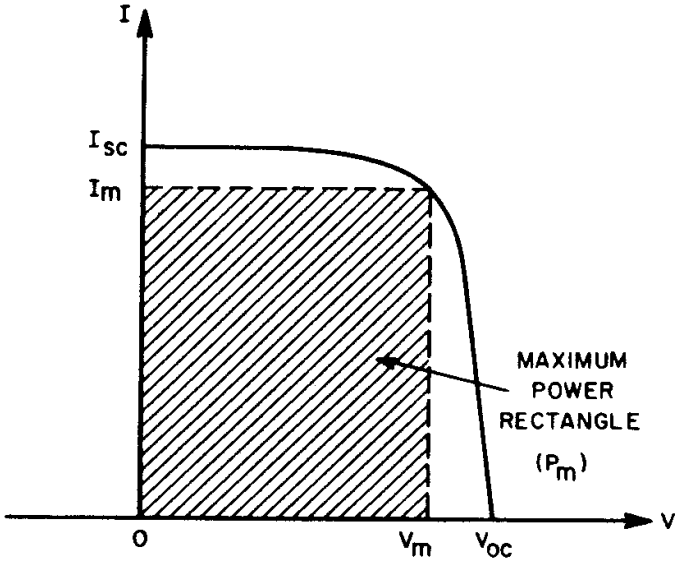

Figure 8: typical current-voltage characteristics of a solar cell under illumination (see text).

2.2 Rechargeable lithium batteries

Nb_2O_5, alike many other transition-metal oxides, exhibits a reversible intercalation of Li^+ ions into its lattice and is used as a positive or negative electrode in batteries. Figure 9 gives the principle of such a device using a positive electrode. The driving force of the battery is the difference between the chemical potential of the negative Li-electrode and the positive Li-ions in Nb_2O_5 electrode. During the discharge, the negative Li-electrode is the source of electrons for the circuit. The electrons come from the oxidation reaction of Li atoms shown in equation (a) and pass via the external circuit (where they do work) to the positive Nb_2O_5-electrode or the cathode, where electrochemical reduction of Nb_2O_5 occurs with intercalation of Li^+ into the oxide according to equation (b). Each of the reaction, (a) and (b), is known as a half-cell reaction, while the sum of the two reactions gives the cell reaction, equation (c).

$$\text{Anode} \quad Li \underset{\text{charge}}{\overset{\text{discharge}}{\rightleftharpoons}} Li^+ + e^- \qquad (a)$$

$$\text{Cathode} \quad xLi^+ + xe^- + Nb_2O_5 \underset{\text{charge}}{\overset{\text{discharge}}{\rightleftharpoons}} Li_xNb_2O_5 \qquad (b)$$

$$\text{Cell} \quad xLi + Nb_2O_5 \underset{\text{charge}}{\overset{\text{discharge}}{\rightleftharpoons}} Li_xNb_2O_5 \qquad (c)$$

The battery can be charged by reversing the discharge process by applying an appropriate potential. Cell voltage of about 2 V and charge density of about 160 ~ 180 mAh/g have been reached with this system [110, 111].

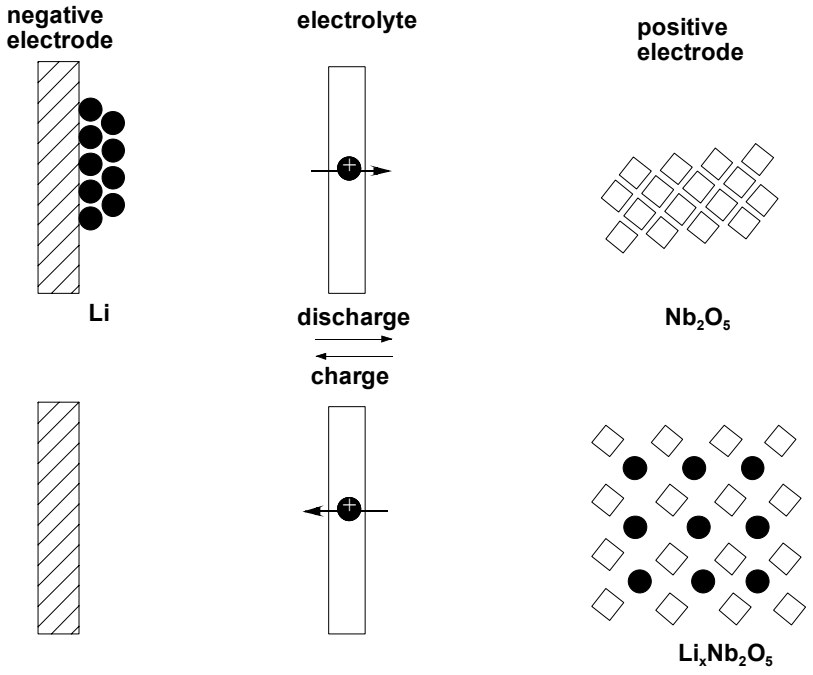

Figure 9: Principle of an insertion Nb_2O_5 electrode-based rechargeable lithium battery [112].

2.3 Electrochromic devices

Electrochromism is defined as a reversible color change of a material caused by the application of an electric current or potential [21, 113]. The current causes oxidation and reduction reactions. An electrochromic device consists of an electrochromic layer (EC) deposited on a conductive glass substrate, an ionic conducting layer which may be a liquid electrolyte or preferentially a solid electrolyte for large area application, and a counter electrode which serves as an ion storage layer (figure 10).

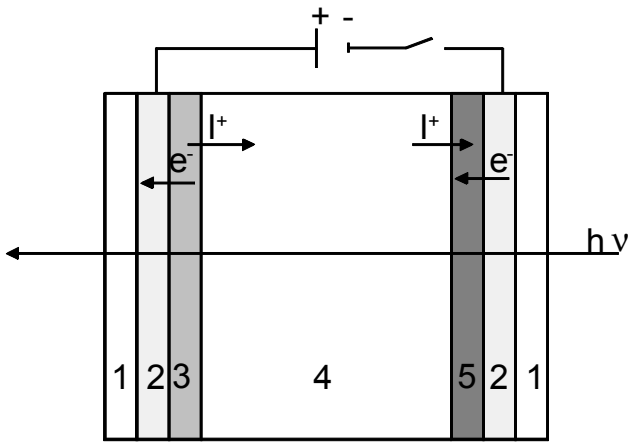

Figure 10: A typical electrochromic device. 1: glass, 2: transparent conducting oxide (TCO), 3: counter electrode or ion storage coating, 4: ion conductor, 5: electrochromic coating. I^+: inserting ion, e^-: electron [114].

Most of electrochromic materials are inorganic oxide of transition metals [21]. Usually the coloration and bleaching of these materials is described schematically by [115]

$$Me O_n + x\, I^+ + x\, e^- \leftrightarrow I_x\, Me O_n \tag{22}$$

where Me is a metal atom, I^+ is a singly charged ion such as H^+, Li^+, Na^+, K^+, Ag^+, e^- is an electron and n depends on the particular type of oxide.

2.4 Physical and chemical properties of Nb_2O_5

Niobium oxide occurs in many forms such as NbO, NbO_2, Nb_2O_3 and Nb_2O_5. Nb_2O_5 is the most oxygen-rich one of the niobium oxides [116]. Crystalline Nb_2O_5 can be obtained by oxidation of metallic niobium or low oxygen niobium oxides, for instance, by heating metallic niobium up about 550°C in the air. Nb_2O_5 powder is produced by reaction of $NbCl_5$ with NO_2 under exclusion of water at 400°C. Amorphous Nb_2O_5 is formed by heating niobium powder between 260°C and 350°C or by dehydration of niobium hydrous oxides. Crystalline Nb_2O_5 is obtained by heating amorphous Nb_2O_5. It is also prepared by hydrolyzing solutions of alkali-metal niobates, niobium alkoxides (e.g., $Nb(OC_2H_5)_5$), or niobium pentachloride, or by precipitation from hydrofluoric acid solutions with alkali-metal hydroxides or ammonia. Depending on the method used, the oxide hydrate formed is either a gel that is difficult to filter

or is flocculent. The oxide hydrate is filtered, washed, and calcined at 800 - 1100°C. The temperature and treatment time determine which of the various crystalline modifications is formed. Nearly all the phase changes are irreversible [117, 118]. Nb_2O_5 coatings can be prepared by many well-known procedures such as anodic oxidation, sputtering, pyrolysis and the sol-gel procedure.

Niobium oxide (NbO) has a unique structure, shown in figure 11, which gives for each metal atom a square coordination. It is what remains of the NaCl structure if all the atoms at the center and vertices of the unit cells are removed [119].

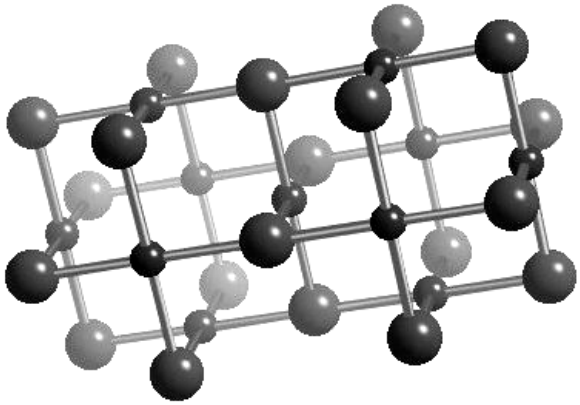

Figure 11: The NbO structure. Small ball: Nb atom, large ball: Oxygen atom [120].

Niobium pentoxide (Nb_2O_5) [CAS-No.: 1313-96-8], also called niobia or niobic acid has a molecular weight MW = 265.81 g/mol and a melting point mp = 1495°C. It is a colourless powder that can only be dissolved by fusion with acidic or alkaline fluxes such as NaOH, $KHSO_4$ or in hydrofluoric acid.

Nb_2O_5 has complex structural relationships. According to the nomenclatures of Brauer [121] and Schäfer et al. [117] niobia exists as TT-, T-, B-, N-, P-, M-, R- and H-Nb_2O_5. Many of these forms are metastable under normal conditions, and some of them are structurally quite similar. Several of these phases are built of MO_6 octahedra sharing edges and corners (figure 12), but this can be done in an almost unlimited number of ways. By partial oxygen loss various Nb^{+5}/Nb^{+4} phases, for example, $Nb_{12}O_{29}$ and $Nb_{22}O_{54}$ can form. The simplest structure, the R-Nb_2O_5, contains blocks with cross sections of 2×2 octahedra. The structure of H-Nb_2O_5 (and α-Nb_2O_5) is highly ordered and consists of two different sizes of ReO_3-type blocks: 5×3 and 4×3 groups of corner-or edge-shared octahedra [122]. M-Nb_2O_5 has a related structure [123]. The high density structure of B-Nb_2O_5 consists of rutile-like ribbons of edge-sharing NbO_6 octahedra [124, 125]. The TT and the T-phase are low temperature forms and do not have a block structure [126]. They have a similar crystal structure because they exhibit a similar x-ray diffraction patterns. However, as the TT phase does not always appear with pure components as starting materials, it was suggested that this form, indexed as pseudohexagonal, may just be a less crystalline form of the T phase, stabilized by impurities such as OH^-, Cl^- or vacancies [127, 128]. The more frequently observed forms are the TT-, T-, M- and H-phases.

The phase transformations of niobium oxide strongly depend on the preparation method of the compound and the heat treatment [126, 130-132]. Figure 13 shows an example of the phases obtained as a function of the temperature starting from amorphous niobium oxide [28]. The T and TT phases are essentially observed below 800°C.

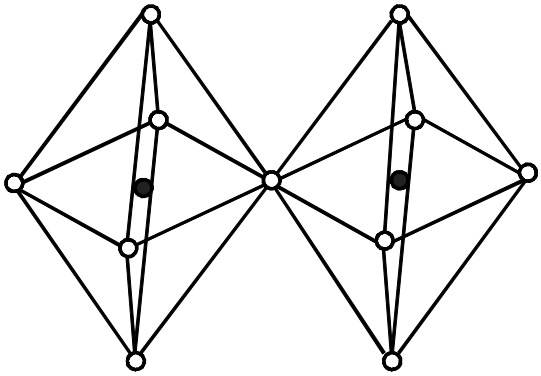

Figure 12: The corner-sharing of NbO_6-octahedra. (●): Nb atom, (○): oxygen atom [129].

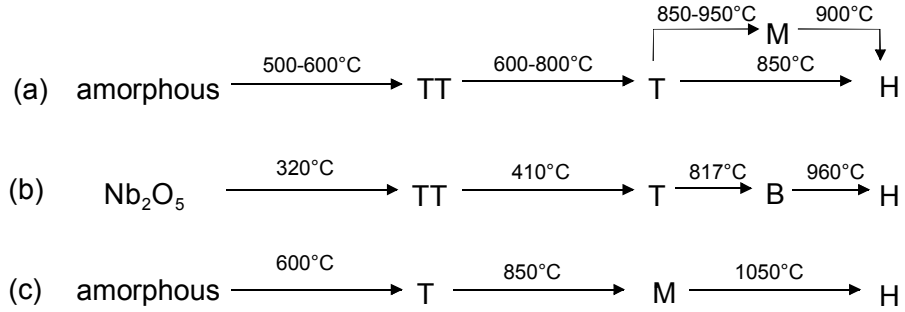

Figure 13: Temperature evolution of the most important crystalline phases of niobium oxide (amorphous, TT, T, M, and H) for different preparation methods according to references [117](a, b) and [121] (c).

Stoichiometric Nb_2O_5 is an insulator [28, 116] with, for example, a conductivity $\sigma = 3 \times 10^{-6}$ S/cm for H-Nb_2O_5 single crystal. However, it becomes a n-type semiconductor at lower oxygen content and $Nb_2O_{4.978}$ has a conductivity $\sigma = 3 \times 10^{3}$ S/cm. The conduction band is built from the 3d orbitals of Nb atoms and the valence band from 2p orbitals of oxygen. The index of refraction n and density ρ both depend on the type of phase: for amorphous niobia n was found to vary between 2.0 and 2.26 and ρ between 4.36 and 5.12 g/cm^3. For the TT and T phase, ρ takes the values of 4.99 and 5.00 g/cm^3 [28, 116].

Traditionally, niobium pentoxide is used in metallurgy for the production of hard materials. In optics it is used as an additive to molten glass to prevent the devitrification and to control the properties such as refractive index and light absorption of special glasses. In electronics its compounds such as $LiNbO_3$ or $KNbO_3$ single crystals are used for the preparation of electroacoustic or electrooptical components such as modulators, frequency doublers and wave filters, and $Pb(Mg_{1/3}Nb_{2/3})O_3$ for the manufacture of ceramic capacitors [133].

However, in recent years its interesting semiconducting properties and the advent of more sophisticated methods of preparation allowed to obtain in a controlled way innovative systems such as highly porous materials, very fine powders and coatings. These new materials have found further important application in the fields of electrochromism, batteries, solar cells and catalysis [28].

2.5 Sol-gel processing

The sol-gel process is a wet-chemical procedure in which a solution of a metal compounds or a suspension of very fine particles in a liquid (referred to as a sol) is converted into a semirigid mass (a gel). The process allows to fabricate ceramic or glass materials in a wide variety of forms: ultra-fine or spherical shaped powders, thin films, ceramic fibers, microporous inorganic membranes, monolithic ceramics and glasses, or extremely porous materials (aerogels). An overview of the sol-gel process is presented in figure 14. It appears attractive because it offers several obvious advantage [134]: (1) low processing temperature, (2) high homogeneity and purity of resulting materials, (3) possibility of various forming process.

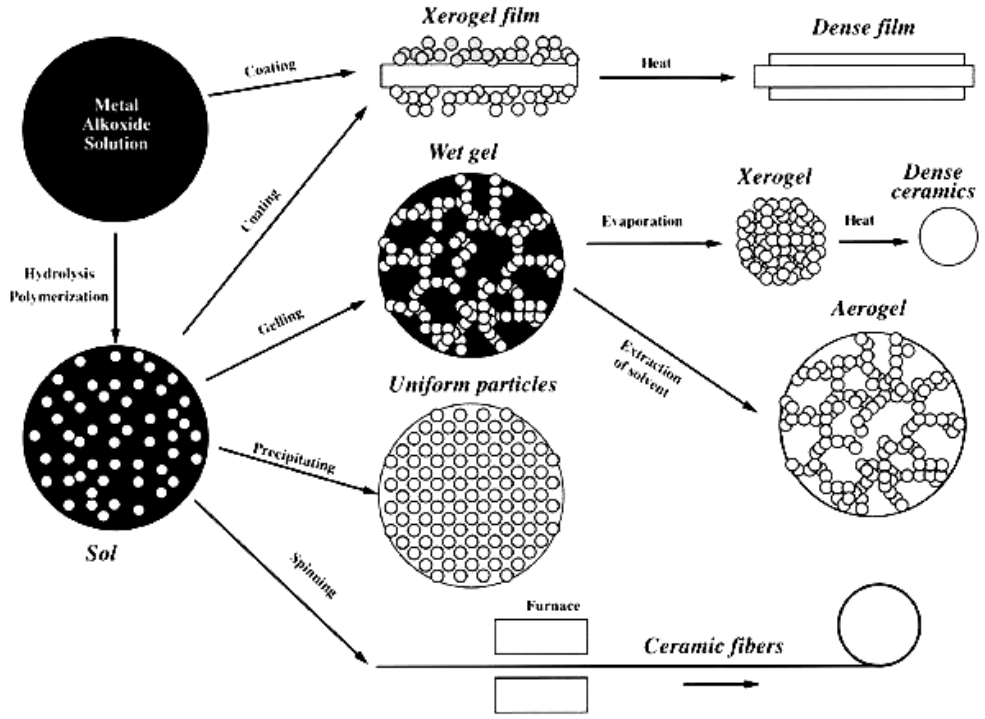

Figure 14: An overview of the sol-gel process and technology [135].

2.5.1 Sols and gels

The starting materials used in the preparation of the sols are usually inorganic metal salts or metal organic compounds such as metal chlorides, metal alkoxides and nano-sized solid particles. Two different sol-gel processes can be distinguished, depending on whether a polymeric or colloidal sol is used *[136]*. A basic flow chart outlining the processing steps for

the two solutions is shown in figure 15. Starting with a colloidal sol, the gelled material consists of identifiable small particles that have been joined together by surface forces to form a network (figure 16b). When a polymeric sol is used, typically a solution of metalorganic compounds (such as metal alkoxides) which undergo slow hydrolysis and polymerization rates, the gelled material in many cases consist of a network of polymeric chains (figure 16a).

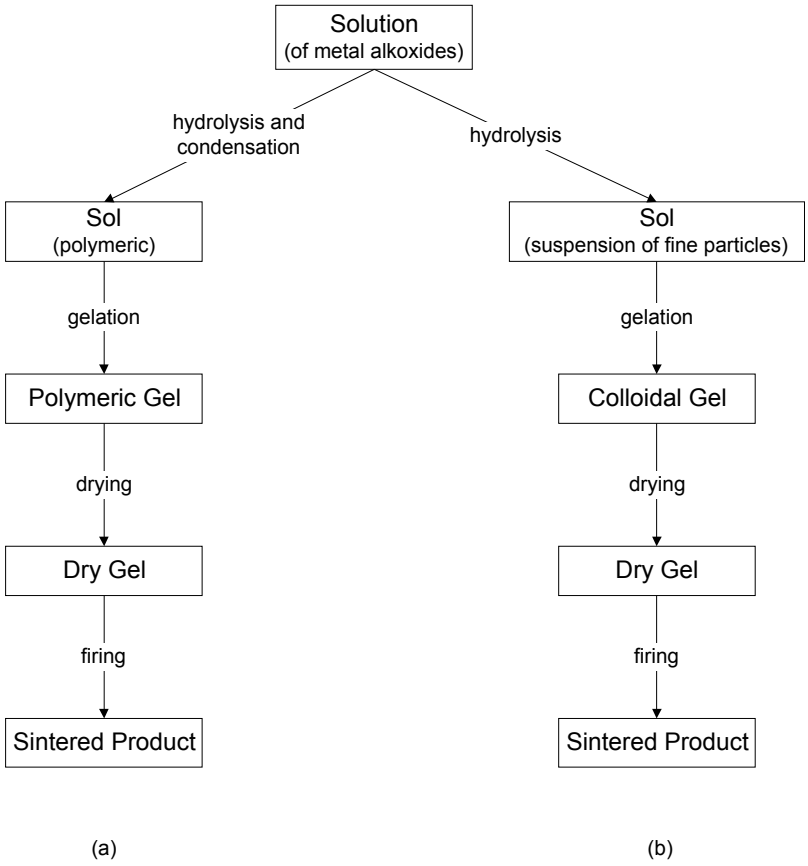

Figure 15: Basic flow charts for sol-gel processing using (a) a solution and (b) a suspension of fine particles [136].

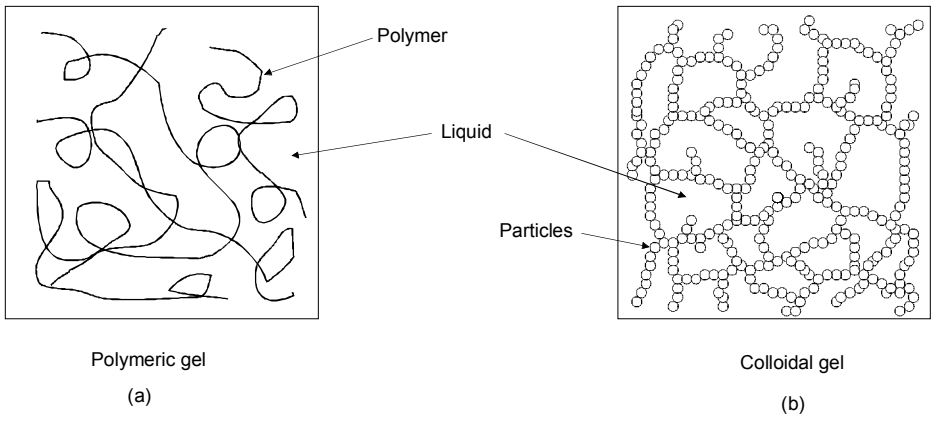

Figure 16: Schematic diagram of the structure of (a) a polymeric gel from a solution and (b) a particulate gel formed from a suspension of fine particles [136].

Single-component colloidal gels are prepared as following: colloidal particles are dispersed in water and peptized with acid or base to produce a sol. Two main methods can be employed to achieve gelation:

(a) removing of solvents from the sol by evaporation to reduce its volume or

(b) changing the pH to slightly reduce the stability of the sol.

The titania system is a good example of a sol-gel process used for the preparation of colloidal gels. $Ti(^{i}OPr)_4$ is hydrolyzed in a large excess of water to form an aggregated precipitate consisting of very fine nanosized colloidal particles This precipitate is peptized (dispersed) by the addition of acids or bases, which will charge the particles by protonation or deprotonation of the surface and lead to a stable and homogeneous, translucent colloidal sol [137].

Polymeric gels are prepared by chemical reaction involving the hydrolysis, condensation and polymerization of metal alkoxides in solution.

hydrolysis: the hydroxyl groups of water become attached to the metal atom by replacing the ligands in the precursor (equation 23).

$$M(OR)_n + xH_2O \rightarrow M(OR)_{n-x}(OH)_x + xROH \tag{23}$$

condensation: the hydroxyl groups merge to form metal-oxygen-metal bonds, releasing a water molecule, resulting in the formation of solid particles or clusters or polymer chains by combining monomers, growth of particles or clusters, and linking of particles or clusters into chains and networks that extend through the sol. An oxolation connects two hydroxide branches releasing a water molecule (equation 24) while an alcoxolation connects a hydroxide branch with an alkoxide branch releasing an alcohol molecule (equation 25).

Oxolation: $$-M-OH \quad + \quad HO-M- \quad \rightarrow \quad -M-O-M- \quad + \quad H_2O \tag{24}$$

Alcoxolation: $$-M-OH \quad + \quad R-O-M- \quad \rightarrow \quad -M-O-M- \quad + \quad ROH \tag{25}$$

A fast hydrolysis continued with a slow condensation generally leads to the formation of polymeric gels. Fast hydrolysis and fast condensation often yield colloidal gels or gelatinous precipitates. In contrast, slow hydrolysis and condensation reactions lead to the production of colloidal solutions. The rates of hydrolysis and condensation can be systematically controlled with pH, electrolyte, metal alkoxide precursors, temperature, solvent, and hydrolysis ratio [138-140].

polymerization of the species formed by the hydrolysis and condensation reactions together with interlinking and cross-linking of the polymeric chains eventually leads to a marked increase in viscosity of the reaction mixture and to the production of a gel, a biphasic system consisting of a continuous solid network having a finite elastic shear modulus and a fluid phase (solvents).

2.5.2 Deposition of sol-gel coatings

Certainly one of the most technologically important aspects of sol-gel processing is that the fluid solution is ideal for preparing thin films by such common processes as dipping, spinning, spraying, screen printing, etc. [140]. More than 80% of the most important commercial products are optical coatings such as antireflection coatings, Schott-type coatings for architectural glass, hydrophilic and hydrophobic coatings, antiscratch and hybrid hard coating for plastics, UV shielding coatings, coatings for heads-up display, colored Ormosil coatings for containers, etc. [141]. Sol-gel film processing has many advantages and has been successfully applied in the following main applications: optical, electronic, protective and porous coatings [140, 142, 143]. Compared to traditional coatings or film forming processes such as thermal spray, CVD and PVD, the sol-gel film formation requires considerably less equipment, is potentially less expensive and has the ability to allow a precise control of the microstructure of the deposited film.

The two main techniques used for producing film are the dip coating process and the spin coating process. The two coating methods are briefly described in the following two sections [144].

2.5.2.1 Dip coating process

In this technique the substrate is immersed in the coating bath and normally withdrawn vertically from the bath at a constant speed. This process can be divided into five stages: immersion, start-up, deposition, drainage and evaporation. The thickness of the deposited liquid film depends on the density, viscosity and surface tension of the solution and on the selected withdrawal speed and can be estimated by the Landau and Levich relation [144, 145]:

$$h_0 = 0{,}94 \frac{(\eta U_0)^{\frac{2}{3}}}{\gamma_{LV}^{\frac{1}{6}} \sqrt{\rho\, g}} \tag{26}$$

h_0 - deposited film thickness

η - viscosity of the liquid

U_0 - withdrawal speed

γ_{LV} - liquid-vapor surface tension

ρ - density of the liquid

g - gravitational acceleration constant

Evidently the film thickness increases with the viscosity of the liquid and the withdrawal speed.

2.5.2.2 Spin coating process

This technique differs from dip-coating in that the depositing film thins by centrifugal draining and evaporation. It can be divided into four stages: deposition, spin-up, spin-off and

evaporation. In the spin-up stage, the liquid flows radially outward, driven by the centrifugal force. In the spin-off stage, the excess liquid flows to the perimeter and leaves the substrate as droplets. The final film thickness is little affected by the deposition and spin-up stages, but is essentially determined by the spin-off stage in which the thickness becomes uniform. The thickness of an initially uniform film during spin-off is described by [144]

$$h(t) = \frac{h_0}{(1 + 4\rho\omega^2 h_0^2 t / 3\eta)^{1/2}} \tag{27}$$

h(t) - thickness with spinning time

h_o - initial thickness

ρ - density of the liquid

η - viscosity of the liquid

ω - angular velocity

t - time

2.5.3 Drying and sintering

Drying accompanies both the dip- and spin-coating processes and leads to the formation of an elastic or viscoelastic gel-like state. Before the evaporation begins, the meniscus formed by the solvent in a pore (figure 17a) is flat. The evaporation of the solvent gives rise to capillary tension which develops at the interface, as the solvent adopts a shape to prevent the exposure of the solid phase to the vapor, and the solid network shrinks (figure 17b). As the network stiffens, the tension rises to a critical value untill the radius of the meniscus drops equals the pore radius (figure 17) and the gel shrinkage stops. After the critical point, the liquid is first removed from the largest pores. The tension in the neighboring small pores deforms the pore wall and causes cracking [146]. A dry gel, called a xerogel, is obtained by removal of the solvent at temperatures up to 150°C [145].

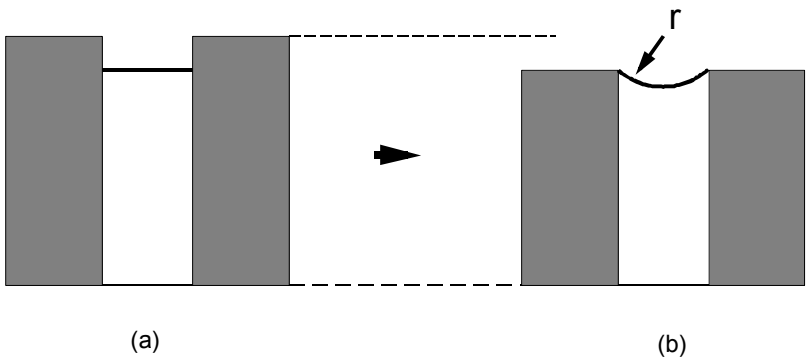

Figure 17: Drying process: (a) the liquid adopts a curved liquid/vapor interface, (b) compressive forces on the solid phase cause a shrinkage [146].

Difficulties arise when trying to prepare microporous films due to an increased tendency for cracking. As the film dries, it shrinks in volume. Since the film is attached to the substrate and

is unable to shrink parallel to it, the reduction in volume is accommodated completely by a reduction in thickness. The critical thickness for crack propagation or for the formation of pinholes has been estimated by [144]

$$h_c = \left(\frac{K_{Ic}}{\sigma \Omega} \right)^2 \tag{28}$$

h_c - critical thickness

K_{Ic} - critical stress intensity

Ω - function that depends on the ratio of the elastic modulus of the film and substrate (for gel films $\Omega \approx 1$)

σ - stress of the film

If the network becomes stiff enough to resist to the capillary stresses, a residual porosity will be formed. The addition of binders into the sol provides a stronger adhesion between the film and substrate and such compounds act as a mechanical support of the film during the drying.

Sintering is the reduction in the surface area of a body, driven by gradients in curvature [147]. Amorphous and crystalline phases can be obtained at different temperatures. The two phases differ strongly in their sintering behaviour.

Crystalline materials sinter by diffusion (transport of matter) whereas amorphous materials sinter by viscous flow [136]. In crystalline materials, matter transport takes place along definite paths: along a surface, through the lattice, along grain boundaries, or through the vapour phase. All of these paths lead to the growth of necks between the particles, producing bonding between the particles, so that the strength of the consolidated powder increases during sintering. In an amorphous materials, viscous flow leads to neck growth as well as to densification with reduction of the surface area.

The sintering of films differs from that of bulk gels in several ways [147]. The initial state of the film is generally denser and less crosslinked than a bulk gel made with the same sol, and these factors enhance the densification rate of the film. The substrate constrains the shrinkage of the film, leading to high stresses that retard the densification and can influence the phase transformations. The substrate is a site for heterogeneous nucleation, and the presence of crystallites make the densification more difficult. In this way the competition between sintering and crystallisation is particularly important in films. Therefore, the crystallisation process and the microstructure of films can be varied by choosing adequate heating rates.

3 State of the art

Sol-gel chemistry provides a convenient approach for the preparation of wide-band-gap semiconductors with distinct advantages over other semiconductor processing routes [138, 139, 148]. These include the ability to tailor surface and bulk properties under ambient conditions, low-temperature processing, and the ability to cast the materials in virtually all shapes or forms [149].

3.1 Sol-gel Nb_2O_5 semiconducting films

Niobia coating solutions have been prepared by the two sol-gel routes described in section 2.5.1 using either colloidal particles or polymeric molecules. Nb_2O_5 gels were first obtained by Alquier et al. [150] with these two classical ways using either niobium chloroalkoxides or the high cost niobium alkoxides as the precursors. Lee and Crayston [151] have studied the kinetics and mechanism for the hydrolysis and gelation of niobium chloroalkoxide solutions in sol-gel processing.

Since then many sol compositions and preparation methods have been tested, most of them to obtain thin electrochromic electrodes. Two different sol preparations have been reported by Aegerter et al. [17, 20, 26, 152-154]. The first sol was made by dissolving $NbCl_5$ in dry n-butyl alcohol. After reacting with sodium butoxide in butanol, the sodium chloride was removed. A second type of sol was prepared by dissolving $NbCl_5$ in butanol and acetic acid. The solution was then sonocatalized for a few minutes resulting in a transparent and viscous solution stable for several months at room temperature. The method was then extended to other alkoxy groups by Schmitt et al. [27] who dissolved niobium chloride in ethanol and by Macek et al. [155-157] who used a sol made by dissolving $NbCl_5$ in propanol, following a method described by Barros Filho et al. [23].

Lampert et al. [158-160] obtained a coating solution by mixing niobium ethoxide, absolute ethanol, and glacial acetic acid while stirring. A clear light yellow solution was obtained after stirring for 2 h.

The colloidal route was used to obtain thick Nb_2O_5 films. Lee and Crayston [161] obtained ca. 5 µm thick film on ITO glass by dissolving $NbCl_5$ in ethanol in the presence of H_2SO_4. Thick films were prepared using the spin coating technique. The electrode was then placed in aqueous solution containing H_2SO_4 to complete the hydrolysis and the gelation.

Hu et al. [162] prepared niobia colloidal suspensions by hydrolysing a niobium alkoxide solution in a triethylamine ethanolic aqueous solution and autoclaving at 250°C. The suspension was then concentrated in vacuum. A few drops of Triton X-100 were then added into the suspension solution. Niobia films were prepared by spreading the colloidal suspension

on a substrate. The films fired at 500°C had the TT structure, were porous and presented a morphology consisting of needles. The thickness of the films was around 6 μm.

Wolf [163], using similar preparation techniques, showed that the specific BET surface area of the sintered materials was in the range of 30 to 50 m^2/g.

Lenzman [164, 165] prepared stable colloidal solutions of Nb_2O_5 based on the hydrolysis of a niobium alkoxide precursor modified with acetylacetone in the presence of a large excess of water, ethanol, and 1,8-diazabicyclo(5.4.0)undec-7-ene(1,5-5) (DBU) solutions. The hydrolysis of the modified alkoxide solution did not lead to the precipitation of the hydrated oxide. This hydrolysed solution was then heated to 230°C in an autoclave for 12 h. A viscous paste, suitable for doctor-blading, was prepared by adding hydroxypropylcellulose. After firing at T > 500°C, 5 μm thick crack-free films were obtained from a single cast. They consisted of an agglomeration of about 20 nm poorly defined particles, several of them having also large needle shape, with a BET area of 55 m^2/g at 600°C.

Sayama et al. [166], Hara et al. [167] and Eguchi et al. [168] prepared aqueous slurries for the doctor-blade process. A commercial Nb_2O_5 powder was ground in a mortar with water, acetylacetone and Triton X-100 to break up the aggregates into a dispersed paste. After drying in air, the Nb_2O_5 films were deposited on conducting glass and then calcined for 1 h at 500°C in air.

3.2 Application

In the last decade, Nb_2O_5 prepared by the sol-gel process became a promising material for possible applications as electrodes in electrochromic (EC) devices, batteries and nanocrystalline solar cells and for catalysis [28].

(a) *Electrochromism:* pure and doped Nb_2O_5 coatings have been thoroughly studied for their electrochromic properties. Although such system colors readily with blue, brown or grey colors in electrochemical cells under Li^+ insertion, the development of EC devices was disappointing and still wait for the discovery of a good counter electrode allowing to store enough Li^+ ions [114, 169].

(b) *Batteries:* There is a definite need for rechargeable microbatteries that can be fully charged in the voltage range 2-3 V as it is required by most integrated circuits. Niobium pentoxide is one of the few candidates for the 2 V class rechargeable Li batteries. The material is used practically as a negative electrode in $Li_xNb_2O_5/V_2O_5$ batteries [170] and more recently as a high energy density $LiAl/Li_xNb_2O_5$ secondary batteries.

(c) *Dye sensitised nanocrystalline solar cell:* Nanocrystalline sol-gel Nb_2O_5 films turned recently a promising material to substitute TiO_2 in dye sensitised solar cell. Hu et al. [162] obtained a quantum conversion efficiency (IPCE) of 40% and an open-circuit voltage of 0.4 V with a cell made with sol-gel Nb_2O_5 film sensitised by the Ru(II)-complex. Wolf [163] obtained

an almost constant conversion efficiency of 2.5% under simulated solar light irradiation up to 1000 W/m^2 (1 sun) and an IPCE of 33% at 550 nm for a cell of 0.45 cm^2 size. Lenzman [164] reported a cell efficiency of 4%, a fill factor of 69%, an open-circuit voltage of 0.595 mV and a short-circuit current density of 9.7 mA/cm^2 for a 0.5 cm^2 Ru(II)-complex sensitised cell made with 15 μm thick films prepared by a hydrothermal sol-gel processing. The current response was found linear between 100 and 1000 W/m^2 solar light irradiation. Sayama et al.[166] reported a conversion efficiency of 2% under AM1.5 (1000 W/m^2) illumination and an IPCE of 32% at 548 nm. An improvement was obtained by dropping a niobium alkoxide on the Nb_2O_5 film electrode and then heat-treating the electrode again at 500°C before the dye adsorption. Eguchi et al. [168] found that a Nb_2O_5-TiO_2 composite electrode had a higher short-circuit current density and thus a higher power output, than those made with pure Nb_2O_5-based electrodes and TiO_2-based electrodes. A combination of Nb_2O_5 with oxides having a higher flat-band potential such as $SrTiO_3$, Ta_2O_5, and ZrO_2 leads to a higher open-circuit.

3.3 Comparison of dye sensitised oxide-based solar cells

Since Grätzel´s discovery [7, 8, 14] many other wide-band-gap semiconductors such as ZnO [108, 109, 166, 167, 171-176], SnO_2 [166, 167, 177-183], $SrTiO_3$ [184, 185] WO_3 [166] [186], CeO_2 [187], In_2O_3 [166] [167], and Nb_2O_5, have been studied. So far TiO_2 is the most successful material for the light-to-electric energy conversion. Grätzel and co-workers have developed nanocrystalline TiO_2 films using a hydrothermal sol-gel processing [19, 137, 188, 189]. The coatings, consisting of crystalline particles with an average size of 15 nm, are porous and have a thickness about 10 μm, with a roughness factor of 780. The overall conversion efficiency measured under 1000 W/m^2 solar simulator irradiation varies typically between 7% and 12% with an open-circuit photovoltage 0.7 - 0.8 V, and an IPCE of 85 to 90%. [5-7, 19, 71, 74, 87, 94, 190]. The stability of these cells sustains at least 10^7 turnovers and the longest reported continuous exposure time has been 10 months, corresponding to about 6 years of outdoor illumination. The first titania dye solar cell manufacturing operation has opened in New South Wales, Australia in 2001 [191].

One key factor for the successful commercial application of such a solar cell is its stability. Tributsch et al. [192, 193] have however confirmed that the ruthenium complex attached to TiO_2 is decomposed photoelectrochemically into fragments and is irreversibly consumed under insufficient regeneration by iodide or from the oxide. One of the reasons of the photodegradation of dye sensitised TiO_2 solar cells is that TiO_2 presents a large photoelectric effect under UV-light illumination [23, 194]. During this process the holes generated from the electron-hole pairs swept to the surface and oxidise the dye attached to TiO_2 into an irreversible product. However, Solaronix has recently reported [195] that modules tested under 2500 W/m² (no UV) for 8300 h at 20°C (equivalent to a 20 years outdoors equivalent) did not change their power output, although the power of similar modules tested at 1000 W/m² (1 sun) at 45°C (3.5 years equivalent) dropped by 15% after 3400 h. A decrease of the power

by 5%, respectively 25% was also observed after a 2200 h test in the dark at 60°C, respectively 80°C. Compared with TiO_2, Nb_2O_5 was shown to have a smaller photoelectric effect in the UV range and this may be an advantage as the undesirable catalytic effect of the sun UV light at the semiconductor/electrolyte interface will be reduced.

As mentioned in section 2.1.3.1, the open-circuit voltage of dye-sensitised solar cells is determined by the potential difference between the electrode potential of the redox system and the Fermi level of the semiconductor electrode (near the flat band potential of a n-type semiconductor). The conduction band of Nb_2O_5 lies at least 250 mV above that of TiO_2 [196-198] and Sayama et al. [166] and Eguchi et al. [168] have confirmed that a Nb_2O_5 solar cell has a higher open-circuit photovoltage for a given kind of dyes.

Table 2 shows the results of several dye-sensitised solar cells. TiO_2 matches well with Ru(II)-complex with two carboxylate groups, as reported by Grätzel [5] and this system transfers efficiently solar energy into electric energy.

Table 2: Parameters of several Ru(II) dye-sensitised solar cells.

Photoelectrode [Reference]	Bandgap [eV]	V_{fb} # (V) (±0.1)	overall η [%]	IPCE [%]	LHE [%]	Φ_{inj} [%]	η_e [%)]	k_{inj} [s^{-1}]
TiO_2[7]	3.2	0.2	10-12	~ 97	98	99.9	99	$>1.4\times10^{11}$
ZnO[109]	3.0		1.2*	14	45	0.85	31	5.4×10^{7}
SnO_2[199]	3.8	0.5	1.4*	22		0.82		4.2×10^{7}
Nb_2O_5[164]	3.2	0.0	4	60				
Nb_2O_5[166]	3.2	0.0	2	18	60			

*: under monochromatic light illumination. #: Data from [196].

4 Experimental procedure

4.1 Synthesis of Nb_2O_5 sols

The detailed synthesis route of Nb_2O_5 sols is shown in figure 18. The niobium chloroethoxide solution was prepared by dissolving 86.46 g of $NbCl_5$ (0.32 m) in 800 ml absolute ethanol. After addition of 38.43 g CH_3COOH (0.64 m), the mixture was submitted to ultrasound (550 W, 20 kHz) for 5 min. De-ionised water, to get different H_2O:Nb ratio, was added to the solution during 90 min, under vigorous stirring, and then the solution was again submitted to ultrasound for 5 min. The solution was boiled with reflux for 2 h and was concentrated under 40 mbar vacuum at 30°C until the Nb_2O_5 solid content is about 90 g/l. The sol was finally filtered through a 0.2 µm polymer filter (FP30/0.2CA, Schleicher & Schuell) to remove the large particles. Such sols can be directly spin coated on substrate. To improve the morphology of the coatings and to increase the coating thickness, PEG with molecular weight ranging between 600 and 20000 and carbon soot have been also added after the refluxing and distillation processes. The sols are stable for several years at room temperature when kept in a closed glass recipient.

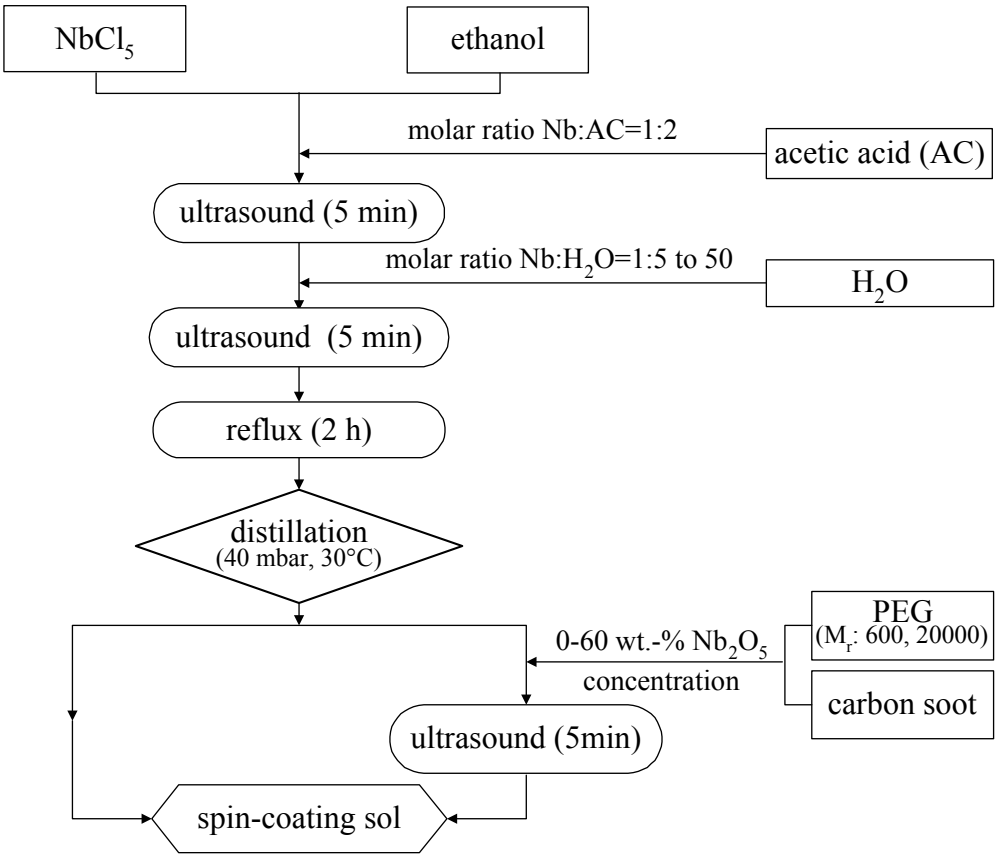

Figure 18: Schematic representation of the synthesis route of Nb_2O_5 sols.

4.2 Preparation of Nb_2O_5 powders

The above sols, with or without additives, were concentrated by evaporating the solvent in air, and then dried in an oven between 100 and 110°C. The solid residues were then ground into powders in an agate mortar. The powders were heated at different temperatures characterisation: thermogravimetric and differential thermal analysis (TG/DTA), Fourier transform infrared spectroscopy (FTIR), X-ray diffraction (XRD), nitrogen adsorption and desorption analysis and high resolution transmission electron microscopy (HRTEM).

4.3 Preparation of Nb_2O_5 films

Nanocrystalline Nb_2O_5 sol-gel films have been produced on different glass substrates by spin coating technique using the above sols. Conducting glass supports (ITO, tin-doped In_2O_3 10 Ω□ (Asahi) or TEC-8 glass, fluorine-doped SnO_2, 8 Ω□ (Libbey Owerns Ford)) were used to build photovoltaic cells, lithium batteries and electrochromic devices. The electrodes were fabricated as follows: the transparent conducting oxide (TCO) glasses were first etched at 90°C by dipping them in concentrated H_2SO_4 for 1 min to facilitate the spreading of the sol on the substrate and to improve the Nb_2O_5 film's adhesion to the substrate. The conductivity of the glasses was not altered by etching, however their optical transmission was slightly changed (figure 19). One edge of the conducting glass was masked with a 10 mm broad Tesa® tape in order to protect a conducting area during the deposition procedure. Single layer Nb_2O_5 film with thickness ranging between 0.05 and 5 μm could be produced by varying on the spinning rate and time. For the dye-sensitised, photoelectrochemical and Li ion storage electrodes, a thin 80 nm and compact coating was first produced by using a 300 μl sol at a spinning rate of 2000 rpm during 15 s in order to improve the adhesion of the thick Nb_2O_5 film and to protect the conducting glass from direct contact with electrolyte solution. Then a thick and porous coating was deposited at 1000 rpm for 3 s. After deposition, the coating was dried at room temperature and then heat treated at 400°C for 10 min, and the deposition procedure was repeated to increase the thickness of the coating. Finally the multilayer coatings were sintered for 30 min in air at temperatures between 400°C and 600°C. For films deposited on borosilicate glass or AF45® glass, the thin coating was omitted and sintering was performed at temperature up to 650°C.

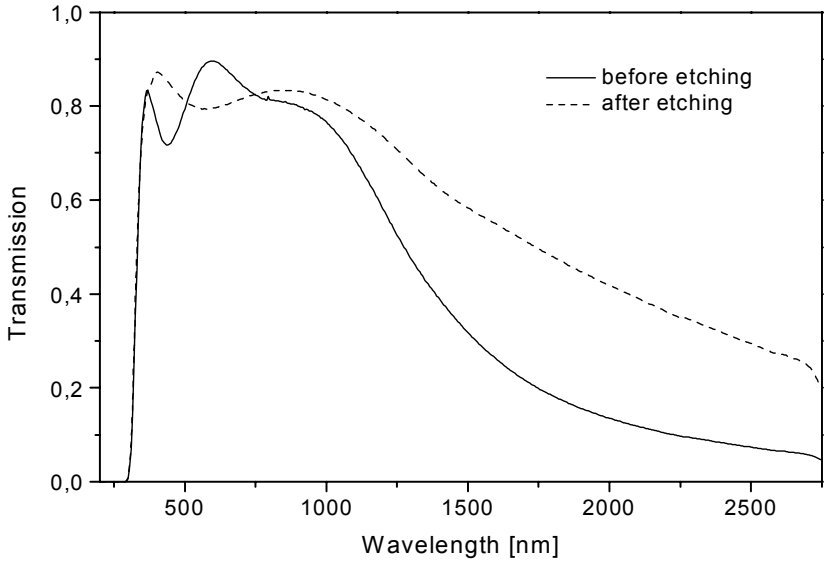

Figure 19: Transmittance spectra of ITO-coated glass before and after H_2SO_4 etching.

4.4 Characterisation of Nb_2O_5 sols, powders and films

4.4.1 Kinematic viscosity

The homogeneity of the coating on the entire substrate and of the layer thickness are influenced by the viscosity of the solution. The kinematic viscosity of the Nb_2O_5 sol was measured by the Ubbelohde method between 1.2 to 10 mm^2/s. The measurement principle is based on the time that needs a defined volume of liquid to flow in a capillary with defined length and diameter [200]. The viscosity is determined by the following equation [201]

$$\nu = K \times t \tag{29}$$

where ν is the kinematic viscosity in mm^2/s, K is the capillary constant in mm^2/s^2, which depends on the length and the diameter of the capillary, t is the flow time in s.

The temperature was kept at 20°C during the measurements.

4.4.2 Photon correlation spectroscopy (PCS)

Particle size and particle size distribution measurements were carried out with a PCS apparatus (ALV/DLS-5000) at 20°C. Prior to the measurements, the required amount of Nb_2O_5 sol was filtered through a 0.2 µm polymer filter to remove the dust particles. The measuring duration was 300 seconds. The measuring angle was kept at 50°.

A schematic set-up of the PCS apparatus is shown in figure 20. The principle of the measurement is based on the analysis of the fluctuations about the time average of the light intensity scattered by the dispersed particles in a liquid medium illuminated by a narrow monochromatic and coherent source (single wavelength laser beam). The total scattered light is

the superposition of the contribution of the individual dispersed particles and is detected at a certain angle with respect to the incident direction. The disperse particles or macromolecules suspended in a liquid medium undergo a Brownan motion which causes fluctuations of the local concentration of the particles, resulting in local inhomogeneities of the refractive index. This in turn results in fluctuations of intensity of the scattered light with time.

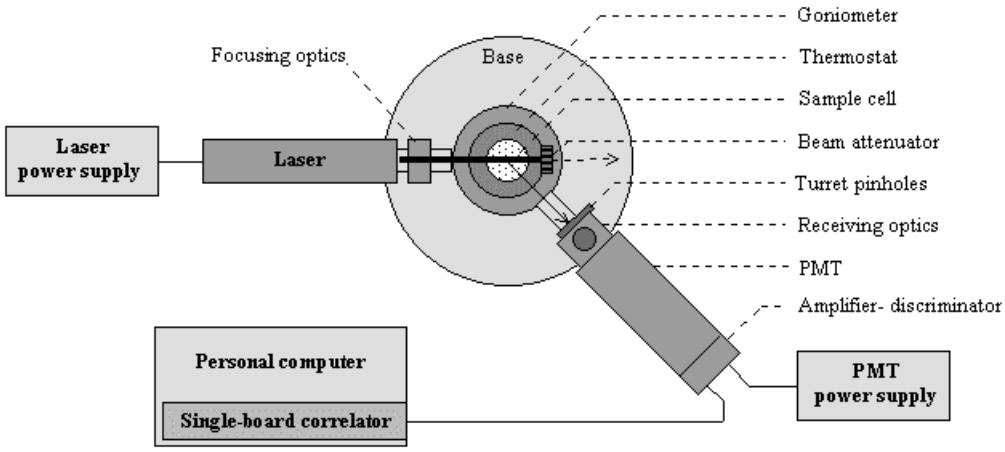

Figure 20: Schematic set-up of the photo correlation spectroscopy apparatus.

4.4.3 Thermoanalysis and mass spectroscopy

Thermogravimetric (TG) and differential thermal analysis (DTA) are thermal analysis techniques which allow to characterise endothermic and exothermic reactions and the weight loss of sample occurring during the heating process. The variation of the temperatures and weight can be detected during phase transformation and decomposition reactions [202, 203].

TG/DTA and mass spectroscopy (MS) were carried out using a Netzsch STA409-QMS 420 apparatus. Xerogels prepared by drying a sol at 110°C were used as samples. An empty alumina crucible was used as reference and all the experiments were carried out under synthetic air atmosphere (80% nitrogen and 20% oxygen, flow rate: 75 cm^3/min). About 70 mg samples were placed in an alumina crucible and the samples were heated up to 800°C at a heating rate of 10 K/min. The temperature difference between sample and reference is recorded by thermocouples. The positive or negative deviations of potential signal of the sample against the reference temperature represents an exothermic or endothermic process, respectively. TG was carried simultaneously during the DTA measurement by recording the change of weight with the temperature.

The molecular weight of fragments have been determined by mass spectrometry (MS). The analysis involves the re-assembling of fragments, working backwards to generate the original molecules [204-206]. In this work the mass spectroscopy was pursued by detecting gaseous reaction products evolved from the samples simultaneously during the DTA/TG analysis. The equipment is hermetically connected by a capillary to the DTA/TG furnace. The MS signals are somewhat delayed due to the local separation between sample and the mass spectrometer and

this caused a small shift of the MS signals towards higher temperature in the diagram. Also, large molecular fragments may condense in the cold capillary and may not arrive in the mass spectrometer.

4.4.4 X-ray diffraction analysis

X-ray diffraction (XRD) provides structural information about the investigated materials [207]. The measurements were carried out using a Siemens D 500 diffractometer with Cu K_α at 40 kV and 25 mA using 2θ scanning from 10° to 80° for powder samples and using a Philips x´Pert MAD diffractometer with Cu K_α at 40 kV and 25 mA using θ/2θ scanning from 15° to 80° for thick coating samples.

The average grain size was estimated from the X-ray line broadening analysis using the Scherrer´s formula

$$d = \frac{k\lambda}{\beta \cos\theta} \tag{30}$$

where d is the average grain size, k is a dimensionless constant ≈ 1, λ is the X-ray wavelength, β is the full width at half maximum of the diffraction peak, and 2θ is the diffraction angle.

4.4.5 High resolution transmission electron microscopy (HRTEM) and scanning electron microscopy (SEM)

The powder´s and coating´s morphology was studied by HRTEM and SEM. HRTEM investigations were performed by means of a Philips CM 200 FEG transmission electron microscopy having a Schottky type field emission gun (FEG) generating a beam energy up to 200 KeV. The samples were prepared by dipping a copper grid coated with carbon film into the Nb_2O_5 powder suspensions. SEM analysis were carried out using a JEOL JSM 6400F equipment at an accelerating voltage of 15 KeV.

4.4.6 Fourier transform infrared spectroscopy (FTIR)

The composition of the dried and heat treated xerogels was investigated by FTIR spectroscopy (Bruker, IFS66V) [208]. 1 wt.-% of the sample was mixed with KBr powder and pressed into a thin plate. The measurements were carried out in vacuum (3 mbar) in order to eliminate the influence of CO_2 in air. This matrix was scanned from wavenumbers 333 to 5000 cm^{-1}.

4.4.7 Coating thickness

A Tencor P-10 Surface Profiler has been used for measuring the surface roughness R_q and the thickness of the films across the substrate [209]. The equipment characterises a surface by

scanning a diamond stylus on it (mechanical finger). The vertical movement of the stylus is transferred into an electrical signal by piezoelectric transducers and passed on to the computer. The analysis is made by a specific software. The resulting trace represents a cross-sectional view with high vertical and spatial resolution.

To measure the thickness, a groove was scratched through the film with a sharp knife. The stylus scanning speed and scanning length were 50 µm/s and 500 µm for thin films and 0.1 mm and 8 mm for thick films. The mean film thickness was calculated by averaging the data obtained at many different position on the sample.

4.4.8 Nitrogen adsorption and desorption

The surface area and pore size distribution of porous nanocrystalline Nb_2O_5 powder or film can be obtained by a gas adsorption technique [210]. Dry samples are usually evacuated and cooled to liquid nitrogen temperature (77 K). At this temperature nitrogen physically adsorbs on the surface of the sample. This process is a reversible condensation or layering of molecules on the sample surface during which heat is evolved. The surface area is obtained by measuring the amount of nitrogen required to form a monolayer on the surface. From such a measurement the total surface area can be calculated knowing the area of nitrogen molecules.

An adsorption isotherm at a define temperature is recorded as the volume of gas adsorbed (cc/g, at STP condition at 273.15 K and 101.325 kPa) versus the relative pressure p/p_o (i.e. the ratio of the sample pressure to the saturation vapour pressure). The isotherms can be qualitatively analysed by comparing their shape to standard isotherm types classified by the IUPAC (International Union of Pure and applied Chemistry) [210-212].

The BET (Brunauer, Emmett and Teller) [213] equation is used to obtain the specific surface area.

$$\frac{P/P_o}{V(1-P/P_o)} = \frac{1}{V_m C} + \frac{(C-1)}{V_m C} \times \frac{P}{P_o} \tag{31}$$

where P is the sample pressure, P_o is the saturation vapour pressure, V_m is the monolayer capacity and C is a function of the energy of interaction between adsorbent and adsorbate, expressed as

$$C = \exp\left(\frac{q_1 - q_L}{RT}\right) \tag{32}$$

where q_1 is the heat of interaction for the first layer and q_L is the latent heat of condensation for the adsorbate.

The constants C and V_m are in practice determined by the slope and the intercept of the straight line obtained by plotting $\frac{P/P_o}{V(1-P/P_o)}$ versus P/P_o.

Finally the BET surface area is the calculated from

$$BET\ surface\ area\ (m^2/g) = \frac{16.2 \times 6.022 \times 10^{23}}{22414 \times 10^{20}} V_m = 4.3525 V_m \quad (33)$$

where the value 16.2 $Å^2$ is the area occupied by one nitrogen molecule and V_m is measured in cm^3 at STP/g.

The average particle size is estimated from the surface area assuming that the particles are spherical (equation 34)

$$d_{BET}\ (nm) = \frac{6000}{S_{BET}(m^2/g) \times \rho\ (g/cm^3)} \quad (34)$$

where d_{BET} is average particle size, S_{BET} is the BET surface area and ρ is the density.

The pore size distribution and porosity of the sample have been obtained by analysing the adsorption and desorption branches of the isotherms using the BJH method (Barrett, Joyner and Halenda) [214]. It is based on a model of the adsorbent as a collection of cylindrical pores. The theory accounts for capillary condensation in the pores using the classical Kelvin equation, which in turn assumes a hemispherical liquid-vapour meniscus and a well-defined surface tension.

The porosity is calculated using equation 35:

$$Porosity_{BET}\ (\%) = \frac{Total\ pore\ volume\ (cm^3/g)}{(Total\ pore\ volume\ (cm^3/g) + \frac{1}{Density\ \rho\ (g/cm^3)})} \times 100\% \quad (35)$$

The pore size distribution determined from the adsorption data reflects the value of the core diameters of the body and that obtained from the desorption data reflects the value of the core diameters of the neck [210] (figure 21).

(a) (b)

Figure 21: Cross-section of interconnected pores (a) ink-bottle pore, (b) cylindrical pore.

The BET surface and pore size distribution of the powders and coatings were studied using a nitrogen adsorption and desorption apparatus (model ASAP 2400, Micromeritics Instrument Corp.) [215]. Prior to measurement the samples were degassed and dehydrated in the integrated vacuum degassing unit at a temperature of 130°C for at least 12 h, and until the vacuum reached 100 mTorr.

The system is controlled by a computer allowing for a fully automated data collection and data evaluation on the basis of the BET and BJH methods. The sample weight was typically ca. 400 mg. The blank BET surface area of an AF45® glass substrate without Nb_2O_5 coating was measured. This value is 0.143 m^2/g , (0.0572 m^2 0.4 g). The influence of glass substrate on the further measurements of the samples was therefore omitted.

4.4.9 Scanning white light interferometry

The topography of the films was observed by using a scanning white light interferometer New View 100 System (Zygo®). Figure 22 illustrates the principle of operation. A white light beam is split in a special interference microscope objective, where part of the light travels to a spot on the sample of interest, and the remainder is directed toward a reference mirror. When the two beams recombine, interference fringes appear at the point of focus. A piezoelectric stack moves the objective in the vertical direction with a scan of 5 to 100 µm. Fourier transform algorithms convert the recorded data into surface topography information which is graphically displayed.

The surface roughness of the coating was characterised using the Root-Mean-Square (rms) of the height profile measured along the sampling length. The equation is

$$R_q = \left[\frac{1}{L} \int_{x=0}^{x=L} Y^2 dx \right]^{1/2} \tag{36}$$

where R_q is the rms roughness (µm), Y is the ordinate height of the curve of the profile, relative to the mean line (µm) and L is the measured length.

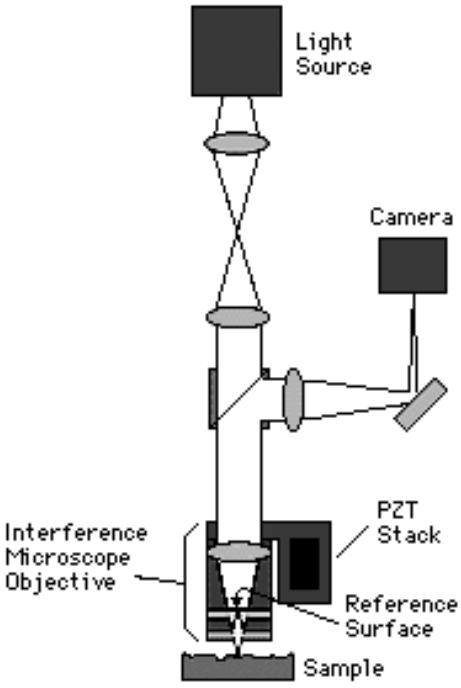

Figure 22:Schematic set-up of a scanning white light interferometer.

4.4.10 Measurements of optical properties

The transmission, reflection and absorption spectra of the samples were carried out using a Varian CARY 5-E UV-VIS-NIR spectrophotometer. The measurements cover the wavelength region from 300 to 3000 nm. The measurements of the refractive index n were carried out with the Variable Angle Specular Reflectance Accessory (VASRA). The sample holder was rotated from an angle varying between 20° and 70° with respect to the plane of incidence of a vertical polarised light (using a +HA-PGT-S1V Glan Thompson Polarisator) at the desired wavelength. This method determines the refractive index [216] of a transparent film by measuring the reflectance at the Brewster's angle θ_B value, the intensity of light reflected by the film is the same as that of the substrate

$$n = \tan \theta_B \tag{37}$$

The value of n can be determined with an accuracy of ± 0.002 for isotropic and homogenous transparent layers.

4.5 Synthesis of the dye ruthenium *cis*-di(thiocyanato)-N,N´-*bis*(2,2´-bipyridyl-4,4´-dicarboxylic acid) complex

The dye was synthesised following the references [19, 217]. The synthesis procedure is described in detail in the Appendix A3. The resulting $RuL_2(NCS)_2 \bullet 2H_2O$ was then purified by a chromatographic separation. Solid $RuL_2(NCS)_2 \bullet 2H_2O$ was dissolved in a small amount of DMF. This solution was passed through a Sephadex LH 20 column (ϕ15×500 mm), using DMF as mobile phase. Most of the violet -red liquid part was collected and then concentrated in a rotary evaporator. Pure crystalline $RuL_2(NCS)_2 \bullet 2H_2O$ was obtained by adding ether into the concentrated solution, centrifuging and drying in a 10^{-2}-10^{-3} Torr vacuum at 40-50°C. The structural characterisation of the dye was carried out by FTIR spectroscopy, UV-VIS-NIR absorbance spectroscopy and ^{1}H-NMR spectroscopy.

4.6 Nb_2O_5 electrode preparation and cell assembly

4.6.1 Preparation of the Nb_2O_5 electrodes

The Nb_2O_5 films were deposited using spin coating technique on TCO glasses. An edge of the conducting glass without coating was connected with an adhesive copper/carbon band 12 mm broad and attached to a conducting wire. Such electrodes were used as working electrodes for photoelectrochemical and electrochemical measurements.

4.6.2 Sensitisation of the Nb_2O_5 electrodes

Dye sensitisation was carried out by soaking the films for 30 h in a 1×10^{-3} M solution of the ruthenium complex in absolute ethanol. This procedure was done immediately after drying the Nb_2O_5 coatings at 130°C for 24 h in order to avoid the rehydration of the Nb_2O_5 surface or the capillary condensation of water vapour from ambient air inside the nanopores of the film. The electrodes were dipped into the dye solution while they were still hot.

The amount of absorbed dye was determined by spectroscopic measurement. For that the adsorbed dye was desorbed from the semiconductor surface by immersion in a 0.1 N NaOH-mixture of water and ethanol (50/50% by volume). The optical absorption of the solution was measured from a plot of the absorbance vs. standard concentrations of the dye.

Some practical information about the microstructural properties of the coatings was obtained using the measurements of the amount of the Ru(II)-complex dye adsorbed in the coatings. The surface area occupied by the dye, S_{dye}, the porosity and the roughness factor are calculated as follows:

$$S_{dye} = N_A \times \Gamma_g \times A_{dye} \times 10^{-18} \tag{38}$$

where S_{dye} is the surface area occupied by the dye (m^2/g), N_A is the Avogadro constant 6.022×10^{23} (mol^{-1}), Γ_g is the number of moles of dye per gram (mol/g), A_{dye} is the area of a dye molecule, assumed to be 1 nm^2 [218].

$$Porosity\ (\%) = \frac{\rho - \rho_p}{\rho} \times 100\% \tag{39}$$

where ρ is the density of Nb_2O_5 (5 g/cm^3 [116]) and ρ_p is the measured value of the porous Nb_2O_5 coating.

$$Roughness\ factor\ (normalised\ for\ a\ 10 \mu m\ thickness) = N_A \times \Gamma_{area} \times A_{dye} \times 10^{-14} \tag{40}$$

where Γ_{area} is number of moles of dye per square centimetre (mol/cm^2 normalised for a thickness of 10 µm)

4.6.3 Electrolyte compositions

Two kinds of electrolyte were used for measuring the photoelectrochemical properties of the non-sensitised electrodes. One was a 0.1 N KCl in 0.1 N HCl aqueous solution, the other was a 0.2 N $LiClO_4$. in aqueous solution.

The electrolyte for measuring the charge and discharge properties and electrochromic properties of the Nb_2O_5 coating was a 1 M solution of $LiClO_4$ dissolved in propylene carbonate (PC).

The electrolytes used for the dye sensitised solar cells and the measurement of their photoelectrochemical properties consisted of mixtures of acetonitrile and propylene carbonate, and the redox system was based on the iodine/triiodide system shown in table 3.

Table 3: Electrolyte compositions used for the dye sensitised solar cells and the measurement of their photoelectrochemical properties.

No.	PC[1] [vol.-%]	ACN[2] [vol.-%]	I_2 [M]	$(Pr)_4NI$[3] [M]	LiI [M]	$(Bu)_4NI$[4] [M]
1	-	100	0.05	0.5	-	-
2	50	50	0.05	0.5	-	-
3	80	20	0.05	0.5	-	-
4	100	-	0.05	0.5	-	-
5	80	20	0.05	-	0.5	-
6	80	20	0.05	-	-	0.5

1) PC: propylene carbonate; 2) ACN: acetonitrile; 3) $(Pr)_4NI$: tetrapropylammonium iodide; 4) $(Bu)_4NI$: tetrabutylammonium iodide.

4.6.4 Cell assembly

4.6.4.1 Photoelectrochemical and electrochemical cells

The determination of the photoelectrochemical, charge-discharge and electrochromic properties were performed using a special single compartment three-electrode cell shown in figure 23. The cell consisted of a work electrode (7 cm^2, ϕ = 30 mm) in contact with the electrolyte solution and 4.9 cm^2 (ϕ = 25 mm) of light radiating area), a 25 × 10 mm platinum as counter electrode. The reference electrode was a 0.01 M $Ag/AgClO_4$ in 1 M $LiClO_4$ PC solution when the electrolyte was an organic medium or a saturated calomel electrode (SCE) when the electrolyte was an aqueous solution. The potentials of the $Ag/AgClO_4$ electrode versus the normal hydrogen electrode (NHE), the SCE and the Li electrode are +0.87, +0.63 and -3.915 V, respectively.

The dye sensitised photoelectrochemical cells were built in a glove box under nitrogen atmosphere with a relative humidity RH < 1%. The cells were sealed using rubber gaskets and O-rings in the glove box. The photoelectrochemical measurement was made in air.

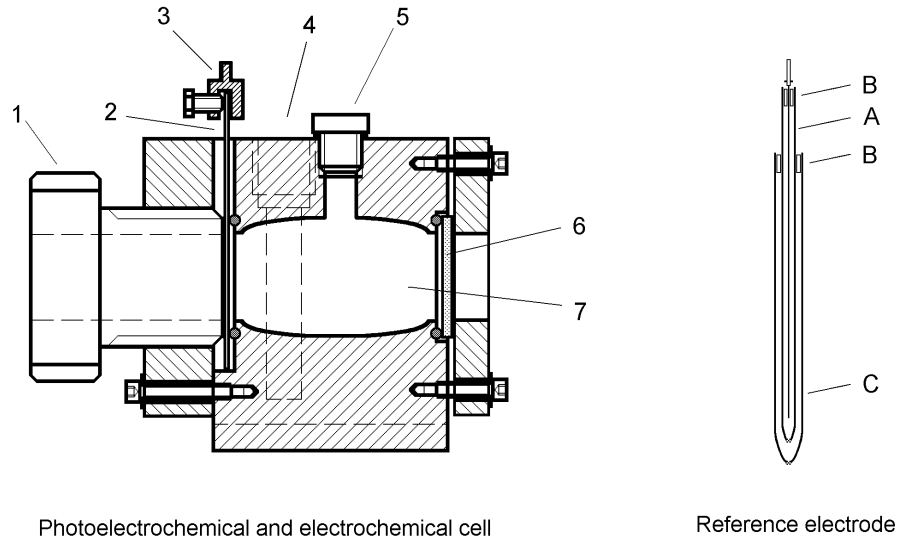

Figure 23: Scheme of the single compartment three-electrode cell for photoelectrochemical and electrochemical measurements. (1) swivelling stopper, (2) working electrode, (3) electrical contact, (4) inlet for reference and counter electrodes, (5) filling, (6) Fused quartz glass disk and (7) electrolyte. Reference electrode: (A) a saturated calomel electrode (SCE) or 0.01 M Ag/AgClO$_4$ in 1 M LiClO$_4$ PC, (B) seal and (C) electrolyte: 0.1 M LiClO$_4$ in PC for Ag/AgClO$_4$ electrode, saturated KCl for SCE.

4.6.4.2 Dye sensitised Nb_2O_5 solar cells

A typical sandwich-type two-electrode electrochemical cell for photovoltaic measurements (solar cell) consists of a dye sensitised Nb_2O_5 electrode, a counterelectrode, a spacer, and an organic electrolyte (figure 24). The counterelectrode was a Pt layer sputtered on a FTO glass. The spacer was a 1.1 mm thick VHB™ acrylic foam tape (3M Scotch™). The used electrolytes are given in table 3. The solar cells were fabricated in a glove box as the presence of water vapour was found to decrease significantly the efficiency of the cell. They were sealed with a two components epoxy resin L and R&G hardener L.

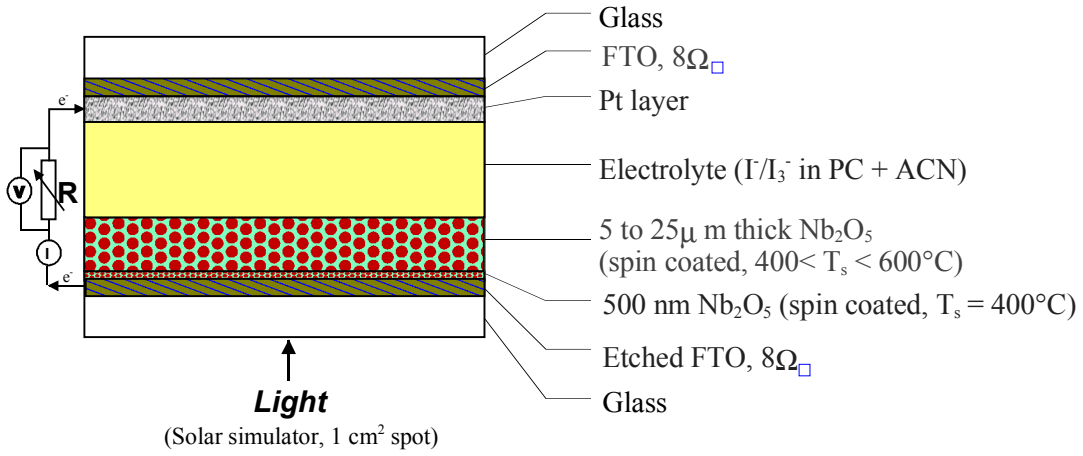

Figure 24: Scheme of a 2 × 2 cm^2 dye sensitised solar cell construction showing the illumination through the dye sensitised Nb_2O_5 layer.

4.7 Photoelectrochemical and electrochemical characterisation

4.7.1 The incident photon to current conversion efficiency (IPCE)

The incident photon-to-current conversion efficiency (IPCE) defined in section 2.1.3.3 (equation 17) is calculated as the ratio of the number of electrons generated by light in the external circuit (n_e) to the number of incident photons (n_p).

$$IPCE\ (\%) = \frac{n_e}{n_p} \times 100 \tag{41}$$

The number of electrons n_e generated by the light per second and per cm^2 ($cm^{-2}s^{-1}$) is expressed as

$$n_e = \frac{i \times 10^{-6}}{e} \tag{42}$$

where e is the elemental charge (1.60218×10^{-19} C) and i is the photocurrent density (A/cm^2).

The flux of incident photons n_p ($cm^{-2}s^{-1}$) is obtained from the following equation

$$n_p = \frac{I_o \times 10^{-3}}{h\nu} = \frac{I_o \times \lambda \times 10^{-12}}{hc} \tag{43}$$

where I_o is the intensity of light (W/cm^2), hν is its energy (eV), λ is the wavelength (nm) and c is the velocity of light (2.99792×10^8 m/s).

The IPCE can be therefore obtained by dividing equation 42 by equation 43

$$IPCE\ (\%) = \frac{124 \times i\ (\mu A / cm^2)}{I_o (mW / cm^2) \times \lambda\ (nm)} \tag{44}$$

The photocurrent action spectra (IPCE) were carried out using a set-up consisting of a UV-visible light source (Müller, Typ SVX 1530), a monochromator (Spex 270M), a potentiostat (Bank, LB 94) and a silicon photodiode (figure 25). The measurements were performed with two different light sources. The IPCE in the UV range (200-400 nm) was measured using a 150 W Xenon lamp and in the visible light range (400-800 nm) using a 150 W Tungsten lamp. The three-electrode cell (figure 23) was employed. The photocurrent in the short circuit condition and the calibrated incident light intensity were simultaneously recorded with a scanning step of 5 nm and analysed by a computer.

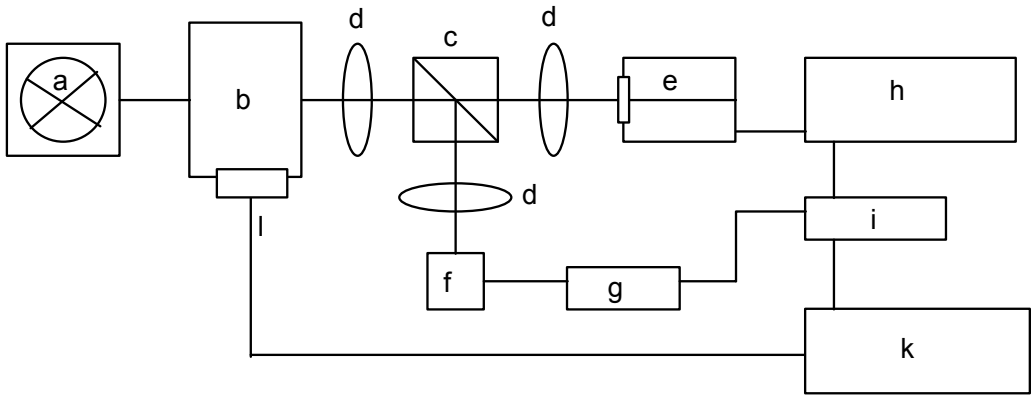

Figure 25: Experimental set-up for IPCE measurements with light source (a) (150 W Xenon lamp or 150 W Tungsten halogen lamp), (b) monochromator with (l) RS 232 interface, (c) beam splitter, (d) lenses (e) photoelectrochemical cell, (f) silicon photodiode, (g) amplifier,(h) potentiostat, (i) A/D converter and (k) computer.

4.7.2 Photoelectrochemical and photovoltaic measurements

A Princeton Applied Research (EG&G) Model 273A potentiostat/galvanostat was used for the photoelectrochemical and photovoltaic measurements. The three-electrode cell shown in figure 23 was used for measuring the photoelectrochemical properties. A 100 W tungsten-halogen lamp (Oriel) with a UV filter (< 400 nm cut-off) was used for excitation of the electrode in the back face (substrate side) configuration. Without notice, the scanning rate was 5 mV/s.

Sandwich-type two-electrode solar cells shown in figure 24 were used for measuring the current-voltage characteristics in the dark and under illumination. A commercial solar simulator with filters to simulate AM 1.5 global condition (Oriel, Model SP81160-1452) was used as the light source. The light intensity was adjusted by setting the lamp power and with a series of square aluminium sliding apertures. The incident light intensity was measured before each experiment with a broadband (0.19-20 μm) thermopile detector (Ophir Optronics, Model 2A-SH and NOVA-display).

The fill factor defined in section 2.1.3.3 is calculated as

$$fill\ factor\,(FF) = \frac{V_m(mV) \times I_m(mA/cm^2)}{V_{oc}(mV) \times I_{sc}(mA/cm^2)} \tag{45}$$

and the solar to electric energy conversion efficiency by

$$\eta(\%) = \frac{100 \times FF \times V_{oc}(V) \times I_{sc}(A/m^2)}{light\ \ intensity\,(W/m^2)} \tag{46}$$

4.7.3 Cyclic voltammetry (CV)

Cyclic voltammograms were carried out using the potentiostat/galvanostat (Princeton Applied Research Model 273A). A potential scan rate of 50 mV/s was used throughout the measurements. Single or multiscan cyclic measurements were performed within the potentials range -2.2 to +1.0 V vs. $Ag/AgClO_4$.

4.7.4 Chronoamperometry (CA)

Chronoamperometry (CA) employs three electrodes with a square wavefunction as the input for the Nb_2O_5 electrode. The double-step technique was used, in which the first step is used to generate a reduction reaction with lithiation and the second is used for the oxidation reaction with delithiation. The potential jumps immediately from the equilibrium potential to -2.2 V for 120 s and then jumps to +1.0 V vs. $Ag/AgClO_4$ for 120 s. The electrode transmission was recorded as a function of time during the voltage supplied to the samples.

The kinetics of coloration and bleaching of electrochromic electrodes may be studied by stepping the potential between the bleached state and the coloured state, while monitoring the time dependence of the current (chronoamperometry) and the transmittance at 550 nm. The current-time response is described by Cottrell equation [105]:

$$i(t) = \frac{nFA\,C_o^*\sqrt{D_o}}{\sqrt{\pi t}} \tag{47}$$

where A is the area of electrode, C_o^* is the bulk concentration of Li^+, D_o is the diffusion coefficient of Li^+ and t is the time.

The coloration efficiency (η) for electrodes is given as:

$$\eta = \frac{\Delta OD \times A}{Q} \tag{48}$$

where ΔOD is the change of the optical density between the bleached and coloured state, A is the area of electrode and Q is the total charge passed during coloration.

4.7.5 Chronopotentiometry (CE)

Chronopotentiometry was used for measuring the charge-discharge properties of Nb_2O_5 electrode. A constant current (-0.2 mA/cm^2) was applied to the electrode to cause a Li^+ insertion (discharge) and the time evolution of the potential of the electrode was recorded. The potential of the electrode rapidly changes toward more negative values until a new second reduction process starts. The current can also be reversed after some time. In our case the current was changed to an anodic current of equal magnitude (+0.2 mA/cm^2) (charge).

4.7.6 Electrochemical impedance spectroscopy (EIS)

4.7.6.1 Basic concept [219, 220]

Impedance spectroscopy is a method to analyse the impedance response of a sample to an external electric stimulus. It is a powerful method for characterising many intrinsic properties that influence the conductivity of materials and their interface with conducting electrodes and medium.

The behaviour of an electrochemical system can be often modelled with an equivalent circuit consisting of discrete electrical components which are representative of the physical and chemical processes taking place in the system. A resistance represents a conductive path that might account for the bulk conductivity of the material or a chemical step associated with a reaction. Similarly, a capacitance is generally associated with a space charge polarisation region. In the AC impedance method, a cell is perturbed with an alternating signal of small magnitude and one observes at steady state the way in which the system follows the perturbation as a function of the frequency. A sine wave input signal of angular frequency ω is the most appropriate for electrochemical studies:

$$U(t) = E\sin(\omega t) \tag{49}$$

The current response of the system is a phase shifted sine wave

$$i(t) = I\sin(\omega t + \phi) \tag{50}$$

where ϕ is a phase shift.

The impedance

$$Z(\omega) = \frac{U(t)}{i(t)} \tag{51}$$

is a complex parameter which can be represented either in polar coordinates (i.e. Bode plot) or in Cartesian coordinates (i.e. Nyquist plot):

$$Z(\omega) = |Z|e^{j\phi}, \quad |Z| = \frac{E}{I} \qquad \text{-Bode plot} \tag{52}$$

$$Z(\omega) = \mathrm{Re}(Z) + j\,\mathrm{Im}(Z) \qquad \text{-Nyquist plot} \tag{53}$$

where Re(ω) and Im(ω) are the real part and the imaginary part of the impedance. The relationships between these quantities are:

$$|Z|^2 = (\mathrm{Re}(\omega))^2 + (\mathrm{Im}(\omega))^2 \tag{54}$$

$$\phi = arc\,\tan\frac{\mathrm{Im}(\omega)}{\mathrm{Re}(\omega)} \tag{55}$$

$$\mathrm{Re}(\omega) = Z_{re} = |Z|\ \cos\phi \tag{56}$$

$$\mathrm{Im}(\omega) = Z_{im} = |Z| \sin\phi \tag{57}$$

The two type of plots used to describe these relationships are illustrated in figure 26 for a typical equivalent circuit of an electrochemical cell

$$Z(\omega) = \frac{U(t)}{i(t)} = R\Omega + \frac{R}{1 + j\omega CR} \tag{58}$$

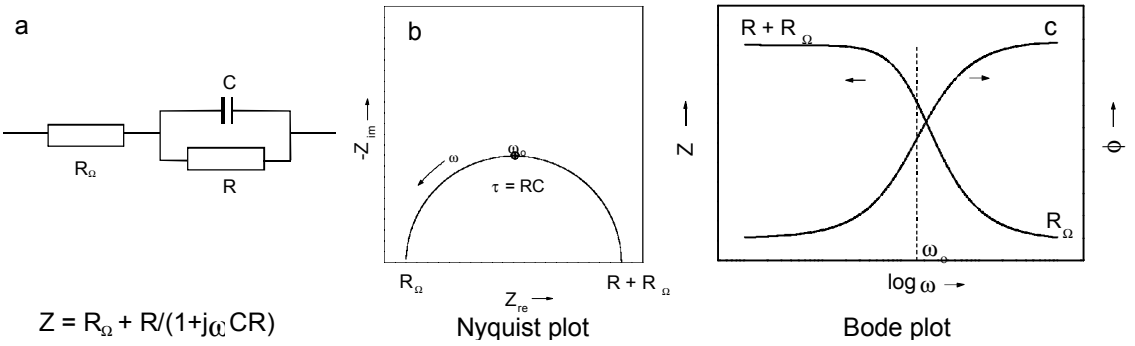

Figure 26: Equivalent circuit and impedance plots of a typical electrochemical cell.

The impedance spectroscopy of many electrochemical systems represented in the Nyquist plot resembles a depressed semicircle, whose centre is at some distance below the Z_{re}-axis (figure 27).

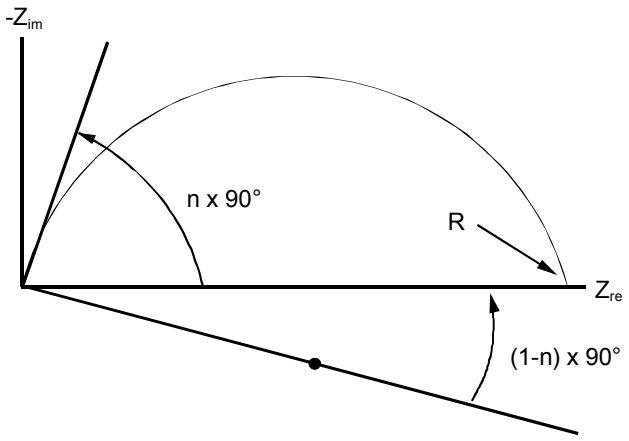

Figure 27: Nyquist plot of a constant phase element (CPE). The semicircle is depressed by an angle of (1-n)×90°.

A constant phase element (CPE) is therefore used as an equivalent circuit to fit the spectrum. It can be thought of having a characteristic intermediate between a capacitor and a resistor, i.e. a ″leaky″ capacitor. Mathematically, a CPE impedance is given by [221].

$$Z = \frac{1}{\omega_o C (j\,\omega/\omega_o)^n} \tag{59}$$

where n is a number smaller than 1 (1 is the value case of a pure capacitance $Z = \frac{1}{j\omega C}$).

A consequence of this simple equation is that the phase angle of the CPE impedance is independent of the frequency and has a value of -(n×90°). This gives the CPE´s name.

Depressed semicircles have been related to various phenomena, depending on the nature of the system being investigated. Most of them have been linked to some non homogeneous property of the system or to a distribution of the value of some physical property of the system. For instance one physical explanation of a CPE behaviour was related to the electrode roughness. For a rough, fractal surface, the fractal dimension D_f of the surface lies between 2 (absolutely flat) and 3 (resembling a porous cube). In this case $n = \frac{1}{D_f - 1}$ [221]. Non homogeneous reaction rates occurring on a surface on which there is a distribution of active sites with different activation energies also leads to a CPE behaviour [219]. A third explanation was related to a varying thickness or composition of a coating. For example, if the conductivity of a coating changes with the distance through the coating, the resulting impedance spectrum can closely approximate that of a CPE with $n = 1 - \frac{x}{d}$ [221], where d is thickness of an insulating surface layer and x is the penetration depth of the conducting material into the insulating layer.

4.7.6.2 Measurements and analysis

Impedance measurements were carried out using an IM6d impedance analyzer (Zahner Elektrik). Impedance spectra were potentiostatically measured by applying an ac voltage of 10 mV amplitude over the frequency range 100 kHz to 100 mHz after the electrode had attained an equilibrium at each potential (figure 28). The single-compartment cell and the light source have been described in section 4.6.4.1 and 4.7.2, respectively.

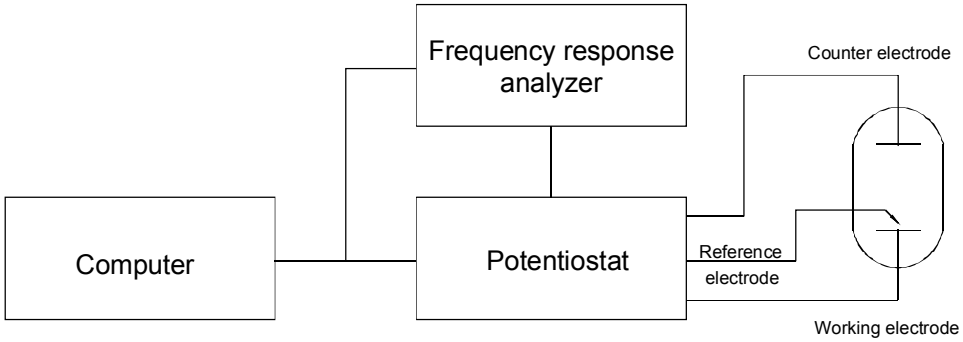

Figure 28: Scheme of the impedance measurement

The simulation of the impedance spectra (IS) with an equivalent electric circuit was done using the software "SIM" supplied by Zahner Elektrik following the flow diagram shown in figure 29. Such fitting is accurately accomplished by the complex non-linear regression least squares fitting (CNRLS) method used in the software.

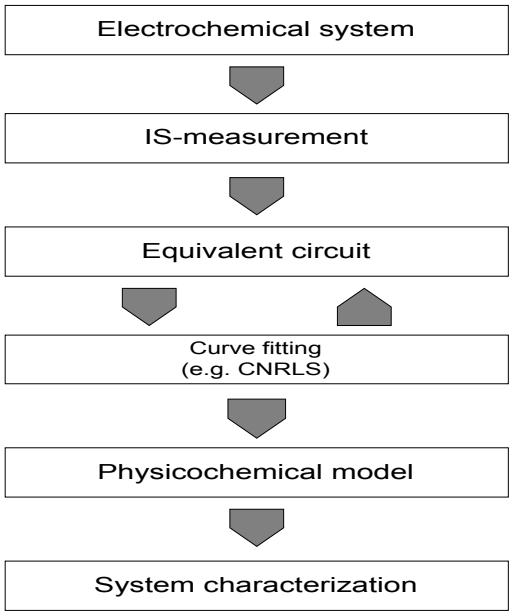

Figure 29: Flow diagram for the measurement and characterisation of the dye-sensitised solar cell.

5 Results and discussion

5.1 Nb_2O_5 sols

The experimental procedure to obtain viscous colloidal Nb_2O_5 solutions was shown in figure 18. In this section, the chemistry of niobium chloroalkoxide precursors for the preparation of stable and viscous Nb_2O_5 sols are discussed.

5.1.1 Niobium chloroethoxide and chloroethoxo-acetate

Niobium chloroethoxides are easily prepared by dissolving $NbCl_5$ in anhydrous ethanol according to equation 60.

$$NbCl_5 + xEtOH \rightarrow NbCl_{5-x}(OEt)_x + xHCl \qquad (x = 2,3) \qquad (60)$$

With an excess of EtOH only one species, $NbCl_2(OEt)_3$, exists in the solution [150, 222, 223].

Although niobium chloroethoxides are less reactive against water than $NbCl_5$ or the pure alkoxides, which produce Nb_2O_5 precipitates, their complexion with acetic acid still retards the hydrolysis and condensation reaction rates and allows to obtain homogeneous colloidal solutions rather than a precipitate. The chemical modification of $NbCl_2(OEt)_3$ is presumed to form niobium chloroethoxo-acetates according to equation 61 and is accompanied by a weak exothermic reaction.

$$NbCl_2(OEt)_3 + yHOAc \Leftrightarrow NbCl_2(OEt)_{3-y}(OAc)_y + yHCl \qquad (y = 0, 1, 2) \qquad (61)$$

The acetate group is a stronger complexing reagent than the ethoxy group so that ethoxy groups are preferentially exchanged by acetate ligands. Niobium atom has a coordination number of 6. According to the infrared spectrum and ^{1}H- and ^{13}C-NMR spectra reported by Griesmar et al. [224], the chloroethoxo-acetates are always a mixture of monomeric and dimeric species (figure 30). For AcOH/Nb = 2, the dimeric ones are the dominant species and have 6-fold coordinated niobium atoms bonded together via carboxylate bridges (figure 30a).

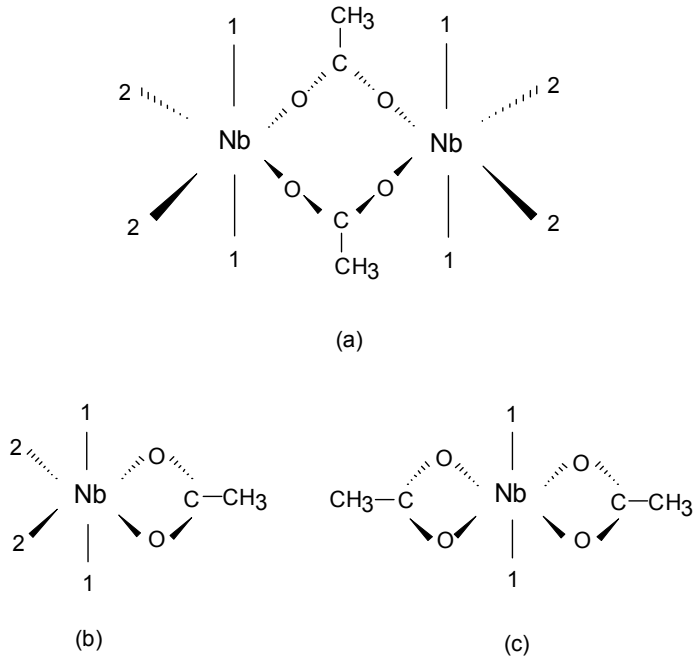

Figure 30: Structure of niobium chloroethoxide modified by acetic acid (AcOH/Nb = 2). (a) Dimeric niobium chloroethoxo-acetate. (b) monomeric niobium chloroethoxo-acetate with one acetate substituent. (c)monomeric niobium chloroethoxo-acetate with two acetate substituents (adapted from [224]). Positions 1 and 2 are occupied by ethoxy group or chloride ion.

5.1.2 Niobium chloroethoxo-acetate hydrolysis

The mechanisms of hydrolysis and condensation are described by the following simplified equations 62 and 63:

Hydrolysis:

$$\begin{aligned} &For\ 1 \le a \le 2: \\ &Nb\,Cl_2(OEt)_{3-y}(OAc)_y + a\,H_2O \leftrightarrow Nb\,Cl_2(OEt)_{3-y-a}(OAc)_y(OH)_a + aEtOH \\ &For\ a = 3: \\ &Nb\,Cl_2(OEt)_{3-y-a}(OAc)_y(OH)_a + 3\,H_2O \leftrightarrow Nb\,Cl_2(OH)_3 + (3-y)EtOH + yAcOH \end{aligned} \tag{62}$$

$NbCl_2(OH)_3$ is a completely hydrolysed product [150].

Condensation and polymersation:

$$nNb\,Cl_2(OEt)_{3-y-a}(OAc)_y(OH)_a \rightarrow \left\lfloor (O)_b\,Nb\,Cl_2(OEt)_c(OAc)_y(OH)_d \right\rfloor_n + nb(H_2O + EtOH) \tag{63}$$

Similar to $Ti(Opr^i)_x(OAc)_y$, the OEt groups and the chloride ions of $NbCl_2(OEt)_{3-y}(OAc)_y$ are preferentially hydrolysed [140, 225], whereas the acetate ligands remain bonded to niobium throughout most of the condensation process. Since they are not hydrolysed, the CH_3COO^- ligands effectively alter the condensation pathway, promoting probably the formation of linear polymers.

For saturated niobium atoms (coordination 6), both hydrolysis and condensation occur by nucleophilic substitution (S_N) mechanisms. This is followed by a proton transfer from the attacking molecule to an ethoxide, a chloride, an acetate- or a hydroxo-ligand during the transition state and the removal of the protonated species as either ethanol, HCl, acetic acid or water.

An excess water leads to a stable colloidal sol. The most likely molecular structure of the niobium chloroethoxo-acetate colloid is shown in figure 31.

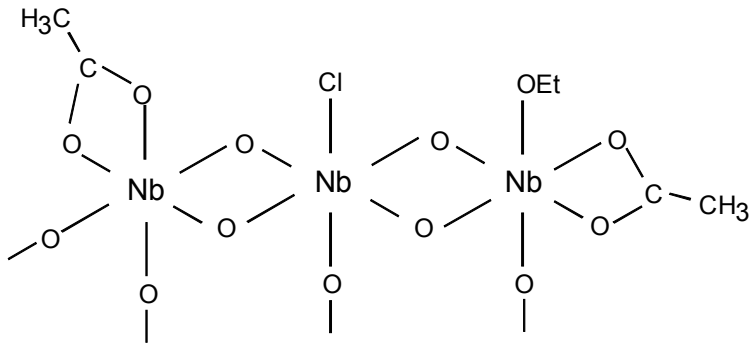

Figure 31: Structural model of the oxopolymer network of the niobium chloroethoxo-acetate colloid (adapted from [224]).

The effect of water content on the hydrolysis and the condensation of niobium chloroethoxo-acetates prepared with a 2:1 glacial acetic acid to chloroethoxide molar ratio was observed by preparing a series of sols with molar ratios of water to niobium atom ranging from 5 to 60. As seen in figure 32, the turbid degree of the sols increases with increasing the molar ratio of H_2O/Nb. Clear and transparent sols are obtained with H_2O/Nb molar ratio up to 25:1 (sol No.1 and 6) while translucent sols are formed when H_2O/Nb = 30:1 and 35:1(sol No.7, 8) and a gel is formed (sol No.10) for H_2O/Nb ≅ 40. A high content of water results in a high degree of hydrolysis, which further promotes the condensing polymerisation.

Table 4 gives the effect of water content on the gelling time. It decreases with increasing the molar ratio H_2O/Nb and when the kinetics of the hydrolysis is faster than that of the condensing polymerisation, a precipitate appears. The translucent gels which contain amorphous precipitates within their network are obtained at a high content of water.

The variation of the sol kinematic viscosity and the colloidal particle size with the H_2O:Nb molar ratio is shown in figure 33. Without water and up to H_2O:Nb = 10, the particle size is smaller than 2 nm, but the viscosity increases. This is due to a partial hydrolysis and a low degree of polymerisation of the niobium chloroethoxo-acetates. The viscosity remains low up to H_2O:Nb = 20 and then increases drastically in parallel with the increase of the particle size, corresponding to the formation of a translucent sol.

Figure 32: Nb_2O_5 sols with different H_2O:Nb molar ratio (before reflux).

Table 4: The effect of water content on gelling time

Sol No.	H_2O/Nb (molar ratio)	Gelling time [min]	Remarks
8	35	830	very soft and white translucent gel
9	37	290	soft and white translucent gel
10	39.1	150	white opaque gel
11	41.5	120	white opaque gel
12	48.3	95	white opaque gel
13	62.9	80	white opaque gel

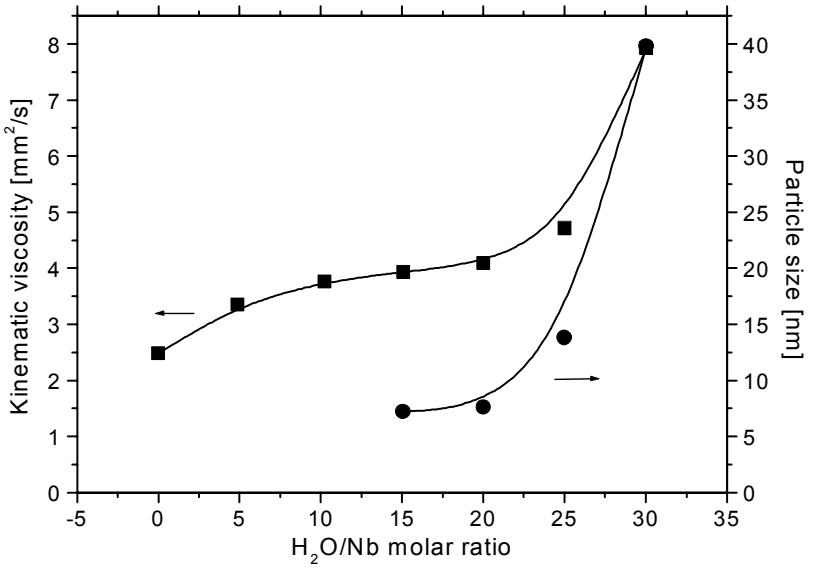

Figure 33: Sol viscosity and particle size of Nb_2O_5 sols as a function of the H_2O:Nb molar ratio (before reflux).

5.1.3 Heat treatment of the sols

The hydrolysis and condensation reactions do not stop with time, but heat treatment which accelerates the hydrolysis and condensation rates can give a stable sol. Figure 34 shows the variation of the particle size after reflux at 96°C. For a given H_2O:Nb ratio the particle size increases slowly with the refluxing time. The origin of the dip observed at around 90 min is still unknown.

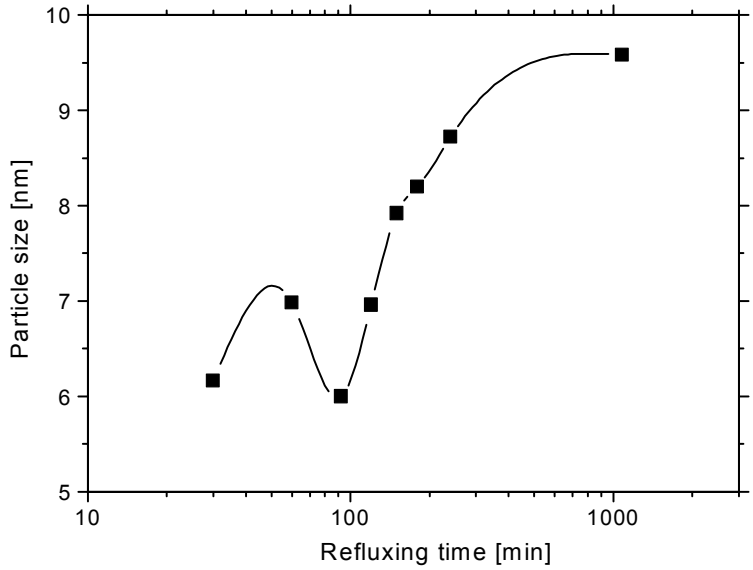

Figure 34: Influence of the refluxing time on the particle size of a niobia sol (H_2O:Nb = 10:1, refluxing temperature 96°C).

A heat treatment of the Nb_2O_5 sol plays an important role in adjusting the properties and the stability of the sol. Figure 35 shows the influence of a 2 h reflux on the viscosity and the particle size. Compared with non-refluxed sols (figure 33), colloidal particles were already observed for H_2O:Nb = 5:1. The particle size increases slowly up to H_2O:Nb = 30:1 but the viscosity of the sols remains constant for H_2O:Nb > 10. Stable Nb_2O_5 sols have been obtained up to a 40:1 H_2O:Nb ratio. For higher value a precipitation occurs readily as soon as the heating is started. The precipitate may be an aggregate of completely hydrolysed niobium chloroethoxo-acetates, $NbCl_2(OH)_3$. Owing to the strong coordinative properties of the OH groups, the complex is not stable as a monomer and olation leads to the formation of a white opaque gel. The heating of the sols therefore increases the hydrolysis rate, leading to the formation of low molecular weight polymerised species, retarding the gel formation. This explains why the viscosity of the sols does not vary with increasing water content and why small colloidal particles are formed.

Figure 36 shows pictures of 2 h refluxed Nb_2O_5 sols with different H_2O:Nb molar ratio. Clear, transparent colloidal sols are obtained up to H_2O:Nb = 10:1 (sol No.15) while translucent colloidal sols with increasing turbidity are formed in the range 15:1 to 40:1 (sol No.16, 20, 21). A white opaque gel is obtained for a ratio 50:1 (sol No.22). No obvious change have been

observed after 33 months. The measurement of X-ray diffraction (not shown) indicates that the colloidal particles are amorphous.

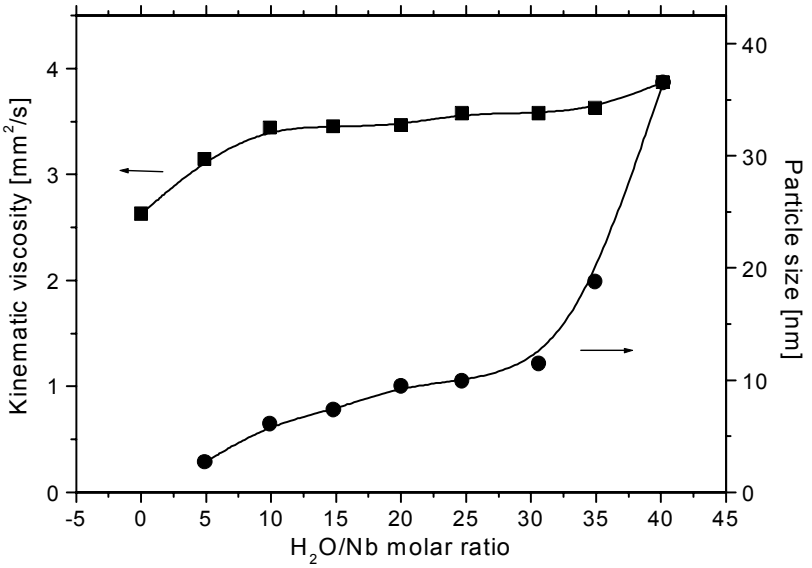

Figure 35: Sol viscosity and particle size of Nb_2O_5 sols as a function of the H_2O:Nb molar ratio (after 2 h reflux).

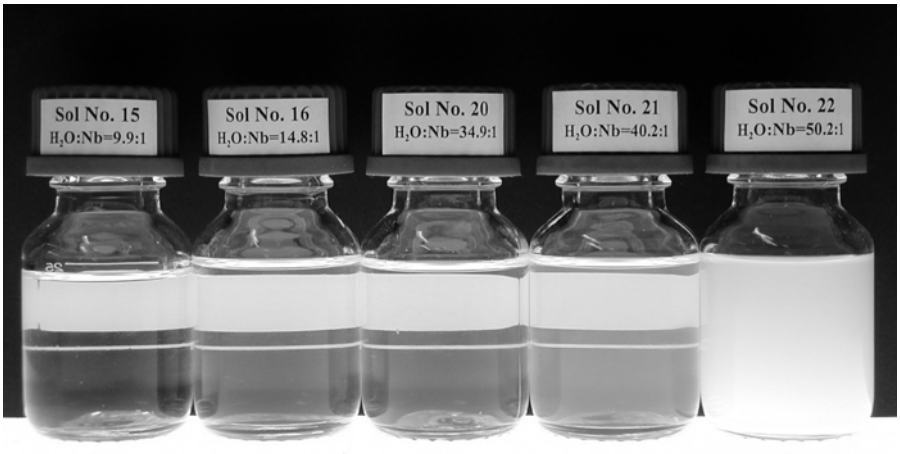

Figure 36: Appearance of Nb_2O_5 sols with different H_2O:Nb molar ratio after a 2 h reflux at 96°C (after 33 months).

5.1.4 Effect of chemical additives

It is known that the reaction schemes as well as the resultant morphology of the sols can be modified by adding chemical compounds such as polymeric and organic molecules. Additives are used to modify the surface tension, to enhance the viscosity of the sols, to vary the compatibility among the colloidal particles, to stabilise the sols or to supply a ceramic skeleton to obtain crack-free nanoporous coatings after sintering.

The additive used in this study is poly(ethylene glycol) (PEG) with different molecular weight. Its effect has been only tested for the niobia sol hydrolysed with a H_2O:Nb ratio of 30.

Figure 37 shows the molecular structure of poly(ethylene glycol). It is assumed that the unshared electron pairs of the ether oxygen, which give strong complex groups to the polymer, can take part in complex chemical reactions in which niobium atoms and chloride ions are released (figure 38). In this way chemically modified Nb_2O_5 colloidal particles may be stabilised and prevented to aggregate. PEG will also provide a support for the gel and prevent the collapse of the pores during the evaporation of the solvent (drying stage) and the shrinkage of the film (sintering stage). As shown later the addition of poly(ethylene glycol) (PEG) effectively allows to obtain thick, crack free and more porous coatings and also to avoid the formation of a Nb_3O_7Cl phase during the sintering process.

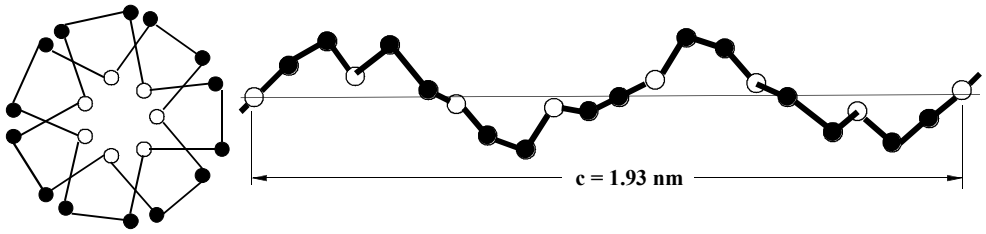

Figure 37: The molecular structure of poly(ethylene glycol), where ● represents the ethylene group and ○ is the oxygen atom [226].

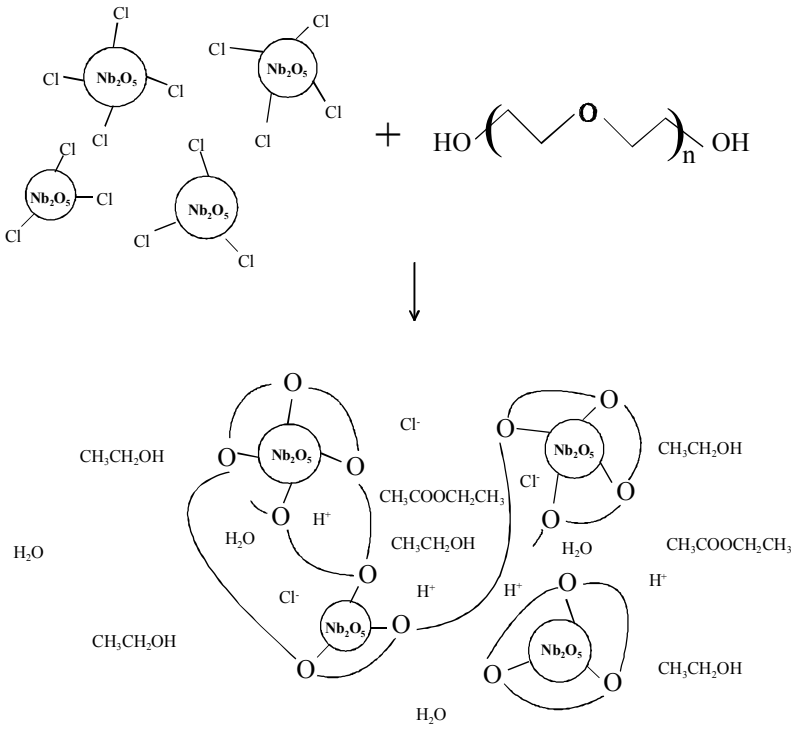

Figure 38: Schematic of physical and chemical effects of the poly(ethylene glycol) as the additive in the Nb_2O_5 sol.

Conclusions

Colloidal Nb_2O_5 sols have been prepared by hydrolysing niobium chloroethoxo-acetates. These precursors have been obtained by complexing, with glacial acetic acid, niobium chloroethoxide prepared by dissolving cheap commercially available $NbCl_5$ in anhydrous ethanol. The stability

of the sols prepared with a H_2O:Nb molar ratio up to 40 has been drastically improved (up to 3 years) by refluxing them at 96°C during 2 h. The kinematic viscosity of the sols which will influence the thickness of the coatings, and the niobia colloidal size can be controlled by varying the H_2O:Nb molar ratio. Typical values are 3.5 mm^2/s and 10 nm respectively for a H_2O:Nb ratio of 30. In order to increase the nanoporosity and BET surface area of the coatings, niobia sols with H_2O:Nb = 30 containing different amount of PEG600, PEG20000 and carbon soot have been also prepared.

5.2 Structural properties of Nb_2O_5 powders

5.2.1 Thermal analysis

In order to study the sintering process of the Nb_2O_5 films, the thermogravimetric and differential thermal analysis (TG/DTA) coupled with a mass spectroscopy (MS) analysis have been carried out for xerogels obtained by drying the sols prepared with different H_2O:Nb molar ratio and with different additives for three days at 110°C.

Niobia xerogels without additive

Figure 39 shows typical DTA/TG/DTG curves for a xerogel obtained from a refluxed sol prepared with a molar ratio H_2O:Nb = 0. The total weight loss at 800°C is 26.6% and occurs in three steps labelled I, II, III. Step I is characterised by a broad endothermic peak at 189°C attributed to the loss of residual free water and alcohol entrapped in the micropores of the powder, as confirmed by the mass spectroscopy analysis (figure 40). The TG curve shows a substantial weight loss of 16.8% from room temperature to about 250°C. Subsequent heating up to 425°C induces only a small weight loss, accompanied by a broad exothermic DTA peak, suggesting a partial crystallisation of the gel and the carbonation of the organic groups chemically bonded to the oxide network. The water evolved (figure 40) comes from the dehydration of the organic ligands. The second step, occurring in the temperature range 420-480°C, is characterised by a sharp exothermic peak at 459°C and a 4% weight loss. It is assigned to the crystallisation process and is accompanied by a loss of structural water by dehydration condensation of hydroxyl groups and the burning of carbon as shown by the MS analysis of the H_2O, CO_2 and O_2 curves (figure 40). A further 5% weight loss is observed from 525°C to 635°C (step III). This stage is linked to the hydrolysis degree of the sols as weight loss appears at around 672°C for H_2O:Nb = 9.9, 660°C for H_2O:Nb = 30.6, and 656°C for H_2O:Nb = 50.2 (figure 108 in appendix A4).

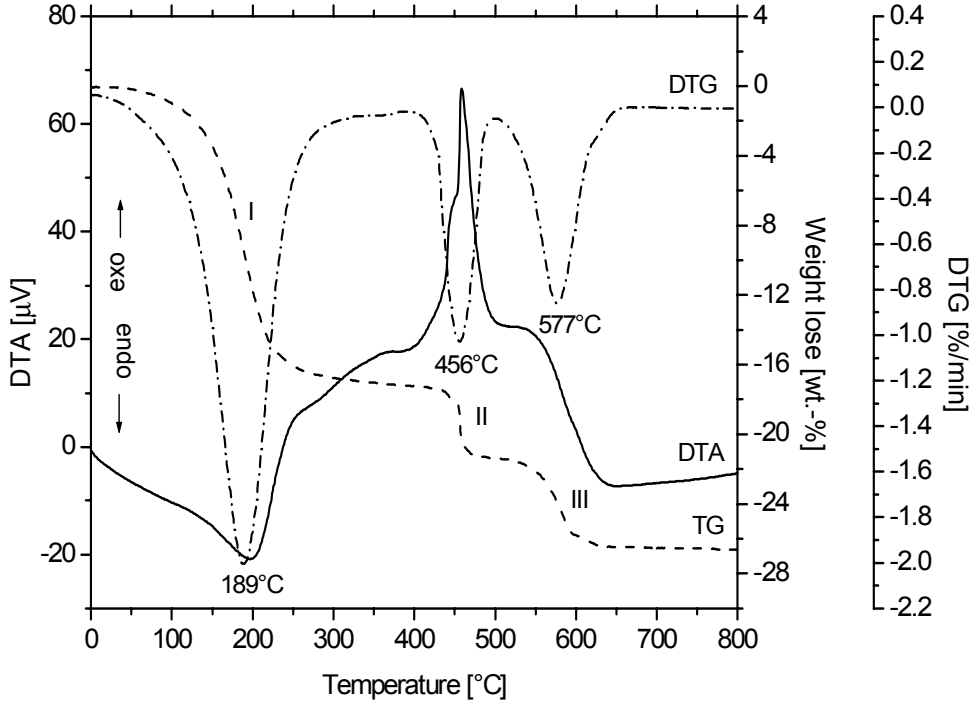

Figure 39: DTA/TG/DTG of a Nb_2O_5 xerogel (molar ratio H_2O:Nb = 0 without additive). Heating rate 10 K/min.

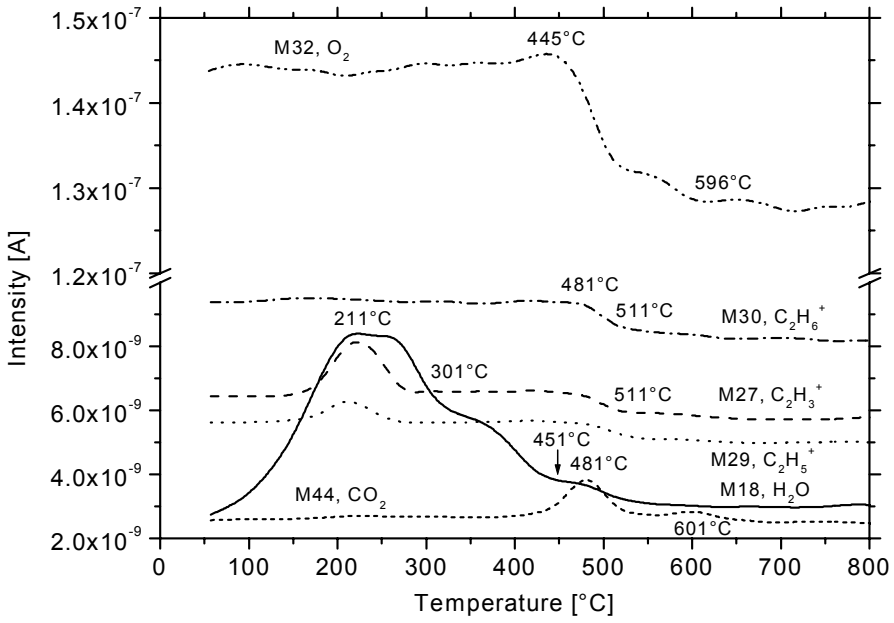

Figure 40: Mass spectroscopy analysis of a Nb_2O_5 xerogel obtained during the DTA/TG run of figure 39.

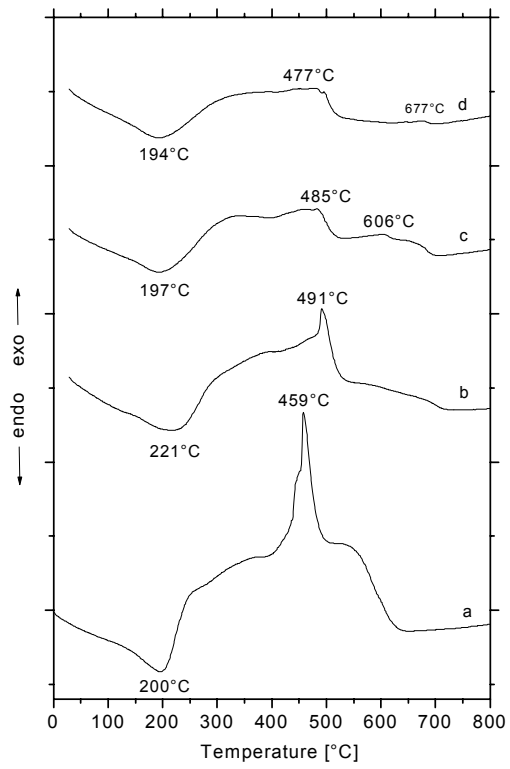

Figure 41: DTA curves of Nb_2O_5 xerogels prepared with different H_2O:Nb molar ratio without additive (a) H_2O:Nb = 0, (b) H_2O:Nb = 9.9, (c) H_2O:Nb = 30.6, (d) H_2O:Nb = 50.2.

Figure 41 shows the DTA curves of Nb_2O_5 xerogels obtained from refluxed sols prepared with different H_2O:Nb molar ratio. The broad endothermic peak between room temperature and about 250°C for all xerogels is due to the evaporation of the water and alcohol physically trapped in the open pores. The exothermic peak at about 470°C, associated with the crystallisation process, the loss of structural water and the burning of carbon, strongly decreases with the water content. This can be understood by inspecting equation 62 which shows that water and acetic acid are released during hydrolysis. Therefore with an increasing H_2O:Nb ratio, less organic groups especially carbon and structural water remain in the network.

Niobia xerogels with additive

Figure 42 shows DTA/TG/DTG curves of a Nb_2O_5 xerogel prepared by adding 20 wt.-% PEG20000 to a substoichiometric hydrolysed sol (H_2O:Nb = 30.6) and figure 43 shows the H_2O and CO_2 mass spectroscopy analysis. The total weight loss during the heating from room temperature to 800°C is 31.7% and takes place in four steps (I, II, III, IV). Step I between 25°C and 165°C is characteristic of an endothermic evaporation of the water and solvent. The weight loss is 6.9%. The 14.8% weight loss of the step II occurring between 165°C and 288°C can be assigned to organic decomposition and oxidation. At 241°C the organic fragments with molecular weight 15, 25, 26, 27, 31, 39, 41, 42, 43, 45, 49, 50, 51, 52, 57, 58, 61, 62, 63, 64, 66, 88, 93 and 95 are detected by mass spectroscopy (figure 110 in appendix A4). Step III

between 288°C and 440°C with a weight loss of 3.7% is due to the carbonation and oxidation of the organic residuals and the partial crystallisation of the xerogel. Step IV between 440°C and 600°C with a 6.3% weight loss is attributed to the removal of hydroxyl groups in the crystalline network and the complete burning of carbon.

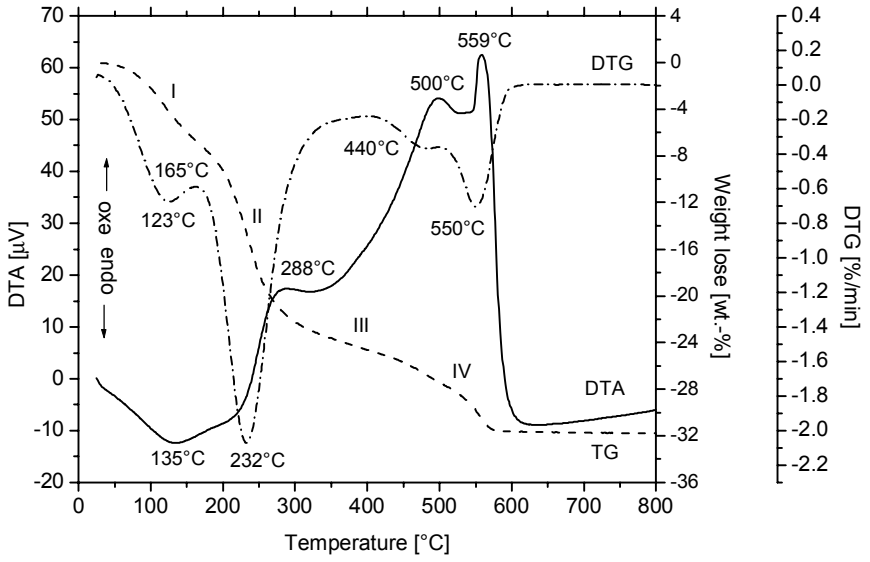

Figure 42: DTA/TG/DTG of Nb_2O_5 xerogel prepared with molar ratio H_2O:Nb = 30.6 and 20 wt.-% PEG 20000. Heating rate 10 K/min.

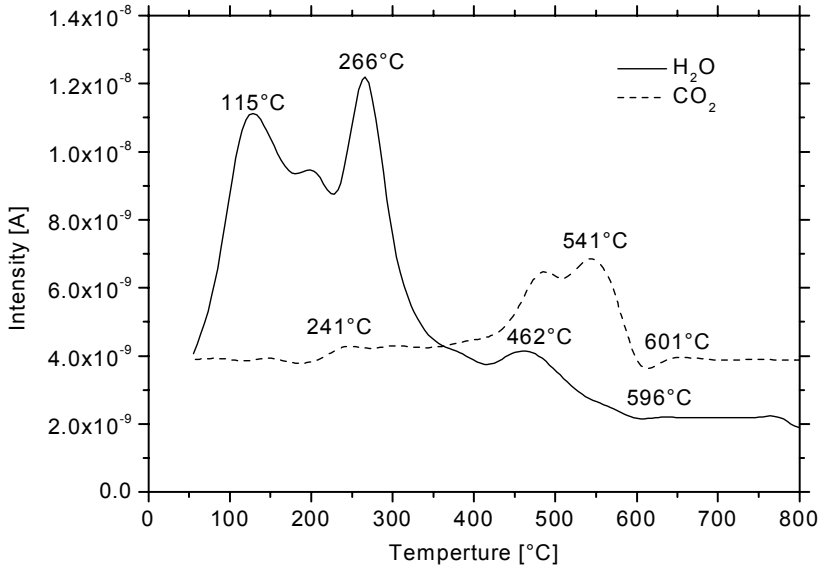

Figure 43: Mass spectroscopy analysis of H_2O, CO_2 of the Nb_2O_5 xerogel obtained during the DTA/TG run of figure 42.

The overall behaviour of the DTA curve of Nb_2O_5 xerogels (H_2O:Nb = 30.6) prepared without and with different additives is quite different (figure 44). The strong exothermic peaks observed between 250°C and 600°C with the modified xerogels are due to the high amount of organic species which are decomposed, oxidised and burned within this temperature range and

which provide a high heat of combustion for calcination. The curves with PEG600 and PEG20000 are however similar (figure 44b and c).

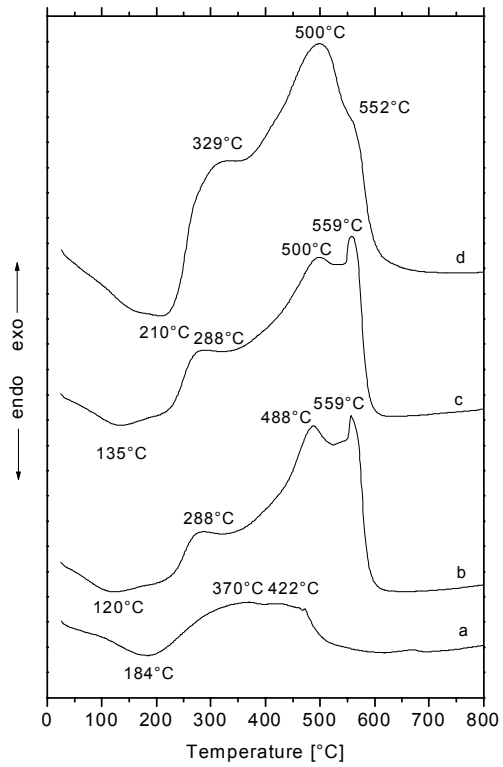

Figure 44: DTA curves of Nb_2O_5 xerogels (H_2O:Nb = 30.6) prepared without additive (a) (figure 41c), and with additive PEG600 (b), PEG20000 (c) (figure 42), PEG20000 + C (d).

5.2.2 Infrared spectroscopy

The purpose of this study is to give further information on the structure of the dried and heat treated gel. Four different xerogels have been measured: one prepared with a nonhydrolysed sol, one prepared with a hydrolysed sol (ratio H_2O:Nb = 30.6) and the same xerogels containing PEG20000 and PEG 20000 + carbon soot.

Nonhydrolysed xerogel

The spectrum of nonhydrolysed xerogel (figure 45) dried at 150°C shows a very large band in the vicinity of 3200 cm^{-1} corresponding to the fundamental stretching vibration of free or bounded -OH hydroxyl groups. The small sharp band at 1605 cm^{-1} is related to molecular water. The bands located in the range 2870 -2970 cm^{-1} can be identified as the C-H stretching vibration of the alkyl groups of the ethoxy and acetate ligands, and those at 1390 and 1445 cm^{-1} as the bending vibration of the same species. The bands in the range 1020 - 1120 cm^{-1} should correspond to the C-O-C_2H_5 stretching vibrations of different ethoxy ligands bound to niobium atoms. The low-energy wavenumber range is mainly dominated by two large bands around 870 and 595 cm^{-1} due to the Nb-O stretching vibrations. This shows that the Nb-O oxo-polymer network is already present at low temperature.

The heat treatment temperature affects the IR behaviour. The intensity of the 3200 and 1605 cm^{-1} bands as well as those related to organic ligands decrease and disappear for T ≥ 450°C in agreement with the DTA/TG/MS results (figure 39 and 40). The carbon dioxide peak at around 2335 cm^{-1} appears for T > 400°C and originates probably from the burning of residual carbon (figure 39 and 40) and unable to escape (closed pores). The temperature behaviour of the Nb-O stretching vibration is summarised in table 5. The broad peaks at 870 and 595 cm^{-1} observed at 150°C shift to 910 and 640 cm^{-1} respectively at 250°C. This is due to the breaking of the Nb-O-C_2H_5 bonds of the oxo-polymer network. As shown in section 2.4 and figure 13a, niobia can have several phases with different structural unity [227]. Therefore the positions of the Nb-O vibration peaks will depend on the sintering temperature. Identification of the position of the peaks with a structural unit has not been performed. But the results obtained at 800°C are consistent with those reported in [228].

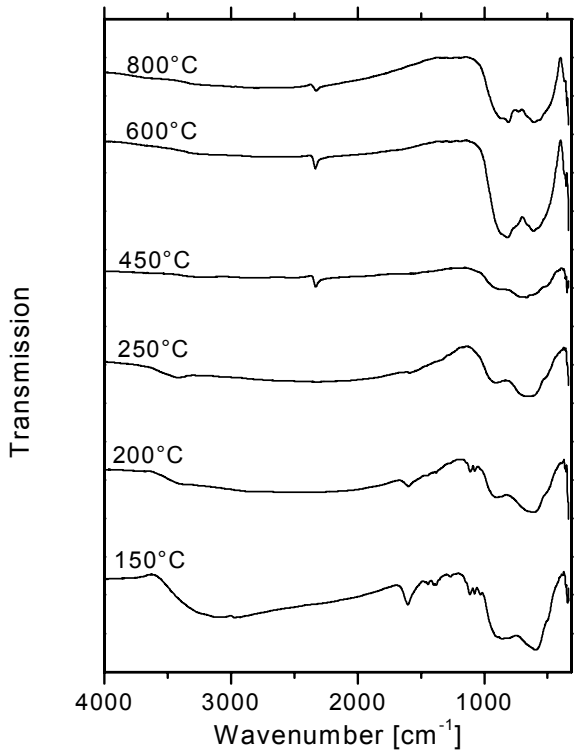

Figure 45: Infrared spectra of nonhydrolysed Nb_2O_5 xerogel (molar ratio H_2O:Nb = 0) heat treated at different temperature.

Table 5: Wave numbers of Nb_2O_5 IR peaks (data from figure 45).

Temperature [°C]	Nb-O vibration wavenumber [cm^{-1}]			
150	870		595	
200	905		610	
250	910		640	
450	865		660	
600	810		600	
800	805	730	605	
white rhombic crystals $Nb_2O_5 \cdot nH_2O$ [228]	805	730	630	365

Hydrolysed xerogel (H_2O:Nb = 30.6)

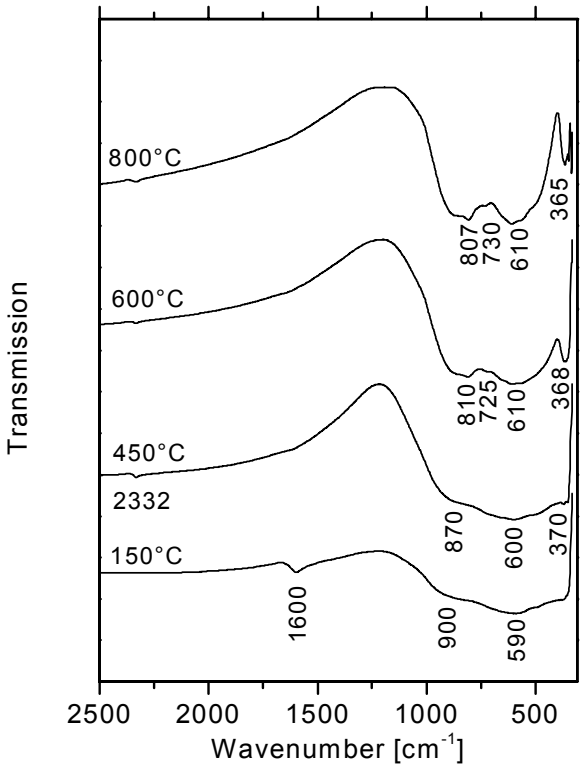

Figure 46: Infrared spectra of hydrolysed Nb_2O_5 xerogel (molar ratio H_2O:Nb = 30.6) heat treated at different temperature.

The temperature behaviour of the infrared spectrum of hydrolysed Nb_2O_5 xerogel is shown in figure 46. The spectrum at 150°C is typical of an amorphous niobium oxide network. The peak at 1600 cm^{-1} is due to the stretching vibration of free water (H-O-H) and the fundamental stretching vibration band (3200 - 3400 cm^{-1}) due to the different O-H hydroxyl groups is not

present (not shown). As before, a weak CO_2 peaks appears around 2332 cm^{-1} for T ≥ 450°C and the Nb-O vibration bands shift toward lower wavenumbers during the crystallisation process and phase transformation and a new peak around 365 cm^{-1} appears.

Hydrolysed xerogels with PEG20000 additive

Figure 47 shows the infrared spectra of PEG20000 and a hydrolysed Nb_2O_5 xerogel (molar ratio H_2O:Nb = 30.6) containing 20 wt.-% PEG20000 heated at different temperatures.

For PEG20000 the bands at 2948 and 2890 cm^{-1} are ascribed to the asymmetric and symmetric CH_2 stretching bands. The C-O-C stretching vibration gives very strong bands at 1150, 1100 and 1060 cm^{-1}. The band at 1470 cm^{-1} is assigned to the CH_2 scissoring mode of the ether methylene units in the PEG chains and those at 1282 and 1245 cm^{-1} are twisting vibration. The bands at 1343 and 960 cm^{-1} correspond to the ether CH_2 wagging and rocking modes, respectively [229-231].

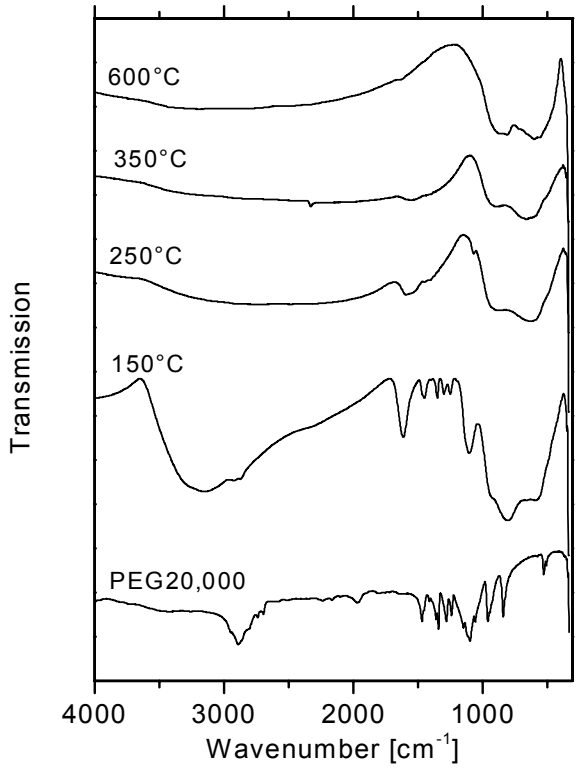

Figure 47: Infrared spectra of hydrolysed Nb_2O_5 xerogel (molar ratio H_2O:Nb = 30.6) with 20 wt.-% PEG20000 heat treated at different temperature and PEG20000.

Almost all the peaks of PEG20000 are found in the spectrum of the xerogel heat treated at 150°C together with the vibration peaks of the free molecular water, OH and Nb-O groups. The PEG peaks are however slightly displaced (table 6). The three strong split peaks at 1150, 1100 and 1060 cm^{-1} corresponding to the C-O-C stretching vibrations merged into one. At 250°C only the C-O-C peak at 1065 cm^{-1} and the CH_2 scissoring mode at 1450 cm^{-1} are observed. As mentioned in section 5.1.3, a complex between the niobium chloroethoxo-acetate colloids and the ether groups of PEG may be formed, resulting in the presence of ether and

CH_2 groups. All the other PEG peaks have disappeared. At 350°C a weak CO_2 vibration peak at 2330 cm^{-1} is again observed. The band at 1620 cm^{-1} shows the presence of water up to 600°C. As noted before, the position of the Nb-O bands shifts slightly with increasing sintering temperature from 862 cm^{-1} and ~645 cm^{-1} (sintering at 250°C and 350°C) to 815 cm^{-1} and 615 cm^{-1} (sintering at 600°C). At this temperature the spectrum is quite similar to that of the standard sample [228].

Table 6: Positions of the IR peaks and their vibrational mode assignments for PEG 20000 and hydrolysed Nb_2O_5 xerogel (molar ratio H_2O:Nb = 30.6) with 40% PEG20000.

PEG20000 [cm^{-1}]	Nb_2O_5 xerogel with PEG20000 [cm^{-1}]		assignments and remarks
	150°C	250°C	
	3150		OH stretching
2948	2920		CH_2 asym stretching
2890	2970		CH_2 sym stretching
	1616	1595	molecular water
1470	1455	1450	CH_2 scissoring
1343	1355		CH_2 wagging
1282, 1245	1300, 1250		CH_2 twisting
1150, 1100, 1060	1105	1065	C-O-C stretching
960	940		CH_2 rocking
	810, 590	862, 645	Nb-O stretching

Hydrolysed xerogel with PEG20000 and carbon soot

Figure 48 shows the infrared spectra of a hydrolysed Nb_2O_5 xerogel containing 20 wt.-% PEG20000 and carbon soot after different heat treatment. A comparison with figure 47 shows that the addition of carbon soot does not alter the infrared spectra of the xerogel. The carbon particles are dispersed in the xerogel network.

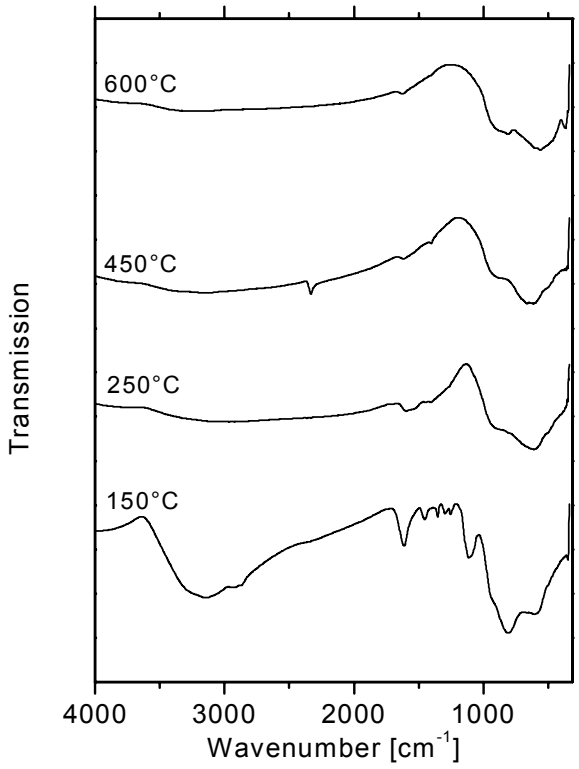

Figure 48: Infrared spectra of hydrolysed Nb_2O_5 xerogel (molar ratio H_2O:Nb = 30.6) with 20% PEG20000 and carbon soot heat treated at different temperature.

5.2.3 X-ray diffraction

The samples were also analysed by powder X-ray diffraction at room temperature for phase identification. Typical spectra are shown in figure 49 for nonhydrolysed and hydrolysed xerogels.

Nonhydrolysed xerogel

For heat treatment below 400°C the samples are amorphous to X-ray. At 400°C the nonhydrolysed Nb_2O_5 xerogel is composed of a mixture of an amorphous and the hexagonal TT phase of Nb_2O_5 [232] and of the orthorhombic phase of Nb_3O_7Cl [233] with fairly weak peaks (figure 49a). As at this temperature the Nb_2O_5 TT phase presents a low crystallinity and is probably stabilised by impurities such as OH^-, Cl^- or vacancies [127], it is reasonable to expect that the Nb atoms may react with binding Cl^- of the network to form Nb_3O_7Cl. With increasing temperature the TT and Nb_3O_7Cl phases transform into the stable orthorhombic T phase [234]. The amount of this crystalline phase increases with the sintering temperature, and that of Nb_3O_7Cl decreases but still persists up to 600°C as observed in a magnified XRD plot (not shown). This is in agreement with the mass spectroscopy results [26].

Hydrolysed xerogel

The XRD pattern of hydrolysed Nb_2O_5 xerogel heated at 400°C shows only an amorphous and the hexagonal TT phase of Nb_2O_5 (figure 49b). The low temperature hexagonal form (TT)

transforms into the stable orthorhombic one (T) on sintering between 400°C to 600°C. The peaks at 2θ = 28.5 and 36.4° start to split into doublets at 600°C showing that the stable orthorhombic phase is formed more easily in a hydrolysed xerogel.

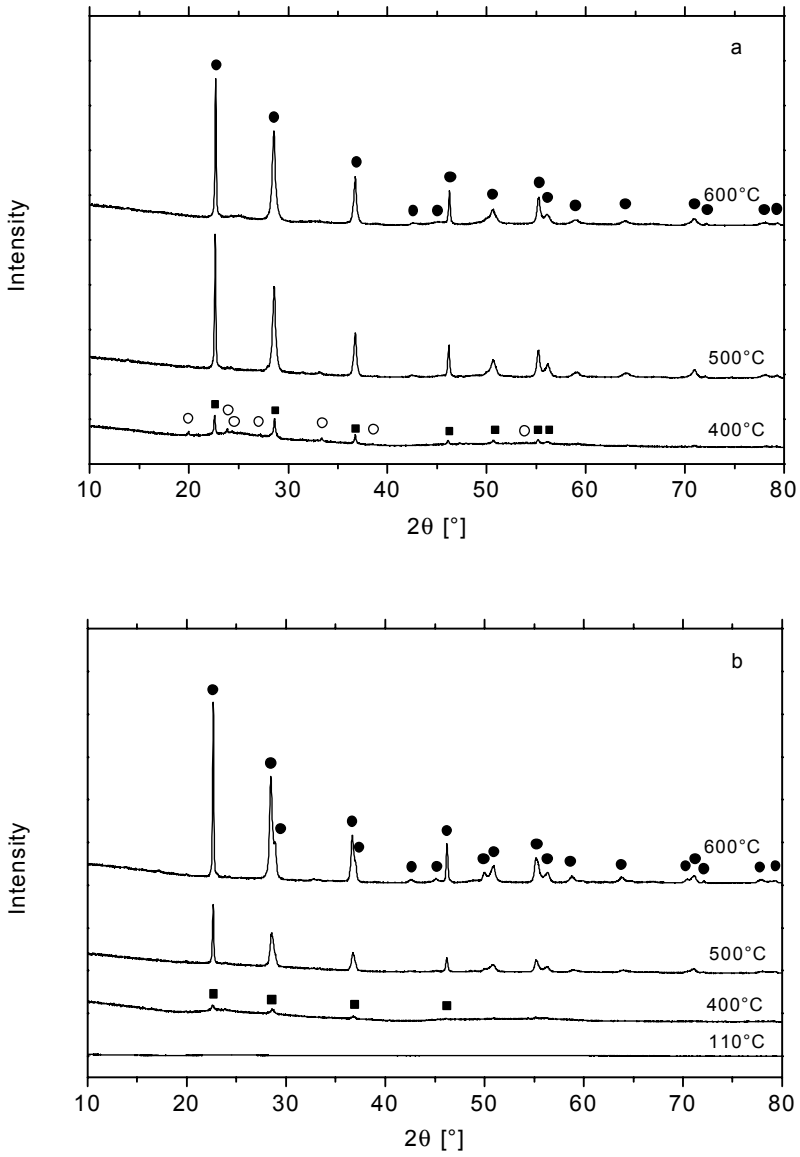

Figure 49: Powder X-ray diffraction patterns of niobium pentoxide xerogel samples sintered at different temperatures. (a) nonhydrolysed Nb_2O_5 xerogel, (b) hydrolysed Nb_2O_5 (H_2O:Nb = 30.6), (■) *TT-phase Nb_2O_5 (No. 28-317),* (●) T-phase *Nb_2O_5 (No. 71-336),* (○) *Nb_3O_7Cl (No. 73-295).*

The results are summarised in table 7.

Table 7: Influence of heat treatment on niobium pentoxide xerogel

Heat treatment [°C]	Nonhydrolysed Nb_2O_5		Hydrolysed Nb_2O_5	
	Phase(s)	Colour	Phase(s)	Colour
110	amorphous	white	amorphous	white
200	amorphous	brown	amorphous	light brown
300	amorphous	black	amorphous	dark brown
400	amorphous, h-Nb_2O_5*, o-Nb_3O_7Cl** (s)	dark grey	amorphous, h-Nb_2O_5	grey
500	h- and o-Nb_2O_5, o-Nb_3O_7Cl (vs)	silver white	h- and o-Nb_2O_5	silver white
600	h- and o-Nb_2O_5, o-Nb_3O_7Cl (vs)	shiny white	h- and o-Nb_2O_5	silver white

*: h- = hexagonal; **: o- = orthorhombic; s = small, vs = very small.

Hydrolysed xerogel with PEG20000 and carbon soot

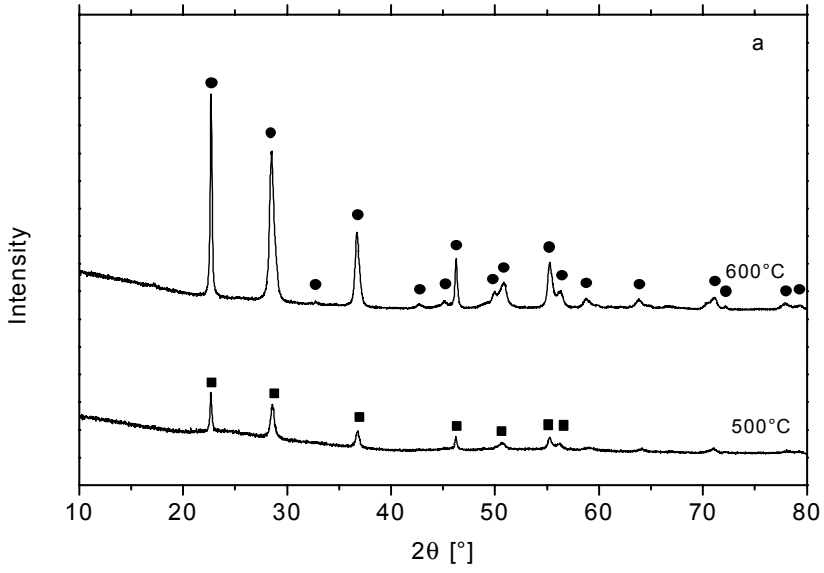

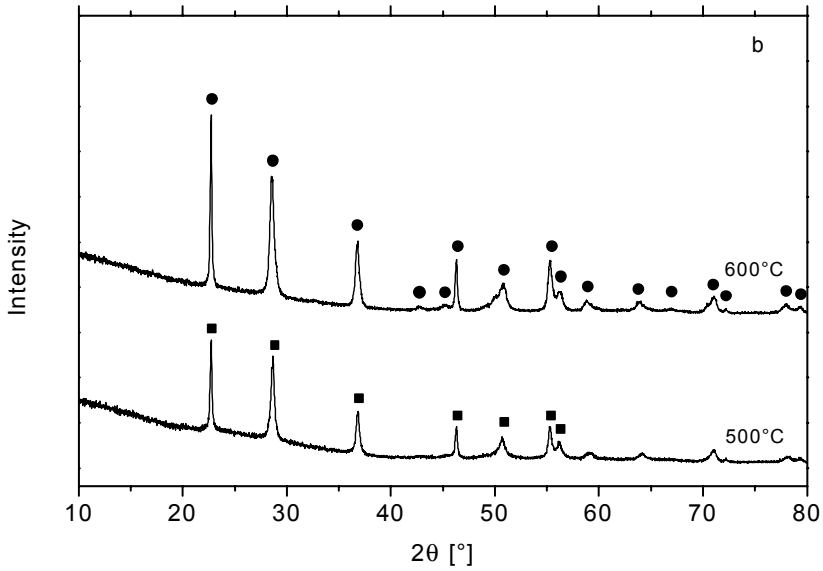

Figure 50: Powder X-ray diffraction patterns of hydrolysed niobium pentoxide xerogel samples (H_2O:Nb = 30.6) sintered at different temperatures. (a) with addition of 20% PEG20000, (b) with addition of 20% PEG20000 and carbon soot, (■) *TT-phase Nb_2O_5 (No. 28-317),* (●) *T-phase Nb_2O_5 (No. 71-873).*

Table 8: Influence of heat treatment on niobium pentoxide xerogel (with additive).

Heat treatment [°C]	Addition of PEG		Addition of PEG and carbon soot	
	Phase(s)	Comments	Phase(s)	Comments
110	amorphous	light yellow	amorphous	dark grey
200	amorphous	yellowish brown	amorphous	dark brown
300	amorphous	black	amorphous	dark violet
400	amorphous, h-Nb_2O_5	dark grey	amorphous, h-Nb_2O_5	dark grey
500	h- and o-Nb_2O_5,	light grey	h- and o-Nb_2O_5	shiny white
600	h- and o-Nb_2O_5,	shiny white	h- and o-Nb_2O_5	shiny white

h: hexagonal (TT); o: orthorhombic (T).

Figure 50 shows the X-ray powder diffraction patterns of hydrolysed Nb_2O_5 xerogel prepared with PEG20000 and carbon soot. Although the overall behaviour remains similar to that for powders prepared with hydrolysed sol, some differences have to be noted. The hexagonal (TT) and orthorhombic (T) phases coexist in the structure up to 600°C and, as before, the amount of the orthorhombic phase increases with the sintering temperature. Moreover the Nb_3O_7Cl phase is never observed (see section 5.3 for a discussion). The results are summarised in table 8.

5.2.4 Nitrogen adsorption and desorption

Xerogels without additive

Figure 51 and 52 show the pore size distributions of nonhydrolysed and hydrolysed Nb_2O_5 xerogels heated treated at 500°C and 600°C, respectively, calculated from the adsorption and the desorption data. Their BET surface area is summarised in Table 9. Porosity and surface area of both systems are quite small. The surface area and pore size distribution of the hydrolysed xerogel decrease with increasing sintering temperature (figure 51b and 52b), while they increase for the nonhydrolysed xerogel (figure 51a and 52a). In the nonhydrolysed gel network the residual carbon from the carbonation of the organic groups is burned above 500°C and leads to an increase of the pore volume and surface area, while for the hydrolysed gel, the organic groups are substituted by OH groups and denser Nb_2O_5 powders are obtained.

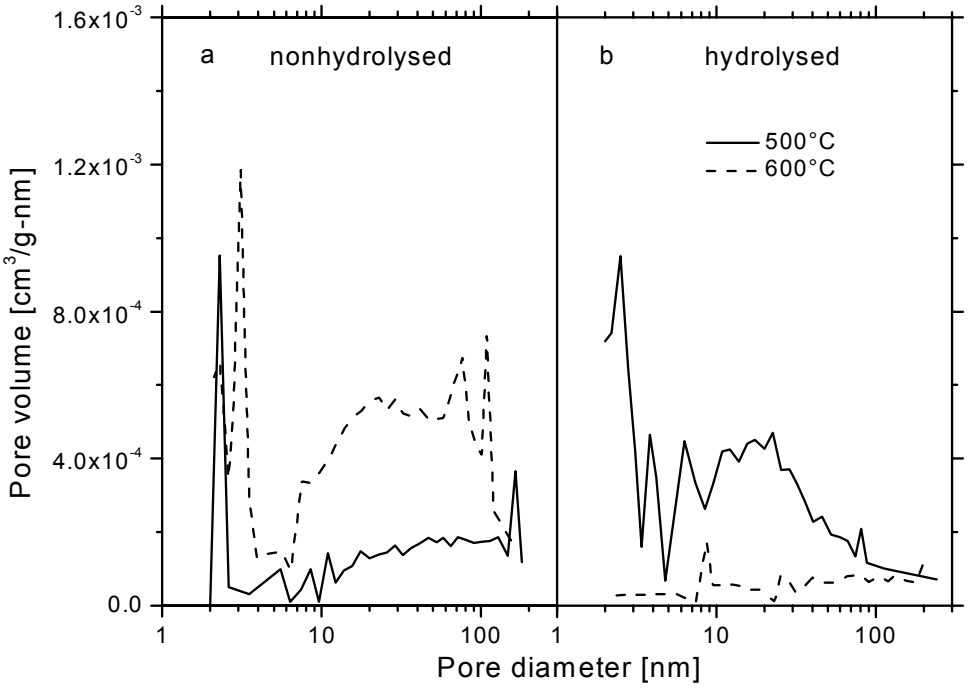

Figure 51: Pore size distributions of Nb_2O_5 xerogels calculated from adsorption data. (a) nonhydrolysed, (b) hydrolysed (H_2O:Nb = 30.6).

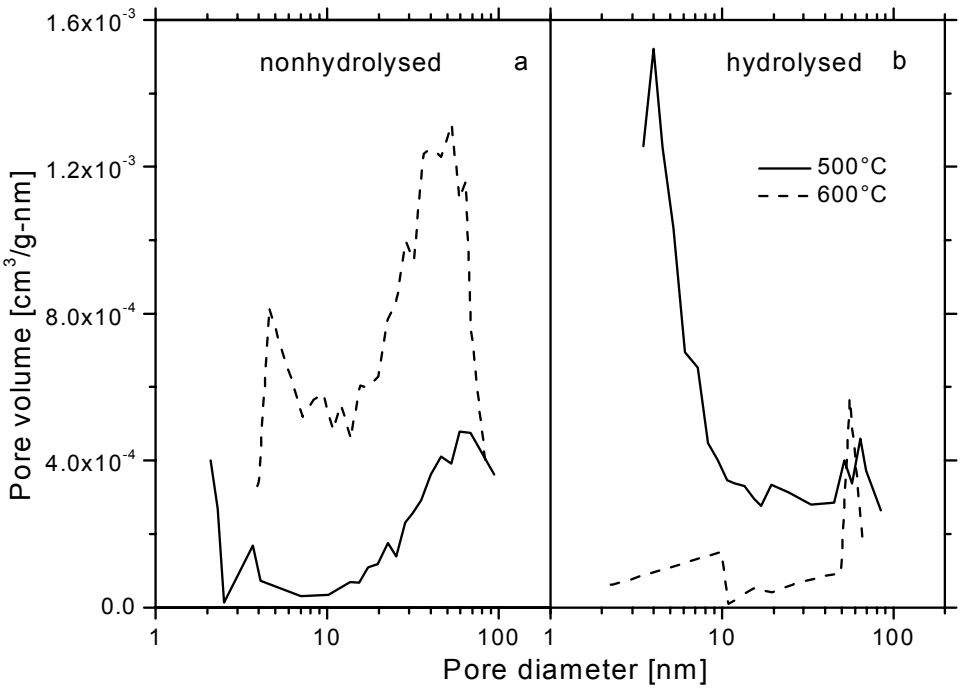

Figure 52:Pore size distributions of Nb_2O_5 xerogels calculated from desorption data. (a) nonhydrolysed, (b) hydrolysed (H_2O:Nb = 30.6).

Table 9: Surface area of xerogels without additive sintered at different temperatures.

Sintering temperature [°C]	nonhydrolysed xerogel [m^2/g]	hydrolysed xerogel [m^2/g]
500	5	7
600	9	4

Xerogels with additive

The pore size distributions are shown in figure 53 and 54 and their microstructural characteristics are given in table 10. An inspection of the figures and table 9 and 10 shows that the incorporation of additives increases drastically the BET surface area and the total pore volume.

The adsorption and desorption data of Nb_2O_5 + PEG and the Nb_2O_5 + PEG + C xerogels sintered at 500°C (see figure 113 in appendix A7) shows that the mesopores have an ink-bottle shape with an average core diameter of 9.6 and 13.1 nm and an average neck diameter of 6.0 and 10 nm, respectively. The pore size distribution shifts towards larger size with increasing sintering temperature and the average core pore diameter remains larger than the average neck diameter (figure 53 and 54). The ink-bottle shape of the pores however evolves toward a more cylindrical shape as the temperature increases.

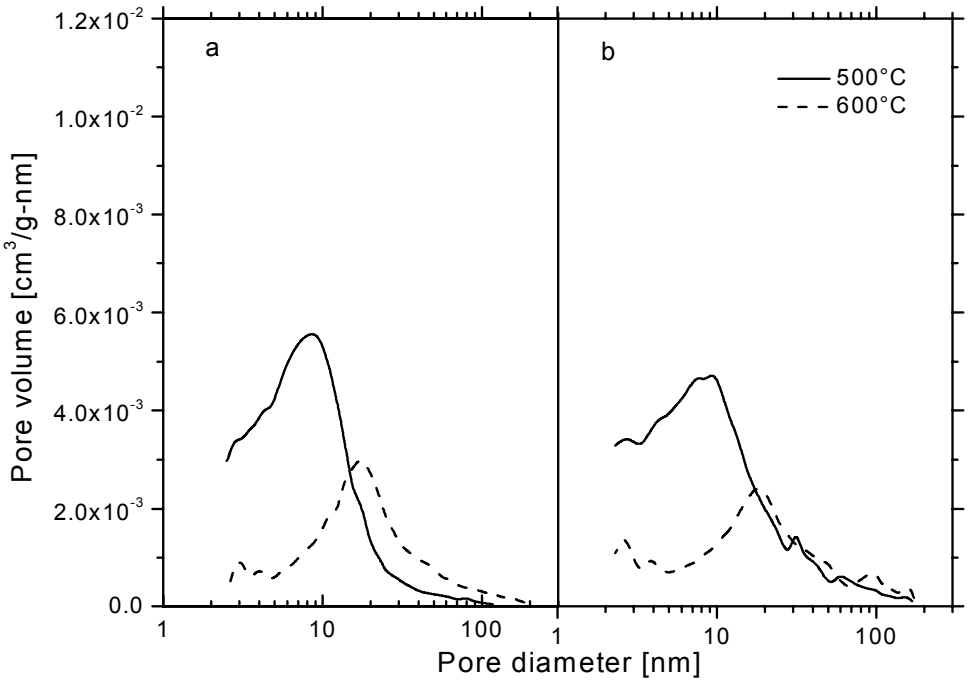

Figure 53: Pore size distributions of hydrolysed Nb_2O_5 xerogels (H_2O:Nb = 30.6) with additives calculated from adsorption data. (a) PEG, (b) PEG and carbon soot.

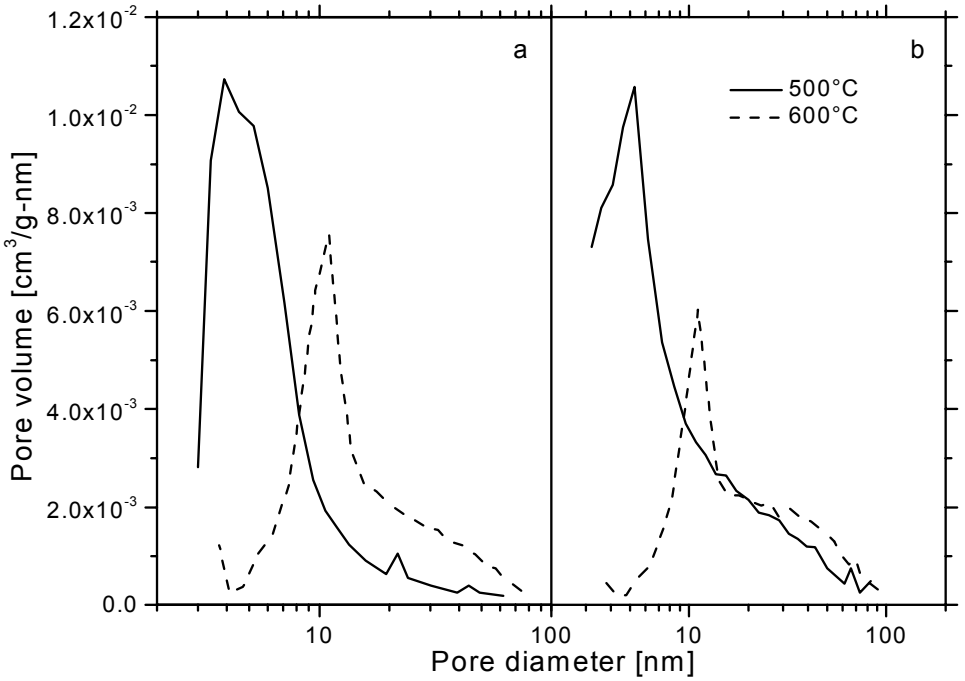

Figure 54: Pore size distributions of hydrolysed Nb_2O_5 xerogels (H_2O:Nb = 30.6) with additives calculated from desorption data. (a) PEG, (b) PEG and carbon soot.

Table 10: Microstructural characteristics of the Nb_2O_5 and TiO_2 powders.

	Nb_2O_5 + PEG		Nb_2O_5 + PEG + C	
	500°C	600°C	500°C	600°C
BET surface area [m^2/g]	39	23	42	22
Average particle size d_{BET} [nm]*	30.8	52.2	28.6	54.5
Total pore volume ≤ 120 nm [$\times 10^{-2}$ cm^3/g]	9.6	10.3	12.7	10.8
Micropore volume [$\times 10^{-2}$ cm^3/g]	0.14	0.1	0.06	0.1
Average pore diameter [nm]	10	18	12.2	19.5
BJH adsorption average pore core diameter (4 V/A) [nm]	9.6	22.1	13.1	25.2
BJH desorption average pore neck diameter (4 V/A) [nm]	6.0	17.2	10	22.5
Porosity [%]	32	34	39	35

*calculated according to equation 34 with a Nb_2O_5 density of 5 g/cm^3 [116]

5.2.5 Morphology

Figure 55 shows transmission electron micrographs of hydrolysed Nb_2O_5 powders sintered at different temperatures. They are all made of aggregates of crystalline particles. The influence of the sintering temperature on the microstructure is obvious. The powder fired at 500°C shows poorly defined small crystalline particles (figure 55a1 and a2), while clearly defined large crystalline particles with a broad size ranging from 10 to 200 nm are obtained at 550° and 600°C (Figure 55b and 55c).

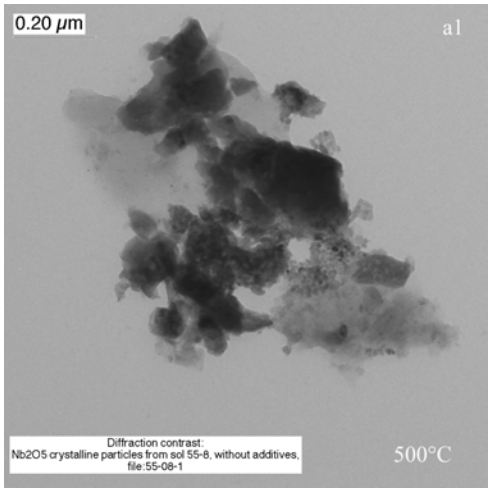

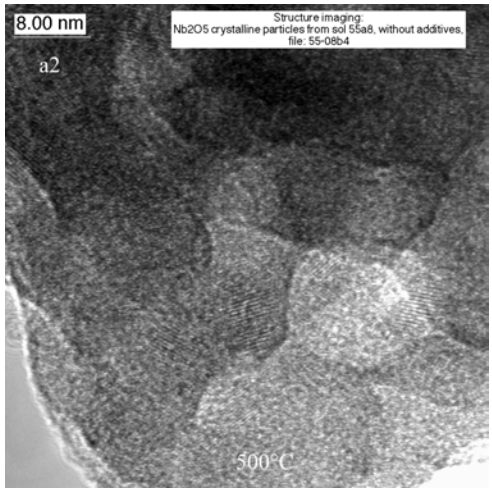

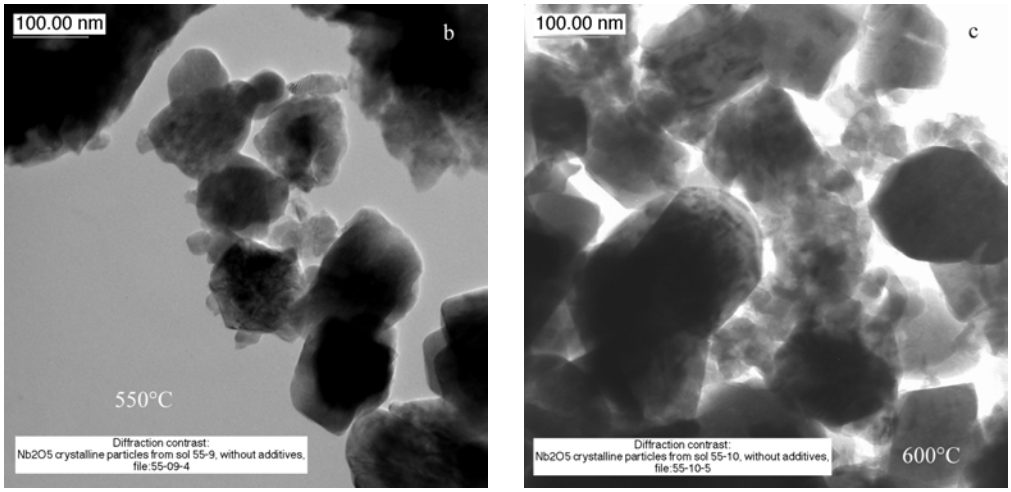

Figure 55: TEM micrographs of hydrolysed Nb_2O_5 xerogels (H_2O:Nb = 30.6) sintered at different temperature. (a1, a2) 500°C, (b) 550°C and (c) 600°C.

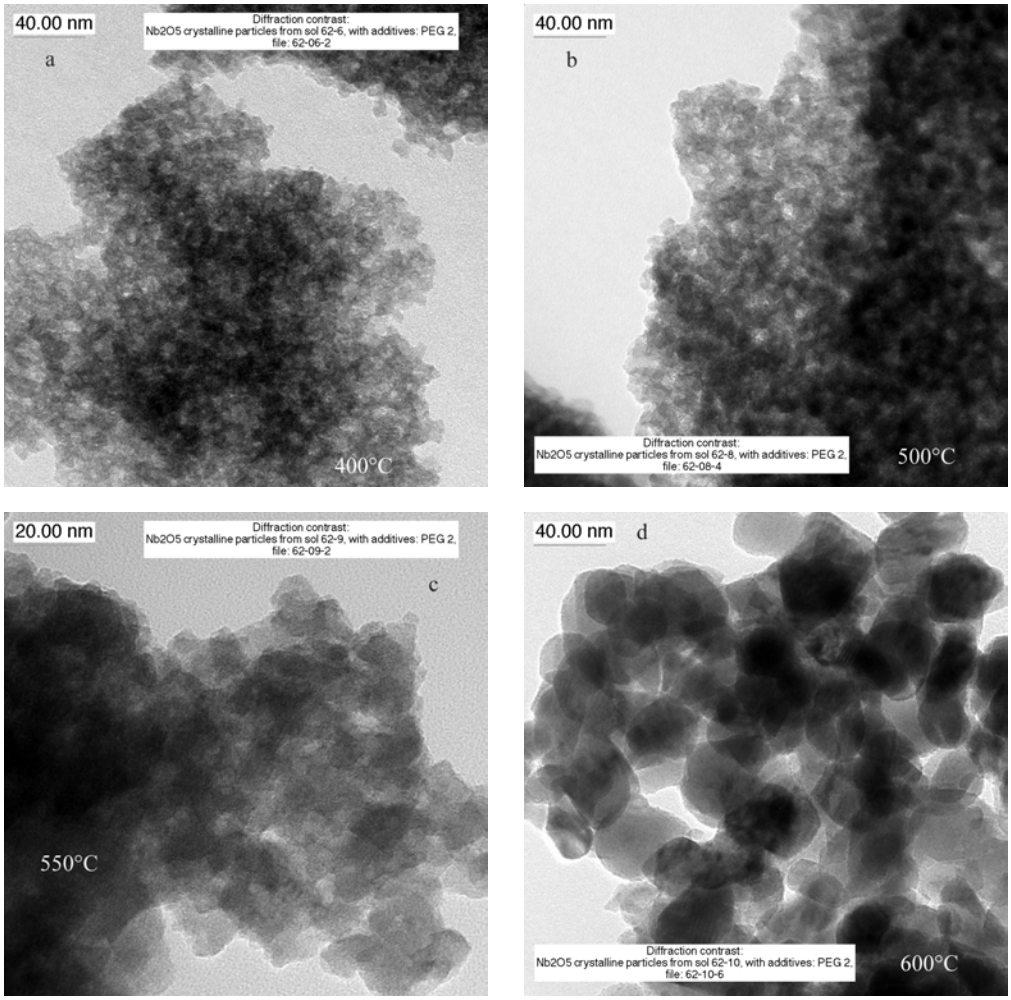

Figure 56: TEM micrographs of hydrolysed Nb_2O_5 + PEG20000 xerogels sintered at different temperature. (a) 400°C, (b) 500°C, (c) 550°C and (d) 600°C.

Figure 56 shows TEM micrographs of hydrolysed Nb_2O_5 + PEG20000 xerogels sintered at different temperature. The results indicate that the addition of PEG hinders the crystalline growth of Nb_2O_5 particles. The powder fired at 400°C shows a porous agglomerate structure consisting mainly of spherical particles with about 5 nm diameter and amorphous particles. After the burn-out of the organic products, the particle size grows to 10 -15 nm (500°C) and to 20 - 50 nm (600°C).

Figure 57 shows TEM micrographs of hydrolysed Nb_2O_5 + PEG20000 + carbon soot xerogel sintered at 600°C. The influence of carbon soot is not obvious. The particle size distribution ranges between 20 and 50 nm.

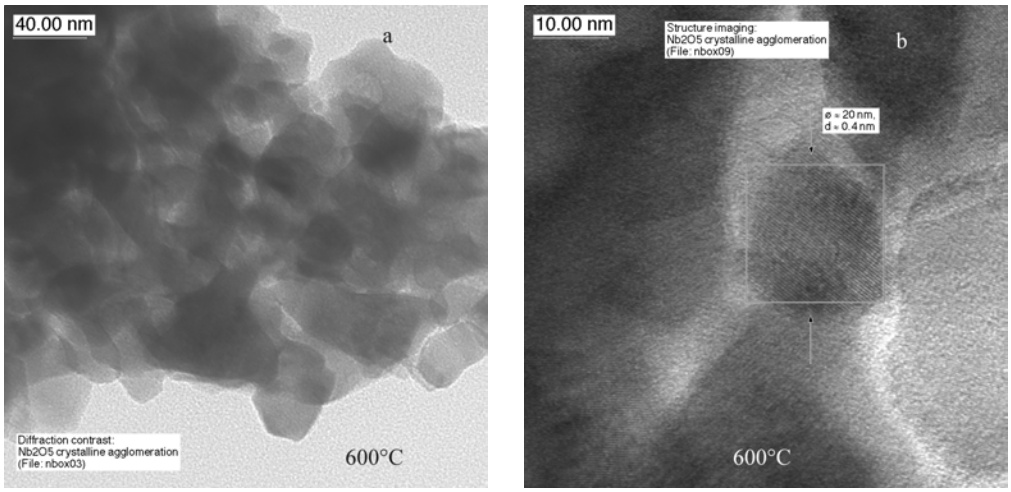

Figure 57: TEM micrographs of hydrolysed Nb_2O_5 + PEG20000 + carbon soot xerogel sintered at 600°C.

Conclusions

The structural evolution of niobia powders sintered up to 600°C strongly depends on the sol composition. The crystalline structure of xerogels prepared without additive evolves from an amorphous state for T < 400°C to the hexagonal-TT form (400-550°C) and finally to a mixture of TT and orthorhombic-T forms at 600°C. However a very low content of the Nb_3O_7Cl crystalline phase was found at all temperature for powders prepared from a nonhydrolysed sol. All these powders present a small porosity and BET surface area and are therefore not promising for our purpose.

The phase evolution of powders prepared from sols with additives follows a similar trend and a mixture of TT and T phases are obtained at high temperature. The Nb_3O_7Cl phase was never observed. The porosity and BET surface area are however much higher and the values obtained slightly decrease with the sintering temperature while those of the average pore size increase. Typical values obtained at 500°C are: BET = 42 m^2/g, total pore volume 12.7×10^{-2} cm^3/g, average pore size 12.2 nm and porosity 39%. The shape of the pores evolve from an ink-bottle shape at T ≈ 500°C to a more cylindric shape as the sintering temperature increases.

TEM micrographs have shown that the size of the particles increases strongly with the sintering temperature for all powders. However the incorporation of the additives strongly hinders the growth of the particles.

5.3 Structural properties of Nb_2O_5 films

5.3.1 X-ray diffraction

Figure 58 shows the temperature evolution of the X-ray diffraction patterns of multilayer coatings made with the most promising sols i.e. (a) a hydrolysed sol (H_2O:Nb = 30.6) (b) the same sol containing 20 wt.-% PEG20000 and (c) the same sol containing 20 wt.-% PEG20000 and carbon soot. In all samples the crystallisation starts at about 400°C, but two broad halos (amorphous material) centered around $2\theta = 25°$ and 55° are present up to 500°C. The temperature evolution of the phases and the crystallite size calculated by the Scherrer´s formula (equation 30) are summarised in table 11.

Films without additive (figure* 58*a)

At 400°C an amorphous, the Nb_2O_5-hexagonal (TT) and the orthorhombic phase of Nb_3O_7Cl [233] are observed. The presence of the Nb_3O_7Cl phase up to 500°C stabilises the phase transformation of the TT phase into the orthorhombic T phase. However the Nb_3O_7Cl phase is thermally decomposed between 550°C and 600°C and at 600°C only the orthorhombic T phase of Nb_2O_5 is observed. The average crystallite size increases with the sintering temperature (table 11). As mentioned in the section 5.2.3, the Nb_3O_7Cl phase is not observed in the hydrolysed xerogel prepared with the same sol. This is due to the different procedures adapted in the preparation of the powders and coatings. The powders were obtained by heating the sols during 3 days at 110°C in air. The reaction of the Cl^- ions bound to the chloroethoxo-acetate colloids with the humidity of air during this laps of time this was probably sufficient to remove all of them so that no Nb_3O_7Cl could be observed. This is not the case for coatings which have been quickly heated to high temperature after processing.

Films with additives (figure 58b and 58c)

The evolution of both systems is similar and the use of PEG with different molecular weight does not affect the results (see figure 112 in appendix A6). At 400°C, similar to powders, amorphous and hexagonal (TT) phase are dominant. The amount of the orthorhombic (T) phase continually increases with the sintering temperature and becomes preponderant at 600°C. As observed for the powders (see section 5.2.5), the presence of PEG stabilises the crystallite size as little variation is observed with the temperature. However the most striking difference is the absence of the Nb_3O_7Cl phase. This result is discussed below and it emphasises the complex role of PEG in the preparation of niobia colloidal sols.

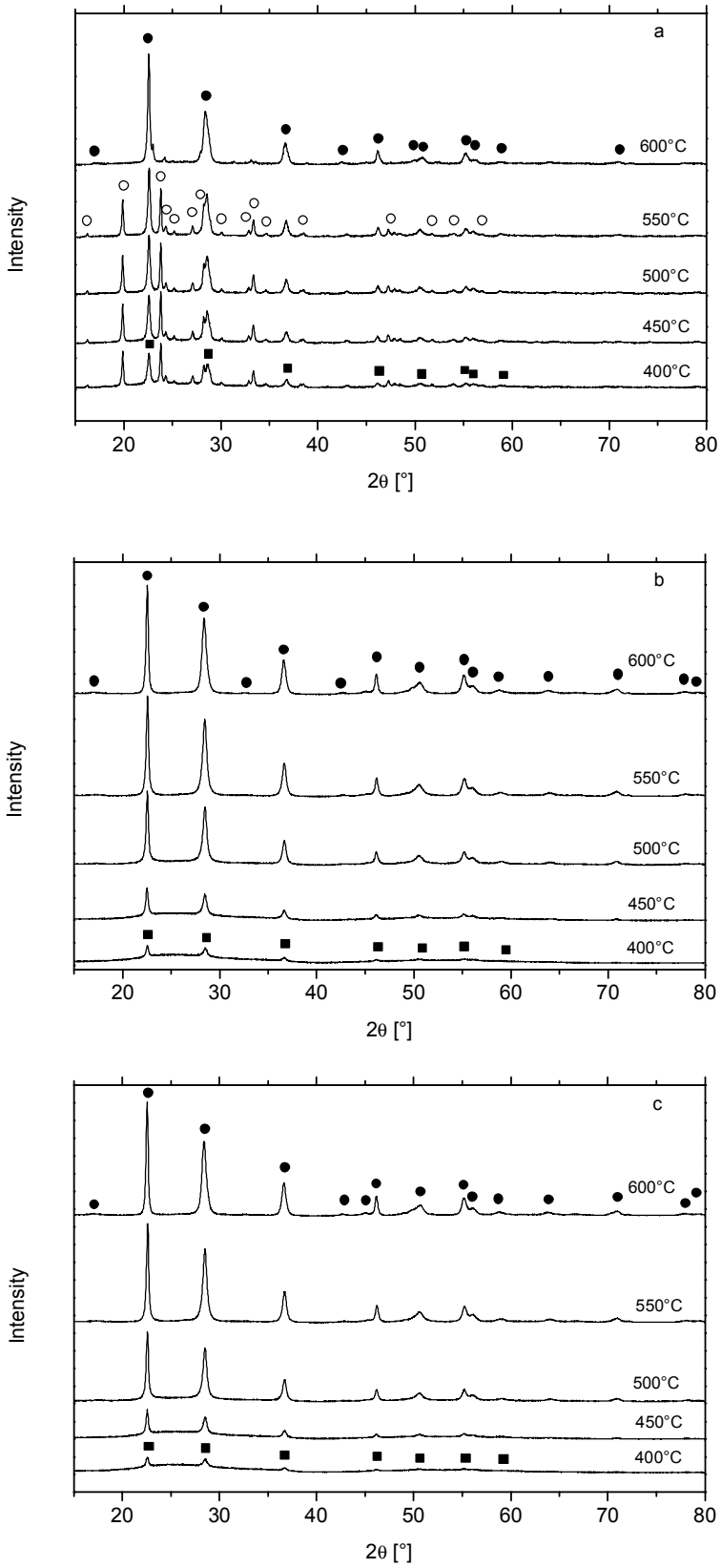

Figure 58: X-ray diffraction patterns of niobium pentoxide coating samples sintered at different temperatures from (a) hydrolysed sol (H_2O:Nb = 30.6), (b) hydrolysed sol with addition of 20% PEG20000, (c) hydrolysed sol with addition of 20% PEG20000 and carbon soot. (■) *TT- phase Nb_2O_5 (No. 28-317),* (●) *T-phase Nb_2O_5 (No. 71-873),* (○) *Nb_3O_7Cl (No. 73-295).*

Table 11: Phase and crystallite size at different sintering temperature (2θ = 23.8°).

T_s [°C]	Nb_2O_5		Nb_2O_5 + PEG		Nb_2O_5 + PEG + C	
	phase(s)	crystallite size [nm]	phase(s)	crystallite size [nm]	phase(s)	crystallite size [nm]
400	h-Nb_2O_5*, o-Nb_3O_7Cl**	24.3 -	amorphous, h-Nb_2O_5	30.2	amorphous, h-Nb_2O_5	31.6
450	h-Nb_2O_5, o-Nb_3O_7Cl	28.2 -	amorphous, h-Nb_2O_5	31.7	amorphous, h-Nb_2O_5	36.6
500	h-Nb_2O_5, o-Nb_3O_7Cl	30.9 -	h- and o-Nb_2O_5	33.3	h- and o-Nb_2O_5	34.5
550	h-Nb_2O_5, o-Nb_3O_7Cl	33.6 -	o-Nb_2O_5	32.5	o-Nb_2O_5	33.2
600	o-Nb_2O_5, o-Nb_3O_7Cl (vs)	34.3 -	o-Nb_2O_5	33.0	o-Nb_2O_5	33.2

*: h = hexagonal; **: o = orthorhombic.

5.3.2 Nitrogen adsorption and desorption

5.3.2.1 Influence of additives

Figure 59 shows the pore size distribution of Nb_2O_5 coatings prepared without and with different additives into the sols. A summary of the microstructure properties is given in table 12. As shown in the next section all the coatings exhibit pores with an ink-bottle shape and narrow necks. The BET surface area increases but the average particle size decreases markedly by adding 20 wt.-% PEG600, PEG20000 and PEG20000 + C to the sols. Assuming spherical crystallites, about 4 of them on average are aggregated in each Nb_2O_5 particle prepared without additive but those obtained by using additives are made of a single crystallite. The BJH adsorption and desorption average pore size are only slightly altered, although the total pore volume and porosity increase by adding the binder.

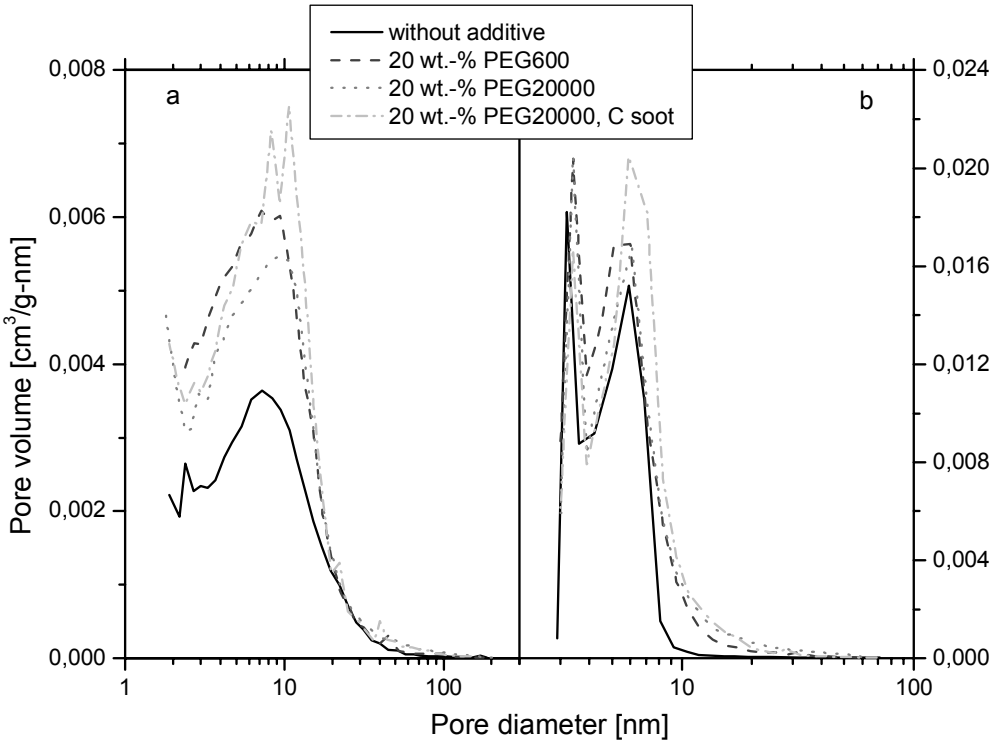

Figure 59: Pore size distributions of Nb_2O_5 coatings prepared without and with adding different additives into the sols calculated from (a) adsorption and (b) desorption data. Sintered at 500°C, 30 min.

Table 12: Influence of the additives on the microstructural characteristics of the Nb_2O_5 coatings sintered at 500°C 30 min.

	Nb_2O_5	Nb_2O_5 + 20% PEG600	Nb_2O_5 + 20% PEG20000	Nb_2O_5 + 20% PEG20000 + C
BET surface area [m^2/g]	24.4	42.6	38.4	44.1
Average particle size [nm]	49.2	28.2	31.3	27.2
Average pore diameter [nm]	9.3	8.9	9.8	9.5
Total pore volume [$\times 10^{-2}$ cm^3/g]	6.0	9.5	9.5	10.5
Micropore volume [$\times 10^{-2}$ cm^3/g]	0.07	0	0	0
BJH adsorption average pore core diameter (4 V/A) [nm]	9.4	8.2	9.2	9
BJH desorption average pore neck diameter (4 V/A) [nm]	5.2	5.5	6.3	6.3
Porosity [%]	23	32	32	34

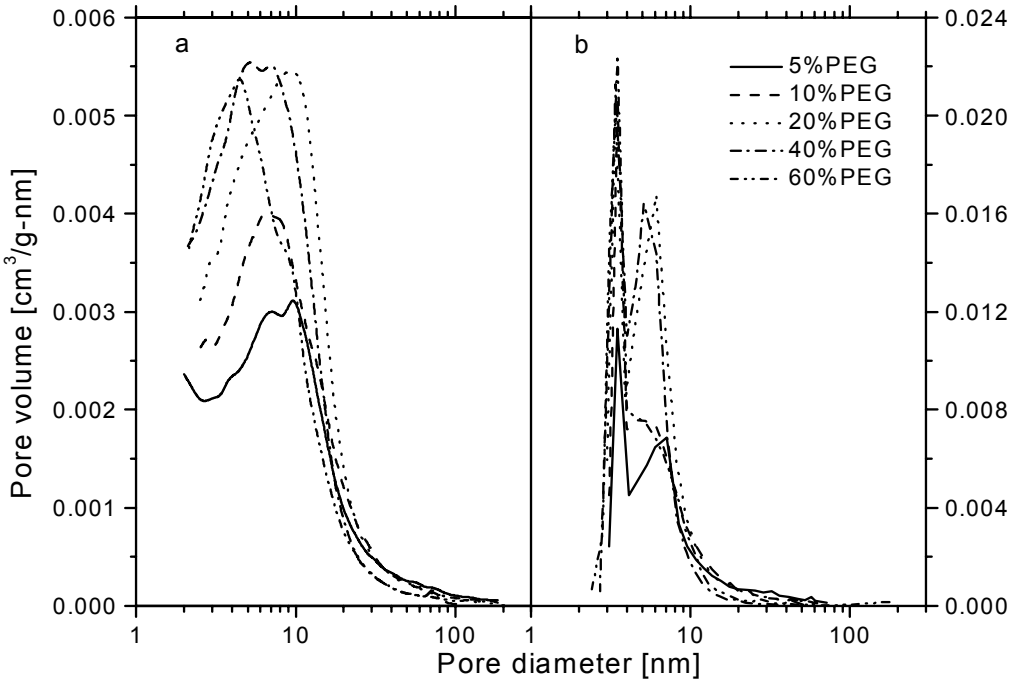

Figure 60:Influence of the amount of PEG20000 on the pore size distribution calculated from (a) adsorption and (b) desorption data. Sintered at 500°C, 30 min.

Table 13: Influence of the amount of PEG20000 on the microstructural characteristics of the Nb_2O_5 coatings sintered at 500°C 30 min.

PEG20000 [wt.-%]	5	10	20	40	60
BET surface area [m^2/g]	24.2	29.5	38.4	37.9	32
Average particle size [nm]	49.6	40.7	31.3	31.7	37.5
Average pore diameter [nm]	10.7	9.8	9.8	8.3	8.0
Total pore volume [$\times 10^{-2}$ cm^3/g]	6.5	7.3	9.5	7.9	6.4
Micropore volume [$\times 10^{-2}$ cm^3/g]	0.05	0.02	0	0	0
BJH adsorption average pore core diameter (4 V/A) [nm]	11	9.8	9.2	7.4	7.4
BJH desorption average pore neck diameter (4 V/A) [nm]	8.3	6.9	6.3	5.3	6.0
Porosity [%]	25	27	32	28	24

To study in more details the influence of the binder addition on the coating microstructure different amounts of PEG20000 were added to Nb_2O_5 sols. The pore size distributions of

coatings sintered at 500°C are presented in figure 60 and the microstructure properties are given in table 13. The average pore diameter and the shape of their distribution are nearly identical for all samples, although the total pore volume, the porosity and the BET surface area are altered by increasing the amount of PEG20000 (figure 60a and 60b), passing by a maximum for about 20 wt.-%.

5.3.2.2 Influence of the sintering temperature

Films without additive

Figure 61 shows typical N_2-adsorption and desorption isotherms of Nb_2O_5 coatings prepared with hydrolysed sols without additive sintered 30 min at 400°C and 650° C, respectively. Coatings sintered at 400°C show an adsorption isotherm of type IV with a hysteresis of type H2, typical of ink-bottle shaped mesopores. At 650°C the adsorption isotherm is also of type IV but the hysteresis tends to the type H1, typical of cylindrical pores.

The pore size distribution calculated from the desorption data (which gives information on the average neck diameter of the pores) is shown in figure 62b and the microstructural characteristics are given in table 14. At 400°C the BJH average neck diameter is very small (3.5nm) with a narrow distribution and the total volume of pores is about 0.04 cm^3/g. With increasing sintering temperature the average neck diameter shifts steadily to higher value, the pore size distribution also increases and the total pore volume slightly increases to a maximum value of 0.072 cm^3/g, at 650°C.

Figure 62a and table 14 show the results obtained from the adsorption isotherms (which gives information on the core diameter of the pores). At all sintering temperatures the pore size distribution is wider than those obtained from the desorption values. The average pore diameter also shifts enormously towards larger values as the sintering temperature is increased.

The BET surface area of the coatings is small and remains practically constant (25 m^2/g) up to 550°C and then slightly decreases while the porosity increases up to 500°C and then remains constant (about 26%).

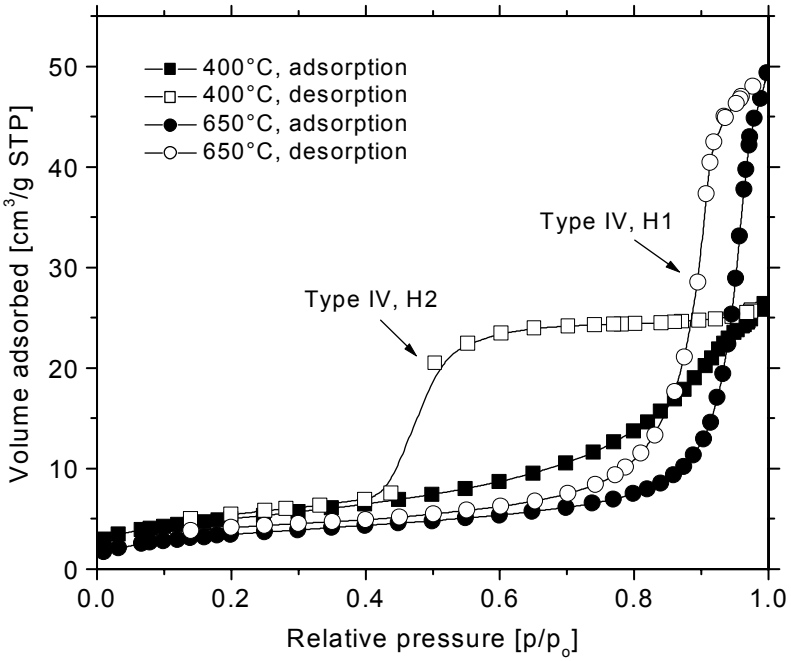

Figure 61: N_2-adsorption and desorption isotherms of Nb_2O_5 coating sintered at 400 and 650°C. Solid symbols: adsorption; open symbols: desorption.

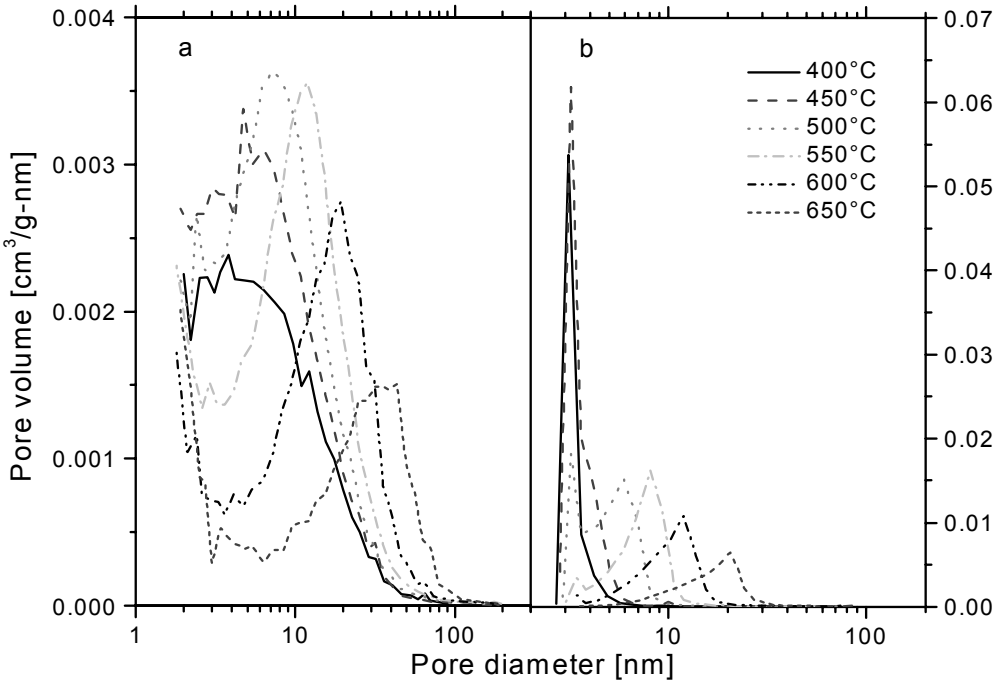

Figure 62: Pore volume distribution of Nb_2O_5 coatings without additive sintered at different temperatures, calculated from adsorption data (a) and desorption data (b).

Table 14: Influence of the sintering temperature on the microstructural characteristics of Nb_2O_5 coatings without additive.

Sintering temperature [°C]	400	450	500	550	600	650
BET surface area [m^2/g]	19.1	24.7	26.2	23.8	17.2	12.9
Average particle size [nm]	62.8	48.6	45.8	50.4	69.7	93.0
Average pore diameter [nm]	8.4	8.5	9.3	12.1	16.9	22.4
Total pore volume [$\times 10^{-2}$ cm^3/g]	4.0	5.3	6.1	7.2	7.3	7.2
Micropore volume [$\times 10^{-2}$ cm^3/g]	0.03	0	0.07	0	0	0
BJH adsorption average pore core diameter (4 V/A) [nm]	8.5	8.0	9.4	11.2	16.6	23.7
BJH desorption average pore neck diameter (4 V/A) [nm]	3.5	3.8	5.2	7.7	10.5	16.8
Porosity [%]	17	21	23	26	27	26

Films with additives

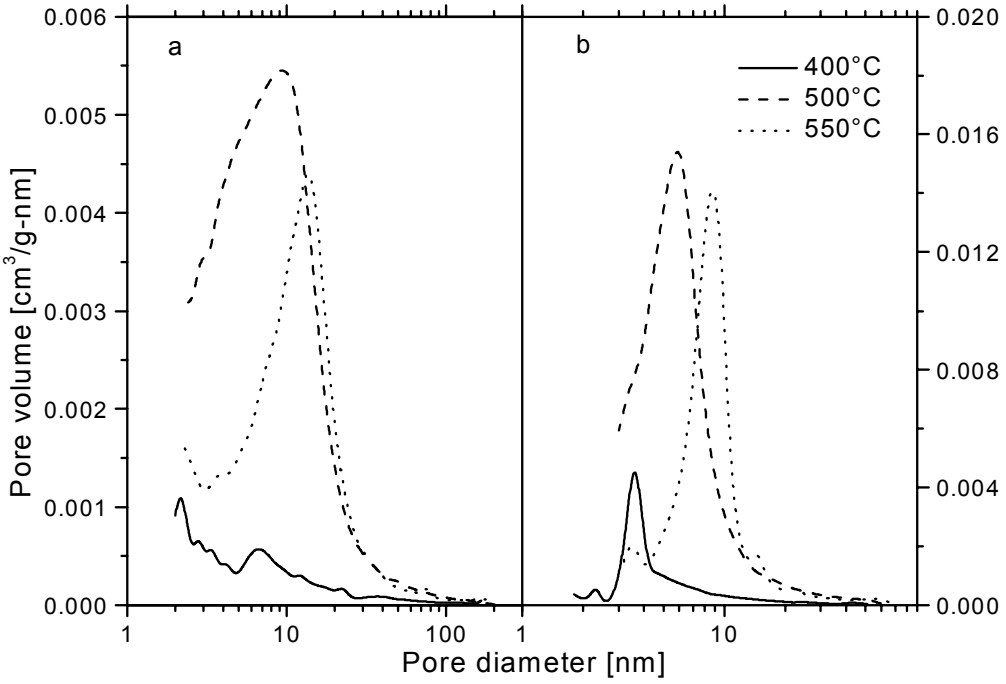

Figure 63: Pore volume distribution of Nb_2O_5 coatings prepared with PEG20000 additive sintered at different temperatures, calculated from adsorption data (a) and desorption data (b).

Table 15: Influence of the sintering temperature on microstructural characteristics of Nb_2O_5 coatings prepared with 20 wt.-% PEG20000 binder.

Sintering temperature [°C]	400	500	550
BET surface area [m^2/g]	4.7	38.4	23.0
Average particle size [nm]	255	31.3	52.2
Average pore diameter [nm]	9.4	9.8	13.2
Total pore volume [$\times 10^{-2}$ cm^3/g]	1.1	9.5	7.6
Micropore volume [$\times 10^{-2}$ cm^3/g]	0	0	0
BJH adsorption average pore core diameter (4 V/A) [nm]	9.8	9.2	11.8
BJH desorption average pore neck diameter (4 V/A) [nm]	6.1	6.3	9.2
Porosity [%]	5	32	28

The coatings prepared by adding 20 wt.-% PEG20000 to the Nb_2O_5 sol were fired at 400, 500 and 550°C in air during 30 min to study the influence of the sintering temperature on the final coating microstructure. The results are shown in figure 63 and table 15. The coating sintered at 400°C possesses a small and narrow pore size distribution due to a large number of residual carbon in the coating. At 500°C the carbon is burned out and this leads to an enormous increase of the pore volume and BET surface area. The decrease in surface area measured at 550°C reveals that the sintering is occurring. The pore size distribution shifts towards larger pores and the number of small pore decreases substantially.

5.3.3 Adsorption and desorption of Ru(II)-complex dye sensitised coatings

Table 16 shows the effect of the different sol preparation on the microstructure of Nb_2O_5 coatings sintered at 520°C for 30 min and of a commercial TiO_2 coating (for comparison) which all have been sensitised with a Ru(II)-complex. For niobia coatings made without and with PEG20000 + C additives, the amount of dye adsorbed Γ_{area} increases from 3.3×10^{-8} to 8.8×10^{-8} mol/cm^2(10µm) and the roughness factor increases from 200 to 530, respectively. The values for the TiO_2 coating are in the same range: 5.9×10^{-8} mol/cm^2(10 µm) and 360 respectively.

Neglecting the reflection and the scattering effects, the light harvesting efficiency LHE (section 2.1.3.3) of 10 µm Nb_2O_5 coatings prepared with Nb_2O_5 and Nb_2O_5 + PEG + C sols is 0.66 and 0.94, respectively while that of the TiO_2 coating is 0.86. Using equation 38 and the BET results of table 15, only 40% of the surface area of the particles has been utilised for the adsorption of the Ru(II)-complex dye. This implies that the ink-bottle shape of the pores (too small neck diameter) hinders the adsorption. Another reason is the possible existence of a concentration gradient of the dye adsorbed between the surface of Nb_2O_5 coating and the glass substrate. The density and porosity are nearly independent of the sol preparation.

Table 16: Comparison of density, porosity, amount of adsorbed dye, surface area and roughness factor of coatings prepared with Nb_2O_5 and Nb_2O_5 + PEG20000 + C sols sintered at 520°C for 30 min and for a commercial TiO_2 coating.

	Nb_2O_5	Nb_2O_5 + PEG + C	TiO_2
Amount of dye Γ_g $\times 10^{-5}$ [mol/g]	1.34	2.74	-
Surface area S_{dye} [m^2/g]	8.1	16.5	-
Amount of dye Γ_{area} $\times 10^{-8}$ [mol/cm^2(10µm)]	3.3	8.8	5.9
BET% of dye coverage	32	40	-
LHE	0.66	0.94	0.86
Density ρ_p [g/cm^3]	2.74	2.70	-
Porosity [%]	45.2	46	-
Roughness factor (10µm thickness)	200	530	360

Table 17 shows the effect of the sintering temperature for Nb_2O_5 + PEG + C coatings. The amount of dye adsorbed on the particle´s surface and the surface area is practically constant up to 550°C and then decreases. The percentage of the BET surface area used by the dye (equation 38) is 34, 40, 45 and 48% for coatings sintered at 500°C, 520°C, 550°C and 600°C, respectively. The increase is due to the improvement of the ink-bottle shape, especially that of the average neck diameter which allows the dye molecules to better diffuse into the structure. The sintering of the particles at higher temperatures leads to a pore coarsening, in which the small pores merge and expand causing a decrease of the density and an increase of the porosity.

Table 17: Influence of the sintering temperature on density, porosity, amount of adsorbed dye, surface area and roughness factor of Nb_2O_5 + PEG + C coatings.

Sintering Temperature [°C]	500	520	550	600
Amount of absorbed dye Γ_g $\times 10^{-5}$ [mol/g]	2.50	2.74	2.56	1.85
Surface area S_{dye} [m^2/g]	15.1	16.5	15.4	11.1
Amount of dye Γ_{area} $\times 10^{-8}$ [mol/cm^2(10µm)]	7.5	8.8	7.3	4.7
BET% of dye coverage	34	40	45	48
LHE	0.91	0.94	0.91	0.78
Density ρ_p [g/cm^3]	2.87	2.70	2.47	2.34
Porosity [%]	42.6	46	50.6	53.2
Roughness factor (10µm thickness)	450	530	440	280

5.3.4 Morphology of the coatings

Figure 64 shows SEM cross-sections of a 6 µm thick coating sintered at 500°C for 30 min with two different magnifications. Figure 64a shows the three-layer structure of the electrode: glass substrate, FTO-layer and the 6 µm thick Nb_2O_5 coating. Figure 64b shows the porous morphology of the coating made of fine nanocrystalline Nb_2O_5 particles. The contact between the nanocrystalline coating and the conducting FTO layer appears good.

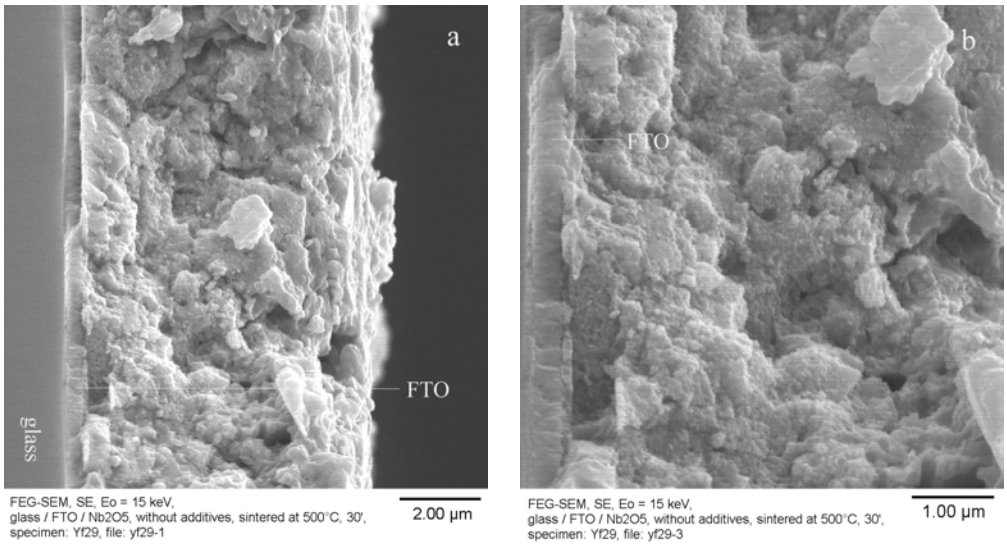

Figure 64: SEM cross-section images of nanocrystalline Nb_2O_5 coating deposited on conducting FTO glass substrate sintered at 500°C for 30 min.

Figure 65 shows 2D (left) and 3D (right) surface topography of porous Nb_2O_5 films prepared with different sols sintered at 520°C for 30 min and measured by scanning white light interferometry. The coating prepared with Nb_2O_5 sol is smoother and has a roughness R_q = 0.31 µm and those prepared with Nb_2O_5 + PEG and Nb_2O_5 + PEG + C are rougher with a roughness R_q = 3.9 and 2.3 µm, respectively.

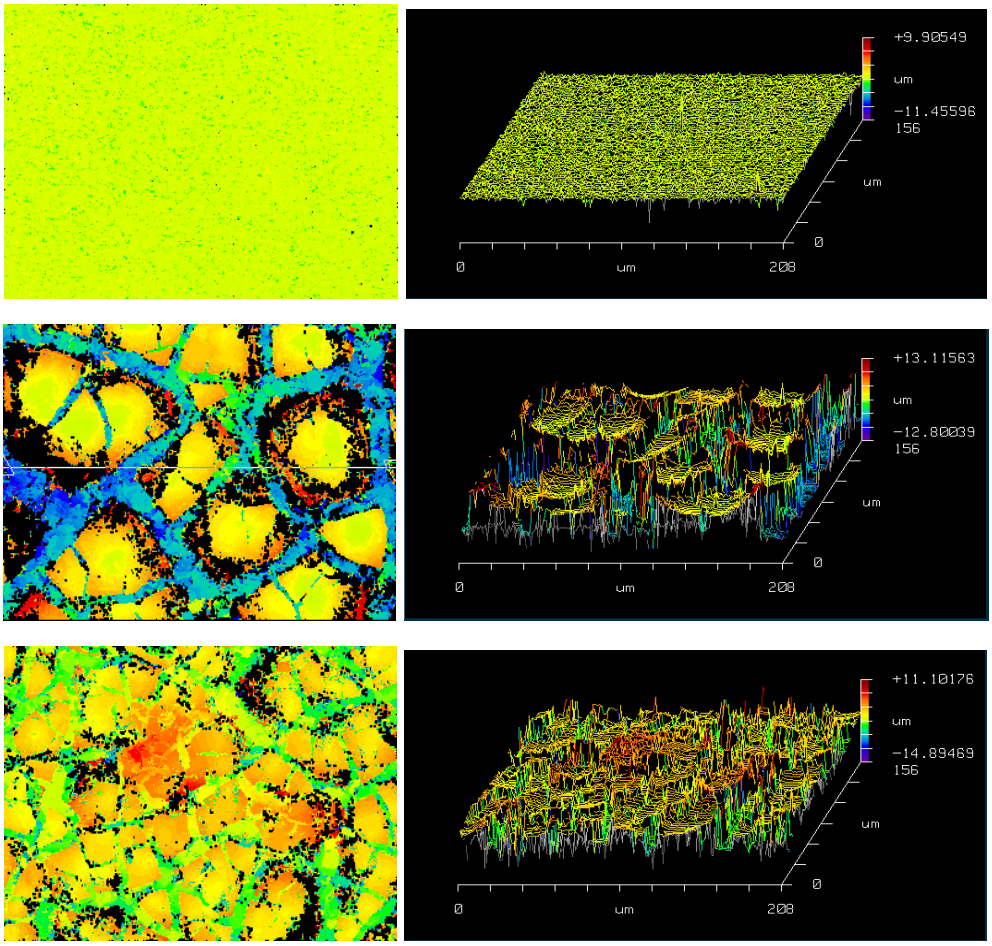

Figure 65: Scanning white light interferometry topography of the Nb_2O_5 films prepared with different sols sintered at 520°C for 30min. Left: two dimension, right: three dimension. Top: Nb_2O_5, middle: Nb_2O_5+PEG, bottom: Nb_2O_5+PEG+C.

Conclusions and discussion

The evolution of the structural properties of multilayer thick coatings have been studied as a function of the sintering temperature for three different systems.

The X-ray data of coatings made without additive are quite different from those of the corresponding powders as a strong Nb_3O_7Cl phase is present together with the TT niobia phase up to 550°C and then is transformed into the stable orthorhombic T phase at 600°C. No particular information have been gained in the study of the nitrogen adsorption and desorption curves as the data are practically similar to that the powders.

The data for coatings made with additives followed that obtained for powders. The results confirm that the incorporation of PEG hinders the growth of the crystallites. The analysis of

the nitrogen adsorption and desorption data also confirm that the incorporation of PEG and carbon soot contributes substantially to improve the porous morphology with however slightly smaller values for the average pore diameter, core and neck diameter and pore volume. At 500°C, optimum results seem to be achieved for a 20 wt.-% PEG20000 incorporation. The Nb_3O_7Cl phase does not exist in those coatings because the complexing effect of PEG with niobium atoms releases Cl^- ions during the preparation of the colloidal sols.

The influence of the sintering temperature on the microstructural characteristic for films made without additive shows that the BET surface area is maximum at 520°C, and that all other parameters (e.g. total pore volume, average pore size diameter, core and neck diameter) become larger at higher temperature. The data for coatings made with additive appear more promising for a sintering at 520°C, except for the core and neck diameter which are slightly larger at higher temperature.

The analysis of the nitrogen adsorption and desorption data for all niobia systems sintered at 520°C and then dye sensitised shows that the addition of PEG and carbon soot also improves the dye coverage, although only 40% of the BET surface area is used. The value increases continuously up to 48% for a sintering at 600°C.

As the performance of a dye sensitised solar cells still depends on many other parameters (electrolyte, etc.), it is difficult at this stage to propose an optimum niobia coating. Nevertheless, from the above results, the characteristics of coatings made from hydrolysed sols with incorporation of PEG and carbon soot sintered at around 600°C appear the most promising because of the higher core and neck diameter of the pores which will facilitate the dye regeneration and the better interconnection between the particles which will decrease the electric resistance of the coating.

The influence of other parameters is described in the following section.

5.4 Non- and dye-sensitised Nb_2O_5 electrodes

5.4.1 Photoelectrochemical properties of non-sensitised Nb_2O_5 electrodes

IPCE

Band gap excitation of TCO/semiconducting films in aqueous electrolytes leads to the oxidation of water by photogenerated valence band holes [235, 236]. This process can be quantified by measuring the photocurrent action spectrum i.e. the incident photon to electron conversion efficiency (IPCE) of such electrodes. Figure 66 shows a comparison of the IPCE spectrum of Nb_2O_5 layers of same thickness (ca. 13 µm) prepared with and without additives and sintered at 600°C and of a commercial TiO_2 electrode 6.25 µm thick. The layers were immersed in aqueous 0.1 N KCl and 0.1 N HCl solution (pH = 1). The data were obtained in a short circuit condition with illumination on the substrate side. They have been corrected for the

absorption of the glass and the FTO conducting electrode. For both materials the IPCE increases for wavelengths shorter than 400 nm but the Nb_2O_5 spectra are slightly shifted to lower wavelengths. Therefore, under UV light irradiation, both materials can be used as photocatalyst for photoelectrolysis of water, photodegradation of residual organic pollution and photosynthesis of organic compounds.

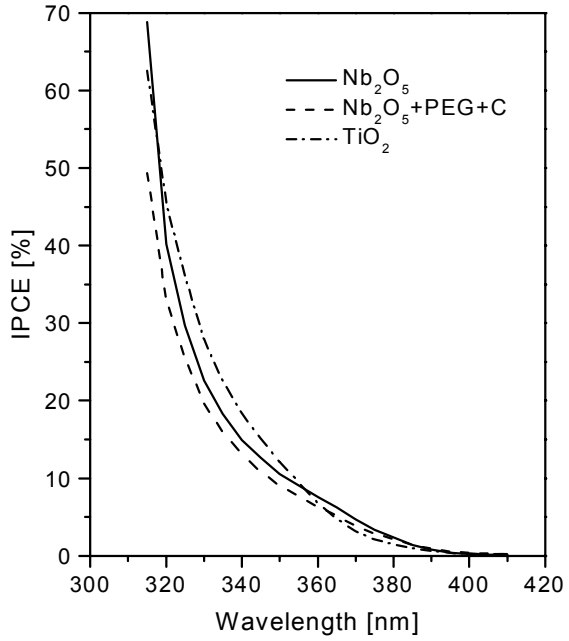

Figure 66: Photocurrent action spectrum of Nb_2O_5 electrodes (ca. 13 µm thick) prepared with and without additivse, sintered at 600°C for 30 min and a commercial TiO_2 (anatase) electrode (6.25 µm thick) measured in aqueous 0.1 N KCl and 0.1 N HCl solution.

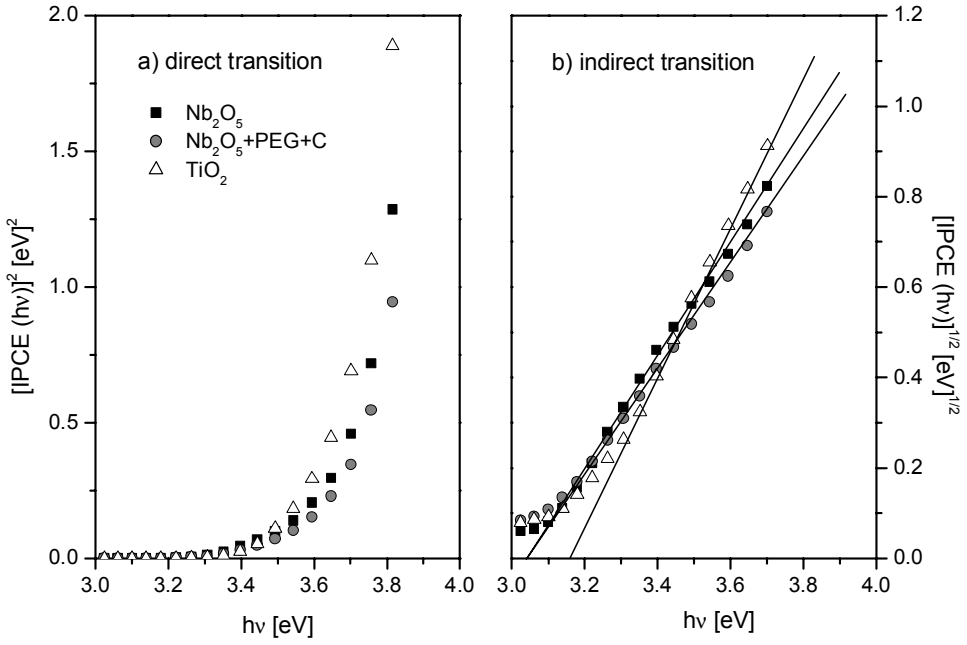

Figure 67: Plots of $[IPCE\ (h\nu)]^2$ (a) and $[IPCE\ (h\nu)]^{1/2}$ (b) vs. $h\nu$ calculated from the data of figure 66.

Neglecting the recombination of electrons and holes in the space charge layer (width W), and assuming that the penetration depth of the light (1/α, α being the optical absorption coefficient) is much higher than W and the hole diffusion length (L), the quantum efficiency (IPCE) can be correlated to the photon energy by the equation [237]

$$IPCE\ (h\upsilon) = A(L+W)(h\upsilon - E_g)^m \qquad (64)$$

where hν is the photon energy (eV), A is a constant, E_g is the band gap energy and m are ½ for a direct electronic transition and 2 for an indirect one.

The plots of $[(IPCE\ (h\nu)]^{1/m}$ vs. hν are shown in figure 67 for the 3 electrodes. For both materials a linear relationship can only be obtained for m = 2 indicating that the excitation process is an indirect transition, in agreement with most of the results reported in the literature. From the extrapolation of the plots, the band gap energy for niobia is about 3.05 eV and that that of TiO_2 is 3.16 eV. The E_g value of Nb_2O_5 only agrees with those reported by Lenzmann [164] for coating sintered at 600°C (3.05 eV) and Barros Filho [238] (3.14 eV). On the other hand Arita et al. [239] found $E_g \cong 3.4$ eV (indirect process), Barros Filho et al. [23] found either $E_g \cong 3.4$ eV or 3.1 eV (indirect process) while Lenzmann [164]] could not decide if the transition was a direct process with $E_g \cong 3.4$ eV or an indirect process with $E_g = 3.05$ eV. The value for TiO_2 (anatase) agree with those of Kavan et al. [237] and Tang et al. [240] (E_g = 3.2 eV) although the same value was reported to be a direct transition by Ninoura et al. [241].

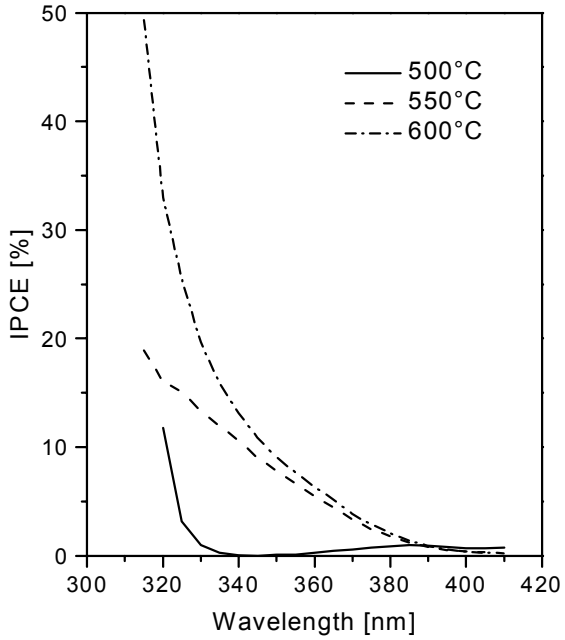

Figure 68: Photocurrent action spectrum of Nb_2O_5 sintered at different temperatures.

Figure 68 shows the photocurrent action spectrum of Nb_2O_5 films sintered at 500°, 550° and 600°C for 30 min. The photoelectrochemical response of the film sintered at 500°C is very small, but increases with the sintering temperature. Although the coatings are crystalline, this shows that the interconnection among the nanocrystallites is only obtained at high temperature

and plays an important role on the photoelectrochemical performance. A low sintering degree leads to the recombination of a large amount of photogenerated electrons and holes at the grain boundaries. The analysis of the curves for 550 and 600°C (not shown) confirms that the excitation process is indirect (m = 2) with the same band gap energy (3.05 eV).

Photocurrent-voltage characteristics

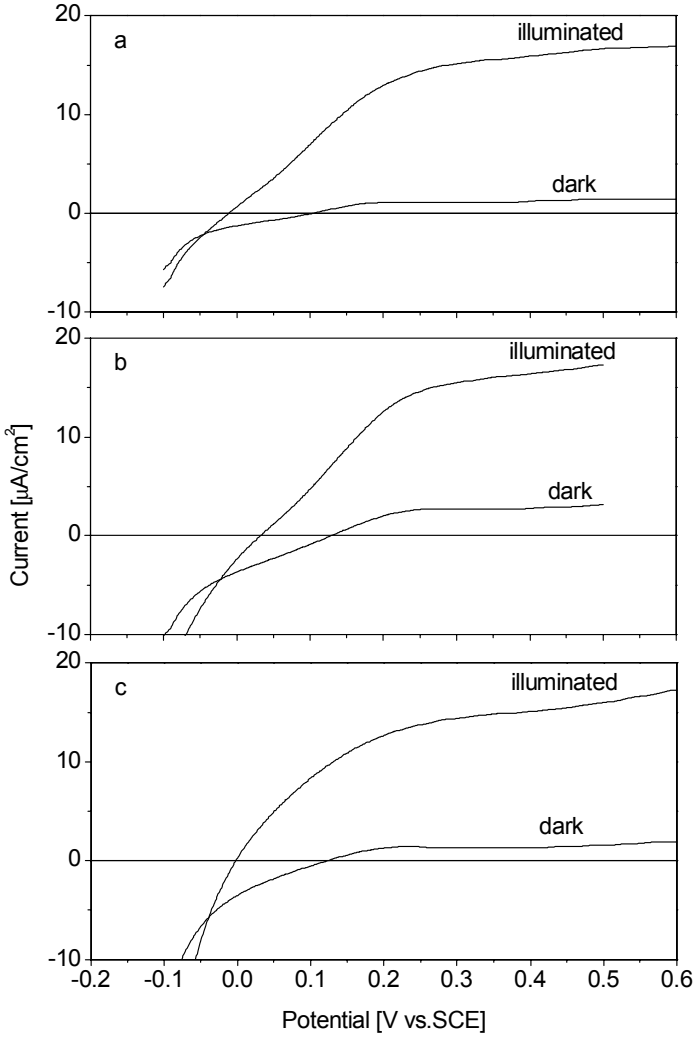

Figure 69: Photocurrent-voltage characteristics of Nb_2O_5 and TiO_2 electrodes measured in aqueous 0.1 N KCl and 0.1 N HCl solution in the dark and under 1000 W/m^2 (AM1.5 direct) illumination. (a) Nb_2O_5, (b) Nb_2O_5+PEG+C and (c) TiO_2.

The photocurrent-voltage characteristics of the Nb_2O_5 electrodes sintered at 600°C and of the TiO_2 electrode measured in the dark and under 1000 W/m^2 (AM1.5 direct) illumination are shown in figure 69. In the dark the electrodes showed a good rectifying property. A cathodic current resulting from the accumulation of electrons in the particles flows under cathodic polarisation and a very small anodic current flows for positive voltages. Under illumination, the anodic photocurrent increases and then levels up. The oxide films have a characteristic of a n-type semiconductor with particles in close contact to each other. The electrons produced by light excitation move through the layer and the circuit and a reduction of H^+ into H_2 ($2H^+ + 2e^-$

$\rightarrow H_2$) occurs at the counter electrode. The photogenerated holes move to the surface of the particles and cause the oxidation of water to O_2 ($H_2O + 2h^+ \rightarrow 1/2O_2 + 2H^+$). The onset potential of the anodic photocurrent determined under high intensity illumination, can be taken as the values of the flat band potential of the semiconductor in the electrolyte [236]. It is -0.01 V vs. SCE for the Nb_2O_5 film prepared with and without additive sol, -0.033 V vs. SCE for the Nb_2O_5 film prepared with additives and 0.0 V vs. SCE for TiO_2. The values for niobia agree with those reported in the literature and determined using the same methodology. Narayanan et al. [242], using niobia pressed pellets found a value of -0.08 V vs. SCE at a pH = 1.85 and -0.6 V vs. SCE at pH = 12.18. Arita et al.[239], using an oxide film made by anodic oxidation got a value of +0.06 V vs. SCE and Lenzmann [164] using sol-gel niobia reported a value close to -0.03 V vs. SCE in aqueous solution of 0.1 M CF_3SO_3H. The value determined for TiO_2 (anatase), -0.06 vs. SCE, also agrees with the those determined by Lenzmann [164] using the same methodology, -0.04 V vs. SCE. However it strongly disagrees with those reported by Kavan et al. [237] for a single crystal (-0.40 V vs SCE at pH = 0) and by Rothenberger et al. for a polycrystalline material [243]. However the methodology for the determination was different.

The current-voltage characteristic of Nb_2O_5 electrodes prepared with and without additives was also measured in aqueous 0.2 N $LiClO_4$ solution (pH = 6.9) (not shown). It is known that the pH of the electrolyte shifts the flat band potential to smaller value. The observed shift was typically about -0.024 V/pH. This value is smaller than those determined by Arita et al. [239] (-0.06 V/pH) and Kavan et al. [244] (-0.05 V/pH). Accordingly, we proposed that

for niobia layer (without additives) E_{fb} (V vs. SCE) = 0.01 - 0.023pH
for niobia layer (with additives) E_{fb} (V vs. SCE) = 0.06 - 0.025pH

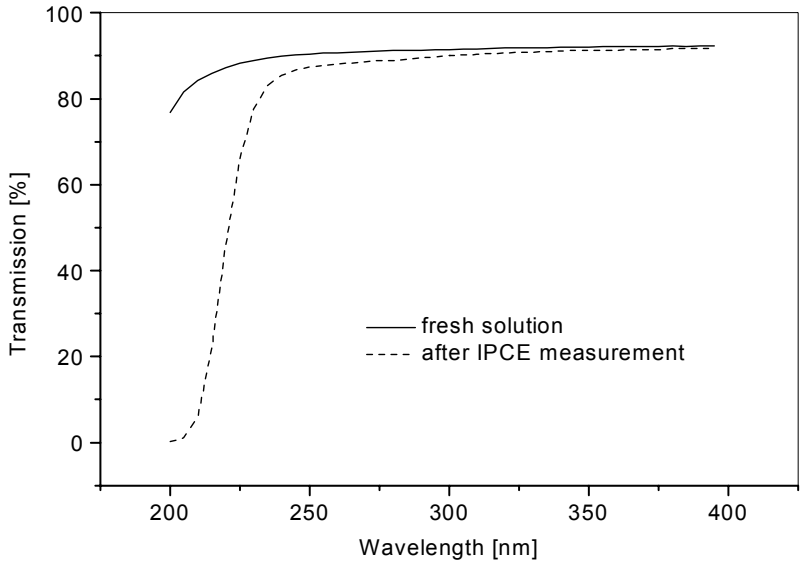

Figure 70: Transmission spectrum of the 0.2 N $LiClO_4$ aqueous solution before and after a photocurrent action spectrum measurement with UV light.

The transmission spectrum of the aqueous 0.2 N $LiClO_4$ electrolyte was affected during a IPCE measurement of the Nb_2O_5 or TiO_2 photoelectrodes (figure 70). The adsorption of the solution in the UV range increases. This implies that a photocorrosion of the semiconductor occurs under UV light illumination.

Conclusions

Non-sensitised niobia and titania (anatase) coatings exhibit photoelectrochemical properties under irradiated by UV light irradiation, i.e. with photons having an energy higher than the band gap. In aqueous acid electrolyte the oxidation of water to O_2 is observed at the electrode and the reduction of H^+ to H_2 is seen at the counter electrode. The shape of the action spectrum is very similar for both materials although it is slightly shifted to lower wavelengths for Nb_2O_5. They follow closely the absorption spectrum. The excitation process was found to be an indirect one with a band gap value of ca. 3.06 eV for Nb_2O_5 and 3.16 eV for TiO_2. The pH of electrolyte shifts the flat band potential toward more negative potential. However the value found, -0.025/pH, is smaller that those reported in the literature.

5.4.2 Photoelectrochemical properties of dye sensitised Nb_2O_5 electrodes

This section describes the solar-to-electric energy conversion of various nanocrystalline Nb_2O_5 films sensitised with the Ru(II) complex, and the influence of PEG addition, sintering temperature, film thickness, type of solvent, type of cation in the redox system and applied potential on their photoelectrochemical properties.

5.4.2.1 Influence of additives

Figure 71 shows the photocurrent action spectrum determined in short circuit condition and the current-potential characteristics of Ru(II) sensitised Nb_2O_5 electrodes sintered at 600°C prepared with and without PEG additives measured with the electrolyte No. 3 (solution of 80 vol.-% PC and 20 vol.-% ACN with 0.5 M $(Pr)_4NI$ and 0.05 M I_2). Both parameters were measured with light irradiation on the substrate side. The values obtained have not been corrected for reflection and absorption loss in the glass/TCO coating. The true IPCE values are obtained by multiplying the results by a factor of about 1.3.

The IPCE spectrum is now displaced in the visible region and its shape follows the absorption spectrum of a Ru(II) complex solution. The maximum IPCE at 545 nm is high and increases from 48% (without PEG) to 66% (with PEG). This is due to the higher specific surface area of the last coating (see section 5.3.2.1).

The photocurrent-potential curves reflect again a semiconducting behaviour and in the dark the electrodes show a good rectifying property. The cathodic dark current corresponds to a recombination current due to the reduction of triiodide ($I_3^- + 2e^- \rightarrow 3I^-$). That for Nb_2O_5 electrode prepared without additive shows a slower rise (figure 71c). Under illumination the

anodic photocurrent is much higher than that presented above for the non-sensitised electrodes as the number of photons adsorbed per unit time is higher. The values obtained for the Nb_2O_5 electrode prepared with additive is slightly enhanced. The values of the potential determined at zero current (about -1.2 V vs. $Ag/AgClO_4$) correspond to the value of the open circuit potential (OCV). It is lower for the electrode made with additives (see section 5.4.3.3 for a discussion).

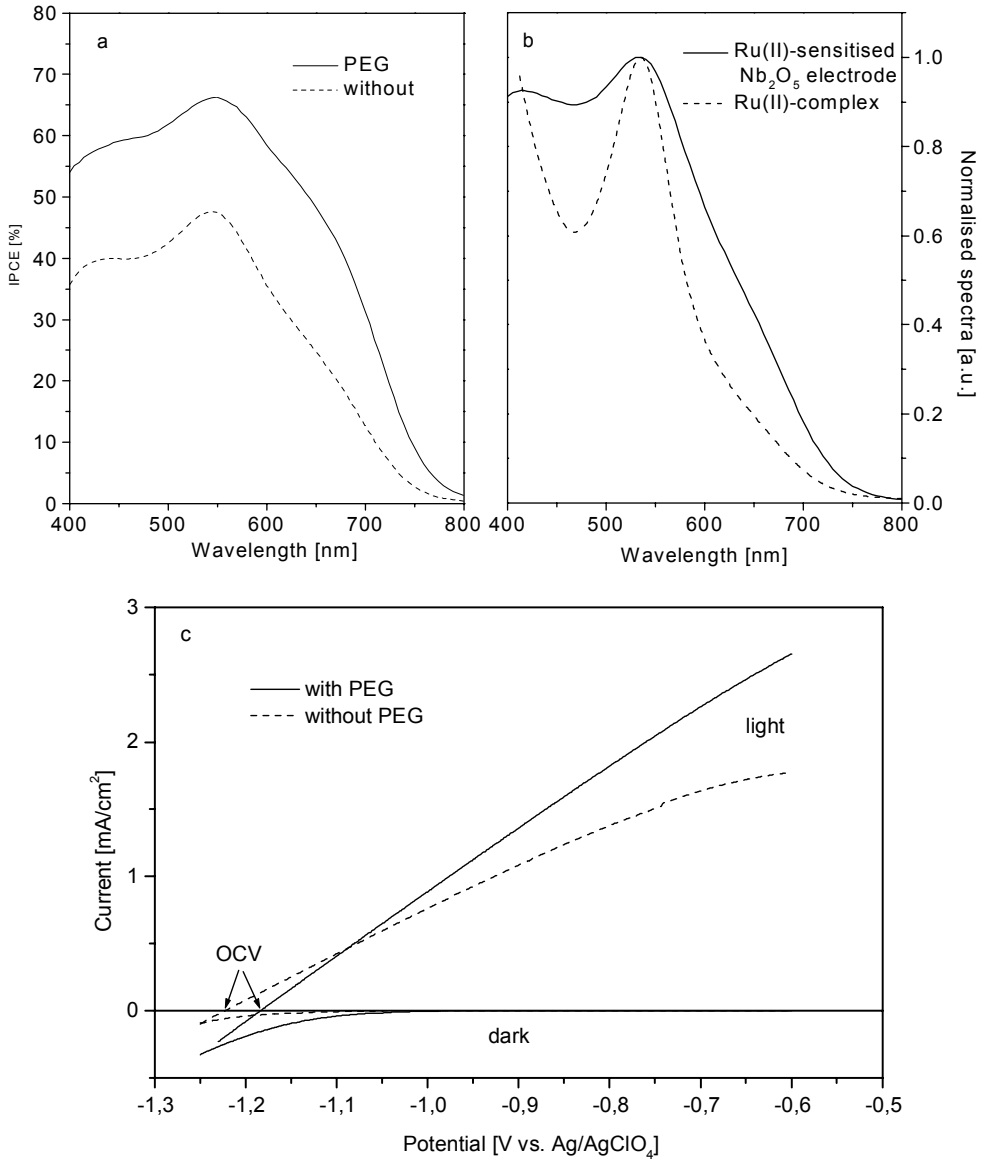

Figure 71: (a) Photocurrent action spectrum of Ru(II) sensitised Nb_2O_5 electrodes prepared with PEG (16 μm thick) and without PEG (14.3 μm thick), sintered at 600°C for 30 min. Electrolyte: No.3, (b) normalised spectra of IPCE and absorbance of Ru(II) complex (c) current-potential characteristics in the dark and under 100 W/m² illumination.

5.4.2.2 Influence of the sintering temperature

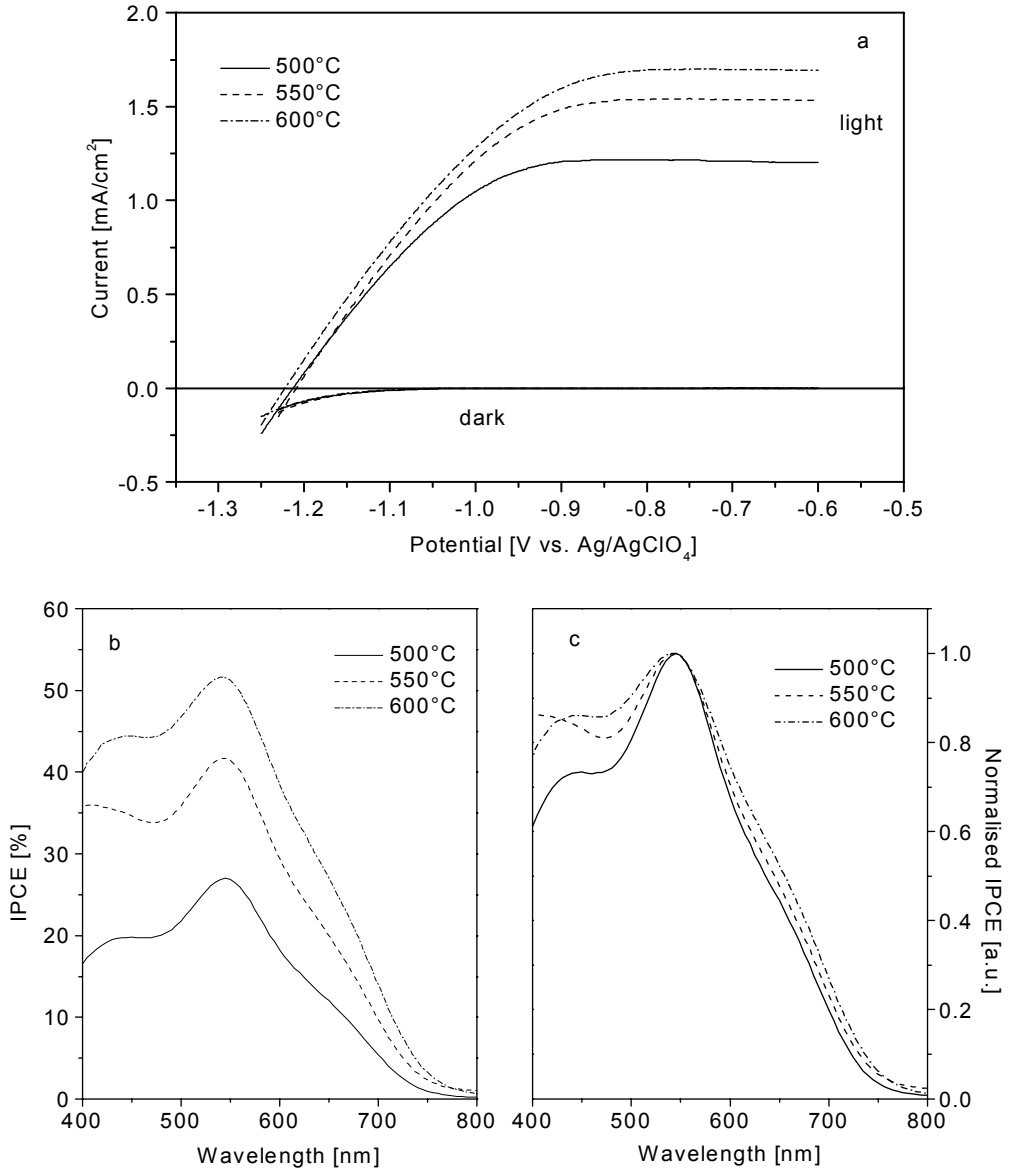

Figure 72: (a) Current-potential characteristics in the dark and under 100 W/m² illumination, (b) photocurrent action spectrum of Ru(II) sensitised Nb_2O_5 electrodes(10 µm thick) prepared with PEG + C and sintered at different temperature and (c) normalised spectra at their maximum IPCE. Electrolyte: No.3.

The effect of the sintering temperature on the current-potential characteristics and the photocurrent action spectrum of 10 µm thick Ru(II) sensitised Nb_2O_5 + 20 wt.-%PEG + carbon soot electrode is shown in figure 72. The dark current curves practically overlap each other. However, under illumination an increase of the photocurrent is observed with the sintering temperature (figure 72a). Figure 72b shows that the overall values of the IPCE also increase with the sintering temperature and is maximum for an electrode sintered at 600°C. When normalised to their maximum value, the curves are slightly red-shifted by increasing the sintering temperature. This was also observed by Lezmann [164] and explained as a decrease of the concentration of defects (possibly oxygen vacancies) giving rise to occupied inter-band

gap states which can back transfer electrons to the excited state of the dye followed by their relaxation to the ground state. At the short wavelength side the relative IPCE´s values also slightly increase with the sintering temperature. This was also observed by Lenzmann [164]. A lower concentration of defects may also reduce the recombination rate of the photogenerating electrons travelling toward the conducting electrode.

5.4.2.3 Influence of the film thickness

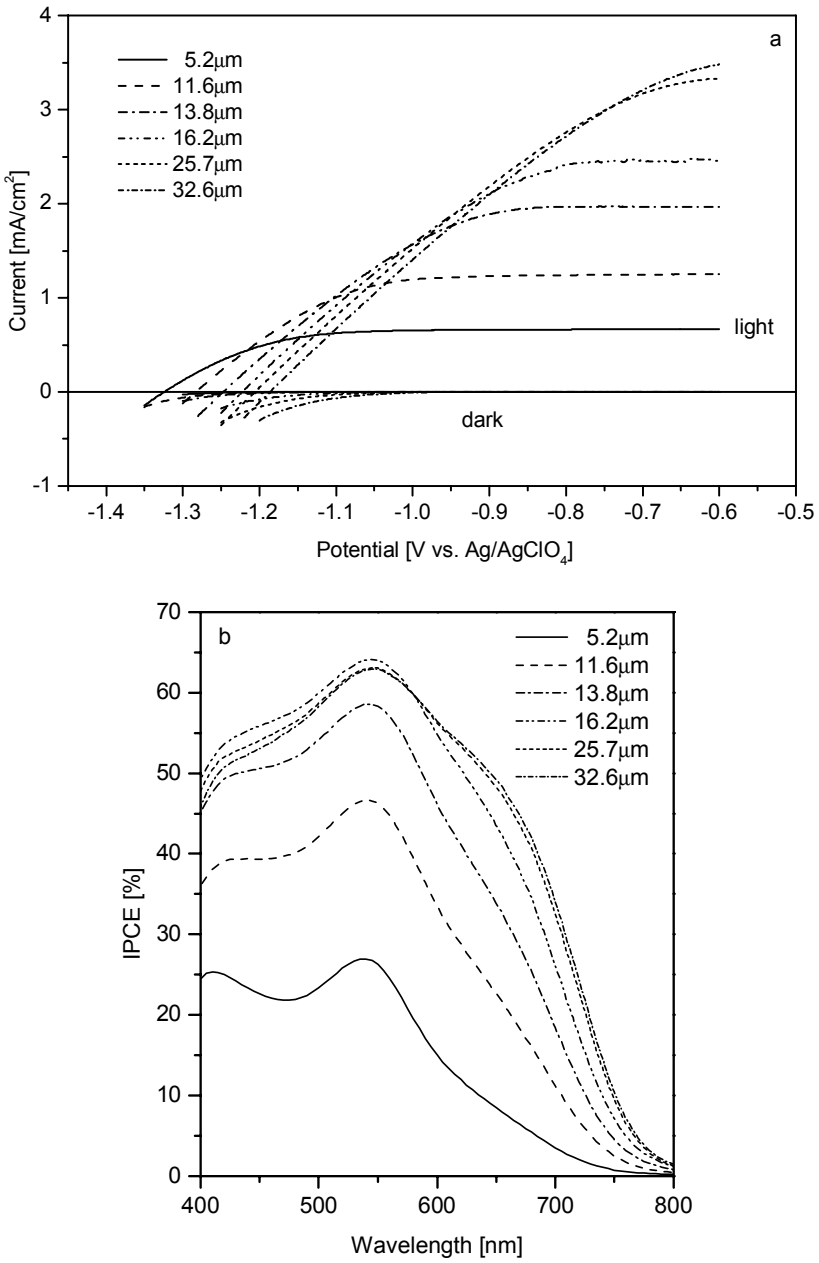

Figure 73:(a) Film thickness dependence of the current-potential characteristic in the dark and under 100 W/m² illumination and (b) photocurrent action spectrum of Ru(II) sensitised Nb_2O_5 electrodes prepared with 20 wt.-%PEG + C soot and sintered at 600°C for 30 min. Electrolyte: No.3.

Figure 73 shows the current-potential characteristic and photocurrent action spectrum of the Ru(II)-sensitised niobia electrodes of different film thickness.

Under illumination the photocurrent increases strongly with the film thickness (figure 73a). For a value of 13.8 μm it is as large as 2 mA/cm^2 at -0.7 V vs. Ag/AgClO$_4$, i.e. 3 times the photocurrent of a 5.2 μm film thickness. Moreover the potential at which a saturation of the anodic photocurrent appears, the potential corresponding to the onset of the anodic current and the potential at which the dark current reaches a zero value shifts towards more positive potential with increasing thickness. The first observation indicates that the fill factor of the solar cell will decrease with the electrode thickness and the last two that the open circuit potential of the solar cell will follow a similar trend. Both effects are due to an increase of the electron-redox recombination (path c, figure 6) with the thickness as the injected electrons have to be transported across a larger number of nanoparticles and grain boundaries and to the increase of the resistance loss. The overall value of the IPCE increases linearly with the film thickness up to 16.2 μm reaching a maximum value of 64% (figure 73b). However the IPCE for $\lambda > 600$ nm is slightly improved for film thickness $d > 16$ μm. This is attributed to the increase of the photon´s path length which increases the probability of absorption at long wavelength light. Thus there is an optimal thickness to obtain a maximum photocurrent, open circuit potential and fill factor.

5.4.2.4 Influence of the type of solvent in the redox system

Figure 74 shows the current-potential characteristic in the dark and under 100 W/m^2 illumination of 10 μm thick Ru(II) sensitised Nb_2O_5 electrodes prepared with additives and sintered at 550°C measured in PC + ACN electrolytes containing different percentage of PC. The cation for all electrolytes is tetrapropylammonium (the composition of the electrolytes is given in table 3).

The electrolyte solution affects strongly the measurements. Under 100 W/m^2 illumination high saturation photocurrents are obtained with the electrolyte 2 (50 vol.-% PC in ACN) and 3 (80 vol.-% PC in ACN). The current drops by a factor of 10 for pure ACN (electrolyte No. 1) and by a factor 2.3 for pure PC (electrolyte No. 4). As it will be shown later (section 5.4.3.3) this is in agreement with the evolution of the charge transfer resistance R_{ct} and the capacitance of the double charge layer C_{dl} . The variation of the potential for the onset of the anodic current is also in agreement with the value of the open circuit potential (section 5.5).

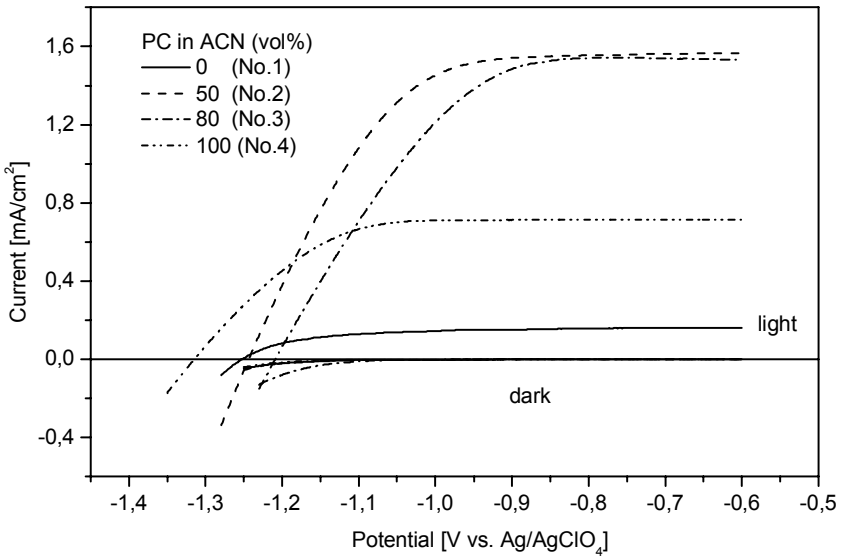

Figure 74: Current-potential characteristics of Ru(II) sensitised Nb_2O_5 electrodes (10µm, sintered at 550°C, 30 min) measured in PC + ACN electrolyte containing different percentage of PC in the dark and under 100 W/m² illumination.

5.4.2.5 Influence of the type of cation in the redox system

Figure 75 shows the current-potential characteristics in the dark and under 100 W/m² illumination and the photocurrent action spectrum of the Ru(II) sensitised Nb_2O_5 electrodes prepared with additives and sintered at 600°C measured in a 80 vol.-% PC in ACN electrolyte containing LiI (electrolyte 5), tetrapropylammonium iodide (electrolyte 3) and tetrabutylammonium iodide (electrolyte 6) as the redox system. The use of an electrolyte containing the smallest cation, Li^+, leads to the highest anodic current at saturation and the lowest potential for the onset of the anodic current. The opposite behaviour is observed for the electrolyte containing the largest cation, tetrabutylammonium (figure 75a). These results agree with Liu et al. [245]. The corresponding maximum IPCE at 545 nm are 64% (Li^+ electrolyte and tetrapropylammonium iodide) and 47% (tetrabutylammonium iodide), respectively (figure 75b).

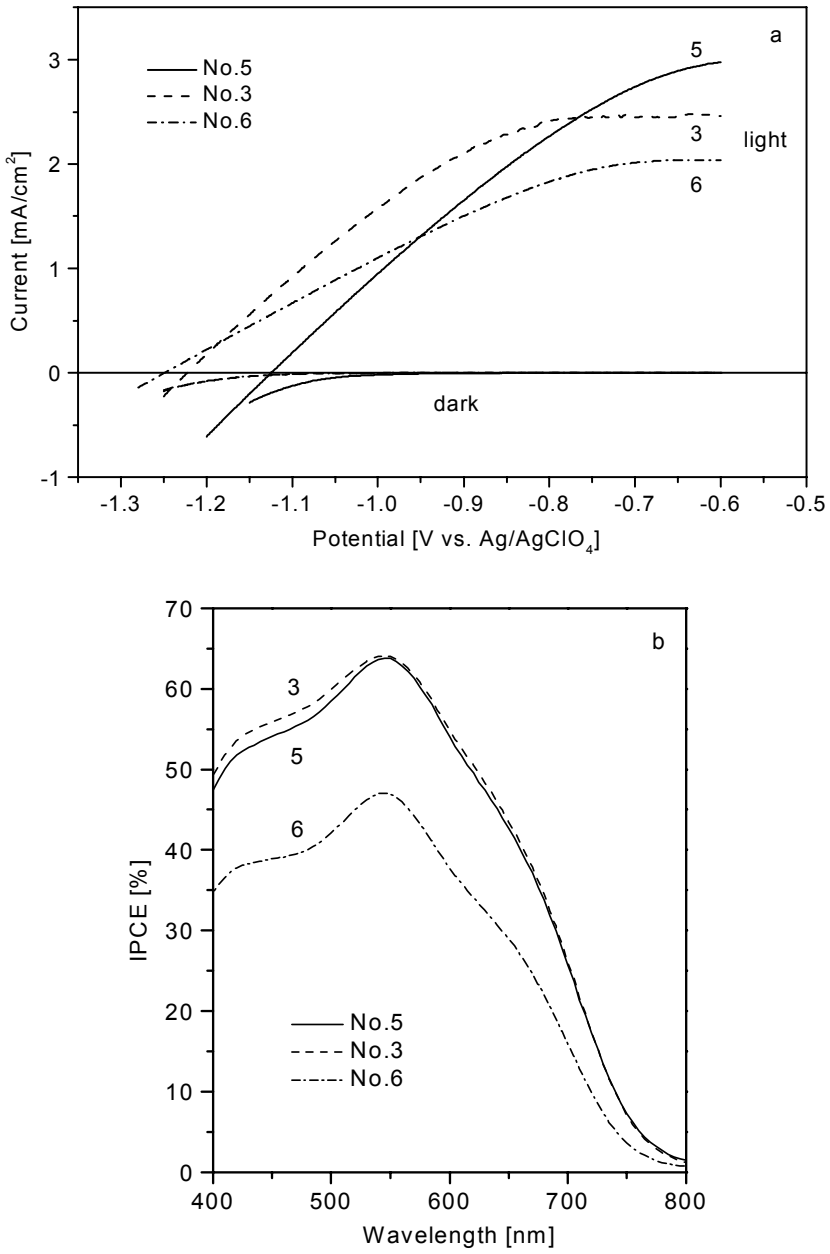

Figure 75: (a) Current-potential characteristics in the dark and under 100 W/m² illumination and (b) photocurrent action spectrum of the Ru(II) sensitised Nb_2O_5 electrodes (prepared with PEG + C, sintered at 600°C for 30 min, thickness of 16 µm) using different cation electrolyte solution.

5.4.2.6 Influence of the applied potential

Figure 76 shows a plot of the IPCE of a 12 µm thick sensitised Nb_2O_5 electrode prepared with PEG + C additives, sintered at 600°C and measured at 545 nm as a function of the applied potential. The value is independent of the applied potential between -1.1 to -0.5 V vs. $Ag/AgClO_4$. Similar results have been obtained with other niobia coatings. Since the light intensity is very small, the anodic current is saturated in the whole potential range. This suggests that the Ru(II) sensitised Nb_2O_5 photoelectrodes possess a high efficient charge

collection. This behaviour is different from that reported for a Ru(II) sensitised ZnO electrode by Redmond et al. [108] and Bedja et al. [109] for which the external potential was found to control directly the Fermi level of the semiconductor and hence modifies the energy gap leading to an increase in the charge collection efficiency.

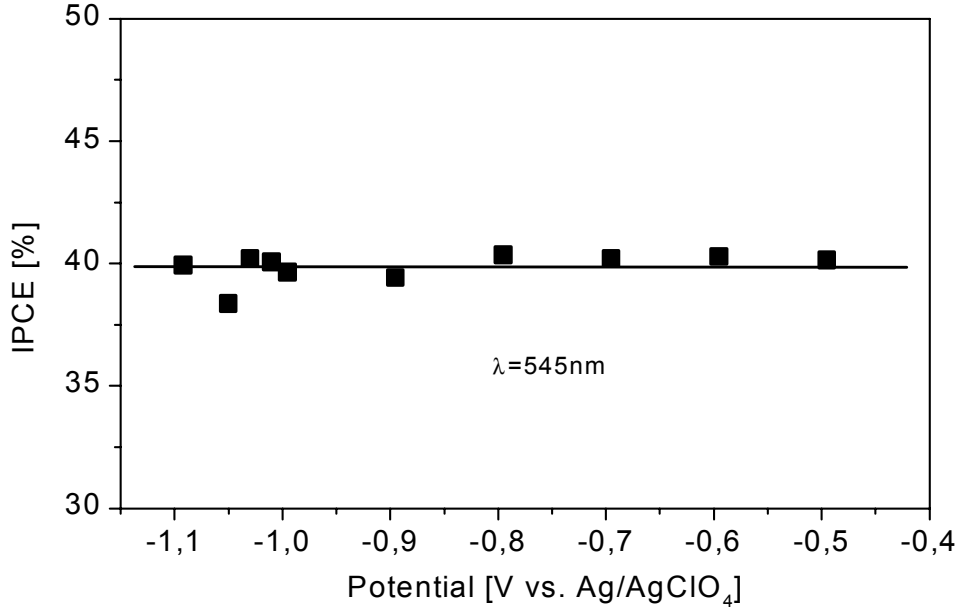

Figure 76: IPCE-potential curve for a 545 nm irradiation of a 12 µm thick Ru(II) sensitised Nb_2O_5 photoelectrode prepared with PEG + C, sintered at 600°C for 30 min.

5.4.2.7 Comparison of Nb_2O_5 and TiO_2 dye sensitised electrodes

Figure 77(a, b) shows the current-potential characteristics in the dark and under 100 W/m^2 illumination and the photocurrent action spectrum of a Ru(II) sensitised Nb_2O_5 sintered at 600°C and a commercial TiO_2 electrodes measured under the same experimental conditions. The thickness of the Nb_2O_5 and TiO_2 films are 9.7 µm and 6.8 µm, respectively. As the IPCE curves were shown to increase scale linearly with the thickness up to 16 µm (figure 73), figure 77b shows also the calculated Nb_2O_5 spectrum for a thickness equal to that of TiO_2 i.e. 6.8 µm.

Figure 77c shows the ratio $(IPCE)_{Nb2O5}/(IPCE)_{TiO2}$ calculated for the same thickness 6.8 µm.

For wavelength up to 750 nm both IPCE have the same shape but the value for Nb_2O_5 are about 65% of that of TiO_2. The same hold for the current-potential characteristics. The constant ratio observed below 550 nm is understandable. The IPCE is defined as equation 17. Moser et al. [107] found for $\lambda < 550$ nm that the electron injection quantum yield from the excited states of the dye molecules into the niobia particles was only 75% of that of TiO_2. Using the values measured for LHE (0.78 for Nb_2O_5 and 0.86 for TiO_2, section 5.3.3) and assuming that η_e is the same for both materials, we get a ratios of 0.59 in good agreement with figure 77c. However the electron injection efficiency for Nb_2O_5 was found to drop rapidly for

$\lambda > 550$ nm and no injection was possible for $\lambda \geq 650$ nm, contrary to TiO_2 for which the yield remains unity up to about 700 nm. Therefore the ratio curve of figure 77c should not remain constant but should drastically decrease with increasing wavelength. Recently, Lenzmann [164] using surface photovoltage spectroscopy (Kelvin Probe) found however that the onset of the electron injection for Nb_2O_5 sintered at 600°C was at 740 nm and only 40 nm blue-shifted (i.e. 0.09 eV) compared to TiO_2. According to this results, the constant IPCE ratio would be somewhat red-shifted but it cannot explain our result for wavelength longer than about 750 nm.

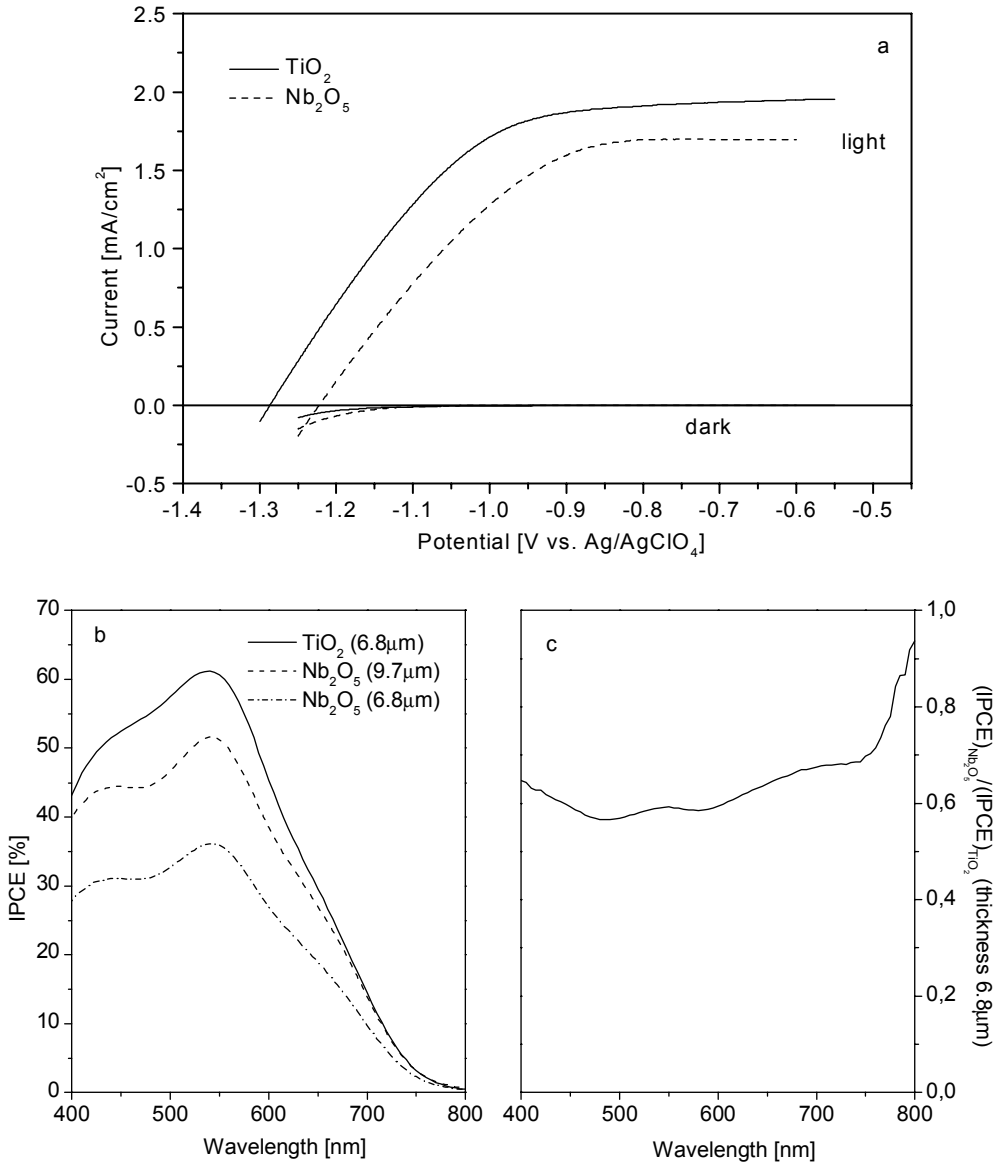

Figure 77: (a) Current-potential characteristics in the dark and under 100 W/m² illumination, (b) measured photocurrent action spectrum; the curve (–•–) has been calculated by multiplying the experimental curve by 0.7. (c) ratio of photocurrent action spectrum of Ru(II) sensitised Nb_2O_5 (Nb_2O_5+PEG+C) calculated for a thickness of 6.8 μm and TiO_2. Electrolyte: No.3.

Conclusions

The IPCE of Ru(II) complex sensitised niobia coatings was effectively shifted into the visible range and the overall shape of the spectrum is identical to that found for TiO_2 coatings. Nb_2O_5 is therefore a promising candidate for solar cell development. However the electro-optical properties strongly depend on many parameters.

An optimum solar cell will require a high IPCE value. To achieve that, the niobia coatings are best prepared using a sol containing additives such as PEG and carbon soot because of the higher specific surface area of these coating. The sintering temperature of the layers should be in the range of 550°C to 600°C and the thickness of the coatings should not exceed about 20 µm. The composition of the electrolyte is of most importance. Mixed solvents of PC in ACN appear better than pure PC or pure ACN and a small size of the cation (e.g. Li^+) is also preferable.

However such requirements will also have an influence on the open circuit potential (OCP) and the fill factor (FF) which are factors that should be also maximised. However the addition of PEG, the increase of the thickness, the addition of PC in ACN and the use of small cation decrease the OCP while the sintering temperature has probably no influence. The highest values have been obtained with on layers made from sols with additives, a sintering between 550°C and 600°C and the use of a PC electrolyte containing tetrapropylammonium iodide. These conditions are unfortunately not those found to optimize the IPCE. The comparison of IPCE and current-potential characteristics of Nb_2O_5 and TiO_2 of same thickness measured in a same electrolyte have also shown that the values obtained for Nb_2O_5 are about 65% of those obtained for TiO_2 and that the IPCE ratio remains practically constant up to 750 nm. This already indicates that niobia coatings will be less efficient than the TiO_2 ones.

It is also necessary to recall that all the current-potential measurements under light (100 W/m^2) have been done using a tungsten-halogen lamp where light filtered by a 400 nm UV filter. The emission spectrum of such a lamp is somewhat different from that of a solar simmulator of the same intensity. This should effect the I vs.V values but should not effect the different comparisons.

It is also worthwhile at this stage to mention that other parameters, as for instance the size and the shape of the cells (as reported later) have also a drastic influence on their final properties. Compromises should therefore be found to build the best complete cells.

5.4.3 Impedance analysis of non-sensitised and Ru(II)-sensitised electrodes

This section shows that complementary information on the photoelectrochemical and the intrinsic properties of non- and dye-sensitised electrodes can be gained by analyzing impedance spectroscopy data (EIS). The experimental details were given in section 4.7.6. We however recall that the results have been obtained in the frequency range 10^{-1} Hz to 10^5 Hz with the

coatings immersed in an electroactive electrolyte. Otherwise noted, it consists of 80 vol.-% PC in ACN containing 0.5 M tetrapropylammonium iodide and 0.05 M I_2 as redox system (electrolyte 3). The size of the coatings was 7 cm². The area of the light spot shined on the coatings was 4.9 cm².

As shown later, all the Nyquist plots consist of two slightly depressed semicircles either completely or partially resolved. They have been described using an equivalent electrical circuit comprising 3 circuits in series: a resistor R_s and two parallel RC circuits each containing a constant phase element (CPE) replacing the capacitors (figure 78). The physical meaning of the electrical elements will be discussed later.

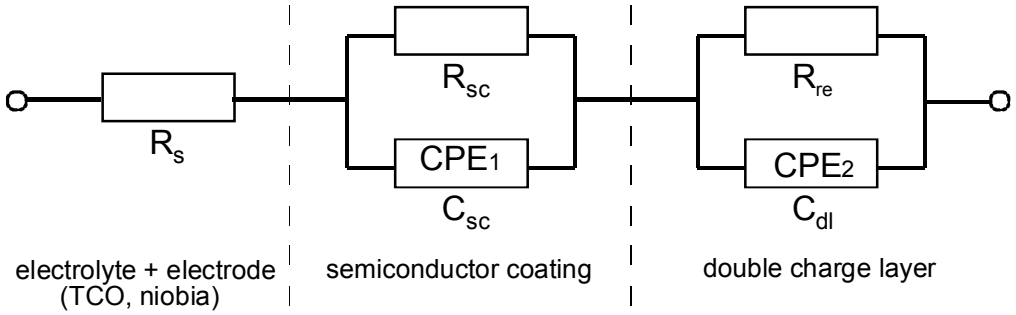

Figure 78: Equivalent circuit of the dye sensitised solar cells used for the analysis of impedance spectra.

For the sake of clarity we first describe the results obtained in the dark and then those obtained under illumination.

5.4.3.1 Impedance spectroscopy in the dark

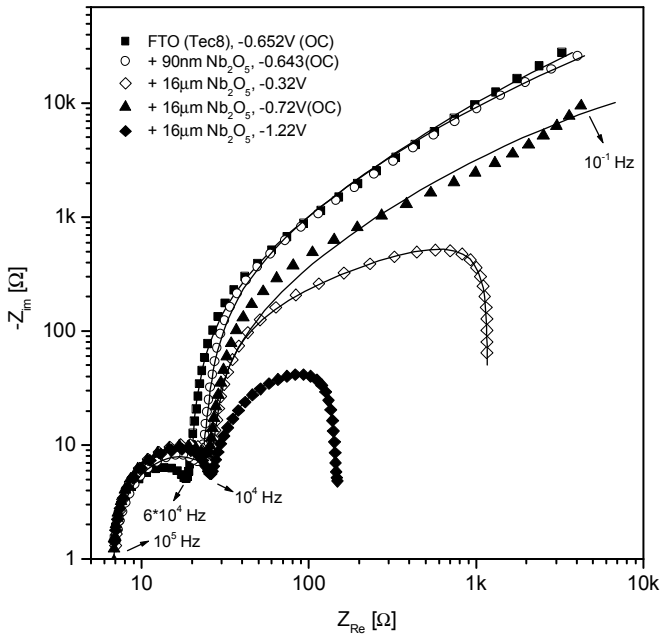

Figure 79: Impedance spectra of FTO, 90 nm and 16 µm thick Nb_2O_5 electrodes in the dark.

As only one paper has been yet reported in the literature for the EIS behavior of semiconducting coatings immersed in an electroactive electrolyte [246], a systematic study has been performed on the following non-sensitised systems: an FTO coating alone, a 90 nm thick Nb_2O_5 deposited on FTO glass, a 16 µm nanocrystalline Nb_2O_5 deposited on the previous system. The thick niobia coatings have been obtained with a sol containing 20 wt.-% PEG and C soot and have been sintered at 600°C.

Figure 79 shows typical experimental Nyquist plots. The upper three curves have been measured at open circuit potential i.e. at a strictly zero dark current (i.e. V = -0.652 V for the FTO coating, V = -0.643 V for the 90 nm thick Nb_2O_5-layer and V= -0.72 V for the 16 µm thick Nb_2O_5 coating) while the other plots, which only refer to the 16 µm thick nanoparticles Nb_2O_5, have been obtained by applying either a lower or a higher potential. Similar behaviors have been obtained for all the other coatings. The solid lines are fit using the model and the agreement is excellent for all the plots.

The plots consist of two slightly depressed semicircles whose resolution depends on the applied potential.

The size of the small semicircles at high frequency (f > 1 kHz) does not change practically with the applied potential. They are well described by the resistance R_s and the first RC circuit and the values of the electrical elements are independent of the applied potential. For all coatings the value of R_s is of the order of 7 ± 1 Ω and corresponds to the resistance of the electrolyte and the FTO conducting coating. R_{SC} is typically of the order of 77 ± 5 Ω/cm² (FTO coating), 95 ± 5 Ω/cm² (90 nm Nb_2O_5) and 120 ± 5 Ω/cm² (16 µm Nb_2O_5). C_{SC} is typically 0.5 µF/cm², 0.4 ± 0.03 µF/cm² and 0.18 ± 0.03 µF/cm² respectively. n is independent of the type of coatings and has the value n = 0.88 ± 0.02. R_{SC} and C_{SC} are characteristics of the semiconducting materials and represent the resistance and the capacitance related to the grain boundaries of the semiconducting coatings and/or to the interface between the coatings. The high value of n indicates that all the coatings have a low roughness.

The size of the large semicircles at low frequency (f < 1 kHz) depends on the type of the material and above all on the applied potential. The semicircles are only fully resolved for applied potential V < - 0.8 V and V > -0.4 V vs. $Ag/AgClO_4$ but all the results can be very well described by the parallel circuit comprising the resistance R_{re} and the CPE2 (C_{dl}) in parallel.

The physical meaning of both electrical elements for the different coatings can be understood by examining the evolution of their values as a function of the applied potential (figure 80), remembering that V ≈ -0.65 V corresponds to the equilibrium potential for which the dark current is strictly zero (open circuit condition).

Figure 80a shows the evolution of the dark current density. For more positive potential than the equilibrium potential, it continuously increases positively and the curves are practically superimposed for all coatings. This dark current originates from the reaction occurring at the negatively bias Pt electrode: $I_3^- + 2e^-$ (from Pt) = $3I^-$ (normal potential in aqueous solution ≈ -

0.4 V vs. $Ag/AgClO_4$). Under the applied field, the so produced I^- ions diffuse through the electrolyte toward the semiconducting electrodes where they transfer back their electronic charge (oxidation) and regenerate the redox system according to the following steps:

$$I^- = I_0 + e^- \text{ (given to the electrode)}; \quad I_2 + I^- = I_3^- \text{ (in the electrolyte)} \tag{65}$$

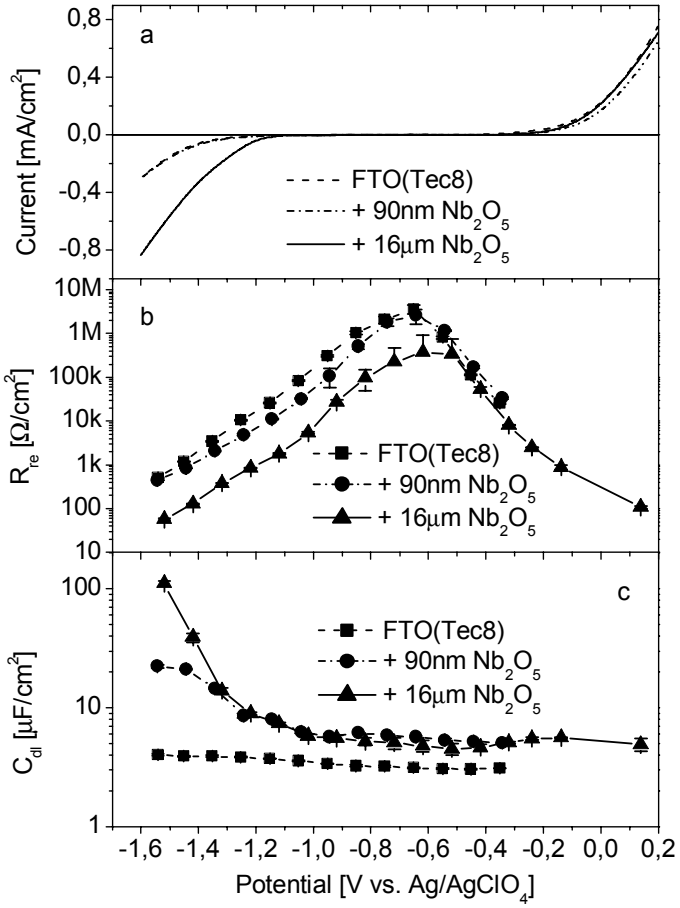

Figure 80: Dark current density, R_{re} and C_{dl} of FTO, 90 nm and 16 µm thick Nb_2O_5 electrodes as a function of the applied potential.

Figure 80b shows the evolution of the resistance R_{re}. It is high at zero dark current, about 3.6 MΩ/cm² for FTO, 2.6 MΩ/cm² for the 90 nm thick niobia and 400 KΩ/cm² for the 16 µm thick Nb_2O_5. All the values strongly decreases under more positive potential, the curves for the different coatings being practically superimposed. It is also remarkable to observe that within the error of the measurements, the evolution of R_{re} is almost identical to that calculated from the ratio $\partial\eta/\partial i$ where η is the difference between the applied potential and the equilibrium potential (overpotential).

On the other hand, the double charge layer capacitance (figure 80c) remains low and constant for all coatings with a value of about 4 µF/cm² for the FTO coating and about 6 µF/cm² for both the niobia coatings. They are therefore independent of both the potential and the value of the surface area (interface or particles) of the coatings indicating that the bulk of the nanoparticles niobia films does not become electroactive.

These results can be explained as followed (figure 81b). The resistance R_{re} acts as a charge transfer resistance and is a measure of the facility of the electronic transfer between I^- and the semiconducting material (equation 65). This transfer is difficult at the equilibrium potential but an increase of the applied field furnishes an extra energy for the electronic transfer and consequently R_{re} decreases. Also, as the surface of the particles as well as of FTO are positively charged, the cation of the electrolyte will be driven away of the semiconducting surfaces. The I^- ion will therefore easily approach the semiconducting surface so that the electronic transfer will be greatly facilitated.

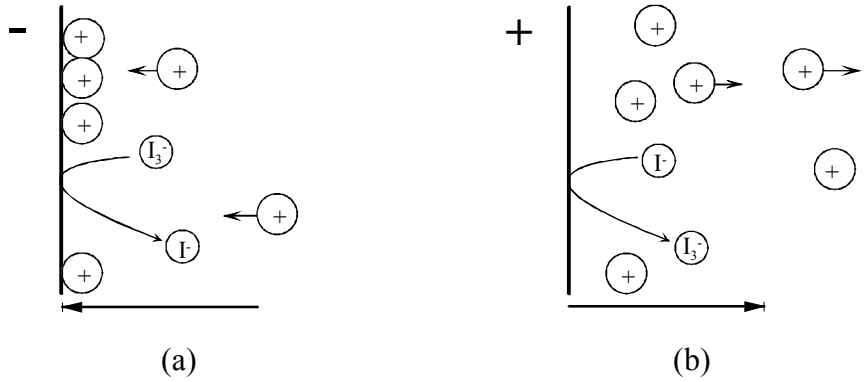

Figure 81: Schematic description of the charge distribution in the double-layer region, (a) V < equilibrium potential, (b) V > equilibrium potential.

It may happen strange that the double charge layer capacitance remains small for all the coatings. This is obvious for the FTO coating, as the surface available for the electronic transfer is that of the geometric area. For the niobia coatings, as the diffusing I^- ions are originating from outside the niobia coatings, the electronic transfer will essentially occur at the interface coating/electrolyte and the participation of the electrolyte inside the pores should be negligible. Therefore the area available to build the double charge layer capacitance is also the geometric area. The capacitance therefore remains small and constant whatever the value of the field is (V > equilibrium potential), the type and the structural configuration of the niobia coatings.

The behavior is somewhat different when more negative potentials than the equilibrium value (about -0.65 V) are applied. Figure 80a shows that a negative dark current flows in all coatings, the one observed for the thick nanoporous Nb_2O_5 coating being however larger. This current originates from the injection of electrons from the now negatively polarized conducting electrode either directly into the electrolyte (case of the FTO coating), or from the FTO electrode into the niobia coatings and then into the electrolyte filling the pores where the oxidation reaction $2e^- + I_3^- \rightarrow 3I^-$ takes place. These negative ions diffuse toward the now positive Pt electrode where they transfer back their charge ($3I^- \rightarrow 2e^-$ (given to Pt) + I_3^-). The higher negative dark current observed for the thick niobia coating is an indication that the electronic current is favored in this material.

Figure 80b shows that the values of R_{re} determined either by EIS or by calculating the ratio $\partial\eta/\partial i$ decrease in a similar fashion by lowering the applied potential. On the other side, the value of C_{dl} (figure c) for the FTO coating remains small (about 4 µF/cm²) in the whole potential range, but it increases and saturates to about 22 µC/cm² for the 90 nm thick Nb_2O_5 coating and it increases to much higher values (without saturation) for the 16 µm thick nanoparticles coating.

This shows that the bulk of the niobia films becomes electroactive at very low potential and that this activity depends essentially on the value of the surface area. The interpretation of these results is not straightforward but qualitatively follows the idea proposed by Zaban et al. [79] and Gregg et al. [103]. For a porous coating deposited on a conducting electrode, the applied potential drops only in the region where it is conductive. In other words when the dark current is small (potential at or near the equilibrium value), the electrons injected into the niobia coatings remain close to the FTO interface so that the total particle´s area available where the reduction reaction of the redox system occurs is small. Therefore the double charge capacitance remains small and the value of the resistance R_{re} which act as a measure of the kinetic of the reaction is high. When the potential is lowered to more negative values, the dark current increases and therefore the injected electrons are driven further by the field into the niobia particles and the cations in the electrolyte (tetrapropylammonium) are driven into the opposite direction (figure 81a). Therefore the value of R_{re} decreases and C_{dl} increases as the available surface of the particles increases. For the FTO coating, C_{dl} remains of course low and constant as the layer is not porous. For the thin 90 nm niobia coating, a simple calculation using the value of S_{BET} and a 50% porosity, shows that the total surface available from the particles is about 6 cm². This explains the small increase of C_{dl} and its saturation (about 6 times the value determined for FTO), observed for $V < -1.4$ V. At or below this value the whole thickness of the coating is electroactive. For the 16 µm thick niobia coating, C_{dl} also increases but to higher values, because the total available surface area of the particles, depending on the potential applied, can be as high as 1000 cm². This should lead to a saturation value of several mF/cm², but this value will only be obtained at very low potential, i.e. when the total area of the particles will be used.

5.4.3.2 Impedance spectroscopy under illumination*

Figure 82 and 83 show typical Nyquist plots of a 10 µm thick Ru(II) dye sensitised nanoporous electrode sintered at 600°C, measured at open circuit potential (i.e. $i = 0$ at $V = -1.334$ V vs. $Ag/AgClO_4$) for different light intensity (figure 82) and measured under 100 W/m² illumination as a function of the applied potential from -1.334 V (open circuit, zero current) to

*The measurements have been done using the fillered tungsten-halogen lamp (spot area 4.9 cm^2) and the values of some parameters will certainly be somewhat altered if similar measurements are made with a solar simulator of some intensity.

-0.638 V (short circuit) (figure 83). The lines calculated from the model and drawn through the experimental points fit well the data.

As expected, the high frequency circle (figure 83) does not drastically change with the applied potential and the values of the circuit elements are typically

$R_s = 12 \pm 1\ \Omega$ $R_{SC} = 75 \pm 5\ \Omega/cm^2$ $C_{SC} = 0.87 \pm 0.03\ \mu F/cm^2$ $n = 0.90 \pm 0.02$

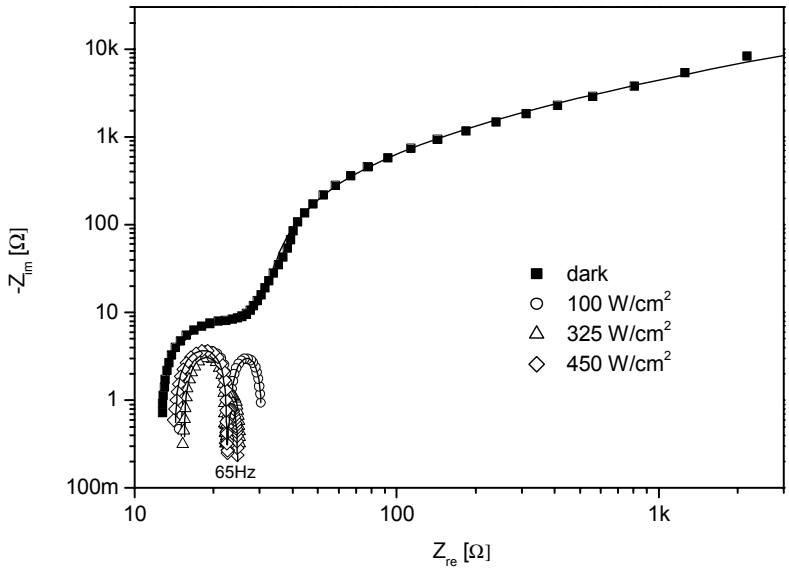

Figure 82: Impedance spectrum of a 10 µm thick nanocrystalline dye sensitised Nb_2O_5-electrode at open circuit potential (-1.334 V), under different illumination.

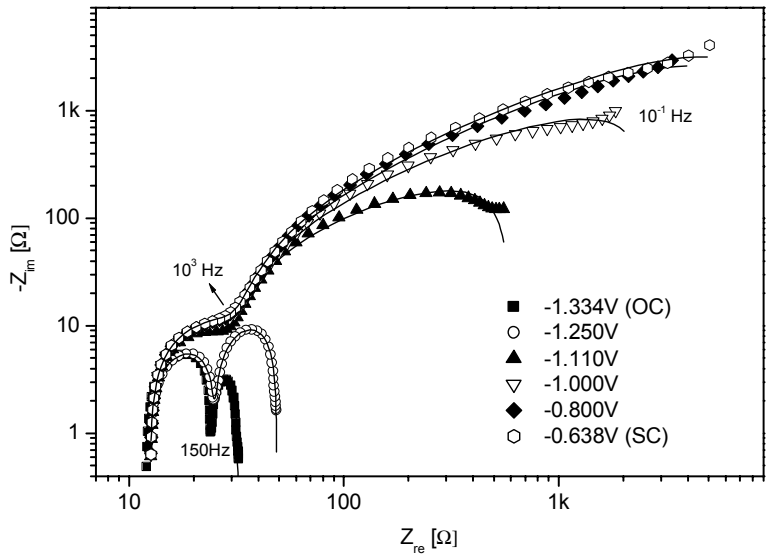

Figure 83: Impedance spectra of a 10 µm thick nanocrystalline dye sensitised Nb_2O_5-electrode measured under illumination of 100 W/m² with different applied potentials: open circuit (oc), short circuit (sc) and externally applied potential vs. $Ag/AgClO_4$.

However, under illumination, considerable variations are observed for the low frequency semicircle. The evolution of the current density, R_{re} and C_{dl} is shown in figure 84. Due to the change of the equilibrium potential when light excites on the layer, the values are here reported

as a function of the "overpotential" η, defined as "applied potential - open circuit potential". η = 0 corresponds therefore to the open circuit potential, i.e. -0.638 V vs. $Ag/AgClO_4$ for the values obtained in the dark and to -1.334 V vs. $Ag/AgClO_4$ for those obtained under illumination.

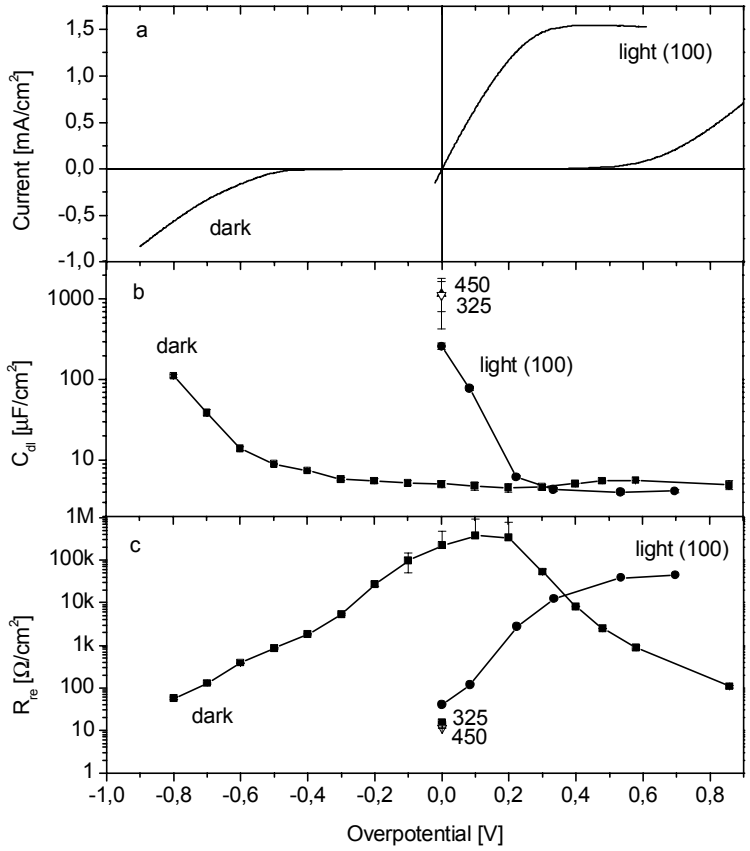

Figure 84: Current density, R_{re} and C_{dl} of 10 µm thick Nb_2O_5 electrodes as a function of the applied potential in the dark and under illumination. The values in parenthesis are in W/m².

The overall evolution of R_{re} and C_{dl} under both conditions appears analogous, just being shifted. However the origin of these components are different as the physico-chemical situation is different. It should be remembered that, when light irradiates the semiconducting system, the Ru(II) molecules (D^0) adsorbed on the surface of the particles are excited and transfer quickly one electron to the particles. This leaves behind positively charged ions (D^+) which will take part to the oxidation of I^- according to the overall reaction $2D^+ + 3I^- \rightarrow 2D^0 + I_3^-$.

At η = 0 no electronic current is flowing through the particles. Therefore, depending on the rates of the different reaction (recombination and oxidative process, path c and 3 respectively in figure 6) a certain equilibrium between electrons and D^+ will be established at the niobia particles and between I^- and I_3^- in the electrolyte filling the pores of the coating. Therefore under light irradiation a double charge capacitance will be built at each particles surface and as the total surface available is high (about 600 cm² in this case) the value of C_{dl} is relatively high, about 280 µF/cm² under 100 W/m² illumination (figure 85). This value increases if the light intensity is increased to higher value than 100 W/m² (figure 84).

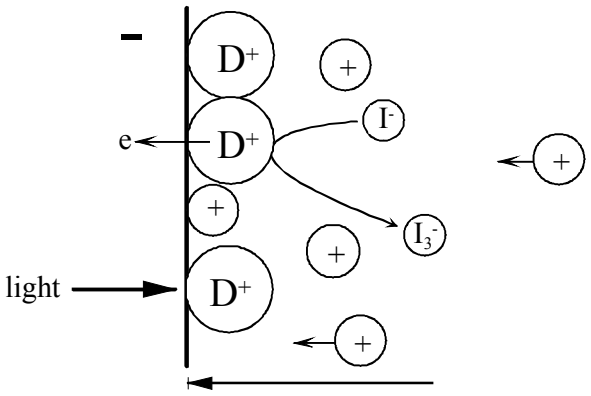

Figure 85: Schematic description of the double charge layer near the dye sensitised Nb_2O_5 surface under illumination at $\eta = 0$.

On the other hand, R_{re} is small, about 55 Ω/cm² under 100 W/m² illumination and still decreases for higher illumination intensity (figure 84).

At $\eta = 0$ this resistance can be regarded as a true charge transfer resistance giving an idea of the facility of the exchange of charges at the particles surface. An exchange current can be calculated as $i_0^{ph} = RT/2FR_{ct}$ (equation *13*) and its value gives a sort of characteristic speed of the exchange of charges. It is relatively high, i_0^{ph} = 0.23 mA/cm², as confirmed by the high initial slope of the current density (figure 84).

When the potential is scanned to more positive value, a current starts to flow through the particles and it is accompanied by an ionic current due to the regeneration of the dye at the Pt electrode ($2e^- + I_3^- \rightarrow 3I^-$). The current density increases initially linearly with η but tends to saturate already for $\eta \approx 0.3$ V. As less charges are available at the particle's surface, C_{dl} therefore decreases drastically down to a few µF/cm² as the current increases and R_{re} starts to increase however at a slower rate as the concentration of I^- is sufficiently high to maintain a high rate of the oxidation reaction. As the potential is scanned to higher value ($\eta > 0.3$ V), the current saturates and R_{re} reaches a maximum value of about 45 kΩ/cm², much lower that that observed in the dark. The saturation of the current is an indication of a limitation of the diffusion of I^- (produced at the Pt electrode) into the pores of niobia as reflected by the increase of R_{re}. A saturation of the current density to higher values will lead to a lower resistance value. This diffusion process within the pores filled by the electrolyte is without any doubt the limiting step to obtain a high value of the current density.

5.4.3.3 Influence of other parameters

The influence of several process parameters and of the electrolyte composition on the EIS results of a dye sensitised nanoporous coating has been further analysed in the dark and under 100 W/m² illumination. The most significant results are reported and discussed below. For memory purpose the values of all the electrical elements determined by fitting the Nyquist plots with the model are given in the appendix A8 in form of tables. All the results have been

obtained at open circuit condition, i.e. at a potential of about -0.75 V vs. $Ag/AgClO_4$ in the dark, and at about -1.25 V vs. $Ag/AgClO_4$ under illumination.

a) Influence of the sintering temperature

The influence of the sintering temperature has been determined for a 10 µm thick nanoporous niobia coating prepared with a sol containing 20 wt.-% PEG and carbon soot.

In the dark the most significant variation was encountered for the high frequency semicircle where the value of R_{SC} drops from 735 Ω/cm² (500°C) to 168 Ω/cm² (550°C) and to 77 Ω/cm² (600°C) and n (CPE1) increases from n = 0.56, n = 0.73 and to n = 0.91 respectively. The decreases of R_{SC} is attributed to a better interconnection between the nanocrystallites with the increase of the sintering temperature (see also next paragraph). The increase of n indicates that the porosity and the roughness of the niobia coating and that of the interface between the Nb_2O_5 film and the TCO coating are both reduced with the sintering temperature in agreement with the results obtained from BET measurements (section 5.3.2.2).

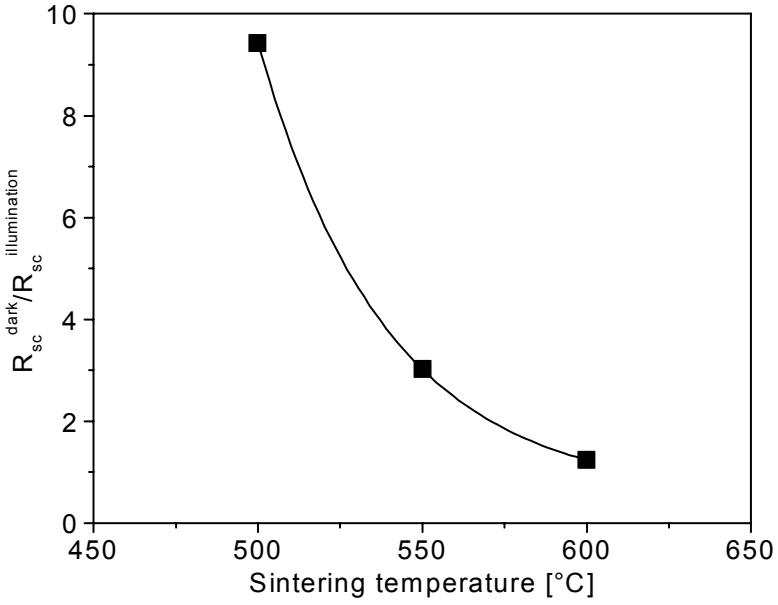

Figure 86: Variation of the ratio $R_{sc}^{dark}/R_{sc}^{illumination}$ with the sintering temperature.

Under 100 W/m² illumination, an increase of C_{dl} (low frequency circle) from 0.79 mF/cm² (500°C) to 1.55 mF/cm² (600°C) is observed. The layer sintered at higher temperature presents therefore a lower $e^- + D^+$ back recombination process (path b, figure 6). For all sintering temperature the value of R_{SC} (high frequency circle) is about 91 Ω/cm². This implies that probably the Nb_2O_5-SnO_2:F interface is not an ideal ohmic contact at 500°C and that it exists an energy barrier at this interface. Under illumination the electrons injected into the Nb_2O_5 conduction band by the excited dye molecules accumulate in the Nb_2O_5 layer causing a decrease of R_{SC}. The ratio $R_{SC}^{dark}/R_{SC}^{illumination}$ (figure 86) is strongly reduced at higher sintering temperature and tends to unity for $T_S \geq 600$°C. The energy barrier at the Nb_2O_5-TCO contact is therefore drastically reduced.

b) Influence of the Nb_2O_5 film thickness

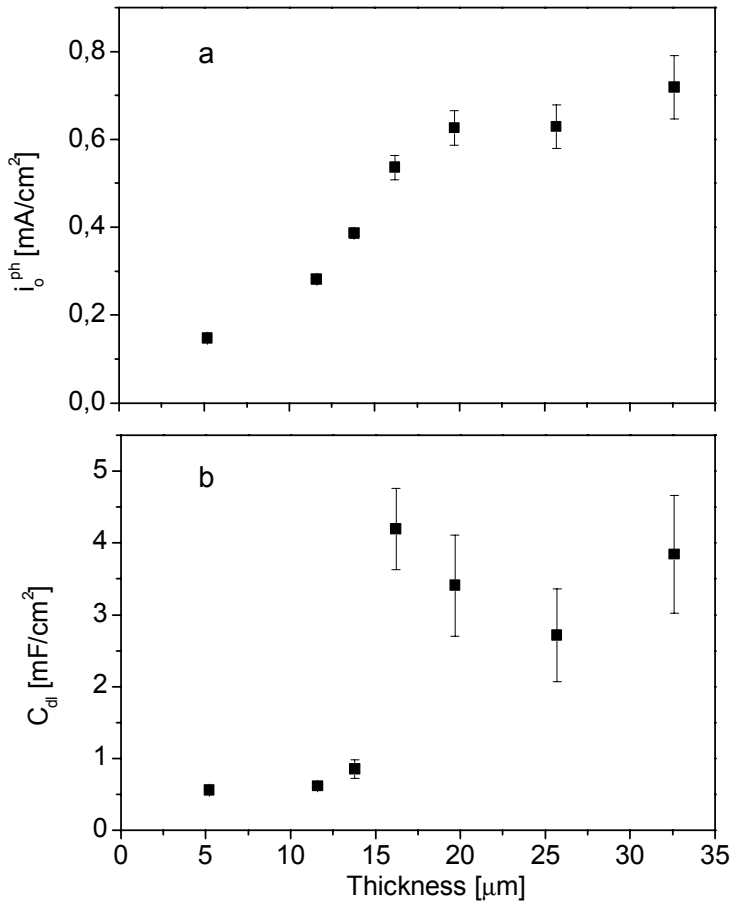

Figure 87: Variation of the exchange current density, i_o^{ph} (a), and of the double charge layer capacitance, C_{dl} (b), with the film thickness under 100 W/m² illumination.

The influence of the thickness on the electric elements has been determined with coatings made from sols containing 20 wt.-% PEG + C soot and sintered at 600°C. When measured under 100 W/m² illumination some parameters show an interesting behavior. This is the case for instance of the exchange current i_o^{ph} and the double charge layer capacitance C_{dl} (low frequency circle) (figure 87). Although the data are somewhat scattered, we observe a definite increase for both parameters up to a thickness of about 16 µm and then a level-up for higher values. It should be remembered that under illumination the whole bulk of the layer is electroactive. Therefore the amount of surface available to absorb the dye increases with the thickness (about 62 cm²/µm). The double charge capacitance should therefore increase with it. The increase of i_o^{ph} (or the decrease of the charge transfer resistance R_{ct}) indicates that the initial slope of the current density increases with the thickness. This was already observed (figure 73) and understandable since the total amount of charge injected into the particles per unit time increases with the thickness. For porous coatings made of nanoparticles it is probably possible to attribute a single "R_{ct}" and "C_{dl}" to each particle. As the particles are in contact, these elements will be connected in parallel in a layer and the measured R_{ct} and C_{dl} will decrease and increase respectively with the thickness. The saturation of C_{dl} and i_0^{ph} for

thickness higher than about 16 µm is now understandable. A similar behavior was already observed with the determination of the IPCE's. The light shined on the substrate side of the system is then absorbed by the coating. Its intensity therefore decreases exponentially with the thickness. Therefore 16 µm appears as the optimum thickness to get a fully electroactive coating. The dye coated niobia particles beyond 16 µm are not excited by the light and therefore do not participate to the photo- and electrochemical reactions. Therefore the values of C_{dl} and i_o^{ph} saturate.

c) Influence of the solvent in the electrolyte

Different compositions of the electrolyte have been tested ranging from pure propylene carbonate (PC) to pure acetonitrile (ACN) but keeping the same redox system, tetrapropylamoniumiodide + I_2. The layers were made with a sol containing 20 wt.-% PEG and C soot, sintered at 600°C and were 10 µm thick.

Figure 88a shows that R_s, measured in the dark or under illumination slightly increases with the concentration of PC in the electrolyte. This is probably due to the increase of the viscosity (figure 88a, right scale) with the amount of PC which lowers the diffusion of the ions contained in the electrolyte.

However larger changes are observed in the analysis of the low frequency semicircle measured under illumination. Both i_o^{ph} and C_{dl} strongly increase to a maximum value (at about 70% PC) and then slightly decrease.

The effect of solvents on dye sensitised TiO_2 solar cell efficiency was reported by Kebede et al. [247] and Stanley et al. [81]. The interaction of I_2, I^- and I_3^- in the electrolyte with various solvents was explained using a donor-acceptor approach. In the solar cell, I_2, I^- and I_3^- are in equilibrium in the dark and in a steady state under constant light intensity.

$$ACN + I_3^- = ACN\,I^+ + 2\,I^- \tag{66}$$

The Lewis acidity of these chemical species are ordered such

$$I^- < I_3^- < I_2 < ACN\,I^+ \tag{67}$$

The I_2 molecules and the $ACNI^+$ solvent complex are therefore better electron acceptors than the negatively charged I^- and I_3^- ions and are expected to scavenge the electrons in the conduction band. Therefore in the presence of ACN as solvent, the rate of the recombination reaction (path c, figure 5 and 6) is increased leading to high value of R_{ct} (or low value of i_o^{ph}) and to a reduced efficiency of the solar cell. A similar behavior is observed for Nb_2O_5: a high amount of ACN leads to a very low value of C_{dl} and i_o^{ph} (figure 88b, c).

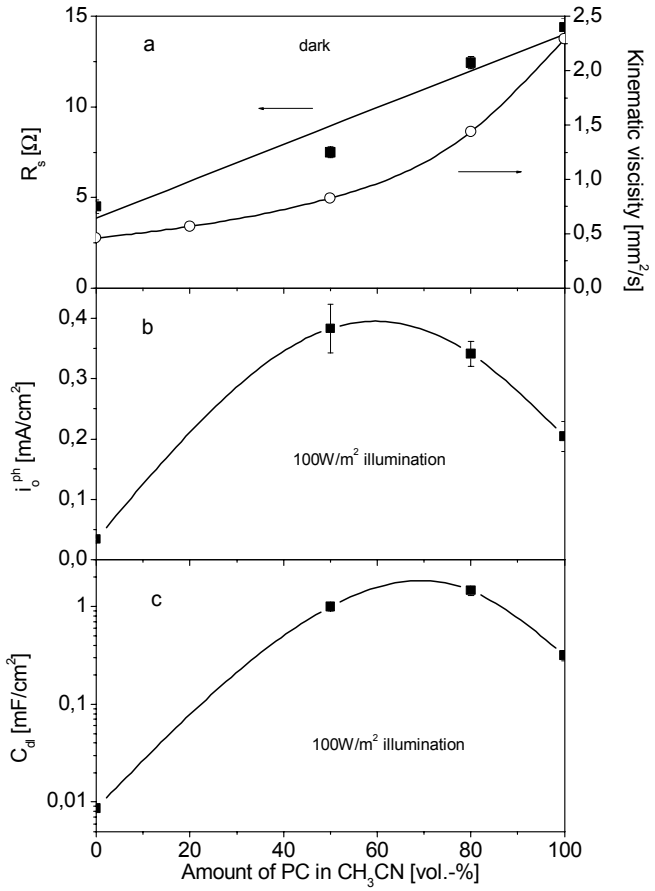

Figure 88: Variation of the resistance, R_s, the kinematic viscosity of the solution, the exchange current density, i_o^{ph}, and the double charge layer capacitance, C_{dl},, with the amount of PC in ACN. (a) in the dark, (b) and (c) under 100 W/m² illumination .

PC was found to successfully convert I_2 into I_3^- [247] and its basicity is stronger than the weak base ACN so that the I-PC bonds is stronger than the I-ACN bond. A similar reaction to that shown by the relation (66) also occurs with PC. As PC molecules intrude the ACN solvation shell of iodine preferentially, a substitution of ACN by PC takes place in the solvation shell when the amount of PC in ACN increases. Since the PCI^+ complex is sterically bulkier than the $ACNI^+$ complex they will not easily approach the Nb_2O_5 particle's surface to interact with the conduction band electrons. Consequently the rate of the recombination reaction (path c, figure 5 and 6) will be smaller and both i_o^{ph} and C_{dl} will increase. This is effectively observed up to a value of about 70% (figure 88b, c).

The viscosity of the electrolyte also increases with the concentration of PC (figure 88a). This certainly limits the diffusion of the redox couples through the pores of the nanoporous electrode. We believe that this explains the slightly lower values of i_o^{ph} and C_{dl} observed for PC concentration > 70%.

d) Influence of the cations in the redox system

The influence of cations on the impedance spectrum is reported for LiI (No. 5), tetrapropylammonium iodid (No. 3) and tetrabutylammonium iodide (No. 6) in the 80/20 vol.-

% PC/ACN electrolyte. CsI and KI as source of iodide could only be partially dissolved in this mixed solution and the results are not given. The Nb_2O_5 layers have been prepared with 20 wt.-% PEG and C soot and sintered at 600°C. Their thickness was 16 µm.

We have noted that the open circuit photovoltage (difference between the open circuit potential measured in the dark and under light) increases from 0.468 to 0.578 V with the increase of the cation radius (Li^+ < tetrapropylammonium < tetrabutylammonium). This effect is caused by the fact that small radius cations are more readily adsorbed on the Nb_2O_5 surface than those having a large radius (see figure 7). A high amount of cation adsorbed on the particles surface increases $\Delta\phi(H)$ (equation 14) leading to a decrease of the photovoltage and an improvement of the electron injection. In other words, the excess of positive charges in the double charge layer is neutralized by the mobile negatively charged I_3^- and I^-. The electron recombination (path c, figure 5, 6) will decrease when more cations are adsorbed because the electrical field screening of electrons due to the diffusion of more I_3^- or I^- will improve [99, 248].

The high frequency semicircle is also influenced by the type of cations in the electrolyte. The larger the cation radius is, the lower is its diffusion in the electrolyte and the larger the resistance R_s is (8.3 Ω for tetrapropylammonium, 14.5 Ω for tetrabutylammonium). It was expected a lower value for Li^+. The one found was however intermediate, 11 Ω. This is probably due to the fact that these ions can be easily solvated.

e) Influence of additives

A comparison has been done for layers sintered at 550°C obtained with sols made with or without PEG additive. The high frequency circle is not significantly affected. However the additive of PEG decreases the charge transfer resistance (and increases the exchange current) by almost a factor two. This is related to the substantial increase of the specific surface area of niobia discussed in section 5.3.2. Similarly with the addition of PEG and under illumination, the double charge layer capacitance C_{dl} also increases about 30 to 50% and n (CPE2) decreases (about 15%). The observation means that a more porous and rougher microstructure was obtained for the particles/electrolyte interface.

f) Comparison of Nb_2O_5 and TiO_2 dye sensitised electrodes

A comparison between a Nb_2O_5 layer made with the sol containing 20 wt.-% PEG and carbon soot, sintered at 600°C and a commercial TiO_2 layer having the same thickness, 6.25 µm, has been realized using identical configuration and measuring conditions.

The overall shape of the Nyquist plots measured in the dark and under illumination is the same.

Under 100 W/m² and in open circuit condition, the main differences were found for

		Nb_2O_5	TiO_2
a)	R_s [Ω]	6.3	9.3
b)	R_{ct} [Ω/cm²]	63	25
	i_o^{ph} [mA/cm²]	0.20	0.51

These most significant results indicate that the sensitised TiO_2 electrode presents a higher initial slope of the current density and that the regeneration rate of the dye is higher than in Nb_2O_5. Therefore cells made with TiO_2 will present a higher fill factor and quantum efficiency and larger photocurrent and consequently a higher light-to-electricity conversion.

		Nb_2O_5	TiO_2
c)	C_{dl} [mF/cm^2]	0.84	0.32

This result shows that a larger amount of dye can be adsorbed on Nb_2O_5 than on TiO_2.

Conclusion

The impedance analysis of niobia coatings have been analysed using an equivalent electrical circuit comprising three circuits in series. All the Nyquist plots consisted of two semicircles, either partly or fully resolved, and have been well fitted with the model.

The results obtained in the dark showed an unusual behavior when the applied potential was lower than the equilibrium potential (zero current). A drastic increase of the double charge capacitance (interface niobia particles/electrolyte) was observed and shown as a characteristic of the nanoparticulate nature of the coating, particularly to the Helmholtz capacity of the Nb_2O_5 surface. The otherwise insulating material becomes electrically conductive and accessible to the potential variation at the back contact and the inner surface of the electrode contributes more and more to the capacitance.

A different behavior was observed under illumination as now all the Ru(II) coated particles become electroactive. The influence of several process parameters (film thickness, sintering temperature) and electrolyte composition have been determined. A comparison between Nb_2O_5 and TiO_2 dye sensitised layer has been performed. The results have basically confirmed those obtained in the previous section. Good solar cell properties should be obtained with niobia coatings prepared from a sol made with PEG and C soot additives, a sintering between 550°C and 600°C and a thickness smaller than about 16 µm. The best electrolytes should be those containing between 50 to 80% PC in ACN. It is also expected a lower efficiency than the one which could be obtained for a TiO_2 coating.

It is however recalled that the results have been obtained with rather large coatings (7 cm² in the dark, 4.9 cm² light spot size). As reported later, the size and geometry of the solar cells are also important parameters and no EIS experiments have been made to test the influence of these parameters. An extrapolation of the results should therefore be taken with care.

5.5 Photovoltaic cells

The results described in sections 5.4 and 5.5 show that many parameters related to the morphology of the layers and the electrolyte composition influence drastically the photovoltaic properties of Nb_2O_5 coatings. Some two-electrode sandwich cells have been prepared following the scheme described in section 4.6.4.2. They have been tested with the solar illuminator (AM 1.5 global) with light intensity up to 1000 W/m².

The first example show the results obtained for a 2 × 2 cm² cell tested with a light spot size of 1 cm². The niobia coating was made with a sol containing 20 wt.-% PEG 20000 and C soot additives which ensures the highest porosity and average pore size (section 5.3.2.1), a high photocurrent (section 5.4.2.1) as well as a low charge transfer resistance (section 5.4.3.3). The coating's thickness was 12.8 μm and they were sintered at 600°C which ensures a good contact between the particles, the highest IPCE (section 5.4.2.2) and a lower back recombination process (path b, figure 6) as shown in section 5.4.3.3. Although higher IPCE's and current-potential characteristics have been obtained with thicker layer (section 5.4.2.3), a somewhat lower thickness was preferred to ensure a better diffusion of the regenerated redox species into the pores of the electrode. The choice should lead however to a lower efficiency. The electrolyte chosen was 80 vol.-% PC in ACN and tetrapropylammoniumiodide + I_2 as redox species (electrolyte No. 3). It should ensure a small rate of recombination and a high exchange current I_o^{ph} (section 5.4.3.3).

Figure 89 shows typical I - V curves obtained for different solar light illumination intensity and figure 90 shows the variation of the light-to-electricity conversion (η, equation 21), the photovoltage at open circuit V_{OC}, the photocurrent at short circuit I_{SC} and the fill factor FF (equation 20, figure 8).

As expected, the conversion efficiency at low illumination intensity is not very high (η ≈ 4% at 100 W/m²) and moreover it decreases continuously with increasing incident intensity. This is due essentially to the fast saturation of the current I_{SC}, but, overall, to the large initial decreases of the fill factor. In a photoelectrochemical cell I_{SC} is related to the incident light intensity I_{inc} by the equation 68 [249]

$$I_{sc} \propto \left(I_{inc}\right)^{\gamma} \tag{68}$$

where γ is the number of photons required to generate an electron for the external circuit. The initial slope is 0.9, close to unity, indicating that the photogeneration of the charge carriers is a single photon process and that the red-ox regeneration is efficient. However the behavior deviates already for I_{inc} > 300 W/cm². The decrease of the fill factor can be due to the too high viscosity of the electrolyte (figure 88a) or to a light intensity increase of the rate of the back reactions (figure 6). This was already reported for TiO_2 by Huang et al. [102] and Nazaeruddin et al. [19]. An increase of the fill factor and open circuit voltage was observed after a

pretreatment of the electrode with 4-tert-butylpyridine blocking the reactions of I_3^- with the electrons of the conduction band.

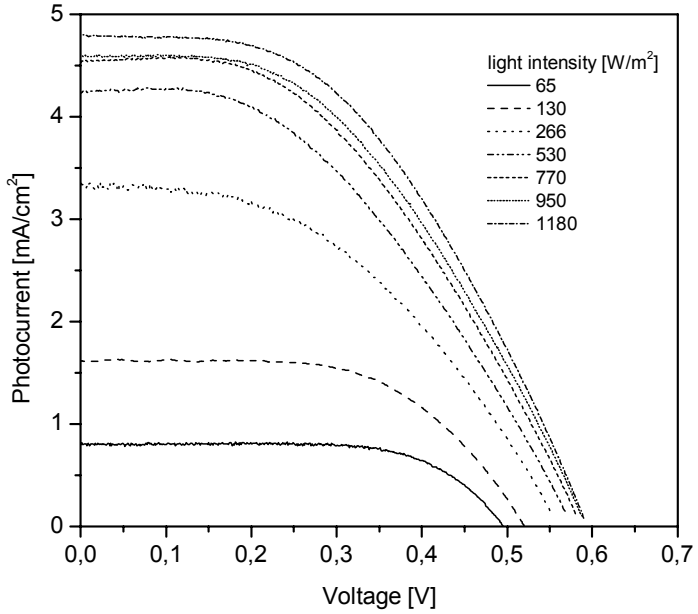

Figure 89: Photocurrent-voltage characteristics of 2 × 2 cm², 12.8 µm thick Ru(II)-sensitised Nb_2O_5 prepared with PEG and C soot, sintered at 600°C measured as a function of the intensity of an AM 1.5 global solar light irradiation (size of light spot is 1 cm²).

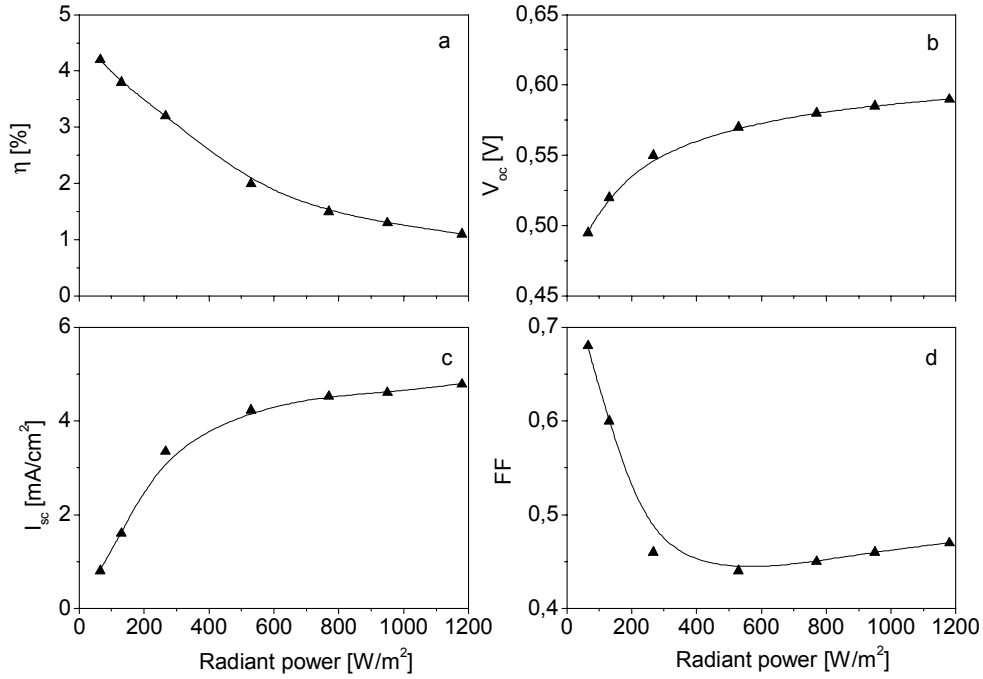

Figure 90: Photovoltaic properties vs. radiant power for the cell described in figure 88. η = light-to-electricity efficiency, V_{OC} = open circuit voltage, I_{SC} = short circuit current, FF = fill factor (spot size was 1 cm²).

There is however other important factors to be considered: the size of the spot light and the size of the cell. The highest efficiency reported for a TiO_2 cell has been obtained for size of a

few mm². The effect of the light spot size on the 2 × 2 cm² Nb_2O_5 cell is reported in figure 91 and 92. Drastic effects are observed when the irradiation spot diameter is smaller than 1 cm: a linear increase of I_{SC} is observed up to 1 sun, the fill factor being however only improved for smaller light spot diameter (< 0.49 cm). The (smaller) decrease of FF still leads to a decrease of η but the variation is much smaller. The chosen square shape of the cells is therefore not adequate and e.g. a 0.5 cm (or even smaller) × 5 cm geometry with electrical contacts made on the 5 cm side of the cell will be much better and probably solve the light intensity dependance of FF and η.

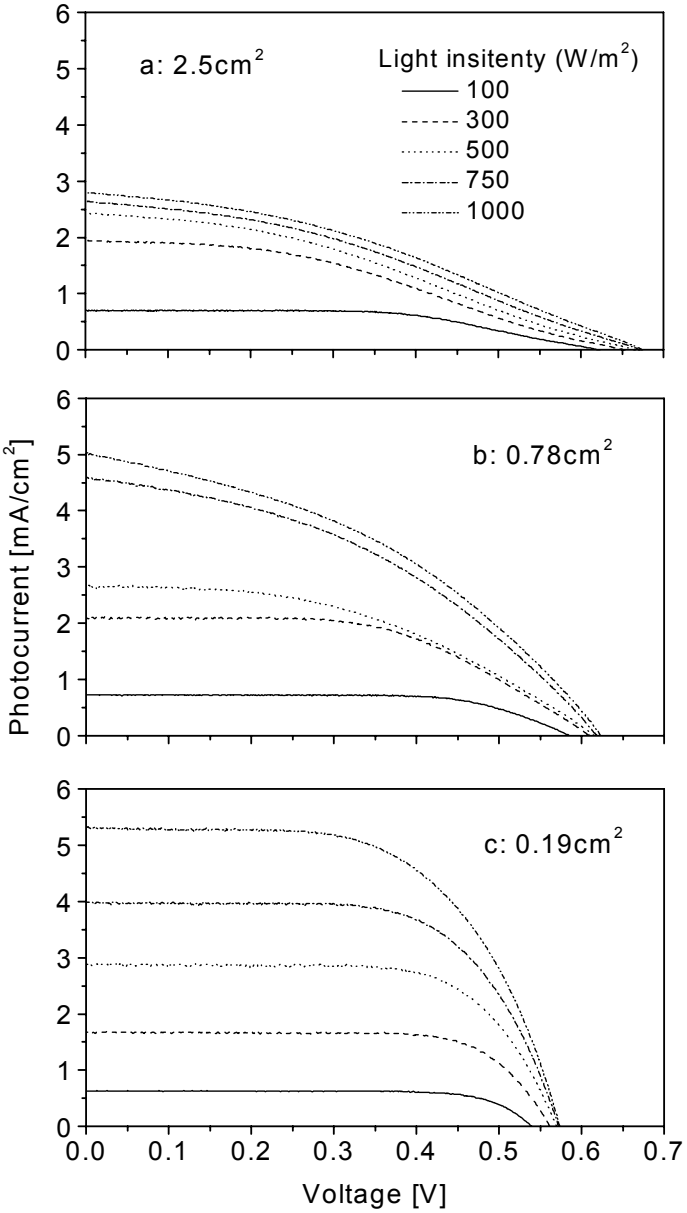

Figure 91: Photocurrent-voltage characteristics of the cell described in figure 89 and 90 measured under three different irradiation areas, a) 2.5 cm² (∅ 1.8 cm), b) 0.78 cm² (∅ 1 cm) and c) 0.19 cm² (∅ 0.49 cm).

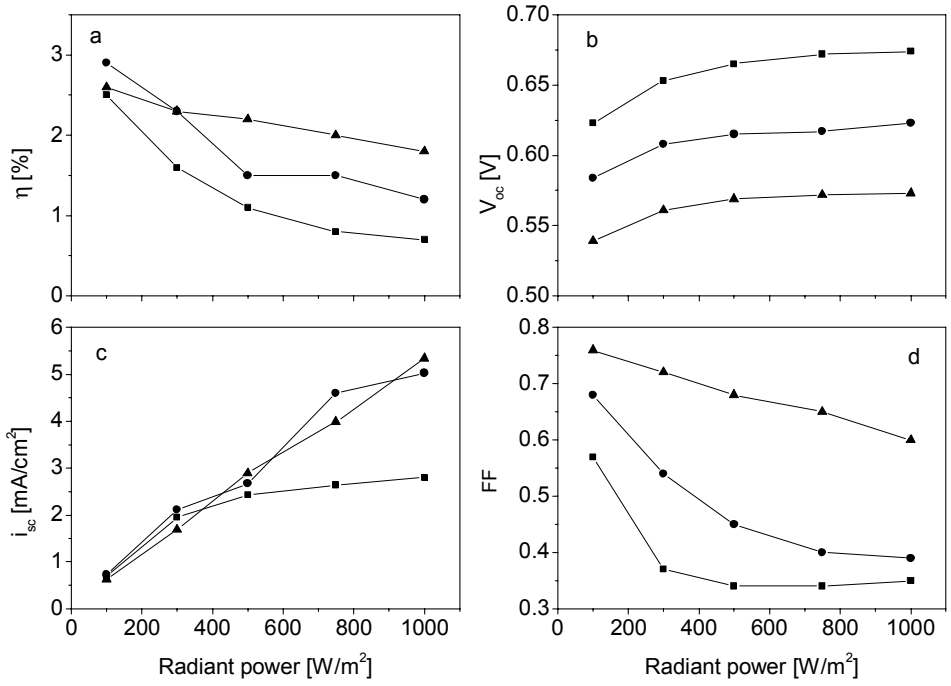

Figure 92: Photovoltaic properties of the cell described in figure 89 measured with different irradiation areas.: (■) *2.5 cm^2,* (●) *0.78 cm^2 and* (▲) *0.19 cm^2.*

A further and still unexplained improvement was observed by changing the electrolyte composition. Figure 93 shows the results of an identical 2 × 2 cm², 12.8 µm thick Nb_2O_5 square cell using the electrolyte composition 1, 2 and 3. The light spot sizes are however not equal but are all small (0.52, 0.63, 0.78 cm² respectively). Following this sequence, we observe a 20% increase of V_{OC}, a linear variation of I_{SC} up to 1 sun irradiation with the electrolyte No. 1 and only a small tendency for saturation at high intensity for the other two electrolytes. The decrease of the fill factor is however again the principal factor that decreases the efficiency of the cell with the light intensity. However values as high as 7% (under 100 W/m²) have been obtained. The geometry of the cells is once again a fundamental parameter which was not foreseen and unfortunately not systematically studied.

Extrapolating the results shown in figure 92 and 93, an efficiency at least as high as 7% and probably independent of the light intensity could be foreseen for square or rectangular Nb_2O_5-cells with a width smaller than about 0.4 cm. No test has been however done.

It is interesting at this point to compare the properties of the Nb_2O_5 cells with those reported in the literature and with those developed at INM or in other laboratories with TiO_2 as electrode material realized.

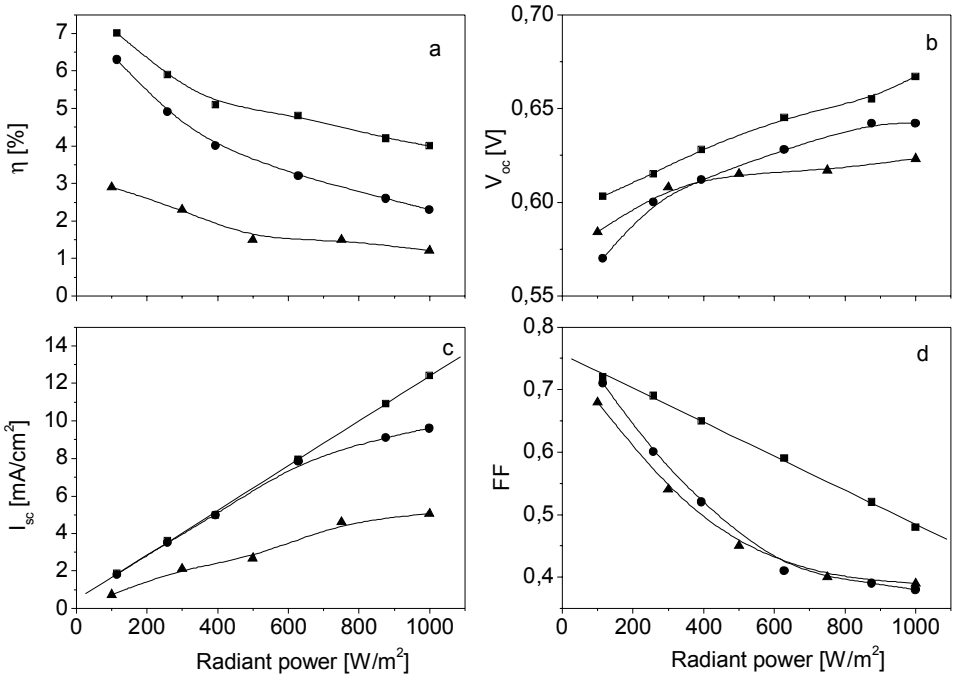

Figure 93: Photovoltaic properties of a 2 × 2 cm² cell using different electrolyte (■) *pure AC (No. 1),* (●) *50 vol.-% PC in ACN (No. 2),* (▲) *80 vol.-% PC in ACN (No. 3).*

a) Comparison between Nb_2O_5 cells

Table 18 shows the results of four different niobia cells tested at 1000 W/m².

Table 18: The results of four different niobia cells tested at 1000 W/m² (best values are in bold).

Size (cm × cm)	η (%)	V_{OC} (V)	I_{SC} (mA/cm²)	FF (%)	Literature and comments
0.67 × 0.67	2.5	-	-	-	from [163]; η constant vs. I_{inc}
0.7 × 0.7	**4** 2.7	0.595 0.59	9.7 4.1	69 **71**	from [164]; thickness 15 µm linear response of I_{SC} vs. I_{inc}
1 × 1	2	0.63	5.0	66	from [166]; thickness 6 to 8 µm
2 × 2	**4** **7** (0.1 sun)	**0.67**	**12.4**	48	this work, thickness 12.8 µm electrolyte (pure ACN), spot ∅ 8 mm linear response of I_{SC} with I_{inc}
	1.9	0.57	5.4	60	this work, thickness 12.8 µm electrolyte (80% PC in ACN), spot ∅ 4.9 mm linear response of I_{SC} with I_{inc}

The analysis of the table's data shows that under 0.1 sun intensity, the best results are obtained for one of our cell (η = 7%). Under 1 sun intensity the efficiency of cells made by Lenzman [164] and us is identical (η = 4%). Our low value is essentially due to the low value of the fill factor 48%, compared to 69% [164] but this is compensated by a higher value of I_{SC} (12.4 vs. 9.7 mA/cm²) and V_{OC} (0.67 vs. 0.595 V).

b) Comparison with TiO_2 cells

Figure 94 shows the results obtained for a 6.25 µm thick, 2 × 2 cm² cell prepared by us with a commercial TiO_2 (INAP) coating and built with the electrolyte No. 1 (pure ACN).

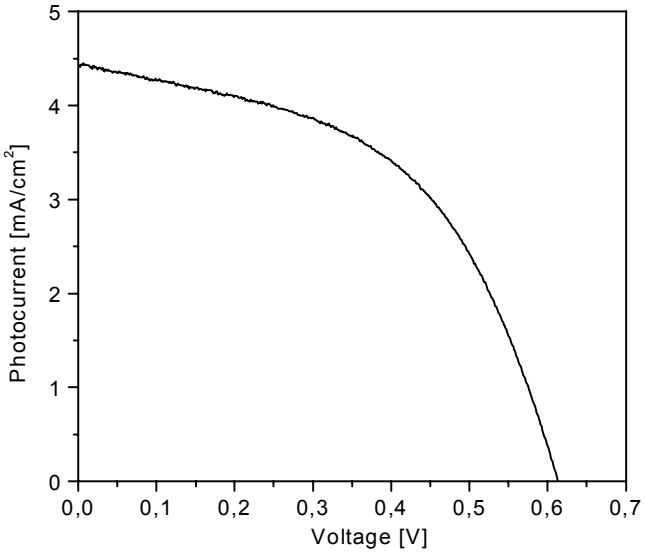

Figure 94: Photovoltaic properties of a 6.25 µm thick, 2 × 2 cm² dye sensitised TiO_2 cell. Electrolyte is No. 1 (pure ACN). Light spot 1 × 1 cm².

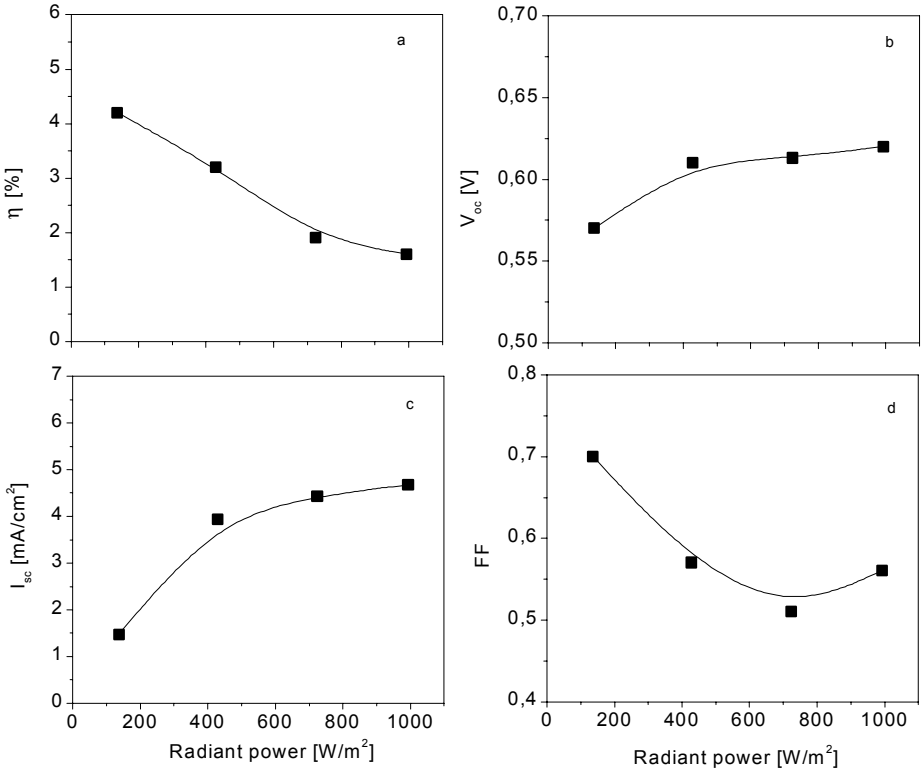

Figure 95: Dependence of the photovoltaic property on radiant power for the Ru(II)-sensitised TiO_2 solar cell using electrolyte solution Redox No. 1.

The overall behavior of η, V_{OC}, I_{SC} and FF (figure 95) is quite similar to that obtained for Nb_2O_5 cells of a similar size irradiated with a large spot (figure 90). I_{SC} increases initially linearly as I_{inc}^{γ} with $\gamma = 0.6$, but saturates to value of 4.6 mA/cm² under 1000 W/m², V_{OC} also increases and saturates at high intensity to 0.6 V, the fill factor is somewhat higher but also strongly decreases down to 55% and is the fundamental parameter which influences the decrease of the efficiency from 4.2 down to 1.6%. We therefore also conclude that the geometry of the cell and the size of the light spot are among the most important parameters to be optimised.

EPFL holds the record for the highest TiO_2 dye cell efficiency, $\eta = 10.4\%$ confirmed at NREL under AM 1.5 sunlight [250]. This cell had a size of 0.186 cm² and made with 10 µm thick TiO_2 sensitised with a Ru(II) complex dye with increased spectral sensitivity to about 920 nm (so-called black dye).

Solaronix [251] reported an efficiency of 10% for a 0.257 cm² (0.5 × 0.5 cm²) using a bis-tetrabutylammonium salt of cis-RuL_2 (NCS) and ACN as electrolyte and tested under AM 1.5 condition (V_{OC} = 0.823 V, I_{SC} = 16.9 mA/cm², FF = 72.5%).

Solaronix also reported typical efficiency of 6% at 1000 W/m² intensity with 8 × 50 mm (4 cm²) cells (5 individual cells per plate). The efficiency increased to 8.18% with 2.36 cm² cell (undisclosed geometry) using the so-called W-configuration, a module of 17 cells with size 0.5 × 8 cm² (4.05 cm²) showed an efficiency of 4.92% under 1 sun, while larger modules with 1.1 cm wide cells exhibited still a lower efficiency of 2% under 1 sun irradiation [195].

INAP [87] has claimed an reproducible efficiency at one sun of 8%, with cells of 1 cm² and 7.6% with cells of 3 cm².

These results confirm that the geometric configuration and the size of the cells are of prime importance.

Conclusion

The properties of several cells have been reported but no systematic studies to optimise them have been realized. A 2 × 2 cm² cell made with the proposed best "sol, coating process and electrolyte" resulted in an efficiency of $\eta = 4\%$ at low level illumination (0.1 sun). The value continuously decreases down to 1.9% at 1 sun as both the short circuit current and the fill factor determined from the I vs. V characteristics drastically degrade with the light intensity. A great improvement has been achieved when the size of the light spot was reduced and an almost constant efficiency was obtained. By using a pure ACN electrolyte, the efficiency was increased to 7% (low light level). This was unexpected as both the I-V characteristics (section 5.4.2.4) and EIS results (section 5.4.3.3) obtained with this electrolyte were the worse

ones. This behavior is still unexplained but may be due to the fact that these results have been obtained with very large coatings (7 cm²).

5.6 Nb_2O_5 thick films as lithium storage electrode in batteries

Nb_2O_5 shows reversible electrochemical behaviour as positive (Li^+ storage) electrodes and may be used to build secondary lithium cells [110, 111]. During the Li^+ charge-discharge process the following reduction and oxidation reactions occurs [110]

$$Nb_2O_5 + x\,Li^+ + x\,e^- \leftrightarrow Li_x\,Nb_2O_5 \qquad (69)$$

In this section the relationship between the charge-discharge characteristics and structural changes of thick nanocrystalline porous Nb_2O_5 electrodes is studied.

5.6.1 Influence of sintering temperature on the charge and discharge properties

The anodic and cathodic charge densities were calculated by integrating the cyclic voltammograms performed between -2.2 and 0.5 V vs. $Ag/AgClO_4$ at a rate of 50 mV/s up to 15 charge-discharge cycles. The thick coatings were made from the niobia + PEG + C sol deposited on a 8 $\Omega_{\square}$ FTO coating and sintered at 500, 550 and 600°C for 30 min. Their thickness was about 22 µm and the size of the sample was 7 cm^2. The electrolyte was PC with 1M $LiClO_4$.

600°C sintering

Figure 96 shows that the cathodic current increases without observing a peak up to the inversion potential, -2.2 V. In the positive voltage sweep an anodic current peak appears at -0.56 V. The shape is similar to what has been observed with electrochromic thin films [114]. The cathodic and anodic charge exchanged were -38.2 and 45.4 mC/cm^2 before the first charge-discharge cycle, and -29.6 and 64.9 mC/cm^2 after 15 cycles, respectively. As the anodic charge is higher than the cathodic one, some other side reactions occur within the electrochemical cell (see below).

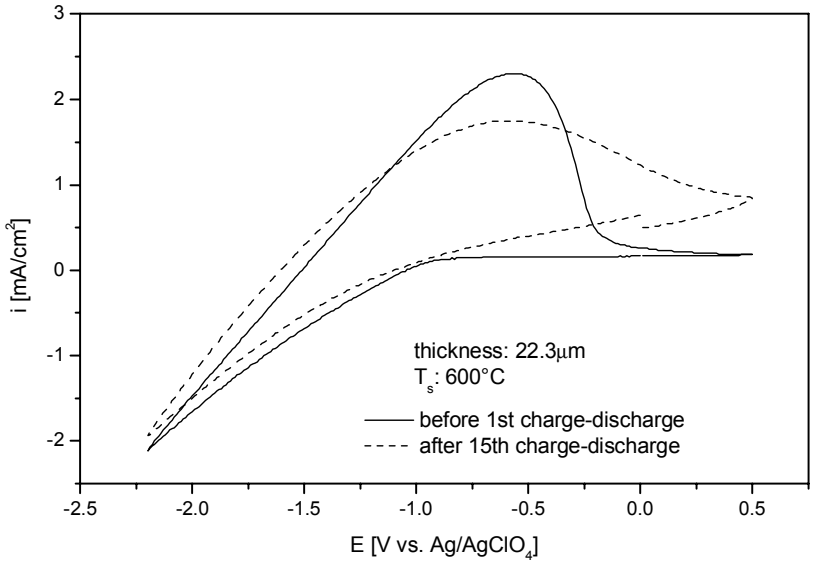

Figure 96: Voltammograms of a 22.3 μm thick Nb_2O_5+PEG film deposited on FTO coated glass, sintered at 600°C for 30 min. Electrolyte 1 M $LiClO_4$-PC, sweep rate 50 mV/s. Size: 7 cm^2.

500°C sintering

Figure 97 shows the voltammograms. No peaks are observed either in the cathodic or the anodic processes. The cathodic and anodic charge exchanged are higher than those obtained for a coating sintered at 600°C, -168.3 and 145.5 mC/cm^2 in the first cycle, but decrease drastically to -47.7 and 59.6 mC/cm^2 respectively after 15 cycles.

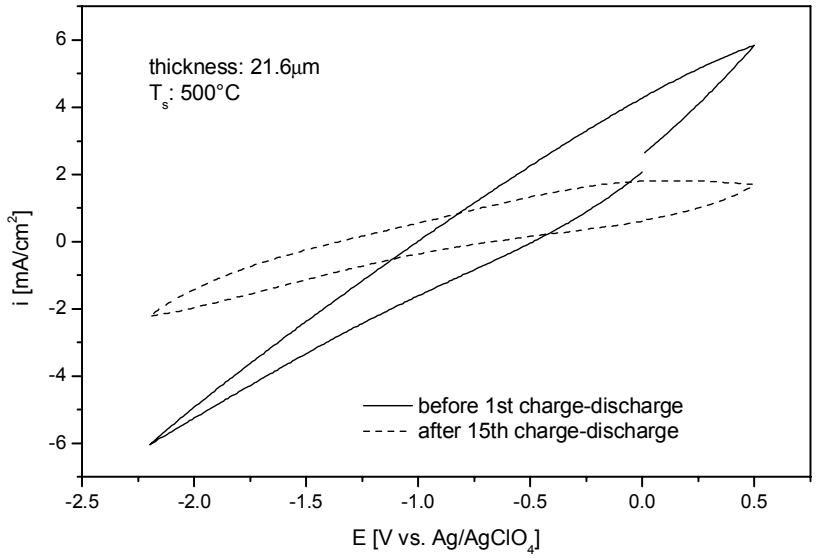

Figure 97: Voltammograms of a 21.6 μm thick Nb_2O_5 film deposited on FTO coated glass by using Nb_2O_5+PEG sol, sintered at 500°C for 30 min. Electrolyte 1 M $LiClO_4$-PC, sweep rate 50 mV/s. Size: 7 cm^2.

Figure 98 shows the potential of batteries made with niobia coatings sintered at 500, 550 and 600°C versus their capacity or the molar amount of Li^+ in the coating. For all coatings a high

discharge capacity of 160 ~ 180 mAh/(g-oxide) is observed during the first charge-discharge cycle corresponding to x = 1.6 ~ 1.8 in $Li_xNb_2O_5$. The potential variation is in the range 3.2 - 2.4 V for coating sintered at 500°C, 3.2 -2.0 V for that sintered at 550°C and 2.6 - 1.4 V for that sintered at 600°C. The discharge capacities for samples sintered at 500, 550 and 600°C decrease however rapidly down to about 25, 25 and 95 mAh/g-oxide, respectively, after 15 cycles. These results are very similar to those obtained with pressed Nb_2O_5 pellet electrodes made of a mixture of sintered polycrystalline niobium oxide powder and graphite [111].

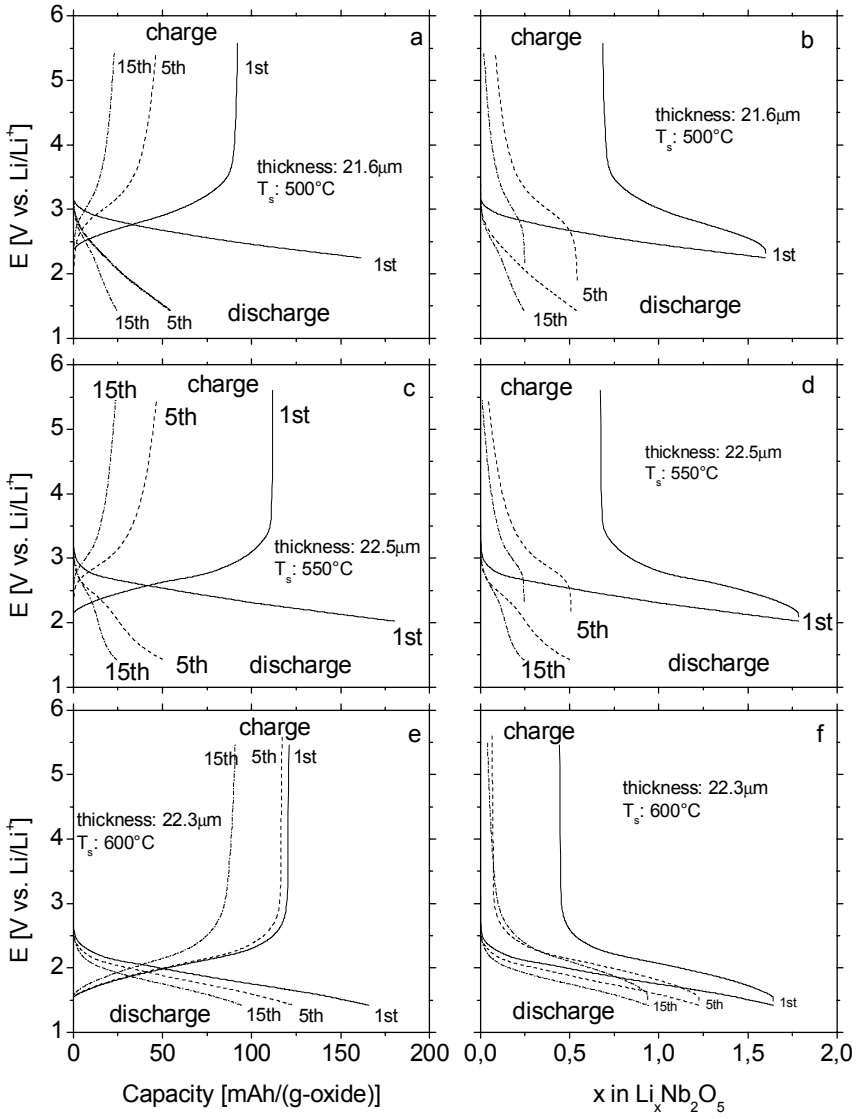

Figure 98: Charge-discharge curves of about 22 µm thick Nb_2O_5 coatings prepared with additive and sintered at (a, b) 500°C, (c, d) 550°C and (e, f) 600°C. Current density: 0.2 mA/cm^2. Cut-off potential: 1.415 V on discharge, 5.415 V on charge. The capacity was calculated by using the measured values of density: $\rho_{500°C}$ = 2.87 g/cm^3, $\rho_{550°C}$ = 2.47 g/cm^3 and $\rho_{600°C}$ = 2.34 g/cm^3.

The figure also shows that after each charge-discharge cycle a high amount of Li^+ ions remain in the coating, the amount being higher during the first few cycles. The initially pure Nb_2O_5 is rapidly transformed into a $Li_xNb_2O_5$ material with x > 0.5 presenting other thermodynamical

properties. The cycling behaviour of the Nb_2O_5 coating sintered at 600°C is better than those sintered at lower temperature. This may be correlated with the crystal structure of the oxide and the interconnection between the particles. Nevertheless a considerable amount of Li^+ remains in the electrode after the 4th recharging which probably results in the remarkable decrease of the charge capacity on cycling.

When the charge-discharge cycles of the electrodes were carried out up to a constant capacity of 20 mAh/(g-oxide), corresponding to x = 0.2 in $Li_xNb_2O_5$, the batteries could be cycled more than 1000 times in the discharge potential range 2.2 to 1.5 V and the charge potential range 1.5 to 3.0 V . This result is also similar to that obtained by Kumagai et. al.[111].

It should be noted that the measurement configuration using a Pt foil electrode as counter electrode (section 4.6.4.1) is not suitable for the charge-discharge measurements and that a lithium counter electrode could have been better. With our configuration several reactions involving the decomposition of propylene carbonate happen during the cycling at the Pt electrode (and probably also at the working electrode). The main cathodic reaction occurring during the Li^+ extraction from Nb_2O_5 coating is catalysed by the presence of trace of water in the electrolyte (about 0.1 wt.-%) and described by [244]:

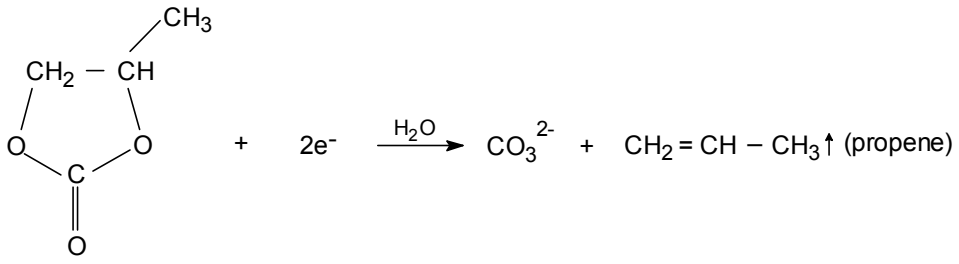

(70)

The main anodic reactions occurring at the Pt electrode during the Li^+ intercalation into Nb_2O_5 coating are described in the references [252-255]:

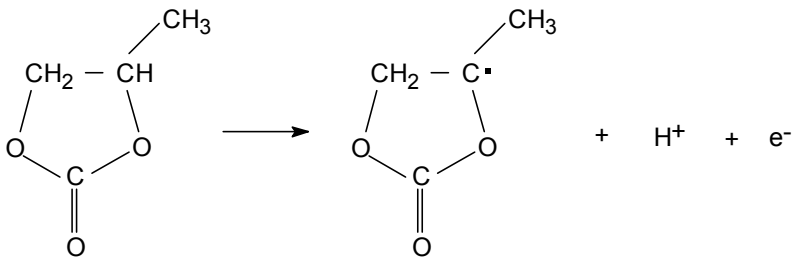

(71)

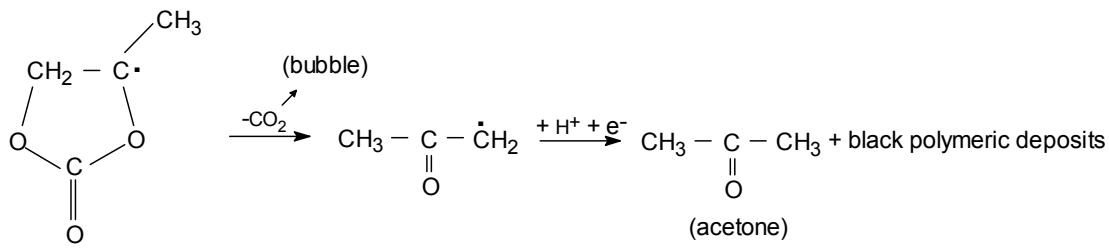

(72)

Initially a radical intermediate forms at the Pt electrode which subsequently decomposes by opening the dioxolane ring and by decarboxylation. Finally acetone and more complex polymeric products are formed. The occurrence of these reactions was verified by the presence of bubbles during the charge-discharge cycles, by the formation of a black deposit on the Pt electrode and the change of colour of the electrolyte initially colourless and which became yellow after 15 cycles. Figure 99 shows the UV-VIS spectrum of the initial electrolyte. A broad band is observed around 270 nm after 15 cycles indicating the presence of acetone as shown by the spectrum of the initial electrolyte to which 0.5 vol.-% of acetone has been added.

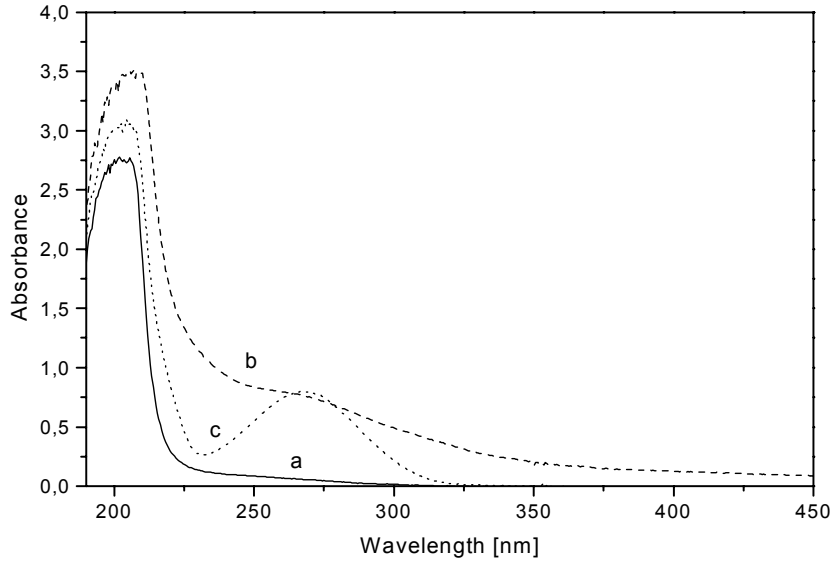

Figure 99: UV-VIS spectra of 1 M $LiClO_4$-PC electrolyte solution (a) before the charge-discharge cycle, (b) after 15th the charge-discharge cycles and (c) 0.5 vol.-% acetone in the electrolyte solution (a).

5.6.2 Influence of film thickness

The charge-discharge curves for Nb_2O_5 + PEG films sintered at 600°C of several thicknesses are shown in figure 100. As seen above, the discharge capacity decreases with the cycle number for all layers. After 15 cycles, the values are 18, 93 and 111 mAh/(g-oxide) for 10.5, 18.2 and 24.4 µm thick films, respectively.

Conclusions

Thick sol-gel coatings can be used to realise secondary lithium batteries. The potential range during the discharge can be adjusted from 3.2 - 2.4 V (coating sintered at 500°C) to 2.6 -1.4 V (coating at 600°C) with capacity up to 250 mAh/g-oxide. However the capacity strongly decreases by repeating the charge-discharge process because of the large amount of Li^+ ions which remains irreversibly into the layer. Nevertheless up to 1000 charge-discharge cycles could be realized when the capacity is limited to 20 mAh/g-oxide. The results are similar to those obtained with 400 µm thick and 13 mm diameter pellets obtained by 49 Mpa

compression molding on a Ni net of a mixture of Nb_2O_5 powder sintered at 600°C and graphite [111]. The advantage of the sol-gel process lies therefore in the possibility to obtained large size flat thin batteries.

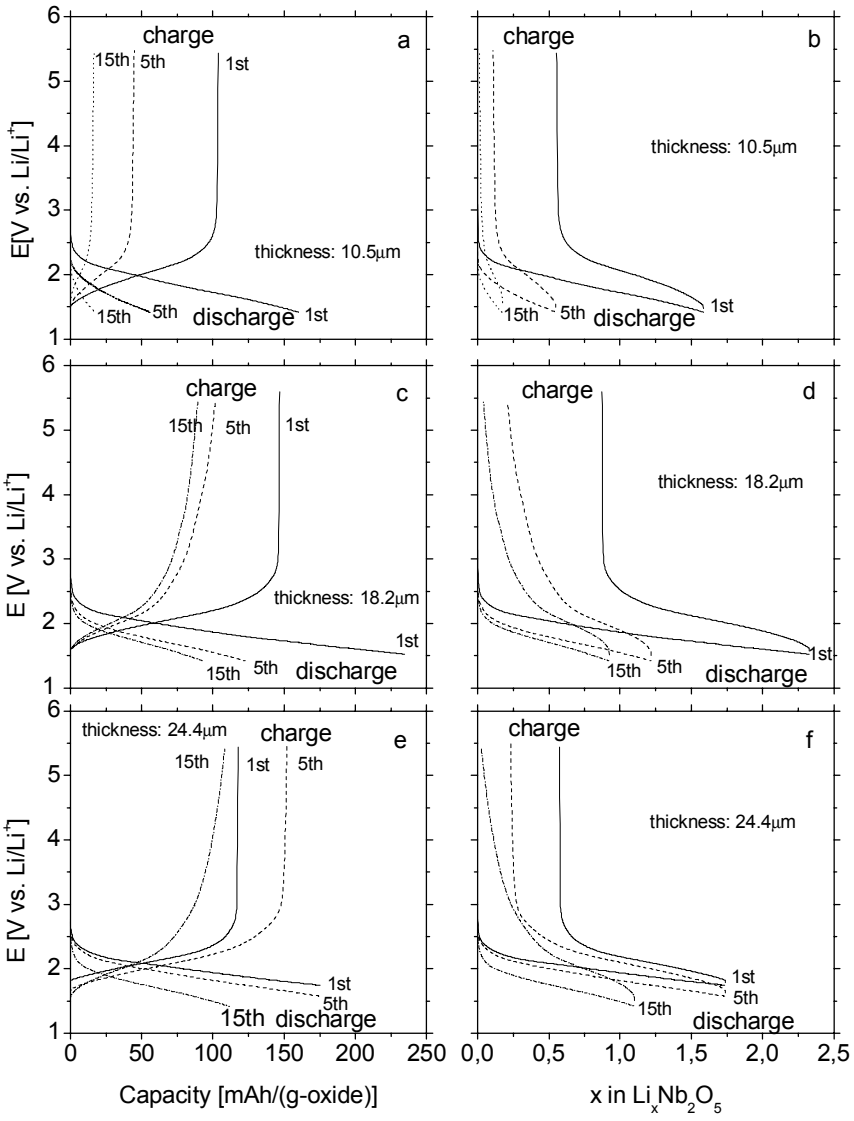

Figure 100: Charge-discharge curves of Nb_2O_5 films with different thickness sintered at 600°C for 30 min. (a, b) 10.5 μm, (c, d) 18.2 μm and (e, f) 24.4 μm. Current density: 0.2 mA/cm^2. Cut-off potential: 1.415 V on discharge, 5.415 V on charge.

5.7 Electrochromic properties of thin Nb_2O_5 electrodes

The electrochromic properties of sol-gel Nb_2O_5 coatings obtained with sols prepared with Nb_2O_5 dissolved in ethanol without addition of water and other additive have been recently and extensively studied at INM [114]. As our sols have a different composition and allow to prepared more porous coating it is worthwhile to present some specific data about the optical and electrochromic properties obtained with thinner coatings (< 200 nm).

5.7.1 Optical properties

Figure 101 shows the transmittance and the reflectance spectra of single layer Nb_2O_5 films prepared by using different sols deposited on FTO glass and then sintered at 520°C for 30 min. The thickness of each coating is of the order of 80 nm. Compared with the FTO coating, the transmission in the visible region slightly decreases by ca. 10%, the reflection in the visible and near IR region increases and the IR reflection above 1760 nm decreases drastically. These results as well as the oscillation observed as a function of the wavelength are due to interference effects.

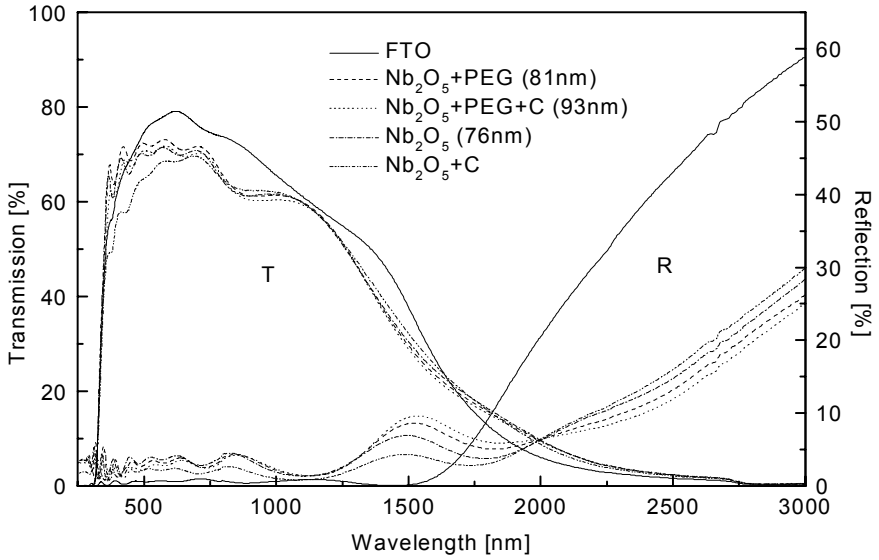

Figure 101: Transmittance and reflectance spectra of thin Nb_2O_5 films prepared by using different sols and deposited on FTO sintered at 520°C for 30 min.

Table 19 gives the refractive index values of the different Nb_2O_5 films (deposited on borosilicate glass) and sintered at 520°C for 30 min. The values are about 2.18 at 550 nm and are independent of the additives used in the preparation of the sols. The values are relatively high for sol-gel layers and lie in the range of values reported for films obtained by evaporation, sputtering, anodisation and CVD [125], i.e. 2.1 to 2.3. This indicates that the porosity of thin niobia coatings is certainly smaller than that of thick coatings.

Table 19: Refractive index of Nb_2O_5 films deposited on borosilicate glass and sintered at 520°C for 30 min, λ = 550 nm.

Sample	Nb_2O_5	Nb_2O_5+PEG	Nb_2O_5+PEG+C
Refractive index	2.16	2.18	2.17

The refractive index increases slightly with increasing sintering temperatures, indicating a decrease of the porosity with the sintering temperature (table 20).

Table 20: Refractive index of Nb_2O_5 films prepared by using the Nb_2O_5+PEG sol and sintered at different temperatures.

Sintering temperature [°C]	400	450	500	550	600	650
Refractive index	2.15	2.14	2.16	2.20	2.19	2.24

5.7.2 Electrochromic properties

Cyclic voltammetry was performed at room temperature on a 1 and a 2 layers Nb_2O_5 /FTO/glass electrodes in a 1 M $LiClO_4$ dissolved in propylene carbonate (PC) electrolyte. Figure 102 shows the cyclic voltammograms of a 81 nm thick single Nb_2O_5 film measured up to 50 cycles. The results are similar to those reported for dip-coated [17, 26] and spin-coated sol-gel pure Nb_2O_5 [160]. The cathodic current related to Li^+ and e^- insertion into the film increases continuously up to the inversion potential (-2.2 V). In the positive voltage sweep the anodic current peak attributed to Li^+ ions extraction appears at -1.5 V. The reduction and oxidation reactions with lithiation (coloration) and delithiation (bleaching) can be represented by equation 69.

During Li^+ ions incorporation into the oxide, Nb^{5+} is reduced to Nb^{+4} by accepting an electron and the film colours [158]. It bleaches and becomes transparent again during the delithiation. The cathodic and anodic charge densities were -3.3 and 3.5 mC/cm^2 for the first cycle and increased to -4.8 and 5.1 mC/cm^2 respectively after 50 cycles. This shows that the electrochemical Li^+ insertion/extraction was practically reversible with these thin films.

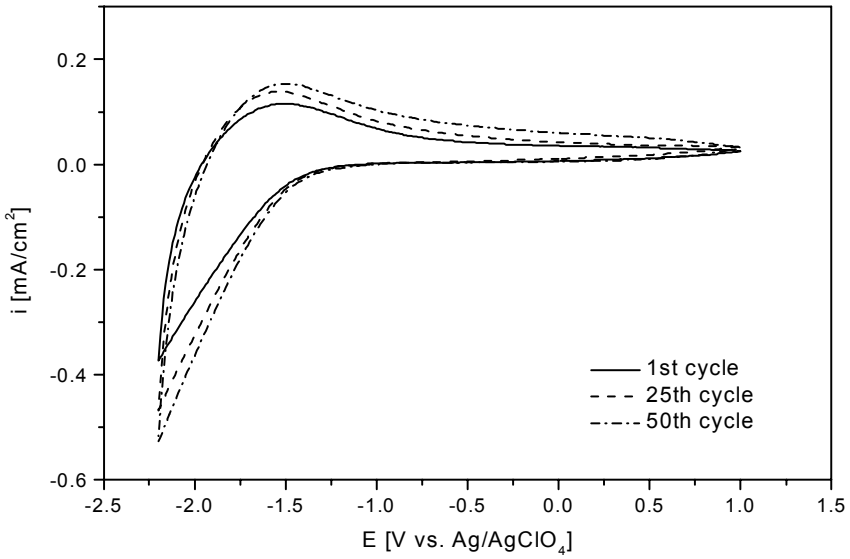

Figure 102: Typical voltammograms of a 81 nm thick Nb_2O_5 film deposited by using the Nb_2O_5+PEG sol on FTO coated glass, sintered at 500°C for 30 min. Electrolyte 1 M $LiClO_4$-PC, sweep rate 50 mV/s.

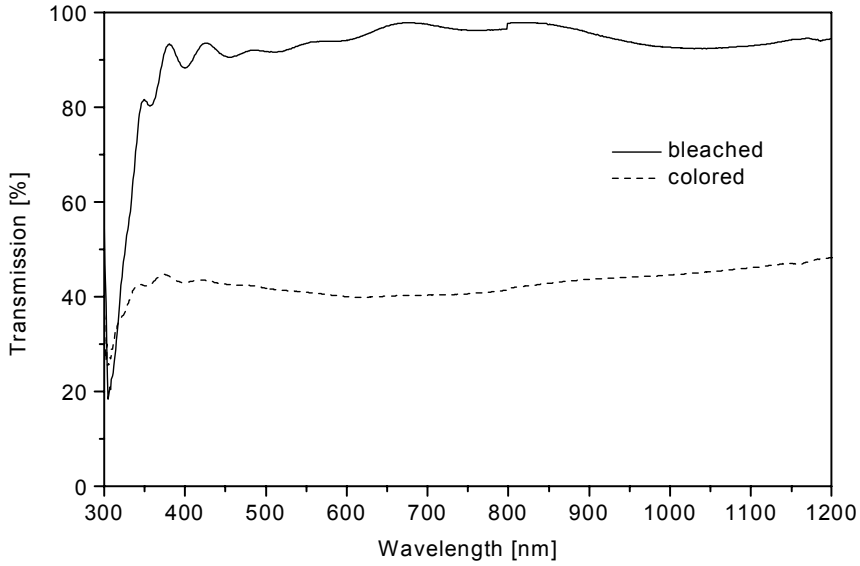

Figure 103: Transmittance spectra of a 2 layer (178 nm) Nb_2O_5 + PEG film on FTO-coated glass electrodes: oxidised (bleached) at 1.0 V and reduced (coloured) at -2.2 V (vs. $Ag/AgClO_4$).

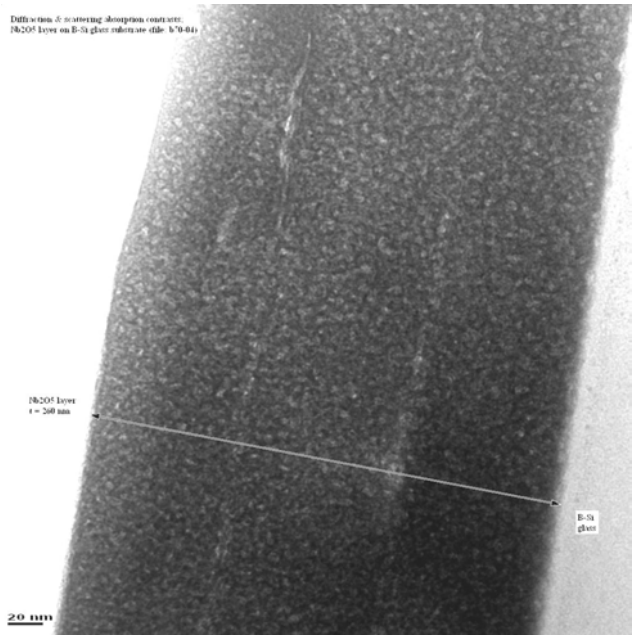

Figure 104: TEM micrograph of three layer niobia coating prepared with additive and sintered at 500°C.

Figure 103 shows the UV-VIS-NIR transmittance spectra of a 178 nm 2 layer thick Nb_2O_5+PEG/FTO glass electrode in the coloured and bleached states. An almost flat decrease in transmittance in the coloured state occurs under applied potential -2.2 V. The colour of the coating was brown-grey while that obtained by Schmitt [114] for a coating sintered at the same temperature was blue. According to the former study such a colour has been observed in pure and doped Nb_2O_5 coatings containing very small particles (< 10 nm). This results is confirmed here (figure 104). The microstructure of thin and thick coatings sintered at the same temperature is therefore quite different. Thin coatings (< 200 nm) contain very small crystallite

particles while thick coatings (> 10 µm) contain much larger particles (about 40 nm). The coloration efficiency and the Li^+ diffusion coefficient of coloration cycle are 15 cm^2/C and 3.9×10^{-10} cm^2/s, respectively. As expected from the low porosity of our thin coatings the coloration efficiency is smaller than that found by Schmitt [114], about 20 cm^2/C.

Figure 105 shows the optical and electrical time response kinetics of Nb_2O_5 film during a coloration and bleaching cycle observed during a 120 s potentiostatic step from 1.0 to -2.2 V and -2.2 to 1.0 V vs. $Ag/AgClO_4$.

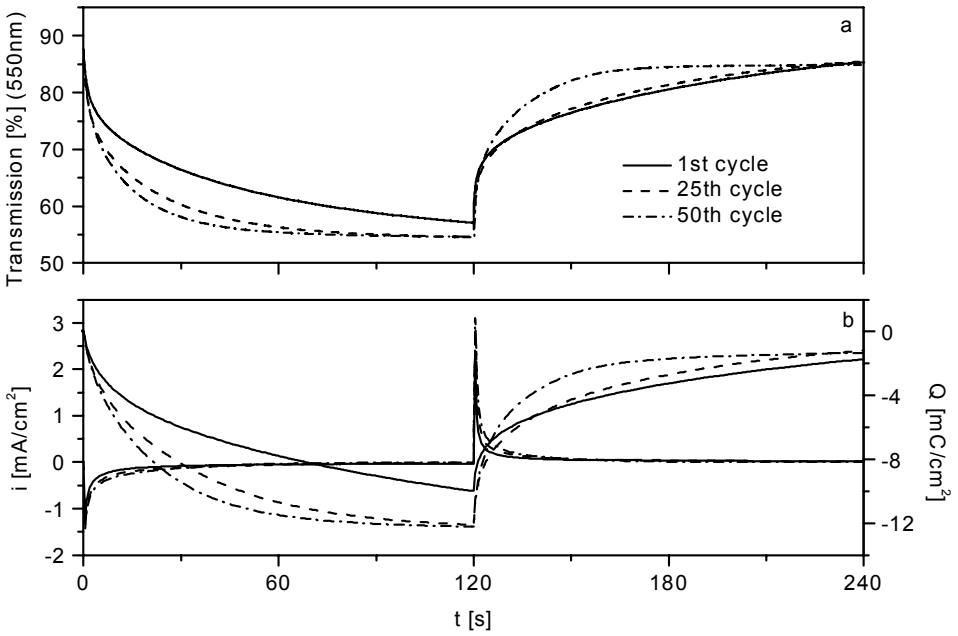

Figure 105: Variation of the transmittance at 550 nm (a), of the current density and the charge density as a function of time (b) for a 81 nm thick Nb_2O_5 film during a potentiostatic step from 1.0 to -2.2 V and -2.2 to 1.0 V vs. $Ag/AgClO_4$.

Table 21 gives the variation of the coloration efficiency and the Li^+ diffusion coefficient for the coloration cycle with the number of cycles. The i-t curves during the coloration follow well a $t^{-0.5}$ dependence, indicating of a Li^+ ions diffusion process across the electrochromic film. The Li^+ injection at the film/electrolyte interface is the rate-determining step [256].

Table 21: The variation of the coloration efficiencies and the Li^+ diffusion coefficients for the coloration cycle calculated from figure 105b.

Number of cycles	0	25	50
η [cm^2/C]	18	17	16
D_o [$\times 10^{-10}$ cm^2/s]	2.4	3.9	4.8

Figure 106 shows the log-log plots of the current density vs. time during the bleaching process. The slope of the plot for the 1st cycle is -0.78, i.e. close to -3/4. A simple diffusion model leads to a $t^{-0.5}$ law. A $t^{-0.75}$ behaviour is representative of a process involving an enhanced migration

of the Li^+ ions through the field developed across the electrochromic films [257]. Therefore, for our electrodes, the Li^+ migration process is dominant in the bleaching process. After 50 cycles the bleaching shows two stages and the slope after 32 s deviates from the -3/4 value and is -2.5. This implies that the bleaching process is more complex than a single migration process.

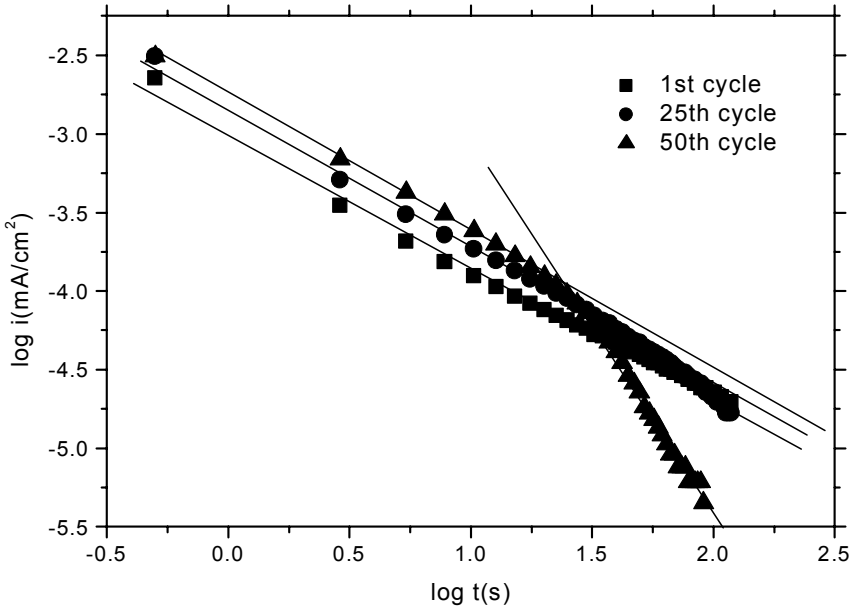

Figure 106: Log-log plots of the bleaching current density vs. time calculated from figure 105b.

The use of sols containing PEG addition has not improved the electrochromic properties of thin optical coatings reported Schmitt [114]. The colouring efficiency of the coating was found even slightly smaller so that further development was not pursued.

6 Summary and perspective

Viscous colloidal Nb_2O_5 solutions suitable for depositing thin and thick niobia films have been synthesised using a cheap $NbCl_5$ as precursor by sol-gel process. A partial hydrolysis of niobium chloroethoxo-acetate obtained by adding a reasonable amount of water leads to a highly viscous and stable solution containing fine colloidal particles. The chemistry of the synthesis process was discussed. A heat treatment of the sols at 96°C (reflux) improves the stability of the sols. PEG as binder provides physically a strong adhesion and mechanical strength of film during drying and sintering processes. On the other hand, its oxygen atoms take place complex reaction with the colloids to release the chloride ions.

Thick Nb_2O_5 coatings have been prepared by sol-gel processes. The morphology and the structure of the coatings were altered by adding polyethylene glycol (PEG) and carbon soot (C) into the sol. All materials start to crystallise at 400°C and the structure consists of single hexagonal phase while the structure of the coating prepared with pure Nb_2O_5 sol consists of hexagonal niobia and Nb_3O_7Cl orthorhombic phases. After sintered at 600°C there is still a very small amount of Nb_3O_7Cl orthorhombic phases in the coating while only Nb_2O_5 orthorhombic phase exists in the coatings prepared with additives. The effect of separation and dispersion of the PEG and the final burn-out of the organic products results in a substantial increase of the surface area and roughness factor which control the amount of dye that adsorbed in the coating. This quantity is directly linked to the enhancement of the light harvesting efficiency (LHE). The specific surface area gradually decreased with the increase of the sintering temperature. The sintering of the coatings alters the pore size distribution, improves the interconnection among the nanocrystallites and the pore shape (from an ink-bottle with narrow necks to a more cylindrical shape) and coarsen the pores. The high specific area, the suitable grain size, a good porosity and the desirable phase composition of the nanocrystalline Nb_2O_5 synthesised with PEG and C in the present work are the properties responsible for the good behaviour of this material used as electrodes in dye-sensitised solar cells. Thermal analysis, infrared spectroscopy, X-ray diffraction and BET surface area analysis have been carried out. The changes of the composition and the microstructure of the compounds have been related to the additives and the heat treatment after preparation. TEM and SEM have confirmed the results. The Nb_2O_5 samples were compared with commercial TiO_2 (P25) supplied by Degussa.

Non-sensitised Nb_2O_5 electrodes exhibit photoelectrochemical properties under UV light irradiation. The band gap of the material was found E_g = 3.06 eV. It was also confirmed that Nb_2O_5 films show a smaller photocataytic effect in the photoelectrolysis of water than TiO_2 coatings.

The photoelectrochemical properties of various Ru(II)-complex sensitised Nb_2O_5 electrodes have been investigated using linear sweep voltammograms and by measuring the photocurrent action spectrum. The additives, the sintering temperature, the film thickness and the type of redox system influence remarkably the photoelectrochemical behaviour of the electrodes. High incident monochromatic photo-to-current conversion efficiency (IPCE) up to 64% at 545 nm have been obtained.

Electrochemical impedance spectroscopy has been also applied to investigate the behaviour of dye sensitised niobia coatings. The Nyquist plots exhibited two semicircles. All the results could be fitted using an equivalent circuit consisting a resistor R_s in series with two circuits containing a resistor and a CPE element in parallel. The values obtained for the electric elements from the simulation were found to depend on the electrode's material, the additives brought into the sol, the sintering temperature of the film, the film thickness and the composition of the electrolyte. The total resistance of the electrolyte and electrode (Nb_2O_5 + TCO) was described by the frequency independent resistor. The first parallel RC circuit at high frequency range was linked to the frequency response of the microstructure of the semiconductor film, the contact property between the film and substrate and the interconnection between the nanocrystallites. The second parallel RC circuit at the low frequency ($f < 1$ kHz) represents the photoelectrochemical property of the dye sensitised electrode, in which R_{ct} stands for a kinetic factor and C_{dl} is a thermodynamic factor.

The photovoltaic performance of solar cells depends strongly on the solvent in the redox system, the geometry of the electrodes and the light intensity. A solar-to-electric efficiency as high as 7% was obtained under 100 W/m^2 illumination but the value continuously decreased for higher intensity. These results are nevertheless better than those reported in the literature. The gradual loss of the conversion efficiency under one sun illumination was interpreted as due to a higher series resistance of the cell and an increase of the rate of the reverse reactions. The efficiency of niobia cells is however lower than those made with TiO_2.

Thick nanocrystalline niobia films have been also studied as Li ion storage electrode for battery. Although they possess a high discharge capacity, the reversibility of the Nb_2O_5 electrode is poor, and only a small amount of the initial discharge capacity could be recovered through a recharging process. It was shown however that the discharge capacity could be controlled by setting a cut-off potential for the discharge. At a lower capacity the Nb_2O_5 films show however a good reversibility up to 1000 cycles.

Thin transparent Nb_2O_5 films have also been prepared by a spinning technique using a Nb_2O_5 + PEG20000 sol and their electrochromic properties have been determined. The lithiation and delithiation process in 1 M $LiClO_4$-PC solution resulted in reasonable changes of the optical transmittance (ΔT_{550nm} = 41%). The study of the kinetics of the coloration and bleaching processes showed that the Li^+ injection at the film/electrolyte interface is the rate-determining step during the coloration, while the Li^+ migratory or a more complex process is responsible

for the bleaching. However no better results as those already published in the literature have been obtained.

Nb_2O_5 is presently the second best material to build Graetzel's type solar cells. Extrapolating the results reported in this work, a constant efficiency of about 7% up to one sun irradiation could be expected if a more adequate cell's geometry is used, e.g. a 0.5×0.5 cm² and a well chosen electrolyte.

Improvement can also be expected if larger pore size can be obtained and by using better dyes, such as the so-called black dye. However even if comparable efficiency is obtained, TiO_2 still remains the best material for such application due to its low price.

However, the price of the nano-TiO_2 is only 7% [195] of the total cost of the materials. As TiO_2 cells should be protected against UV irradiation (special glass or filter) and as Nb_2O_5 present a lower photocatalytic behavior (section 5.4.1), it is believed that niobia can still be considered as a promising system for large size individual cells or modules.

7 Appendix

A1 List of chemicals and substrates

Table 22: Name, formula, molecular weight (M. W.), purity, and supplier of the chemicals used.

Name	Formula	M. W. [g/mol]	Purity	Supplier
Acetic acid	CH_3COOH	60.05	>99%	Fluka
Acetone	CH_3COCH_3	58.08	≥99.0%	Fluka
Acetonitrile	CH_3CN	41.05	≥99.5%(GC)	Kluka
Anhydrous lithium iodide	LiI	133.84	≥98%(AT)	Fluka
Anhydrous lithium perchlorate	$LiClO_4$	106.39	99%	Chempur
2,2´-Bipyridine-4,4´-dicarboxylic acid	$COOH(C_5H_3N$-$C_5H_3N)COOH$	244.2		Alfa
Carbon soot	C	12.01		Aldrich
Cesium iodide	CsI	259.81	≥99.5%	Riedel-de Haen
De-ionised water	H_2O	18.02		INM
Diethylether	$C_2H_5OC_2H_5$	74.12		Fluka
(DMF) N,N-Dimethylformamid	$HCON(CH_3)_2$	73.1	≥99.9%(GC)	Fluka
Ethanol	C_2H_5OH	46.07	≥99.8%	Merck
Iodine	I_2	253.81	≥99.8%(RT)	Fluka
Niobium(V) chloride	$NbCl_5$	270.18	99+%	Chempur
P25	TiO_2	79.9		Degussa
Perchlore acid	$HClO_4$	100.46	≥60(T)	Fluka
Polyethylene glycol	$HO(C_2H_4OC_2H_4)_nOH$	570-630		Fluka
Polyethylene glycol	$HO(C_2H_4OC_2H_4)_nOH$	16000-24000		Fluka
Potassium iodide	KI	166.01	>99%	Fluka
Propylene carbonate	$C_4H_6O_3$	102.09	≥99(GC)	Fluka
Ruthenium(III) chloride hydrate	$RuCl_3 \bullet xH_2O$	207.43+aq	41.19 Ru-%	Heraeus
Sodium hydroxide	NaOH	40	≥98%(T)	Fluka
Sodium thiocyanate	NaSCN	81.07	≥98%(AT)	Fluka
Sulphuric acid	H_2SO_4	98.08	95-97%	Fluka
Tetrabutylammonium iodide	$(CH_3CH_2CH_2CH_2)_4N(I)$	369.38	≥98%(AT)	Fluka
Tetrapropylammonium iodide	$(CH_3CH_2CH_2)_4N(I)$	313.27	≥98%(AT)	Fluka

Table 23: Purposes of the used substrates

Substrate	Size [mm]	Thickness [mm]	Purpose
FTO (TEC-8)/glass	40 × 50	3	dye-sensitised, photoelectrochemical, Li ion storage and electrochromic electrodes, dye absorption and desorption, SEM and TEM
ITO/glass	40 × 50	1	dye-sensitised and electrochromic electrodes
Borosilicate glass	40 × 40	2	XRD, TEM and SEM
AF45®	40 × 40	0.4	Nitrogen adsorption, dye absorption and desorption

A2 List of equipment

Table 24: Equipment used in the research

Apparatus/measurement	Model	Producer
Centrifuge	Hermel Z 323	Jochen Thieme
Coating-XRD	x´Pert MAD	Philips
Digital Camera	C-2000 Z	Olympus
Drying furnace	UT 6060	Heraeus
DTA-TG	QMS 420	Netzsch
FTIR-spectroscopy	IFS 66V	Bruker
Glove box	2201-C	Mecaplex
Heat treatment furnace	K 750/1	Heraeus
High temperature oven	L3/R	Nabertherm
HRTEM	CM 200 FEG	Philips
Impedance analyzer	IM6d	Zahner Elektrik
Light source	SVX 1530	Müller Elektrik Optik
Light source	100 W tungsten-halogen lamp	Oriel
Monochromator	Spex 270M	Jobin Yvon-Spex
N_2 adsorption-desorption	ASAP 2400	Micromeritics Instrument Corp.
PCS	ALV/DLS-5000	ALV-Laser Vertriebgesellschaft m.b.H.
Potentiostat	LB 94	Bank
Potentiostat/Galvanostat	273A	EG&G PAR
Powder-XRD	D 500	Siemens
Profilometer	P-10 Surface Profiler	Tencor
Refrigerator		Liebherr
Rinsing machine	Professional IR 6001	Miele
Rotary evaporator	WB2000	Heidolpy
Scanning white light	New view 100 system	Zygo

interferometer		
SEM	JSM 6400F	JEOL
Solar simulator	SP81160-1452	Oriel
Spectrophotometer	Cary 5E	Varian
Spin coater	1001, CPS II controller	Convac
Sputter system	TPG 300	Balzers
Termopile detector	2A-SH, NOVA-display	Ophir Optronics
Ubbelohde viscometer	AVS 410	Schott
Ultrasound	XL2020	Misonix
Vacuum drying furnace	VTR5036	Heraeus

A3 Synthesis of the dye ruthenium *cis*-di(thiocyanato)-N,N´-*bis*(2,2´-bipyridyl-4,4´-dicarboxylic acid) complex

cis-$RuL_2Cl_2 \bullet 2H_2O$ (L = 2,2´-bipyridyl-4,4´-dicarboxylate) was obtained by refluxing under nitrogen atmosphere 0.515 g (2 mmol) of $RuCl_3 \bullet xH_2O$ and 1.026 g (4.2 mmol) of 2,2´-bipyridine-4,4´-dicarboxylic acid (L) in 200 ml of N,N-dimethylformamid (DMF) for 8 h. After cooling, the traces of RuL_3 were filtered. Most of the DMF solvent was evaporated under 20-25 mbar at 70°C, and *cis*-RuL_2Cl_2 was precipitated with acetone. The crystals were filtered off , washed two times with acetone and dried in vacuum at 40°C for 4 h. 0.921 g of $RuL_2Cl_2 \bullet 2H_2O$ was obtained. The structure is given in figure 107.

cis-di(thiocyanato)-N,N´-*bis*(2,2´-bipyridyl-4,4´-dicarboxylic acid)-ruthenium(II) dihydrate, $RuL_2(NCS)_2 \bullet 2H_2O$ was synthesised as follows. 0.0.921 g (1.3 mmol) $RuL_2Cl_2 \bullet 2H_2O$ was dissolved in 90 ml DMF. To this solution was added 60 ml of 0.1 M aqueous NaOH in order to deprotonate the carboxy groups. 1.061 g (13.1 mmol) of sodium thiocyanate was dissolved in 5 ml of H_2O and subsequently added to the above solution. The reaction mixture was then heated to reflux for 6 h under nitrogen atmosphere, under magnetic stirring was maintained. After this time, the reaction mixture was allowed to cool, and the solvent was removed in a rotary evaporator under 20-25 mbar at 60-70°C. The resulting solid was dissolved in 50 ml of H_2O and filtered through a 1.2 µm polymer filter. The pH of this filtrate was lowered to 2 by adding dilute $HClO_4$, and the filtrate was placed in a refrigerator overnight. After reaching room temperature, the crystalline solid was separated from solvent by a centrifuge (model Hermle Z323) at 5000 rpm for 4 min. The solid was washed well with pH 2.9 $HClO_4$ aqueous solution two times and with 20 ml of acetone-ether solution (1:10) and then dried in vacuum at 50°C for 6 h. 0.8 g of $RuL_2(NCS)_2 \bullet 2H_2O$ was obtained. The structure is given in figure 107.

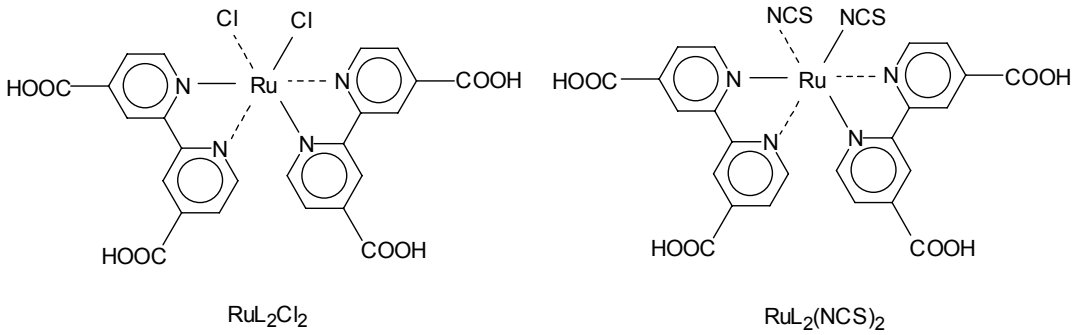

Figure 107: Structure of RuL_2Cl_2 and $RuL_2(NCS)_2$.

A4 Further thermal analysis results

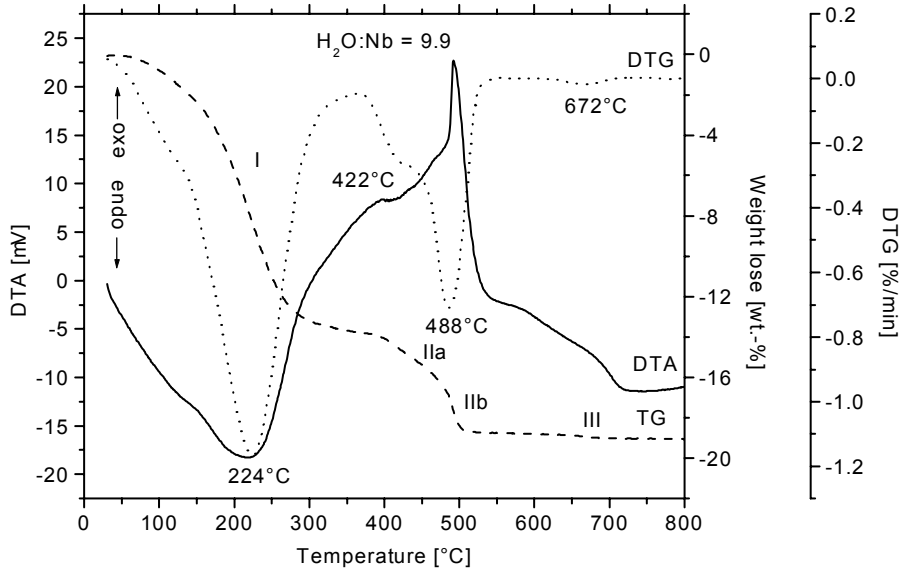

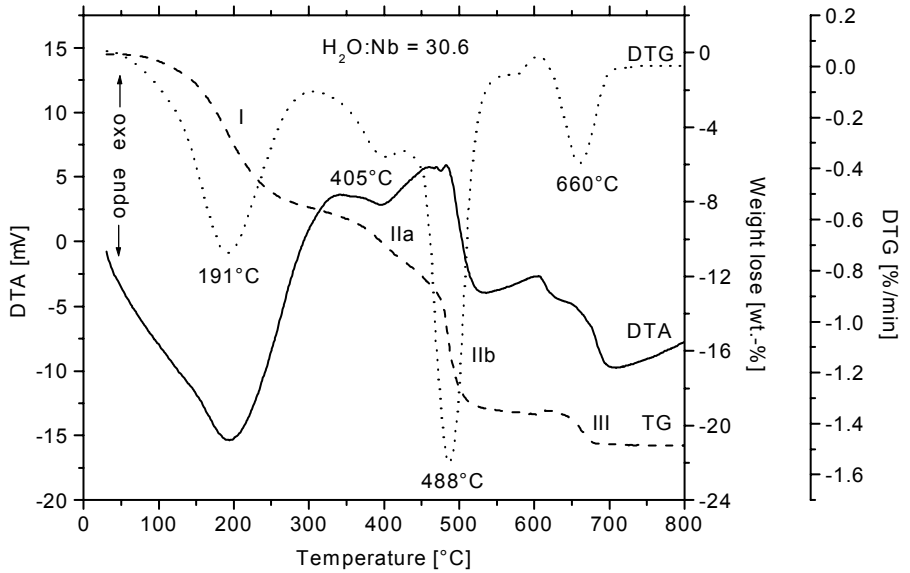

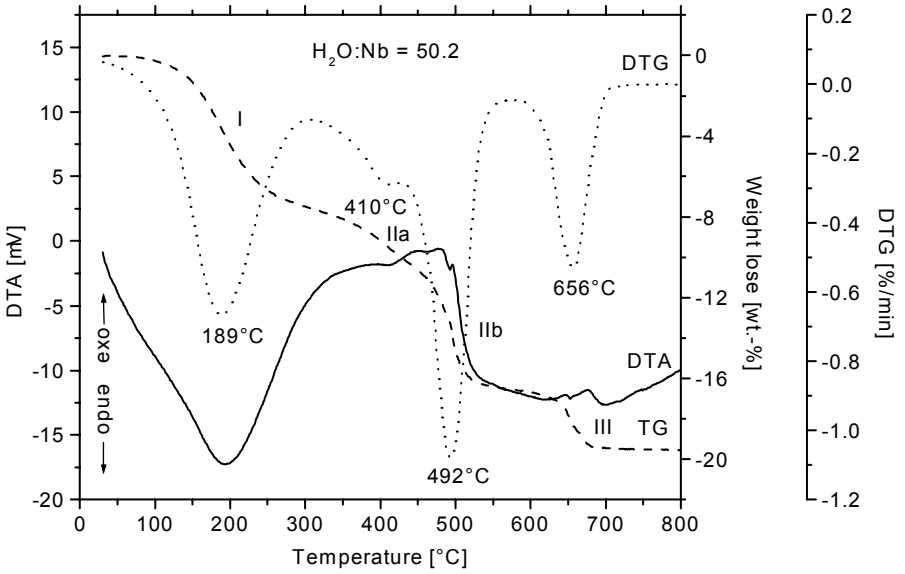

Figure 108: DTA/TG/DTG of Nb_2O_5 xerogels prepared with different H_2O:Nb molar ratio.

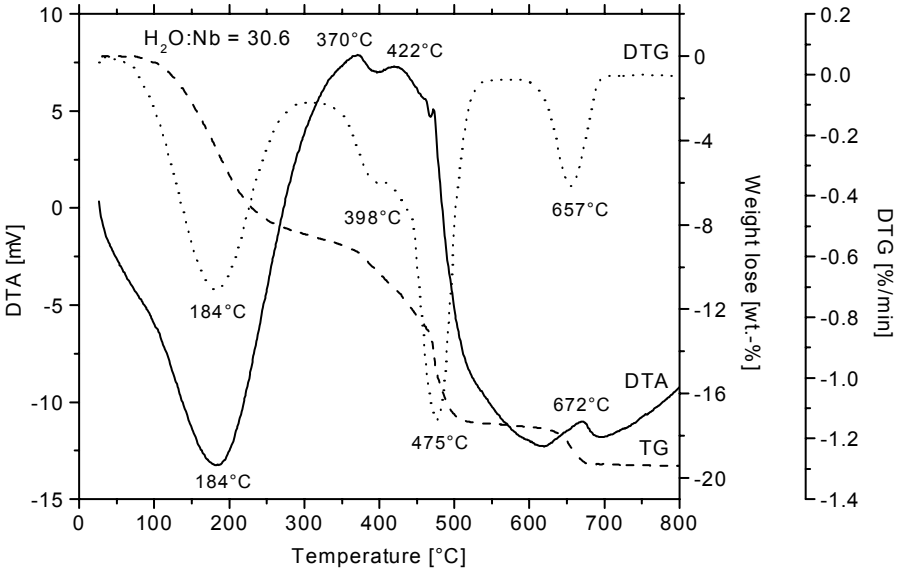

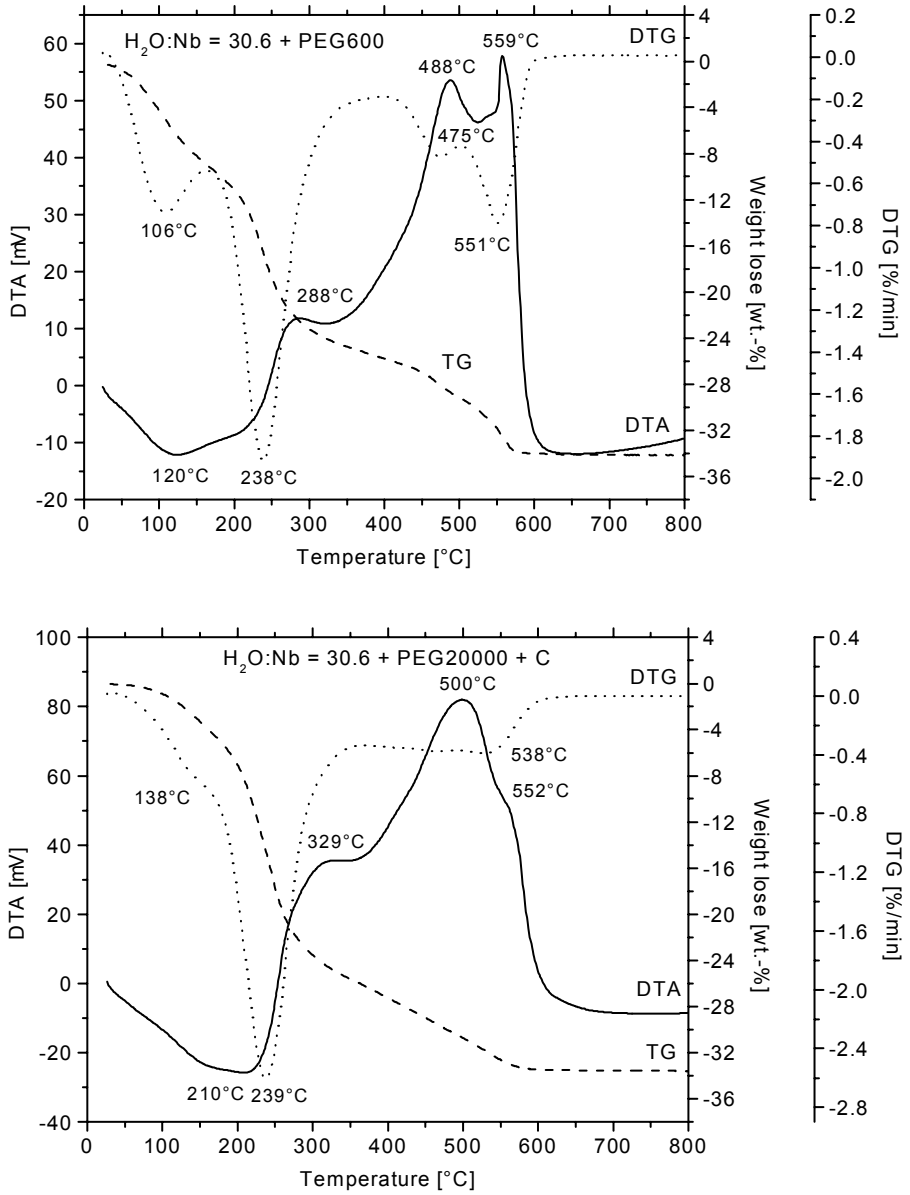

Figure 109: DTA/TG/DTG of Nb_2O_5 xerogels prepared by hydrolysis and without and with additives.

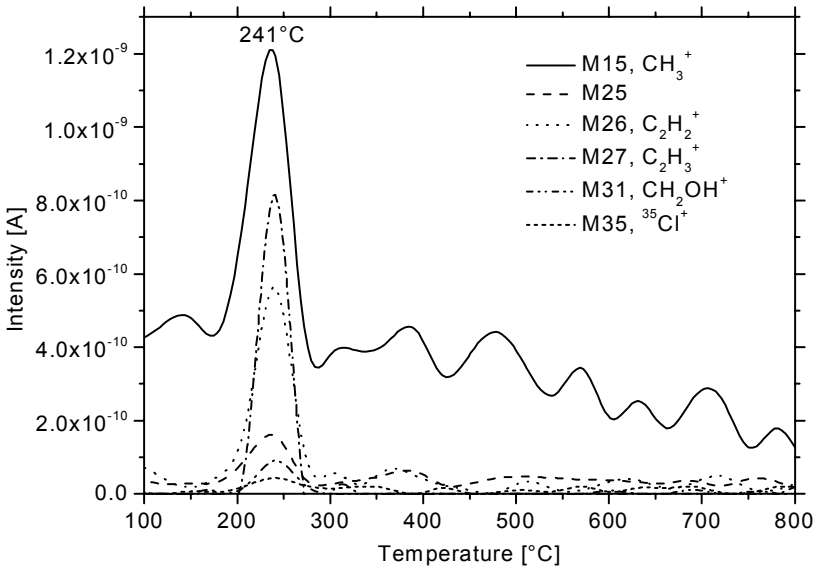
241°C
M15, CH_3^+
M25
M26, $C_2H_2^+$
M27, $C_2H_3^+$
M31, CH_2OH^+
M35, $^{35}Cl^+$
Intensity [A]
Temperature [°C]

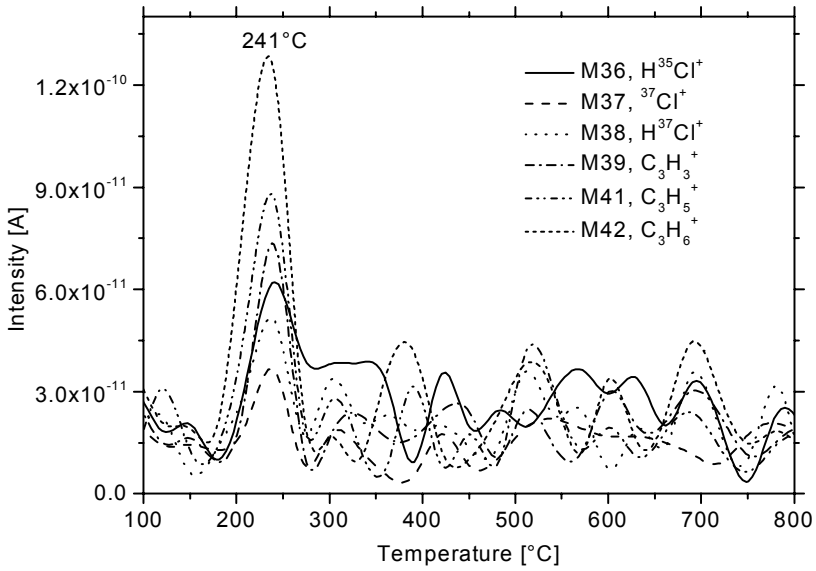
241°C
M36, $H^{35}Cl^+$
M37, $^{37}Cl^+$
M38, $H^{37}Cl^+$
M39, $C_3H_3^+$
M41, $C_3H_5^+$
M42, $C_3H_6^+$
Intensity [A]
Temperature [°C]

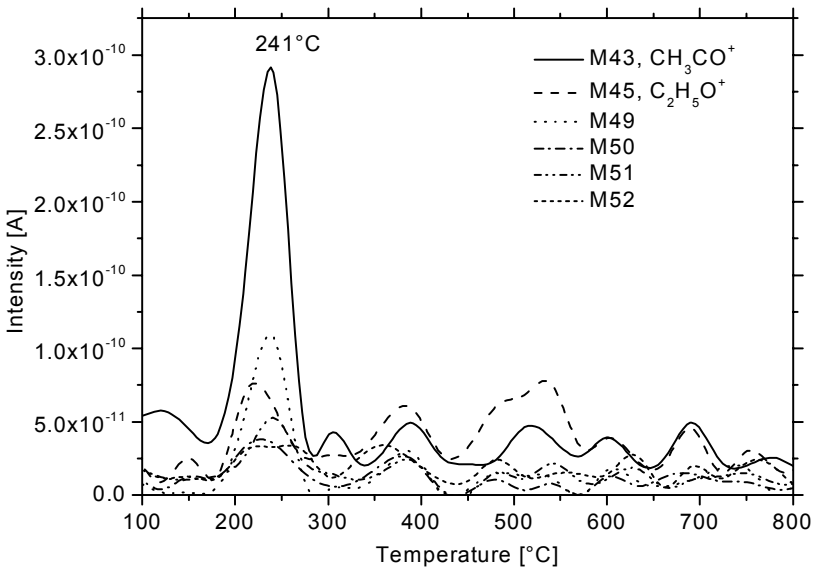
241°C
M43, CH_3CO^+
M45, $C_2H_5O^+$
M49
M50
M51
M52
Intensity [A]
Temperature [°C]

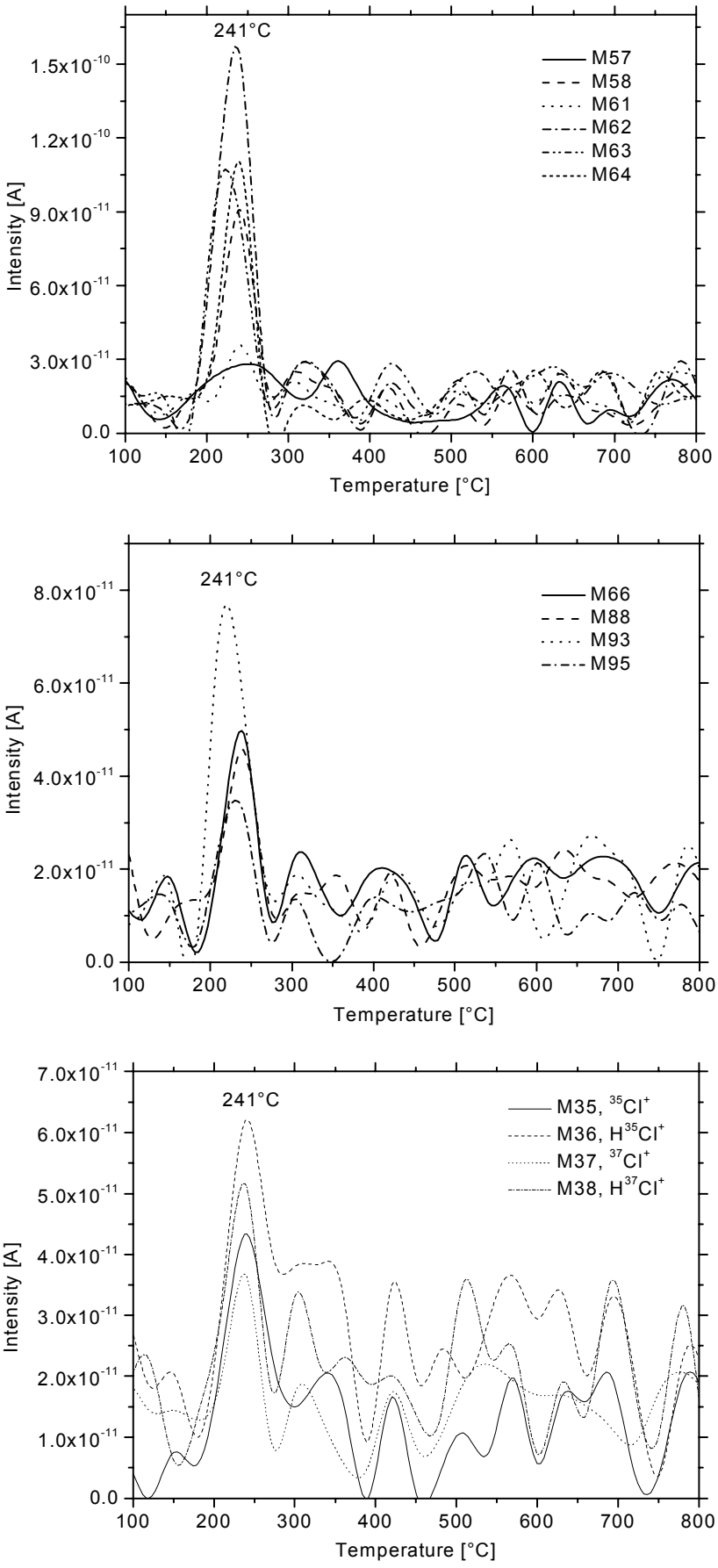

Figure 110: Mass spectroscopy of the Nb_2O_5 xerogel (H_2O:Nb = 30.6, 20 wt.-% PEG20000) analysed during the DTA/TG run of figure 42.

A5 Further infrared spectroscopy spectrum

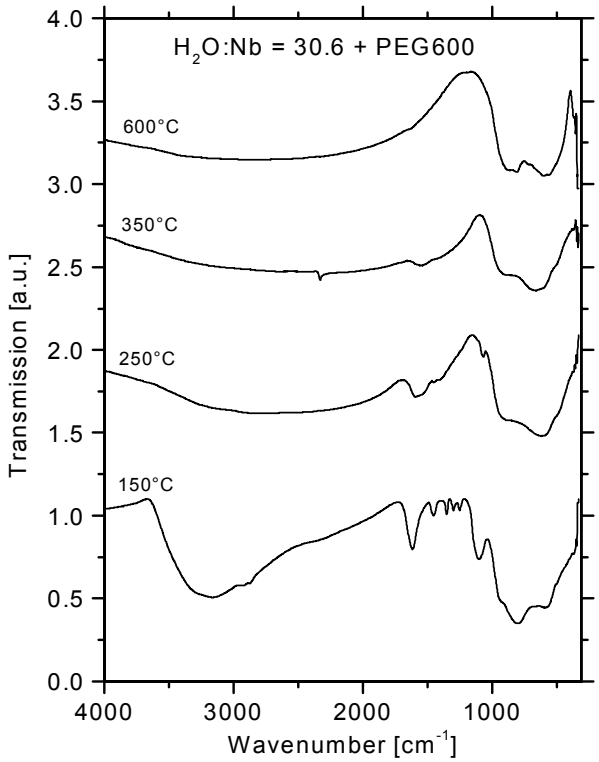

Figure 111: Infrared spectra of hydrolysed Nb_2O_5 xerogel (H_2O:Nb = 30.6) with 20 wt.-% PEG600 heat treated at different temperature.

A6 Further X-ray diffraction datum

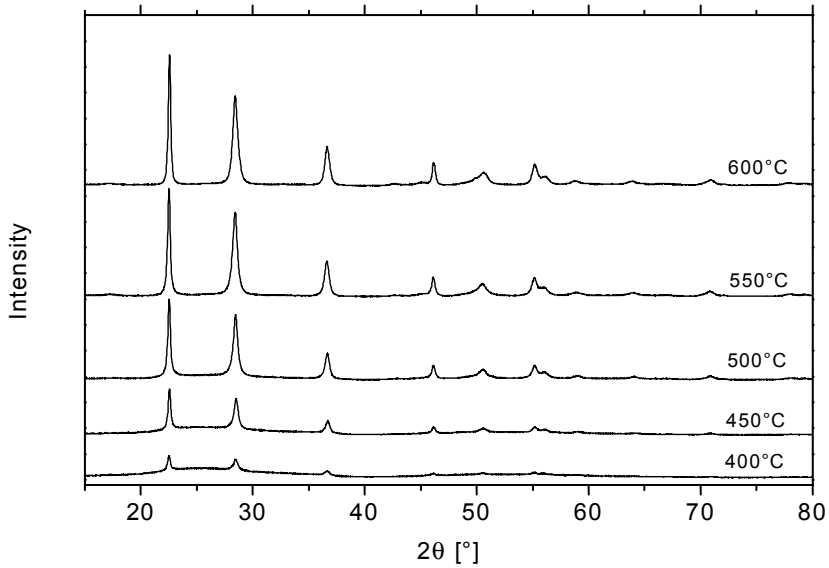

Figure 112: X-ray diffraction patterns of Nb_2O_5 coatings (H_2O:Nb = 30.6, 20 wt.-% PEG600) sintered at different temperature.

A7 Further nitrogen adsorption and desorption

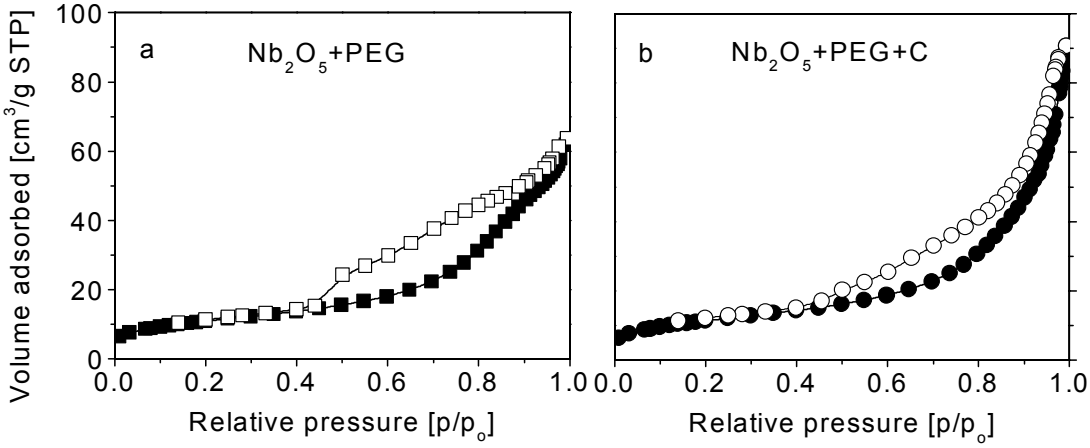

Figure 113: N_2-adsorption and desorption isotherms of Nb_2O_5 xerogels with additives sintered at 500°C. Solid symbols: adsorption; open symbols: desorption.

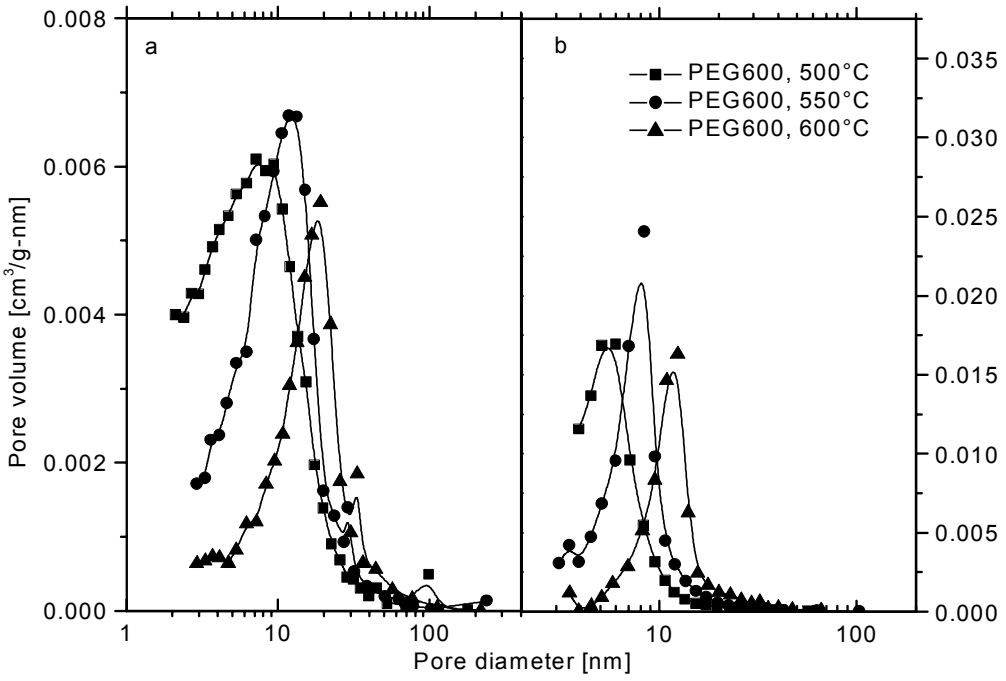

Figure 114: Pore volume distribution of Nb_2O_5 coating prepared with PEG600 binder sintered at different temperature. Calculated from adsorption data (a) and desorption data (b).

Table 25: Influence of the sintering temperature on microstructural characteristics of Nb_2O_5 coatings prepared with PEG600 binder.

Sintering temperature [°C]	500	550	600
BET surface area [m^2/g]	42.6	36.2	24.6
Total pore volume [$\times 10^{-2}$ cm^3/g]	9.5	10.8	10.5
Micropore volume [$\times 10^{-2}$ cm^3/g]	0	0	0
Average pore diameter [nm]	8.9	11.9	17.1
BJH adsorption average pore diameter (4 V/A) [nm]	8.2	11.1	16.6
BJH desorption average pore diameter (4 V/A) [nm]	5.5	8.2	12.1
Porosity [%]	32	35	34
Average particle size [nm]	255	31.3	52.2

A8 Further electrochemical impedance spectroscopy

Influence of the sintering temperature

Table 26: Values obtained for the elements of the equivalent circuit from the simulation of impedance data of dye sensitised solar cell made with 10 µm thick Nb_2O_5-electrodes sintered at different temperatures in the dark (at open circuit potential and using electrolyte No. 3).

T_{sinter}	OCV	R_s	R_{sc}	CPE1		R_{ct}	CPE2	
[°C]	[V]	[Ω]	[Ω]	C_{sc} [µF]	n	[Ω]	C_{dl} [mF]	n
500	-0.703	14.5	105	7.1	0.56	61.5k	0.049	0.98
550	-0.791	12.4	24	5.0	0.73	57.7k	0.049	0.99
600	-0.680	14.2	11	5.6	0.91	52.8k	0.040	0.93

Table 27: Same as table 26 but measured under 100 W/m^2 illumination.

T_{sinter} [°C]	OCV [V]	R_s [Ω]	R_{sc} [Ω]	CPE1		R_{ct} [Ω]	CPE2	
				C_{sc} [µF]	n		C_{dl} [mF]	n
500	-1.225	11.7	11	3.4	0.93	8.3	3.9	0.81
550	-1.247	14.9	8	5.1	0.96	7.6	7.1	0.83
600	-1.252	13.2	9	4.8	0.96	7.6	8.2	0.85

Influence of the solvent in the electrolyte

Table 28: Values obtained for the circuit elements of the equivalent circuit from the simulation of the impedance data of a dye sensitised solar cell made with an electrolyte containing different amount of PC in ACN (in the dark), The electrolyte No. are defined in table 3.

Electrolyte No.	OCV [V]	R_s [Ω]	R_{sc} [Ω]	CPE1		R_{ct} [kΩ]	CPE2	
				C_{sc} [µF]	n		C_{dl} [µF]	n
1	-0.666	4.51	19	5.5	0.77	208	39	0.98
2	-0.636	7.5	15	6.1	0.78	165	23	0.90
3	-0.791	12.4	24	5.0	0.73	58	49	0.99
4	-0.767	14.4	32	3.0	0.78	94	21	0.90

Table 29: Same as table 28 but Values obtained for the circuit elements of the equivalent circuit from the simulation of the impedance data of figure 115.

Electrolyte No.	OCV [V]	R_s [Ω]	R_{sc} [Ω]	CPE1		R_{ct} [Ω]	i_o^{ph} [mA/cm^2]	CPE2	
				C_{sc} [µF]	n			C_{dl} [mF]	n
1	-1.282	4.5	11	4.0	0.92	76	0.03	0.04	0.67
2	-1.268	7.7	9	4.3	0.95	6.7	0.38	4.9	0.84
3	-1.247	14.9	8	5.1	0.96	7.6	0.34	7.1	0.83
4	-1.331	17.7	14	2.7	0.96	12.6	0.20	1.6	0.86

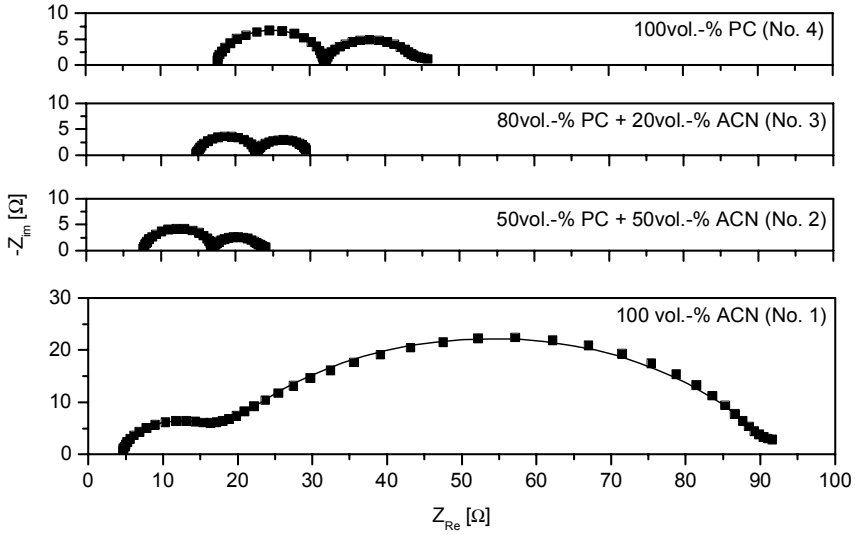

Figure 115: Impedance spectra of the dye sensitised Nb_2O_5-electrode using different amount of PC in ACN at open circuit potential and under 100 W/m^2 illumination.

Influence of the cations in the redox system

Table 30: Values obtained for the circuit elements of the equivalent circuit from the simulation of the impedance data of figure 116, The electrolyte No. are defined in table 3.

Electrolyte	V_{oc}	R_s	R_{sc}	CPE1		R_{ct}	i_o^{ph}	CPE2	
No.	[V]	[Ω]	[Ω]	C_{sc} [µF]	n	[Ω]	[mA/cm^2]	C_{dl} [mF]	n
5	0.468	11	10	3.7	0.95	4.3	0.59	20.5	0.87
3	0.503	8.3	12	3.2	0.95	4.8	0.54	20.6	0.88
6	0.578	14.5	19	2.3	0.92	4.8	0.54	17.0	0.91

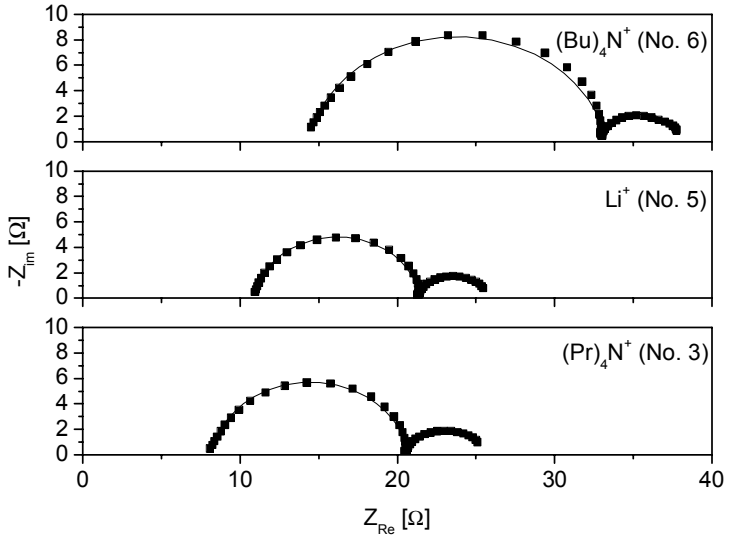

Figure 116: Impedance spectra of the dye sensitised Nb_2O_5-electrode using different cation in the redox system at open circuit potential and under 100 W/m^2 illumination.

Influence of additives

Table 31: Values obtained from the simulation for the elements of the equivalent circuit of the impedance data of the dye sensitised solar cell made with the Nb_2O_5-electrodes prepared with and without additive sintered at 550°C. Electrolyte: No. 3.

Additive	I_{inc}	OCV[1]	R_s	R_{sc}	CPE1		R_{ct}	i_o^{ph}	CPE2	
	[W/m²]	[V]	[Ω]	[Ω]	C_{sc} [µF]	n	[Ω]	[mA/cm²]	C_{dl} [mF]	n
without	dark	-0.753	11.0	26	1.94	0.85	49.1k		0.05	0.96
PEG[2]	dark	-0.869	11.0	23	2.74	0.88	8.6k		0.04	0.77
without	100	-1.238	12.4	22	1.83	0.92	8.0	0.32	9.0	0.86
PEG	100	-1.193	10.4	23	2.66	0.89	4.8	0.54	11.9	0.73
without	325	-1.299	10.8	29	1.40	0.90	3.3	0.79	9.2	0.78
PEG	325	-1.236	10.4	24	2.51	0.89	2.4	1.07	13.7	0.64

1: open circuit potential vs. $Ag/AgClO_4$. 2: PEG: polyethylene glycol MW = 20000

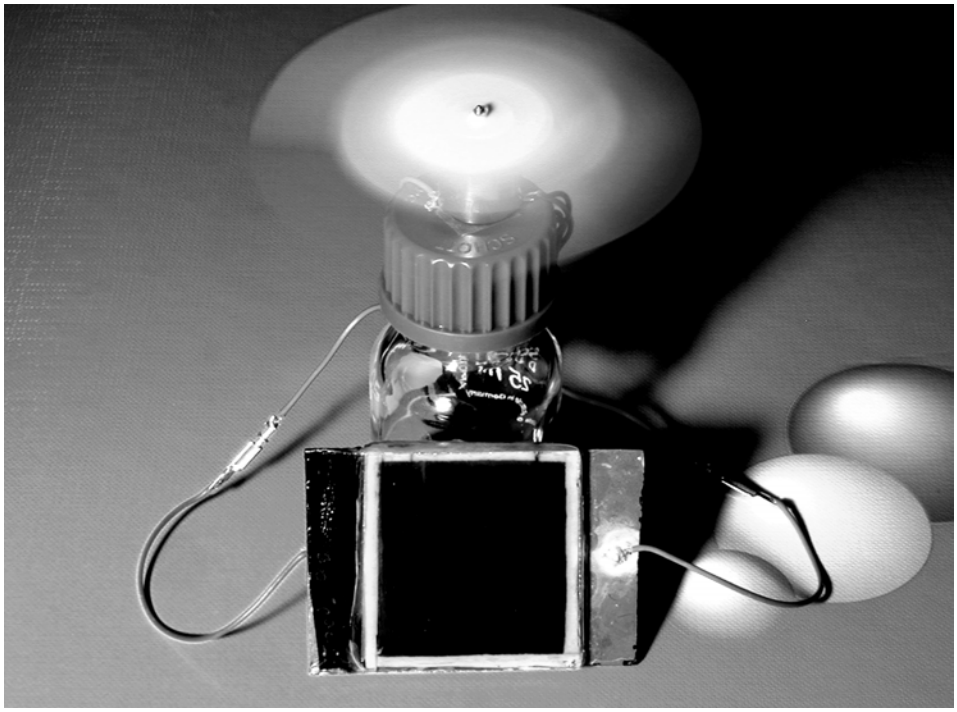

Figure 117: A photograph of a dye sensitised Nb_2O_5 solar cell.

A9 Publication and presentation of this research work

1998

- Y. P. Guo, S. Heusing, M. A. Aegerter, "Photovoltaic energy conversion in dye sensitised nanocrystalline Nb_2O_5 solar cell", in Proc. International Conference on Glass ICG XVIII, San Francisco, July 5-10, 1998 (CD-ROM).
- Y. P. Guo, S. Heusing, M. A. Aegerter, "Photovoltaic energy conversion in dye sensitised nanocrystalline Nb_2O_5 solar cell", in Kurzreferate 72 Deutsche Glastechnische Tagung 25-27.05.1998, Münster, 96-99 (Germany).
- Y. P. Guo, M. A. Aegerter, "Photovoltaic energy conversion in dye sensitised nanocrystalline Nb_2O_5 solar cell", Abstract and Poster presented at the 12th International conference on Photochemical Conversion and Storage of Solar Energy (IPS-12), 09. - 14.08.1998, Berlin.

1999

- Y. P. Guo, M. A. Aegerter, "Ru(II)-sensitised Nb_2O_5 solar cell made by the sol-gel process", in Proc. of the 2nd International Conference on Coatings on Glass, September 06-10, 1998, Saarbrücken (Germany), and Thin Solid Films 351 (1999), 290-294.
- Y. P. Guo, S. Heusing, M.A. Aegerter, "Photovoltaic energy conversion in dye sensitised nanocrystalline Nb_2O_5 solar cell", in 9th CIMTEC-World Forum on New Materials Symposium VII - Innovative Materials in Advanced Energy Technologies (Faenza, Italy), P. Vincenzini (Ed.) Techna Sr., 1999, 585-595.
- Y. P. Guo, M. A. Aegerter, "Effect of Nb_2O_3-Electrode Microstructure on the Efficiency of Nanocrystalline Dye-Sensitised Solar Cells", Abstract and Poster presented at the 10th Internaional Workshop on Glasses, Ceramics, Hybrids and Nanocomposites form Gels, 19-24. Sept. 1999, Yokohama Symposia, Japan.

2000

- Y. P. Guo, M. A. Aegerter, "Nanocrystalline sol-gel Nb_2O_5 films for photovoltaic energy conversion", in K. Grassie(Ed.): Functional Materials, Wiley-VCH, Weinheim, 2000, 250-255 (Proc. of the EUROMAT 99; Vol. 13).

2001

- M. A. Aegerter, M. Schmitt, Y. P. Guo, "Sol-gel niobium pentoxide coatings: Applications to photovoltaic energy conversion and electrochromism", in Proceedings of the conference Solar Energy and Applied Photochemistry SOLAR 01, 03. - 08. April 2001, Cairo/Egypt. In International Journal of Photoenergy, 4(1), 1-10, 2002.

2002

- Y. P Guo, S. Heusing, M. A. Aegerter, "Characterization of non-sensitized and Ru(II)-sensitized sol-gel Nb_2O_5 electrodes by impedance spectroscopy", in Proceesings of SPIE Sol-Gel Optics VI, Seattle, USA, 7.-11. Juli 2002, SPIE Vol. 4804 (2002) 34-43.

8 References

[1] K. Emery, *Mat. Res. Soc. Bull.* **6** (1994), 64-66.

[2] Y. Kuwano, *Adv. Mater.* **9** (1997), 295-297.

[3] K.I. Chopra, S.R. Das, *Thin film solar cells*, Plenum Press. New York, 1983.

[4] D. Meissner, *Solarzellen: Physikalische Grundlagen und Anwendungen in der Photovoltaik*, Vieweg Verlag, 1993.

[5] M. Grätzel, *Comments Inorg. Chem.* **12** (1991), 93-111.

[6] M. Grätzel, *Stud. Phys. Theor. Chem.* **78** (1992), 95-109.

[7] B. O´Regan, M. Grätzel, *Nature (London)* **353** (1991), 737-740.

[8] M. Grätzel, *Mat. Res. Soc. Bull.* (1993), 61-66.

[9] A.J. McEvoy, M. Grätzel, *Sol. Energy Mater. Sol. Cells* **32** (1994), 221-227.

[10] M. Grätzel, *J. Sol-Gel Sci. Technol.* **2** (1994), 673-677.

[11] M. Grätzel, *Chem.-Ing.-Tech.* **67** (1995), 1300-1305.

[12] M. Grätzel, *Proc. - Indian Acad. Sci., Chem. Sci.* **107** (1995), 607-619.

[13] K. Kalyanasundaram, M. Grätzel, *Coord. Chem. Rev.* **77** (1998), 347-414.

[14] M. Grätzel, *Prog. Photovolt. Res. Appl.* **8** (2000), 171-185.

[15] G. Chmiel, J. Gehring, I. Uhlendorf, D. Jestel, *Proceeding of 14th European PV Solar Energy Conference* (Vienna), (1998), 53.

[16] *PV Insider´s Report*, 29 March, (1997).

[17] C. Avellaneda, M.A. Macedo, A.O. Florentino, D. Barros Filho, M.A. Aegerter, in Proc. SPIE's Meeting Sol-Gel Optics III, San Diego, USA, 24 - 29 July (1994), 2288, 422-34.

[18] C. Avellaneda, A. Pawlicka, M. Atik, M.A. Aegerter, in *Proceeding of XVII international congress on glass* (Beijing), Bd. 4, (1995), 465-470.

[19] M.-K. Nazeeruddin, A. Kay, I. Rodicio, R. Humphry-Baker, E. Müller, P. Liska, V. Valchopoulos, M. Grätzel, *J. Am. Chem. Soc.* **115** (1993), 6382-6390.

[20] A. Pawlicka, M. Atik, M.A. Aegerter, *J. Mater. Sci. Lett.* **14** (1995), 1568.

[21] M.A. Aegerter, “Sol-gel chromogenic materials and devices", in Structure abd Bonding: Vol. 85, "Optical and Electronic Phenomena in Sol-Gel Glasses and Modern Applications", Eds. R. Reisfeld and C. Jørgensesn, Springer Verlag, (1996), 149 -194.

[22] M.A. Aegerter, C.O. Avellaneda, A. Pawlicka, M. Atik, *J. Sol-Gel Sci. Technol.* **8** (1997), 689-696.

[23] D. Barros Filho, P.P. Abreu Filho, U. Werner, M.A. Aegerter, *J. Sol-Gel Sci. Technol.* **8** (1997), 735-742.

[24] A. Pawlicka, M. Atik, M.A. Aegerter, *Thin Solid Films* **301** (1997), 236-241.

[25] C.J. Barbe, F. Arendse, P. Comte, M. Jirousek, F. Lenzmann, V. Shklover, M. Grätzel, *J. Am. Ceram. Soc.* **80** (1997), 3157-3171.

[26] M. Schmitt, S. Heusing, M.A. Aegerter, A. Pawlicka, C. Avellaneda, *Sol. Energy Mater. Sol. Cells* **54** (1998), 9-17.

[27] M. Schmitt, M.A. Aegerter, in Switchable materials and flat panel displays, 21-22 July 1999 Denver, Colorado/ed. Carl M. Lampert. Bellingham, WA: SPIE, (1999), (SPIE Proceedings; 3788), 93-102

[28] M.A. Aegerter, *Sol. Energy Mater. Sol. Cells* **68** (2001), 401-422.

[29] *http://acre.murdoch.edu.au/refiles/pv/text.html*.

[30] C.A. Koval, J.N. Howard, *Chem. Rev.* **92** (1992), 411-433.

[31] A.J. Bard, R. Memming, B. Miller, *Pure Appl. Chem.* **63** (1991), 569-596.

[32] D. Meissner, in *Solarzellen, Physikalische Grundlagen und Anwendungen in der Photovoltaik* (Ed.: D. Meissner), Vieweg, Braunschweig, (1993), 137-150.

[33] R. Memming, in *Electrochemistry II, Topic in Current Chemistry* (Ed.: E. Steckhan), Bd. 143, Springer Verlag, Berlin, (1988), 79-112.

[34] S.R. Morrison, *Electrochemistry at Semiconductor and Oxidized Metal Electrodes*, Plenum, New York, (1980).

[35] Y.V. Pleskov, *Solar Energy Conversion, a Photoelectrochemical Approach*, Springen Verlag, Berlin, (1990).

[36] K. Rajeshwar, L.M. Peter, A. Fujishima, D. Meissner, M. Tomkiewicz, *Photoelectrochemistry, in The Electrochemical Society Preoceedings* (Pennington, NJ), Bd. 97-20, (1997).

[37] H. Tusumbomura, H. Kobayashi, *Crit. Rev. Solid State Mater. Sci* **18** (1993), 261-326.

[38] H.J. Lewerenz, H. Jungblut, *Photovoltaik, Grundlagen und Anwendungen*, Springer Verlag, Berlin, (1995).

[39] S. Licht, D. Peramunage, *Nature* **345** (1990), 330.

[40] S. Licht, D. Peramunage, *J. Electrochem. Soc.* **139** (1992), L23-L26.

[41] D. Peramunage, S. Licht, *Solar Energy* **52** (1994), 197-204.

[42] Y. Nakato, H. Tsubomura, *Electrochim. Acta* **37** (1992), 897-907.

[43] R. Tenne, A. Wold, *Appl. Phys. Lett.* **47** (1985), 707.

[44] N.S. Lewis, *Appl. Phys. Lett.* **45** (1984), 1095-1097.

[45] M. Rosenbluth, C.M. Lieber, N.S. Lewis, *Appl. Phys. Lett.* **45** (1984), 423-425.

[46] M. Rosenbluth, N.S. Lewis, *J. Am. Chem. Soc.* **108** (1986), 4689.

[47] H. Kobayashi, Y. Kogetsu, K. Ikezumi, Y. Nakato, *J. Electroanal. Chem.* **371** (1994), 53-58.

[48] S. Licht, *Appl. Phys. Lett.* **46** (1985), 608.

[49] G. Hodes, *Nature* **285** (1980), 29-30.

[50] K.C. Chang, *Science* **196** (1977), 1097.

[51] B.A. Parkinson, A. Heller, B. Miller, *Appl. Phys. Lett.* **33** (1978), 521-523.

[52] B.A. Parkinson, A. Heller, B. Miller, *J. Electrochem. Soc.* **126** (1979), 954-960.

[53] A. Heller, J. Lewerenz, B. Miller, *Ber. Bunsenges. Phys. Chem.* **84** (1980), 592-595.

[54] A.T. Howe, *J. Chem. Soc., Chem. Commun.* (1983), 1407-1408.

[55] D. Cahen, Y.W. Chen, *Appl. Phys. Lett.* **45** (1984), 746.
[56] A. Heller, B. Miller, F. Thiel, *Appl. Phys. Lett.* **38** (1981), 232.
[57] Y. Nakato, K. Ueda, H. Yano, H. Tsubomura, *J. Phys. Chem.* **92** (1988), 2316.
[58] H. Tsubomura, Y. Nakato, *Nouv. J. de. Chemie* **11** (1987), 167-171.
[59] L.G. Casagrande, N.S. Lewis, S.M. Kelso, *170th Electrochemical Society Meeting* (San Diego), (1986), Abstr. No. 607.
[60] H.J. Lewerenz, H. Goslowsky, K.D. Husemann, S. Fiechter, *Nature* **321** (1986), 687.
[61] K. Nakatani, S. Matasudaira, H. Tsubomura, *J. Electrochem. Soc.* **125** (1978), 406.
[62] G. Kline, K. Kam, D. Canfield, B.A. Parkinson, *Solar Energy Materials* **4** (1981), 301-308.
[63] A. Heller, *J. Electrochem. Soc.* **125** (1978), 1159.
[64] H. Tributsch, in *New trends and applications of photocatalysis and photoelectrochemisrey for environmental problems* (Ed.: M. Schiavello), (1988).
[65] F. Willig, H. Gerischer, *Top. Curr. Chem.* **61** (1976), 31.
[66] H. Gerischer, *Photochem. Photobiol.* **16** (1972), 243.
[67] R. Memming, *Photochem. Photobiol.* **16** (1977), 243.
[68] T.H. James, in *Theory of the photographic process*, 4th Edition., Macmillan, New York, 1977.
[69] J.W. Weigl, *Angew. Chem., Int. Ed. Engl.* **16** (1977), 374.
[70] K.-P. Charle, F. Willig, in *Modern Aspects of Electrochemistry* (Eds: B.E. Convey, J.O.M. Bockris, R.E. White), Bd. 19, Plenum, New York, (1988), 359.
[71] A. Hagfeldt, B. Didriksson, T. Palmquist, H. Lindström, A. Schönecker, H. Rensmo, S.-E. Lindquist, *Sol. Energy Mater. Sol. Cells* **31** (1994), 481-488.
[72] M.L. Lampert, *Sol. Energy Mater. Sol. Cells* **34** (1994), 307-321.
[73] S.-E. Lindquist, H. Lindström, H. Rensmo, S. Södergren, A. Solbrand, H. Pettersson, *SPIE* **2255** (1994), 803-810.
[74] G. Smestad, C. Bignozzi, R. Argazzi, *Sol. Energy Mater. Sol. Cells* **32** (1994), 259-272.
[75] Y.-C. Shen, L. Wang, Z.-H. Lu, Y. Wei, Z.Q. -F., H.-F. Mao, H.-J. Xu, *Thin Solid Films* **257** (1995), 144-146.
[76] M. Matsumoto, H. Miyazaki, K. Matsuhiro, Y. Kumashiro, Y. Takaoka, *Solid State Ionics* **89** (1996), 263-267.
[77] B. O´Regan, D.T. schwartz, *J. Appl. Phys.* **80** (1996), 4749-4754.
[78] G.-L. Zhao, H. Kozuka, T. Yoko, *J. Ceram. Soc. Jpn., Int. Ed.* **104** (1996), 164-168.
[79] A. Zaban, A. Meier, A.J. Nozik, B.A. Gregg, *Electrochem. Soc. Proc.* **97-13** (1997), 306-316.
[80] K. Murakoshi, R. Kogure, Y. Wada, S. Yanagida, *Sol. Energy Mater. Sol. Cells* **55** (1998), 113-125.
[81] A. Stanley, B. Verity, D. Matthews, *Sol. Energy Mater. Sol. Cells* **52** (1998), 141-154.

[82] W. Kubo, K. Murakoshi, T. Kitamura, Y. Wada, K. Hanabusa, H. Shirai, S. Yanagida, *Chem. Lett.* (1998), 1241-1242.

[83] M. Gomez, J. Rodriguez, S.-E. Lindquist, C.G. Granqvist, *Thin Solid Films* **342** (1999), 148-152.

[84] M. Gomez, J. Rodriguez, S. Tingry, A. Hagfeldt, S.-E. Lindquist, C.G. Granqvist, *Sol. Energy Mater. Sol. Cells* **59** (1999), 277-287.

[85] G. Smestad, *Sol. Energy Mater. Sol. Cells* **55** (1998), 157-178.

[86] B.W. Jing, H. Zhang, M.H. Zhang, Z.H. Lu, T. Shen, *J. Mater. Chem.* **8** (1998), 2055-2060.

[87] K.P. Hanke, *Z. Phys. Chem. (Munich)* **Bd. 212** (1999), 1-9.

[88] J. Weidmann, T. Dittrich, E. Konstantinova, I. Lauermann, I. Uhlendorf, F. Koch, *Sol. Energy Mater. Sol. Cells* **56** (1999), 153-165.

[89] S. Yanagida, S. Kambe, W. Kubo, K. Murakoshi, Y. Wada, T. Kitamura, *Z. Phys. Chem. (Munich)* **Bd. 212** (1999), 31-38.

[90] M.M. Gomez, J. Lu, A. Hagfeldt, C.G. Granqvist, *Sol. Energy Mater. Sol. Cells* **64** (2000), 385-392.

[91] D. Kuciauskas, G. Sauve, M. S. Freund, H. B. Gray, J. R. Winkler, N.S. Lewis, *Abstracts of Papers of the american Chemical society* 222: 287-CHED Part 1 Aug. (2001) and 221: 231-ORGN Part 2 Apr. (2001).

[92] P.M. Sommeling, H.C. Rieffe, J.A.M. Roosmalen, A. Schönecker, J.M. Kroon, J. Wienke, A. Hinsch, *Sol. Energy Mater. Sol. Cells* **62** (2000), 399-410.

[93] S. Lee, Y. Jun, K.-J. Kim, D. Kim, *Sol. Energy Mater. Sol. Cells* **65** (2001), 193-200.

[94] Z.-S. Wang, C.-H. Huang, Y.-Y. Huang, Y.-J. Hou, P.-H. Xie, B.-W. Zhang, H.-M. Cheng, *Chem. Mater.* **13** (2001), 678-682.

[95] M. Okuya, K. Nakade, S. Kaneko, *Sol. Energy Mater. Sol. Cells* **70** (2002), 425-435.

[96] M. Grätzel,, Institute of Physical Chemistry II Swiss Federal Institut of Technology, Lausanne, (1995).

[97] R. Stangl, J. Ferber, J. Luther, *Sol. Energy Mater. Sol. Cells* **54** (1998), 255-264.

[98] J. Ferber, R. Stangl, J. Luther, *Sol. Energy Mater. Sol. Cells* **53** (1998), 29-54.

[99] D. Cahen, G. Hodes, M. Grätzel, J.F. Guillemoles, I. Riess, *J. Phys. Chem. B* **104** (2000), 2053-2059.

[100] M. Grätzel, *Heterogeneous photochemical electron tranfer*, CRC Press, Inc., (1989).

[101] D. Matthews, P. Infelta, M. Grätzel, *Sol. Energy Mater. Sol. Cells* **44** (1996), 119-155.

[102] S.Y. Huang, G. Schlichthörl, A.J. Nozik, M. Grätzel, A.J. Frank, *J. Phys. Chem. B* **101** (1997), 2576-2582.

[103] B.A. Gregg, A. Zaban, S. Ferrere, *Z. Phys. Chem. (Munich)* **Bd. 212** (1999), 11-22.

[104] University of Freiburg, *http://www.fmf.uni-freiburg.de/~biomed/FSZ/dsc.htm*.

[105] A.J. Bard, L.R. Faulkner, *Electrochemical methodes: Fundamentals and applications*, John Wiley & Sons, (1980).

[106] H. Tsubomura, H. Kobayashi, *Crit. Rev. Solid State Mater. Sci* **18** (1993), 261-326.

[107] J.-E. Moser, M. Wolf, F. Lenzmann, M. Grätzel, *Z. Phys. Chem. (Munich)* **Bd. 212** (1999), 85-92.

[108] G. Redmond, D. Fitzmaurice, M. Grätzel, *Chem. Mater.* **6** (1994), 686-691.

[109] I. Bedja, P.V. Kamat, X. Hua, A.G. Lappin, S. Hotchandani, *Langmuir* **13** (1997), 2398-2403.

[110] N. Kumagai, S. Komaba, N. Kumagai, *Proc. MRS*, Bd. 575, (1999), 39.

[111] N. Kumagai, K. Tanno, *Denki Kagaku* **50** (1982), 704-707.

[112] M. Winter, J.O. Besenhard, M.E. Spahr, P. Novak, *Adv. Mater.* **10** (1998), 725-763.

[113] P.M.S. Monk, R.J. Mortimer, D.R. Rosseinsky, *Electrochromism Fundamentals and applications*, VCH GmbH, (1995).

[114] M. Schmitt, *Entwicklung dotierter und undotierter Nb2O5 Sol-Gel-Schichten zur Anwendung als färbende Elektrode in elektrochromen Systemen*, Ph. D. dissertation, Universität des Saarlandes, (2000).

[115] U. Kölle, M. Grätzel, *Inorg. Chem.* **24** (1985), 2253.

[116] Gmelin-Institut für Anorganische Chemie derMax-Planck-Gesellschaft zur Förderung der Wissenschaften, Nio und Sauerstoff, in *Gmelins handbuch der anorganischen Chemie, 8 Auflage, 49 Tl.Bl, Verlagg Chemie GmbH, (1970).*

[117] H. Schäfer, R. Gruehn, F. Schulte, *Angew. Chem.* **78** (1966), 28-41.

[118] H. Schäfer, A. Dürkop, M. Jori, *Z. Anorg. Allg. Chem.* **275** (1954), 289-296.

[119] F.A. Cotton, G. Wilkinson, *Advanced inorganic chemistry*, 5Th Edition., John Wiley & Sons, New York, 1988.

[120] *http://www.webelements.com/webelements/compounds/text/Nb/Nb1O1-12034570.html.*

[121] G. Brauer, *Z. Anorg. Allg. Chem.* **248** (1941), 1-31.

[122] B.M. Gatehouse, A.D. Wadsley, *Acta Crystallographica* **17** (1964), 1545.

[123] W. Mertin, S. Anderson, R. Gruehn, *J. Solid State Chem.* **1** (1970), 419.

[124] F. Leves, W. Pelter, H. Wulf, *Naturwissenschaften* **51** (1964), 633.

[125] C.G. Granqvist, *Handbook of inorganic electrochromic materials*, Elsevier Science B. V., Amsterdam, (1995).

[126] T. Ikeya, M. Senna, *J. Non-Cryst. Solids* **105** (1988), 243-250.

[127] E.I. Ko, J.G. Weissman, *Catal. Today* **8** (1990), 27.

[128] E.I. Ko, J.G. Weissman, *Catal. Today* **8** (1990), 27-36.

[129] C.G. Granqvist, in *The CRC Handbook of Solid State Electrochemistry* (Eds: P.J. Gellings, H.J.M. Bouwmeester), CRC Press, Inc., Boca Raton, (1997), 587-615.

[130] F. Izumi, H. Kodama, *Z. Anorg. Allg. Chem.* **440** (1978), 155.

[131] A.A. McConnell, J.S. Anderson, C.N.R. Rao, *Spectrochim. Acta* **32A** (1976), 1067.

[132] J.G. Weissman, E.I. Ko, P. Wynblatt, J.M. Howe, *Chem. Mater.* **1** (1989), 187-193.

[133] G.R. Lee, J.A. Grayston, *Adv. Mater.* **5** (1993), 434-442.

[134] J.D. Mackenzie, in *Ultrastructure processing of ceramics, Glasses and compositites* (Eds: L.L. Hench, D.R. Ulrich), Wiley, new York, (1984), 15-26.

[135] *http://www.chemat.com/html/solgel.html*.

[136] M.N. Rahaman, *Ceramic processing and sintering*, Marcel Dekker, Inc., (1995).

[137] B. O´Regan, J. Moser, M. Anderson, M. Grätzel, *J. Phys. Chem.* **94** (1990), 8720-8726.

[138] R. Roy, *Science* **238** (1987), 1664.

[139] L.L. Hench, J.K. West, *Chem. Rev.* **90** (1990), 33.

[140] C.J. Brinker, G.W. Scherer, *Sol-gel science: the physics and chemistry of sol-gel processing*, Academic Press, New York, (1990).

[141] D.R. Uhlmann, G. Teowee, *J. Sol-Gel Sci. Technol.* **13** (1998), 153-162.

[142] R.B. Pettit, C.S. Ashley, S.T. Reed, C.J. Brinker (Ed.: L.C. Klein), Noyes, Park Ridge, New York, (1988), 91-99.

[143] S. Sakka, *J. Sol-Gel Sci. Technol.* **2** (1994), 451-455.

[144] C.J. Brinker, A.J. Hurd, P.R. Schunk, G.C. Frye, C.S. Ashley, *J. Non-Cryst. Solids* **147&148** (1992), 424-436.

[145] C.J. Brinker, A.J. Hurd, in *Sol-gel science and technology, Ceramic Transaction vol. 55* (Eds: E.J.A. Pope, S. Sakka, L.C. Klein), The American Ceramic Society, Los Angels, (1995), 157-171.

[146] G.W. Scherer, *J. Am. Ceram. Soc.* **73** (1990), 3-14.

[147] G.W. Scherer, *J. Sol-Gel Sci. Technol.* **8** (1995), 353-363.

[148] C.J. Brinker, G.W. Scherer, *Sol-gel science*, Academic Press, New York, 1991.

[149] C.G. Guizard, A.C. Julbe, A. Ayral, *J. Mater. Chem.* **9** (1999), 55-65.

[150] C. Alquier, M.T. Vandenborre, M. Henry, *J. Non-Cryst. Solids* **79** (1986), 383-395.

[151] G. Lee, R., J.A. Crayston, *J. Mater. Chem.* **4** (1994), 1093-1100.

[152] C.O. Avellaneda, M.A. Macedo, A.O. Florentino, M.A. Aegerter, in *SPIE's International Symposium on Optical Materials Technology for Energy Efficiency and Solar Energy Conversion XIII*, (18-22/04/94), Freiburg, Alemanha. 38-51.

[153] M.A. Aegerter, C.O. Avellaneda, in *Ceramics Transactions Sol-Gel Science and Technology*, **55** (1995), 223 - 234.

[154] C.O. Avellaneda, A. Pawlicka, M.A. Aegerter, *J. Mat. Sci.: Materials in Electronics* **33** (1998), 2181.

[155] M. Macek, B. Orel, U.P. Krasovec, *J. Electrochem. Soc.* **144** (1997), 3002-3010.

[156] M. Macek, B. Orel, *Sol. Energy Mater. Sol. Cells* **54** (1998), 121.

[157] B. Orel, U. Opera Krasovec, M. Macek, F. Svegl, U. Lavrencic stangar, *Sol. Energy Mater. Sol. Cells* **56** (1999), 343-373.

[158] N. Özer, D.-G. Chen, M.L. Lampert, *Thin Solid Films* **277** (1996), 162-168.

[159] N. Özer, M.D. Rubin, M.L. Lampert, *Sol. Energy Mater. Sol. Cells* **40** (1996), 285-296.

[160] N. Özer, T. Barreto, T. Büyüklimanli, M.L. Lampert, *Sol. Energy Mater. Sol. Cells* **36** (1995), 433-443.

[161] G.R. Lee, J.A. Crayston, *J. Mater. Chem.* **1** (1991), 381-386.

[162] L.-L. Hu, M. Wolf, M. Grätzel, Z.-H. Jiang, *J. Sol-Gel Sci. Technol.* **5** (1995), 219-226.

[163] M. Wolf, *Untersuchung nanokristalliner Materialienn in den System Nb/O und Nb/Ta/O für die Anwendung in farbstoffsensobilisierten, phoroelektrochemischen Solarzellen*, Ph. D. Dissertation, Universität Freiburg, (1998).

[164] F. Lenzmann, *Mesoporous, Nanoparticulate films of Nb_2O_5 and ZrO_2 preparation and characterization*, Ph. D. Dissertation, Institute of Physical Chemistry, Swiss Federal Institute of Technology, (2000).

[165] F. Lenzmann, V. Shklover, K. Brooks, M. Grätzel, *J. Sol-Gel Sci. Technol.* **19** (2000), 175-180.

[166] K. Sayama, H. Sugihara, H. Arakawa, *Chem. Mater.* **10** (1998), 3825-3832.

[167] K. Hara, T. Horiguchi, T. Kinoshita, K. Sayama, H. Sugihara, H. Arakawa, *Sol. Energy Mater. Sol. Cells* **64** (2000), 115-134.

[168] K. Eguchi, K. Koga, K. Sekizawa, K. Sasaki, *J. Ceram. Soc. Jpn., Int. Ed.* **108** (2000), 1067-1071.

[169] C.O. Avellaneda, Ph. D. dissertation, Universty of Sao Paulo, Brazil, (1999).

[170] N. Kumagai, K. Tanno, T. Nakajima, N. Watanabe, *Electrochim. Acta* **28** (1983), 17.

[171] G. Heiland, W. Bauer, M. Neuhaus, *Photochem. Photobiol.* **16** (1972), 315.

[172] M. Splitler, M. Lübke, H. Gerisher, *Ber. Bunsenges. Phys. Chem.* **83** (1979), 663.

[173] T. Yamase, H. Gerisher, M. Lübke, *Ber. Bunsenges. Phys. Chem.* **83** (1979), 658.

[174] P. Hoyer, H. Weller, *J. Phys. Chem.* **99** (1995), 14096-14100.

[175] T. Tao, L. Bahadur, *J. Electrochem. Soc.* **144** (1997), 179-185.

[176] H. Rensmo, K. keis, H. Lindström, S. Södergren, A. Solbrand, A. Hagfeldt, S.-E. Lindquist, L.N. Wang, Muhammed, *J. Phys. Chem. B* **101** (1997), 2598-2601.

[177] M. Kirishnan, X. Zhang, A.J. Bard, *J. Am. Chem. Soc.* **106** (1984), 7371.

[178] M. Shiimura, K. Shakushiro, Y. Shimura, *J. Appl. Electrochem.* **16** (1986), 683.

[179] H. Sato, M. Kawasaki, K. Kasatani, Y. Higuchi, T. Azuma, Y. Nishiyama, *J. Phys. Chem.* **92** (1988), 754.

[180] A. Haraguchi, Y. Yonezawa, R. Hanawa, *Photochem. Photobiol.* **52** (1990), 307.

[181] I. Bedja, S. Hotchandani, P.V. Kamat, *J. Phys. Chem.* **98** (1994), 4133-4140.

[182] I. Bedja, S. Hotchandani, R. Carpentier, *J. Appl. Phys.* **75** (1994), 5444-5446.

[183] K. Tennakone, P. Bandaranayake, G. Kumara, A. Konno, *Jpn. J. Appl. Phys. 2* **40** (2001), L732-L734.

[184] J. Moser, K. Brooks, M. Grätzel, *J. Phys. Chem. B* **103** (1999), 9328-9332.

[185] F. Lenzmann, J. Krueger, S. Burnside, K. Brooks, M. Grätzel, D. Gal, S. Ruhle, D. Cahen, *J. Phys. Chem. B* **105** (2001), 6347-6352.

[186] I. Shiyanovskaya, M. Hepel, *J. Electrochem. Soc.* **146** (1999), 243-249.

[187] A. Turkovic, Z.C. Orel, *Sol. Energy Mater. Sol. Cells* **45** (1997), 275-281.

[188] N. Vlachopoulos, P. Liska, J. Augustynski, M. Grätzel, *J. Am. Chem. Soc.* **110** (1988), 1216-1220.

[189] R.R. Bacsa, M. Grätzel, *J. Am. Ceram. Soc.* **79** (1996), 2185-2188.

[190] A. Kay, M. Grätzel, *Sol. Energy Mater. Sol. Cells* **44** (1996), 99-117.

[191] *Materials today*, Bd. July, 2001, 13.

[192] R. Grünwald, H. Tributsch, *J. Phys. Chem. B* **101** (1997), 2564-2575.

[193] M. Turrion, B. Macht, P. Salvador, H. Tributsch, *Z. Phys. Chem. (Munich)* **Bd. 212** (1999), 51-57.

[194] A. Hagfeldt, *Microporous and polycrystalline semiconductor electrodes studied by photoelectrochemical methods supported by quantum chemical calculations and photoelectron spectroscopy*, Ph. D. Dissertation, Uppsala, (1993).

[195] T.B. Meyer, A. Azam, A.F. Meyer, *The International Symposium on Optical Science and Technology, SPIE´s 47th Annual Meeting* (Seattle, Washington USA), 7 to 11 July (2002).

[196] H.H. Kung, H.S. Jarrett, A.W. Sleight, A. Ferretti, *J. Appl. Phys.* **48** (1977), 2463-2469.

[197] R. Vogel, P. Hoyer, H. Weller, *J. Phys. Chem.* **98** (1994), 3183-3188.

[198] R. Vogel, H. Weller, *SPIE* **1729** (1992), 82-92.

[199] I. Bedja, P.V. Kamat, S. Hotchandani, *J. Appl. Phys.* **80** (1996), 4637-4643.

[200] Gebüder Haake GmbH, *Einführung in praktische Viskosimetrie*, (1981).

[201 Schott Geräte, *Operating instructions, Ubbelohde viscometer*.

[202] D. Krug, *Untersuchungsmethoden in der Chemie: Einführung in die moderne Analytik*, Georg Thieme Verlag, Stuttgart, (1986).

[203] W.F. Hemminger, H.K. Cammenga, *Methoden der Thermischen Analyse*, Springer Verlag, Berlin, Heidelberg, (1989).

[204] M. Hesse, *Spektroskopische Methoden in der organischen Chemie*, Georg Thieme Verlag, Stuttgart, (1984).

[205] D.H. Williams, I. Fleming, *Strukturaufklärung in der organischen Chemie*, Georg Thieme Verlag, Stuttgart, (1985).

[206] K.-P. Zeller, *Untersuchungsmethoden in der Chemie: Einführung in die moderne Analytik*, Georg Thieme Verlag, Stuttgart, (1986).

[207] H. Krischner, B. Koppelhuber-Bitschnau, *Röntgenstrukturanalyse und Rietveldmethode*, Friedr. Vieweg & Sohn Verlagsgesellschaft mbH., (1994).

[208] J.M. Julian, D.G. Anderson, A.H. Brandau, J.R. McGinn, A.M. Millon, *An infrared spectroscopy atlas for the coatings industry*, Federation of societies for coatings technology, Blue Bell, Pennsylvania, (1991).

[209] *Tencor P-10 Surface Profiler User Manual, Tencor Instruments, Mountain View.*

[210] S.J. Gregg, K.S.W. Sing, *Adsorption, surface area and porosity*, 2nd Edition, Academic Press Inc. (London) Ltd, (1982).

[211] Normenausschuß Bauwesen (NABau) in DIN Deutsches Institut für Normung e. V, *Deutsche Norm* (1998), DIN 66134: 61998-66102.

[212] Normenausschuß Bauwesen (NABau) in DIN Deutsches Institut für Normung e. V, *Deutsche Norm* (1998), NABau 11.42.08 Nr 20-98.

[213] Normenausschuß Bauwesen (NABau) in DIN Deutsches Institut für Normung e. V, *Deutsche Norm* (1997).

[214] E.P. Barrett, L.G. Joyner, P.P. Halenda, *J. Am. Chem. Soc.* **73** (1951), 373-380.

[215] Micromeritics ASAP, *Manual of Micromeritics ASAP 2400*.

[216] O.S. Heavens, *Optical properties of thin films*, (1965).

[217] P. Liska, N. Vlachopoulos, M.-K. Nazeeruddin, P. Comte, M. Grätzel, *J. Am. Chem. Soc.* **110** (1988), 3686-3687.

[218] M.-K. Nazeeruddin, P. Liska, J. Moser, N. Vlachopoulos, M. Grätzel, *Helv. Chim. Acta* **73** (1990), 1788-1803.

[219] J.R. Macdonald, *Impedance spectrocopy: emphasizing solid materials and system*, John Willy & Sons Inc., (1987).

[220] C. Gabrielli, Technical report number 004/83, Solartton Instruments, (1980).

[221] *Zahner Meßtechnik, IM6 Owner´s manual*.

[222] C. Sanchez, J. Livage, M. Henry, F. Babonneau, *J. Non-Cryst. Solids* **100** (1988), 65.

[223] G.R. Lee, J.A. Crayston, *J. Chem. Soc., Dalton Trans.* (1991), 3073-3076.

[224] P. Griesmar, G. Rapin, C. Sanchez, J. Livage, *Chem. Mater.* **3** (1991), 335-339.

[225] B.E. Yoldas, I.K. Lloyd, *Ceram. Bull.* **18** (1983), 1171-1177.

[226] Kirk-Othmer, *Encyclopedia of chemical technology*, John wiley & sons, Inc., (1982).

[227] L.A. Aleshina, V.P. Malnenko, A.D. Phouphanov, N.M. Jakovleva, *J. Non-Cryst. Solids* **87** (1986), 350-360.

[228] Pihiladelphia, PA: Sadtler Laboratory Research, *The infrared spectra handbook of inorganic compounds*, (1984).

[229] D. Dolphia, A. Wick, *Tabulation of infrared spectral data*, john Wiley & Sons. Inc., (1977).

[230] J.B. Lambert, H.F. Shurvell, L. Verbit, R.G. Cooks, G.H. Stout, *Orgnic structural analysis*, Macmillan Publishing Co., Inc., (1976).

[231] P. Harder, M. Grunze, R. Dahint, G.M. Whitesides, P.E. Laibinis, *J. Phys. Chem. B* **102** (1998), 426-436.

[232] JCPDS-international Centre for Diffraction Data, JCPDS card No. 28-317, (1998).

[233] JCPDS-international Centre for Diffraction Data, JCPDS card No. 73-295, (1998).

[234] JCPDS-international Centre for Diffraction Data, JCPDS card No. 71-873, (1998).

[235] J.O.M. Bockris, S.U.M. Khan, *Surface electrochemistry: A molecular level approach*, Plenum Press, (1993).

[236] R. Memming, *Semiconductor electrochemistry*, Veley-VCH Verlag GmbH, (2001).

[237] L. Kavan, M. Grätzel, S.E. Gilbert, C. Klemenz, H.J. Scheel, *J. Am. Chem. Soc.* **118** (1996), 6716-6723.

[238] D. Barros Filho, *Comportamento Fotoeletroquimico de Films Finos Sol-Gel de Nb_2O_5 Sensibilizados com Complexos Polipiridinicos de Rutenio*, Ph. D. Dissertation, Universidade de Sao Paulo, 1997.

[239] M. Arita, Y. Hayashi, *Mater. Trans. JIM* **35** (1994), 233-237.

[240] H. Tang, K. Prasad, P.E. Sanjines, P.E. Schmid, F.J. Levy, *Applied Physics* **75** (1994), 2042.

[241] H. Minoura, M. Nasu, Y. Takahashi, *Ber. Bunsenges. Phys. Chem.* **89** (1985), 1064.

[242] S.R. Narayanan, B. Viswanathan, R.P. Viswanath, T.K. Varadarajan, *Indian J. Technol.* **19** (1981), 449-452.

[243] G. Rothenberger, D. Fitzmaurice, M. Grätzel, *J. Phys. Chem.* **96** (1992), 5983-5986.

[244] L. Kavan, K. Kratochvilova, M. Grätzel, *J. Electroanal. Chem.* **394** (1995), 93-102.

[245] Y. Liu, A. Hagfeldt, X.-R. Xiao, S.-E. Lindquist, *Sol. Energy Mater. Sol. Cells* **55** (1998), 267-281.

[246] G. Kron, T. Egerter, G. Nelles, A. Yasuda, J.H. Werner, U. Rau, *Thin Solid Films* **403-404** (2002), 242-246.

[247] Z. Kebede, S.-E. Lindquist, *Sol. Energy Mater. Sol. Cells* **57** (1999), 259-275.

[248] A. Zaban, A. Meier, B.A. Gregg, *J. Phys. Chem. B* **101** (1997), 7985-7990.

[249] C. Nasr, S. Hotchandani, P.V. Kamat, S. Das, K.G. Thomas, M.V. George, *Langmuir* **11** (1995), 1777-1783.

[250] R.D. McConnell, *Renewable & Sustainable Energy Reviews* **6** (2002), 273-295.

[251] *www.solaronix.ch*.

[252] E. Cattaneo, B. Rasch, W. Vielstich, *J. Appl. Electrochem.* **21** (1991), 885.

[253] P. Novak, W. Vielstich, *J. Electrochem. Soc.* **137** (1990), 1681.

[254] S. Wasmus, W. Vielstich, *Electrochim. Acta* **38** (1993), 541.

[255] L. Kavan, P. Krtil, M. Grätzel, *J. Electroanal. Chem.* **373** (1994), 123-131.

[256] R.S. Crandall, B.W. Faughnan, *Appl. Phys. Lett.* **28** (1976), 95.

[257] B.W. Faughnan, R.S. Crandall, M.L. Lampert, *Appl. Phys. Lett.* **27** (1975), 275.